

Report Prepared by:

**Alberto A. Sagüés
Noreen D. Poor
Leonardo Cáseres
Mersedeh Akhoondan**

FINAL REPORT

**DEVELOPMENT OF A RATIONAL METHOD FOR PREDICTING CORROSION
RATES OF METALS IN SOILS AND WATERS**

Contract No. BD497

Final Report to Florida Department of Transportation

**A. A. Sagüés
Principal Investigator
Department of Civil and Environmental Engineering**

**University of South Florida
Tampa, FL 33620
October 31, 2009**

Technical Report Documentation Page

1. Report No. BD497		2. Government Accession No.		3. Recipient's Catalog No.	
4. Title and Subtitle DEVELOPMENT OF A RATIONAL METHOD FOR PREDICTING CORROSION RATES OF METALS IN SOILS AND WATERS				5. Report Date October 31, 2009	
				6. Performing Organization Code	
7. Author(s) A. A. Sagüés, N. D. Poor, L. Cáseres, M. Akhoondan				8. Performing Organization Report No.	
9. Performing Organization Name and Address Department of Civil and Environmental Engineering University of South Florida Tampa, FL 33620				10. Work Unit No. (TR AIS)	
				11. Contract or Grant No. BD497	
12. Sponsoring Agency Name and Address Florida Department of Transportation 605 Suwannee St. MS 30 Tallahassee, Florida 32399 (850)414-4615				13. Type of Report and Period Covered Final Report	
				14. Sponsoring Agency Code	
15. Supplementary Notes					
16. Abstract <p>Methods used by the Florida Department of Transportation for predicting corrosion rates of metallic piling, anchors, and metallic drainage pipe used in highway construction were examined and updates were proposed as needed. Pile and anchor procedures were found to be generally adequate, with caution on the possibility of enhanced underground corrosion and new modalities of microbiologically induced corrosion. Special attention was given to the case of aluminized steel drainage pipe due to recent cases of extensive premature corrosion of spiral-ribbed pipes made of that material. That corrosion, affecting in particular the formed pipe ribs and associated with manufacturing deficiencies, took place under nominally mild environmental conditions. Laboratory tests sought to establish whether a corrosion prediction method based on scaling tendency of the soil water was a better predictor of corrosion than the presently used method based on environmental resistivity and pH values. The results were supportive of the scaling tendency method under relatively aggressive accelerated test conditions. However, tests with a less nominally aggressive water indicated that under those conditions the aluminized layer may fail to provide cathodic protection to base steel exposed at highly strained areas of the material such as those that may exist at formed ribs. Microbial influenced corrosion (MIC) was found to be a potentially important component of field corrosion of the metallic components studied, and a recommendation for inclusion of MIC in future design guidelines was made. FDOT analysis methods for chloride, sulfate pH and resistivity were assessed and potential improvements were tested. Revised test procedures were formulated and proposed for adoption.</p>					
17. Key Words			18. Distribution Statement This report is available to the public through the NTIS, Springfield, VA 22161		
19. Security Classif. (of this report)		20. Security Classif. (of this page)		21. No. of Pages 294	22. Price

DISCLAIMER

The opinions, findings, and conclusions expressed in this publication are those of the authors and not necessarily those of the State of Florida Department of Transportation.

SI* (MODERN METRIC) CONVERSION FACTORS

APPROXIMATE CONVERSIONS TO SI UNITS

Symbol	When You Know	Multiply By	To Find	Symbol
LENGTH				
in	inches	25.4	millimeters	mm
ft	feet	0.305	meters	m
yd	yards	0.914	meters	m
mi	miles	1.61	kilometers	km
AREA				
in ²	square inches	645.2	square millimeters	mm ²
ft ²	square feet	0.093	square meters	m ²
yd ²	square yard	0.836	square meters	m ²
ac	acres	0.405	hectares	ha
mi ²	square miles	2.59	square kilometers	km ²
VOLUME				
fl oz	fluid ounces	29.57	milliliters	mL
gal	gallons	3.785	liters	L
ft ³	cubic feet	0.028	cubic meters	m ³
yd ³	cubic yards	0.765	cubic meters	m ³
NOTE: volumes greater than 1000 L shall be shown in m ³				
MASS				
oz	ounces	28.35	grams	g
lb	pounds	0.454	kilograms	kg
T	short tons (2000 lb)	0.907	megagrams (or "metric ton")	Mg (or "t")
TEMPERATURE (exact degrees)				
°F	Fahrenheit	5 (F-32)/9 or (F-32)/1.8	Celsius	°C
ILLUMINATION				
fc	foot-candles	10.76	lux	lx
fl	foot-Lamberts	3.426	candela/m ²	cd/m ²
FORCE and PRESSURE or STRESS				
lbf	poundforce	4.45	newtons	N
lbf/in ²	poundforce per square inch	6.89	kilopascals	kPa
APPROXIMATE CONVERSIONS FROM SI UNITS				
Symbol	When You Know	Multiply By	To Find	Symbol
LENGTH				
mm	millimeters	0.039	inches	in
m	meters	3.28	feet	ft
m	meters	1.09	yards	yd
km	kilometers	0.621	miles	mi
AREA				
mm ²	square millimeters	0.0016	square inches	in ²
m ²	square meters	10.764	square feet	ft ²
m ²	square meters	1.195	square yards	yd ²
ha	hectares	2.47	acres	ac
km ²	square kilometers	0.386	square miles	mi ²
VOLUME				
mL	milliliters	0.034	fluid ounces	fl oz
L	liters	0.264	gallons	gal
m ³	cubic meters	35.314	cubic feet	ft ³
m ³	cubic meters	1.307	cubic yards	yd ³
MASS				
g	grams	0.035	ounces	oz
kg	kilograms	2.202	pounds	lb
Mg (or "t")	megagrams (or "metric ton")	1.103	short tons (2000 lb)	T
TEMPERATURE (exact degrees)				
°C	Celsius	1.8C+32	Fahrenheit	°F
ILLUMINATION				
lx	lux	0.0929	foot-candles	fc
cd/m ²	candela/m ²	0.2919	foot-Lamberts	fl
FORCE and PRESSURE or STRESS				
N	newtons	0.225	poundforce	lbf
kPa	kilopascals	0.145	poundforce per square inch	lbf/in ²

*SI is the symbol for the International System of Units. Appropriate rounding should be made to comply with Section 4 of ASTM E380.

EXECUTIVE SUMMARY

The Florida Department of Transportation (FDOT) has a large inventory of metallic structural components in direct contact with soil and water, including metallic culvert pipe made of solid and clad aluminum alloy, galvanized steel, or aluminized steel; structural steel piling (both steel shapes and pipe), galvanized tie strips in mechanically stabilized earth (MSE) walls, and buried metals in a variety of additional engineering applications. Corrosion is the most important durability limitation factor in these components, which must operate for long design service lives ranging from decades to 100 years and beyond. Premature replacement of buried metallic components damaged by corrosion is costly and reliable means are needed for predicting the corrosion rates of metals in soil and waters.

The objective of this project is to develop a rational basis for predicting corrosion rates of structural metals in soil and water service. In addition, the work is intended to develop or confirm practical methods for forecasting, and for the supporting analysis to measure the environmental parameters used as input.

Priority areas were selected by concentrating on components and materials with large impact on construction and not addressed by other recently completed investigations. The selected areas were metallic piling and anchors, and metallic drainage pipe. Because of unexpected severe deterioration of aluminized steel drainage pipe in several Florida locations observed in 2005, much of the project effort was focused on the performance of that material in culvert applications.

Properties of soil and water that influence corrosion rates of buried metals include temperature, oxygen concentration, resistivity, pH, and scaling tendency; presence of acids, alkalis, and salts; soil particle size distribution, porosity, and water content; and microbial activity. The characteristics of the associated modes of deterioration and needs for improvement of analysis methods were evaluated at the onset of the project. Chloride and sulfate analysis were selected for development of alternative test methods. Resistivity and pH method refinements were addressed as well.

Microbial activity was also selected as a new area of environmental characterization. A potentially important factor in corrosion in the field may be the presence of microbiologically-influenced corrosion (MIC). The above field observations and laboratory experiments were examined combined with results of a literature review. It was concluded that carbon steel, stainless steel, galvanized steel and aluminized steel buried in soil or immersed in natural waters are susceptible to localized corrosion due to MIC. Biofilms that develop from microbial activity on metal surfaces in natural waters can promote or inhibit corrosion, however, placement of metal structures or components in polluted or

stagnant water tends to thicken biofilms and accelerate corrosion. Tests that define soil aggressiveness per this mechanism should include organic matter content and water content to capture the potential for MIC.

A review of ca. 2008 FDOT and alternative design guidelines for steel pipe, H-pile, and sheet pilings, ground anchors (tie-backs), and wall anchor bars was conducted. Potential improvements for future versions of the FDOT Structure Design Guidelines include adopting depth-specific corrosion rates for steel pilings to a depth greater than 1 m (3 ft) below the water table; adoption of uniform and pitting corrosion guidelines for ground anchors (tie-backs), and design service life provisions for corrosion control measures in both pilings and anchors. Recent experiences outside Florida of accelerated corrosion in both freshwater and marine environments with high nutrient levels suggest that corrosion rates at the waterline could be in some instances as much as an order of magnitude greater than expected. The operating mechanism is not sufficiently known and awareness of this issue in inspection and monitoring is recommended.

Examination of the current durability forecasting methods used by FDOT for galvanized and for clad aluminum pipe, and of alternatives to those methods, did not show compelling evidence for changing procedures at this time. Until recently, the FDOT method to project durability of aluminized steel type 2 was considered to be similarly adequate. However, unexpected corrosion failures of aluminized pipe recently took place in central Florida locations after only a few years of service, much less than the predicted service life. Environmental conditions fell under relatively mild regimes per conventional classifications. Corrosion damage took place mostly at the pipe ribs and seams, which were found to be frequently affected by cuts from manufacturing deficiencies. Under those conditions of large breaks that expose steel, the aluminized coating, which is intended primarily as a barrier, is not expected to produce strong galvanic protection. Field half cell potential measurement results were consistent with that expectation. The service life estimation methods in present use do not have provisions for consideration of the effect of substantial localized aluminized coating damage. The following items in this summary address those issues.

A total alkalinity, hardness and CO₂ environmental content corrosion prediction method associated with scaling tendency was examined as a possible alternative to the current FDOT pH- and resistivity- based method. The focus on these tests (three model solutions) was on stagnant water conditions and a 300 ppm chloride content, to create a relatively aggressive environment and reveal trends in moderately short test intervals. For unblemished aluminized steel the findings tended to support retaining the present FDOT guidelines for durability forecasting regardless of scaling tendency, at least for environments that approach the low end of the recommended resistivity application range and have neutral to mildly alkaline conditions. In contrast, for blemished surface conditions with significant amounts of exposed base steel and for the same environmental

conditions as above, the scaling tendency method would appear to be a more appropriate alternative. The tests with blemished aluminized steel showed that galvanic protection was provided by the surrounding aluminized surface to base steel exposed at coating breaks in the three solutions tested. In the least aggressive of the three, however, protection developed only after a period of thousands of hours, when some corrosion of the base steel had already taken place.

It is strongly cautioned that other environmental parameters such as biological contributions may influence the corrosion performance of the Al/Fe system, and that eventual changes in existing guidelines should consider not only the specific results of this investigation but also the entirety of the performance record of aluminized steel pipe. Tests with solutions more representative of field conditions (one already examined here as noted below) and additional field surveys are planned for a continuation investigation.

Tests with mechanically formed aluminized steel samples showed that forming stresses caused cracks in the inner brittle coating layer, but also at the more ductile outer layer. The cracks expose small amounts of base steel to the water medium, promoting significant increase in half cell potential. Immersion cell experiments with a relatively benign solution representative of field conditions showed that the convex portion of specimens that were strongly formed by spherical indentation was susceptible to early corrosion development. Undeformed aluminized surfaces showed much less deterioration during the same test interval. This solution was not aggressive enough to induce strong manifestations of localized passivity breakdown or passive film dissolution of the aluminized coating at least in the short term. Therefore, the aluminized coating did not provide substantial galvanic protection of the steel substrate under those conditions, resulting in early corrosion of exposed steel in formed regions. Those findings may explain in part why early corrosion was experienced at the field locations under nominally mild environmental conditions. Similar tests were conducted with two of the more concentrated solutions noted earlier. Preferential corrosion of the formed steel took place (at least in short duration experiments) in a solution with low scaling tendency, but much less so for a solution with high precipitating tendency. Tests with regular production rib deformations are planned for a continuing investigation.

FDOT analysis methods for soil and water pH, resistivity, chloride, and sulfate were examined in detail and changes recommended. For all methods, it was recommended to implement laboratory chain-of-custody and labeling requirements; transport in tightly sealed containers in the dark at temperatures between freezing and 30°C; return samples to the testing lab within 24 hours of sampling whenever possible followed by immediate refrigeration, and to analyze water and soil samples within 28 days. Individual method recommendations include measuring pH in the field and reporting this measurement as field pH; for chloride and sulfate analyses centrifugation after extraction to separate soil from

water, and implementing measurement of a standardized solution and method blank to be carried through the entire procedure for quality assurance/quality control. Also for chloride and sulfate it is recommended to use a UV/VIS spectrophotometer and quantitative sample concentrations from a standard sulfate calibration solution. For sulfate analyses, filtration of extracts is recommended to very fine (0.2 μm) filter to remove suspended particles. Proposed revised procedures for the above are provided.

TABLE OF CONTENTS

DISCLAIMER.....	II
EXECUTIVE SUMMARY	IV
ACKNOWLEDGEMENTS	XIII
1 INTRODUCTION	1
1.1 Project Scope.....	1
1.2 Objectives	3
1.3 Approach.....	3
1.4 Priority Areas: Materials, Components, and Environmental Service Conditions.....	4
2 FACTORS THAT AFFECT CORROSION OF METALS IN WATER AND SOIL	6
2.1 Natural Waters	8
2.2 Natural Soils.....	9
2.3 Modified Environments	13
2.3.1 Engineered backfill.....	13
2.3.2 Industrial, agricultural, or urban sites.....	14
2.3.3 Stray current corrosion	14
2.4 FDOT Environmental Classifications Relevant to the Project Priority Areas	15
2.5 Summary and Conclusions	18
3 CORROSION MODES AND ESTIMATED SERVICE LIFE PREDICTION METHODS OF METALLIC PILING AND ANCHORS	19
3.1 Scope.....	19
3.2 Permanent Steel Piles	19
3.2.1 FDOT design guidelines.....	20
3.2.2 Potential alternative approaches	22

3.3 Soil and Rock (Ground) Anchors and Soil Nails.....	30
3.3.1 FDOT design guidelines.....	30
3.3.2 Potential alternative approaches	32
3.4 Discussion of FDOT and Alternative Durability Estimation Methods for Pilings and Anchors	34
3.4.1 Steel pilings.....	34
3.4.2 Anchors	36
3.5 Summary and Conclusions	37
4 METALLIC DRAINAGE PIPE CORROSION - FOCUS ON ALUMINIZED STEEL	38
4.1 Scope.....	38
4.2 FDOT Design Guidelines for Metallic Drainage Pipe.....	38
4.2.1 Materials and FDOT guidelines.....	38
4.2.2 Potential alternative approaches and recommendation - clad aluminum pipe.....	40
4.2.3 Potential alternative approaches and recommendation- galvanized pipe	40
4.3 Corrosion Resistance of Aluminized Steel Type 2	45
4.3.1 Manufacture and surface morphology of aluminized steel type 2....	45
4.3.2 Overview of aluminum corrosion	46
4.3.3 Pitting corrosion of aluminum	47
4.3.4 Prior field studies on the durability of aluminized steel type 2	49
4.3.5 Galvanic corrosion of aluminized steel type 2	50
4.4 Service Life Prediction Methods for Aluminized Steel Type 2.....	53
4.4.1 FDOT service life estimation method for aluminized steel pipe.....	53
4.4.2 Potential alternative approaches for aluminized steel pipe.....	54
4.5 Summary and Conclusions	55
4.6 Issues for Investigation on Aluminized Steel Performance.....	56
5 CONDITION OF DEFORMED COATING ON IN-SERVICE RIBBED ALUMINIZED STEEL TYPE 2 CULVERT PIPING	57
5.1 Field Experience and Analyses - St. Cloud, Florida	57
5.1.1 Soil and water samples examined.....	57
5.1.2 Water and soil chemistry	57
5.1.3 Visual assessment of the pipe metal coupons	60
5.1.4 Microscopic examination	67
5.1.5 Measurements of half-cell potentials in the field.....	73

5.1.6 Discussion of significance of findings from the St. Cloud, Florida site	74
5.2 Field Experience and Analyses - SR 586 Project, Curlew Road, Pinellas County.....	77
5.2.1 Observations and interpretation	77
5.3 Forming Strain	78
5.4 Summary and Conclusions	79
6 CORROSION OF ALUMINIZED STEEL TYPE 2 IN SCALE FORMING WATERS	81
6.1 Introduction.....	81
6.2 Experimental Procedure	82
6.2.1 Composition of aluminized steel type 2	82
6.2.2 Test solutions	82
6.2.3 Test cell configuration and electrochemical impedance spectroscopy (EIS).....	84
6.2.3.1 As-received test specimens	85
6.2.3.2 Blemished test specimens.....	86
6.2.4 Macrocell configuration and galvanic current measurements.....	86
6.2.5 Direct assessment of corrosion rates	87
6.3 Results.....	88
6.3.1 As-received specimens	89
6.3.2 Blemished specimens	96
6.3.3 Macrocell assemblies	113
6.3.4 Uncoupled steel specimens	117
6.3.5 Coating thickness measurements	118
6.4 Discussion	119
6.4.1 As-received specimens	119
6.4.2 Blemished specimens	132
6.4.3 Galvanic macrocells	140
6.4.4 Computation of the nominal corrosion current density	142
6.5 Conclusions	155
7 CORROSION ASSESSMENT OF MECHANICALLY FORMED ALUMINIZED STEEL	158
7.1 Introduction.....	158
7.2 Experimental Procedure	158

7.3 Results and Discussion	162
7.3.1 Metallographic analysis.....	162
7.3.2 Direct observation of corrosion performance.....	163
7.3.3 EIS measurements.....	164
7.4 Continuation Studies.....	167
7.4.1 Experimental methods.....	167
7.4.2 Results and discussion.....	167
7.5 Summary and Conclusions	175
8 EVALUATION OF ALTERNATIVE SERVICE LIFE ESTIMATION METHODS FOR ALUMINIZED STEEL TYPE 2 CULVERT PIPING	176
8.1 Estimates of Service Life	176
8.2 Results and Discussion	177
8.2.1 Service life estimates for as-rolled aluminized steel type 2	177
8.2.2 Service life estimates for blemished aluminized steel type 2.....	180
8.2.3 Status of service life estimation for aluminized steel	182
8.3 Summary and Conclusions	183
9 A SENSITIVE TEST TO ASSESS THE CATHODIC BEHAVIOR OF ALUMINIZED STEEL TYPE 2 IN SCALE-FORMING WATERS.....	184
9.1 Introduction.....	184
9.2 Experimental Procedure	185
9.3 Results.....	186
9.3.1 Microstructure analysis.....	186
9.3.2 Solution composition	187
9.3.3 E _{OC} and CYP trends.....	187
9.4 Discussion	191
9.5 Summary and Conclusions	196
10 MICROBIOLOGICALLY-INDUCED CORROSION	198
10.1 Introduction.....	198
10.2 Background.....	198
10.2.1 Features of MIC	198
10.2.2 Characteristics of bacteria that are agents of MIC	200
10.2.3 Mechanisms of MIC.....	204

10.2.4 MIC Monitoring	208
10.2.5 Control of MIC	209
10.2.6 Risk factors/risk factor models and mechanistic models for MIC	210
10.3 Enumeration of MIC-Related Bacteria in Florida Soils	213
10.4 Enumeration of Bacteria from Culvert Piping Soil, Sediment, Water, and Corrosion Product	215
10.4.1 Culvert pipe failure in Clearwater, FL	215
10.4.2 Culvert pipe failure in St. Cloud, FL.....	216
10.4.3 Culvert test pipe exhumation at Nassau Sound, FL	217
10.4.4 Culvert test pipe investigation in Wisconsin	220
10.5 Summary and Conclusions	220
11 PROPOSED MODIFICATIONS FOR METHODS TO DETERMINE DURABILITY FORECASTING INPUT PARAMETERS	222
11.1 Proposed Changes to FDOT Methods for pH, Resistivity, Chloride, and Sulfate Analysis	222
11.1.1 Sample collection, transport, and storage	222
11.1.2 Chloride method.....	225
11.1.3 Sulfate method	227
11.2 Summary and Conclusions	236
12 PROPOSED DURABILITY FORECASTING METHOD	237
13 REFERENCES	239
APPENDIX A SUMMARY OF VISUAL ASSESSMENT AND E_{OC} TRENDS FOR ALUMINIZED STEEL TYPE 2 IN WATERS OF VARYING SCALING TENDENCIES.....	264
APPENDIX B RESULTS OF MICROBIAL ANALYSIS FROM SOIL SAMPLES TAKEN FROM NASSAU SOUND, FLORIDA	265
APPENDIX C PROPOSED PH METHOD	266
APPENDIX D PROPOSED RESISTIVITY METHOD	269
APPENDIX E PROPOSED CHLORIDE METHOD.....	272
APPENDIX F PROPOSED SULFATE METHOD	277

ACKNOWLEDGEMENTS

The assistance with field inspections of many collaborators at the FDOT State Materials Office and from Concorr Florida, Inc. is greatly appreciated, as is that of numerous student participants in the University of South Florida College of Engineering Research Experience for Undergraduates program and staff from the USF Nanomaterials and Nanomanufacturing Research Center. The technical contributions to this research by Dr. Hector Videla, Dr. Luciano Viecelli Taveira, and Dr. Mirta Barbosa are also recognized.

1 INTRODUCTION

1.1 Project Scope

The Florida Department of Transportation (FDOT) has a large inventory of metallic structural components in direct contact with soil and water, including metallic culvert pipe made of solid and clad aluminum alloy, galvanized steel, or aluminized steel; structural steel piling (both steel shapes and pipe), galvanized tie strips in mechanically stabilized earth (MSE) walls, and buried metals in a variety of additional engineering applications. Corrosion is the most important durability limitation factor in these components, which must operate for long design service lives (DSL) ranging from decades to 100 years and beyond. Premature replacement of buried metallic components damaged by corrosion is costly not only because of the price of the new unit, but also because of the associated road demolition and service outage. Thus, it is much to the benefit of FDOT to have in place reliable means of predicting the corrosion rates of metals in soil and waters so that materials selections commensurate with the desired DSL are made.

The durability design criteria currently adopted by FDOT use as input the type of alloy and some parameters representative of the environmental service conditions of the unit. For example, for metallic drainage culverts those parameters include the environmental electrical resistivity, chloride content, and pH. Of those parameters, pH is particularly important in assessing aggressiveness of the water/soil for metallic alloys. The pH is an indicator of the molar concentration $[H^+]$ of hydronium ions ($pH = -\log [H^+]$). These ions promote the corrosion of metals by compromising the stability of passive layers and furthermore are an available species to be reduced in the cathodic reaction driving corrosion after its initiation. Resistivity is an inverse indication of the total ionic content of the medium including not only hydronium ions but also other species such as chloride ions that promote metal de-passivation. In addition, a medium with low resistivity permits better electrochemical coupling between cathodic and anodic sites on the metal surface, thus increasing the local rate of corrosion.

An example of the present approach adopted by FDOT is the "California" method (California Test Method 643, 1999) adapted for the FDOT Culvert Service Life Estimator (Cerlanek and Powers, 1993), which uses pH, together with resistivity, as key input parameters to forecast the durability of galvanized steel pipe. In this method, low values of pH (within a certain range) and resistivity forecast a short service life. Surface water, however, may have a relatively low pH (high $[H^+]$) and still not be very aggressive, because other dissolved species not considered in the California method may precipitate a protective scale on the metal surface. Conversely, high pH by itself within the specified range may not guarantee extended service life if the water does not promote the formation of a protective scale. These factors have been long

recognized by the use of scaling tendency indices to predict water corrosivity in other applications. For example, the Langlier Index uses alkalinity, hardness and pH to determine whether carbonate precipitation is likely in residential water distribution systems (AWWA, 1999). Similar limitations exist for the unqualified application of resistivity, which as a parameter cannot differentiate between the presence of beneficial or of detrimental ions in the medium.

Limitations like those exemplified above for the present corrosion forecasting method for galvanized pipe (and by extension to other galvanized steel components) exist also for other alloys commonly used by the FDOT. The durability of aluminum alloy culvert pipe is also estimated at present based on the pH and resistivity of the medium. The tolerance of passive films on aluminum to high pH conditions, however, tends to be less than that of films on a galvanizing zinc layer. Moreover, unlike the case of galvanized steel, the predominant form of corrosion in aluminum is pitting. The pit morphology also depends on whether plain aluminum alloy or Alclad aluminum (where the outer skin is a different, zinc-rich aluminum alloy) is used. All these complicating factors introduce much uncertainty in the durability prediction of aluminum alloys, which cannot be reliably covered by a simple resistivity/pH combined parameter. Comparable issues apply to predicting durability of increasingly popular aluminized steel, often in the form of aluminized steel type 2 produced by dipping steel strip in a molten aluminum bath. This treatment results in a thin aluminum-over-aluminum/iron alloy dual layer on top of the steel substrate, which improves the low pH resistance of the component compared to that of galvanized steel. Durability predictions by FDOT for this material (Cerlanek and Powers, 1993) are based only on resistivity and pH and do not take into account the system complexity and variety of responses possible. Similar concerns exist for other alloys that range from low cost materials such as plain steel for sheet piling to high cost choices such as stainless steel or nickel alloys for specialty applications where very high reliability is needed.

In mid 2005, unexpected severe deterioration of aluminized steel pipe was observed in storm water piping in City of St Cloud, Florida, and subsequently in storm water piping in Pinellas County and Pasco County. The deteriorated pipes were only a few years old, in contrast to a DSL of many decades predicted by FDOT methods. FDOT has a large inventory of aluminized steel drainage pipe and it is critical to determine the cause of early deterioration and ways to predict how and when similar damage may occur. Special activities toward identifying causes were initiated and produced initial findings as follows: some of the deterioration was found to be clearly the result of mechanical deficiencies created during fabrication of the pipes. Severe corrosion associated with the formed ribs on the aluminized steel sheet, however, suggested that mechanical distress of the aluminized layer during manufacture initiated early corrosion of the underlying plain steel. Early findings indicated also that the soil and water surrounding the affected pipes represented moderately aggressive conditions, conditions under which the underlying steel may corrode, but the aluminized

layer may not provide galvanic protection as the aluminum remains largely passive. Therefore, there may be a vulnerability window of combined material forming-environmental conditions where ribbed aluminized pipe is particularly prone to early corrosion. Conditions may include the presence of microbiologically- induced corrosion (MIC) or similar factors not normally included in assessments of soil or water corrosivity for estimating durability of metallic drainage pipe.

1.2 Objectives

The following broad objectives address the issues noted in the Project Scope:

- To develop a rational basis for predicting corrosion rates of structural metals in soil and water service, seeking to resolve the inadequacies indicated above. To develop or confirm practical methods for forecasting, and for the supporting analysis to measure the environmental parameters used as input.
- To identify causes of recent instances of severe unexpected corrosion of ribbed aluminized pipe, and conduct initial evaluation of impact on durability.

1.3 Approach

The overall objectives were addressed with the following specific approach tasks, keyed to Chapters in this report. The aluminized steel pipe corrosion incidents occurred while the project was already in progress, and much of the project emphasis was directed toward that issue.

- Establish priority areas of research, including materials, components, and environmental service conditions (Chapter 1, next section).
- Review environmental and service factors for corrosion relevant to Florida and to the project objectives (Chapter 2).
- Identify existing FDOT forecasting and analysis methods in the priority areas, evaluate alternatives and propose resolution. (Chapters 3-4).
- Examine by laboratory testing the corrosion evidence from field extracted and as-produced aluminized steel type 2 culvert piping (Chapter 5).
- Determine experimentally basic mechanisms of corrosion of aluminized steel type 2 with and without surface distress, and assess the effect of

variables relevant to the use of a potential alternative forecasting method. (Chapter 6).

- Assess experimentally the corrosion effect of mechanically forming aluminized steel (Chapter 7).
- Evaluate significance of the findings from the previous two tasks in formulating alternative durability forecasting models for aluminized steel. Formulate tentative durability forecasts for assessment in future work. (Chapter 8).
- Evaluate experimentally a polarization test as a means to identifying the factors responsible for the cathodic component of corrosion of aluminized steel (Chapter 9).
- Establish through field and laboratory microbiological testing to which extent microbiologically-induced corrosion (MIC) can be a contributing factor to corrosion of aluminized steel culvert piping (Chapter 10).
- Conduct laboratory and field testing to confirm and refine analysis methods for obtaining input parameters for forecasting method(s) (Chapter 11).
- Summarize findings on retaining or modifying forecasting methods (Chapter 12).

1.4 Priority Areas: Materials, Components, and Environmental Service Conditions

At the onset of the project the principal investigators and the FDOT State Materials Office project managers met to establish the metallic engineering components, alloy and metallic composites, and environmental service conditions in greatest need of assessment.

Some metallic components that are critical to the FDOT mission were nevertheless not included in this investigation, as there are recently completed or ongoing research efforts fulfilling durability design needs. For example, a study completed in 1998 (Sagüés, 2000) and a just-completed follow up investigation (Berke and Sagüés, 2009) have developed detailed information on predicting corrosion rates of metallic galvanized reinforcement in reinforced earth walls. Likewise, FDOT has an extensive research program addressing durability of concrete reinforcement that has already developed sophisticated methods for durability forecasting in that service environment (Sagüés, et al., 2001). Corrosion of high strength steel strand in post-tensioned tendons has also been addressed in a separate FDOT effort (Wang and Sagüés, 2005).

Discussion of the remaining needs and later project priorities resulted in selection of the following components and respective materials of construction as the focus of the present investigation:

**Table 1-1
Priority Component Classes and Materials**

Components		Materials
Metallic Piling	Foundation Piling (H,I; Pipe)	Steel
	Sheet Piling	Steel
Metallic Anchors	Prestressed Soil Anchors	Steel (High Strength)
	Dead Man Anchors	Steel
	Soil Nails	Steel
Metallic Drainage Pipe	Corrugated, Ribbed	Galvanized Steel
		Aluminized Steel
		Aluminum

The environmental service classifications that FDOT has in place for metallic material selection and durability forecasting are reviewed in the present project with provision for consideration of one or more of the following categories:

- Environment: pristine, rural, urban, industrial/mining
- Region: inland, coastal
- Elevation in soil: surface, buried/uniform depth, buried/mixed depth
- Physical soil characteristics: engineered (special, backfill), natural (rock, gravel, sand, silt, clay)
- Water exposure: tidal, submerged, episodic

2 FACTORS THAT AFFECT CORROSION OF METALS IN WATER AND SOIL

A brief overview of factors that affect corrosion of metals in water and soil are presented in this chapter, with an emphasis on study priority materials and environmental conditions as identified in Chapter 1.

Metal corrosion can occur through electrochemical uniform attack at the metal surface, galvanic coupling, pitting, or de-alloying; in crevices at metal junctions or at granular boundaries within a metal; or due to environmentally-induced cracking, hydrogen damage or erosion corrosion (Jones, 1996). Corrosion of metals submersed in natural waters or soils may be also affected by the presence of microorganisms (Videla, 1996), a phenomenon known as “microbiologically-influenced corrosion” or MIC.

Key environmental factors that affect the corrosion of metals in both soils and waters are temperature, pH, and oxygen availability. Halide ions, notably Cl^- , aggravate corrosion as they promote breakdown of protective passive films (Jones, 1996). Gas dissolution and diffusion, solid precipitation or dissolution rates, and chemical reaction rates are all temperature-dependent, for example. For iron corroding in an open water solution containing dissolved oxygen, the corrosion rate doubles for every 30 °C up to 80 °C, where the increased oxygen diffusion rates are overcome by the significantly reduced water solubility of oxygen (Uhlig and Revie, 1985). Soils in northern Florida are thermic, with average annual temperatures between 15 and 22 °C and a greater than 6 °C temperature change between winter and summer, while soils in peninsular Florida are hypothermic, with average annual temperatures >22 °C and a greater than 6 °C temperature change between winter and summer (NRCS, 1999). Thus, for all other soil factors being equal, buried metal tends to corrode at a higher rate in peninsular Florida than in northern Florida due to temperature effects.

Strong acids like hydrochloric acid and sulfuric acid atmospherically deposit to surface waters and soils; carbonic acid is a weak acid formed by the dissolution of carbon dioxide into rain, surface or soil waters, and organic acids are weak acids produced by decaying organic matter. Water-dissolved acids increase the corrosion rates of aluminum and iron when the hydronium ion concentration increases above 10^{-4} M (pH 4). The corrosion rate is enhanced below pH 4 because the protective passive film is dissolved and the increased hydronium ion concentration shifts the cathodic rate limiting step from the oxygen diffusion to the uncorroded metal to hydrogen gas production at the reaction anode (Jones, 1996).

Strong alkali such as sodium hydroxide, calcium hydroxide or lime, and sodium carbonate can influence corrosion rates as well. Aluminum corrosion at ambient temperature is accelerated at a hydroxide concentration above $\sim 10^{-6}$ M (pH 8), as hydroxide ions effectively dissolve the passive film on aluminum

(Jones, 1996). Zinc, the coating for galvanized steel, also experiences high corrosion rates at high as well as low pH values. In contrast, the corrosion of iron and steel is usually mitigated in alkaline (but not extremely so) conditions as they promote the stability of the steel passive film (Uhlig and Revie, 1985).

Oxygen both helps and hinders corrosion of iron and steel: as oxygen diffuses to freshly exposed iron the initial corrosion rate can be high, but as a corrosion product layer (rust) builds up on the metal surface, the corrosion rates are reduced. Further corrosion is then limited by the diffusion of oxygen through the oxide layer to the unaltered metal surface. In distilled water, the corrosion rate of mild steel is proportional to the dissolved oxygen content up to ~12 mg/l; beyond this oxygen content, the corrosion rate may fall to a low value as the metal surface tends to become passivated. The critical oxygen content goes up with higher salt concentrations and a passive rust layer does not form for steel immersed in seawater (Uhlig and Revie, 1985).

Corrosion is also enhanced when differences in the partial pressure of oxygen exist across an iron or steel surface forming a “differential oxygen cell” (Jones, 1996). The corrosion enhancement affects the steel in the low oxygen zone due to a complex combination of factors that are often misrepresented (Martins and Nunes, 2006). Such a cell might happen on a small scale, as in the crevices of a structural joint, but also in a large scale as in a structural component buried in soil. For a vertical steel column penetrating horizontal soil layers, a differential oxygen cell may form at the boundary between a layer of coarser and finer grained soil. A vertical steel column partially or only periodically submerged in water may corrode preferentially near the boundary of the water and air.

Aerated water that flows within piping or around metal structures delivers oxygen to the metal surface and thus facilitates corrosion. If the flow velocities and associated turbulence are sufficient, then “erosion corrosion” can occur, which can be aggravated by suspended abrasive particles. Intermittent water flow through culvert piping can have a similar effect (Bednar, 1989). Tomlinson (1994) discussed five different zones of corrosion, each with a difference corrosion rate, for steel piles in marine environments (Table 2-1).

Table 2-1
Corrosion Rates for a Steel Pier Penetrating Air, Seawater, and Sediment
 (Morley and Bruce, 1983, as cited in Tomlinson, 1994)

Zone	Corrosion Rate, mm/yr
Splash zone	0.09
Intertidal zone	0.04
Low-water zone	0.09
Immersion zone	0.05
Buried zone	0.02

Organic matter present in natural waters and soils are a source of food and energy for microscopic organisms including bacteria and fungi that are commonly associated with microbiologically-influenced corrosion (MIC). The role of organic matter in MIC is further explained in Chapter 10.

2.1 Natural Waters

In natural waters, not only do the water temperature, pH and dissolved oxygen content affect the corrosion rate of immersed metals, but so do water hardness, salt content manifested by conductivity (or resistivity if so expressed) , and dissolved gases of carbon dioxide and hydrogen sulfide.

Hard waters contain higher concentrations of dissolved calcium and magnesium—cations that have a tendency to precipitate out of solution to form a protective calcium carbonate scale. For drinking water, this scaling tendency may be predicted by the Langelier Saturation Index (LSI), which is the difference between the measured pH of the water and the pH at which the water is saturated with calcium carbonate. A positive LSI indicates the water is supersaturated with calcium carbonate and scale formation is favored, while a negative LSI indicates that scale dissolution is favored (Snoeyink and Jenkins, 1980; AWWA, 1999). The total alkalinity, calcium concentration, ionic strength, pH, and temperature of the water are required to calculate an LSI, but the resulting predictions will not likely be valid for surface waters with suspended or dissolved solids that may complicate the calcium carbonate precipitation chemistry. Moreover, in natural waters calcium carbonate may precipitate on suspended particles instead of the metal surface, and thus confer no protective scale (Uhlig and Revie 1985).

Bednar (1989) reported that the combination of higher annual rainfalls and higher temperatures in some climatic regions produces a “soft and pure” groundwater that is more corrosive because of its low mineral content, a result of the perpetual leaching of soluble salts by rainfall and the chelation of metals by organic acids from decomposing vegetation. Bednar (1989) describes a scaling tendency that accounts for the roles of bicarbonate and multivalent cations, corrected for the presence of carbonic acid, in forming stable precipitates (Equation 2-1).

$$\text{Alkalinity} + \text{Hardness} - \text{Free CO}_2 \text{ (ppm)} \quad (2-1)$$

Aluminum has been a satisfactory choice for soft water (e.g., in distilled water lines) in which heavy metal ions were removed. Traces of metals like copper or iron can plate out on aluminum surfaces and create galvanic cells that result in localized losses of aluminum (Uhlig and Revie, 1985). In laboratory studies, Cásares and Sagüés (2005) found that exposure of type 2 aluminized steel to waters containing differing amounts of calcium (hardness), bicarbonate (alkalinity) and 370 ppm chloride yielded extremely low corrosion rates for high

total alkalinity and a positive LSI. In the absence of alkalinity or precipitating hardness, the chloride caused early pitting of the aluminized layer.

Certain salts such as sodium chloride, potassium chloride, sodium sulfate and sodium iodide affect the conductivity of water but not its pH. Sodium chloride is abundant in sea water and brackish water. When the conductivity of water is low, the metallic anodic and cathodic regions cannot be widely separated and much of the corrosion involves local cell action. The metal ions created near the local anodes react with the hydroxide ions released at the nearby local cathodes tending to form a protective metal hydroxide coating, which then can act as a diffusion barrier in mitigate corrosion. When the conductivity of water is high, the anode and cathode can be further apart (significant macrocell action) and the hydroxide ions released at the cathode may not efficiently reach the anodic region lessening the opportunity for protective scale formation. Corrosion rates are greater for increasing sodium chloride concentrations up to ~3% or about that of seawater; above that, the depassivating effect of chloride is counter-balanced by lower dissolved oxygen concentration, and corrosion rates are reduced with increasing chloride content. Calcium and magnesium minerals present in seawater may mitigate corrosion by precipitating as calcium carbonate or magnesium hydroxide on the metal surface.

Carbonic acid found in surface waters represents carbon dioxide equilibrium between the atmosphere and a well-mixed water surface layer; nearer to water sediments or in groundwater, carbonic acid is present due to the release of carbon dioxide during microbial respiration. Carbonic acid is mildly corrosive but can form protective ferrous carbonate scales on metal surfaces. Hydrogen sulfide is another gas that is often found in groundwater and is corrosive to carbon steel but not greatly to aluminum or aluminum alloys (Uhlig and Revie, 1985, Jones, 1996; Oshe et al., 2001). Certain environmental conditions promote sulfate-reducing bacteria, which produce this toxic gas.

2.2 Natural Soils

In addition to soil pH, temperature and oxygen content, soil porosity (synonyms in the context of corrosion are aeration, drainage and texture), electrical conductivity, dissolved salts, moisture content, and reduction/oxidation (redox) potential are soil properties that affect the corrosion rates of buried metals (Uhlig and Revie, 1985; Escalante, 1989). A porous soil like sand permits both air and water flow. Air moving through a dry soil or dissolved in water can accelerate corrosion by providing oxygen to the metal surface, or hinder corrosion if a passive film or protective deposits are promoted on the metal surface. Corrosion of carbon steel and zinc-coated steel bars positioned above and below the water table (Camitz and Vinka, 1989), and of carbon steel piles driven through disturbed and undisturbed soils (Escalante, 1989) are offered as evidence. Moreover, an aerated soil is less amenable to growth of sulfate-reducing bacteria that can cause severe pitting in buried iron piping.

In a quest to establish corrosion rates for coal and iron ore transported in the steel compartments of ships, Gardiner and Melchers (2002) developed a theoretical construct that corrosion of iron in soil is controlled by the electrical resistivity and oxygen permeability of the soil. Their construct was based on experimental studies by Gupta and Gupta (1979) and by Wang (1997) [as cited in Gardiner and Melchers (2002)], and assumed that the moisture content of the soil determined which of these two corrosion parameters dominated. Below the “critical moisture content” of a given soil, corrosion is controlled by the soil resistivity, which is inversely proportional to moisture content; and above the critical moisture content the diffusion rate of oxygen to the metal surface controls as corrosion shifts from the gas- to water-phase kinetics. Gardiner and Melchers (2002) defined critical moisture content as the ratio of soil water to soil air at which corrosion rates were maximized.

Using this construct, Gardiner and Melchers (2002) mathematically explored the relationship between the corrosion rate of mild steel and critical moisture content of porous media for variable inputs of media particle size, particle density, porosity, cover depth and salt concentration. For a 20 mm cover depth, 100 ppm salt concentration, spherical particle with 2.65 g cm^{-3} density and a porosity of 45% typical of clean sand, the modeled corrosion rate decreased linearly from 0.15 mm yr^{-1} to 0.10 mm yr^{-1} for particle diameters of 0.6 mm to 2.0 mm, respectively. Corrosion rates also decreased with depth of cover and increased with salt content, as expected, but were insensitive to particle porosity or particle density. Modeled critical moisture contents were in the range of ~50% to ~70%, and increased with particle diameter but decreased with depth of porous media and salt concentration. These results suggest that steel and similar metals may corrode faster in sandy soils just above the water table, where water saturation near the critical moisture content is probable.

Salts and organic acids contribute to the corrosivity of a soil, and in general, a more conductive soil is also more corrosive. The *change* of soil conductivity along the length of a pipeline, however, may be a manifestation of factors that may cause more severe corrosion at localized zones than would be predicted by the averaged conductivity alone. Corrosion rates do not predictably increase with depth of burial from the surface.

Corrosion literature shows a preference for resistivity, with units of ohm-cm and as the reciprocal of conductivity, to describe the ability of a soil to carry current (Palmer, 1989). Soil resistivity is typically determined for the soil in its natural condition in the field by a 4-pin Wenner array resistance measurement (ASTM, 2006). Laboratory methods, typified by FDOT Designation FM 5-551 (FDOT, 2000b) specify increasing moisture content until a minimum resistivity value is obtained (roughly a saturation condition), which is then reported as the resistivity. It is important to differentiate between values obtained under both methods as the in-place resistivity depends on the moisture content of the soil,

while the laboratory measurements are for a standardized condition. Table 2-2 gives examples of steel corrosion classification schemes based on resistivity alone as determined in minimum-resistivity laboratory tests. Resistivity values discussed in the remainder of this chapter correspond to this method of measurement unless otherwise indicated.

Table 2-2
Steel Pipe Corrosion Classification

Soil Resistivity, Ω -cm		Corrosion Classification
Palmer, 1989*	Escalante, 1989*	
0 – 1,000	0 - 900	Very severely corrosive
1,001 – 2,000	900 – 2,300	Severely corrosive
2,001 – 5,000	2,300 – 5,000	Moderately corrosive
5,001 – 10,000	5,000 – 10,000	Mildly corrosive
>10,001	>10,000	Very mildly corrosive

*Citing different references.

The US Department of Agriculture Soil Survey Geographic (SSURGO) data base contains soil property data useful in predicting the corrosivity of a soil. Shown in Figure 2-1, for example, is a spatial plot of the risk of corrosion of uncoated steel for Florida soils, based on Romanoff (1957). This spatial plot was prepared from soil property data from the SSURGO database with Geographical Information Systems (GIS) software. Romanoff's (1957) guidance is summarized in Table 2-3.

Lower resistivity by itself is an indicator of potentially more efficient macrocell coupling between anodic and cathodic regions with consequent increase in the rate of galvanic corrosion if conditions are favorable. Lower resistivity is also an indication of increased ionic content of the water in contact with the soil. Since chloride and sulfate ions are usually an important fraction of the total ionic content, lower resistivity often reflects a higher content of these corrosion-promoting species. Therefore, resistivity is sometimes preferred as the sole descriptor of environmental aggressiveness. It is possible however that if no other innocuous ionic contributors are present, a soil or water could have moderately high resistivity and still contain a potentially harmful amount of chloride or sulfate. Results summarized by Elias (1990) indicate that exceeding 100 ppm chloride or 200 ppm sulfate (as fraction of soil mass) could result in appreciable corrosion rates (with respect to relatively thin component cross sections) in galvanized soil reinforcement. Consequently, both of those values or at least the one for chloride have been used as supplemental limits to identify highly corrosive conditions, as illustrated in the next section. Another common supplemental indicator is pH to delimit conditions aggressive to steel, by specifying a lower limit, usually 5 or 6 for steel. For galvanized steel which as noted earlier can experience corrosion at high pH values, an upper limit near pH 10 is also established.

Table 2-3
Guide for Estimating the Risk of Corrosion in Uncoated Steel
(Romanoff, 1957)

Property	Limits		
	Low	Moderate	High
Drainage class and texture	Excessively drained, coarse textured soil; well drained, coarse to medium textured soil; moderately well drained, coarse textured soil; or somewhat poorly drained, coarse textured soil	Well drained, moderately fine textured soil; moderately well drained, medium textured soil; somewhat poorly drained, moderately coarse textured soil; or very poorly drained soils with a stable high water table	Well drained, fine textured or stratified soil; moderately well drained, fine textured and moderately textured or stratified soil; somewhat poorly drained, medium to fine textured or stratified soil; or poorly drained soils with a fluctuating water table
Total acidity (meq/100 g)	<8	8-12	≥12
Resistivity at saturation (ohm/cm)	≥5,000	2,000-5,000	<2,000
Conductivity of saturated extract (dS/m)	<0.3	0.3-0.8	>0.8

2.3 Modified Environments

2.3.1 Engineered backfill

Replacement of excavated soils in road construction projects involves placement of backfill—either replacement with excavated soil or with a substitute backfill. Backfill performs several functions: provides structural integrity, stores and drains water, acts a barrier to electrical current (or for anode ground beds in a cathodically protected system is a conductor of electrical current), protects pipe or structure from damage from rocks or rubble, and restricts public access to buried metal (AISI, 1999; Robarge, 1999; Elias, 2000). Placement, compaction, and properties of backfill are typically specified; properties specified may include chemical composition, particle size distribution, drainage requirements, and soil plasticity. For example, CALTRANS (2003) states that in general imported backfill used as structure backfill should not be more corrosive than native soil material but for aluminized steel type 2 culvert piping, backfill must have a pH between 5.5 and 8.5 and a resistivity of 1,500 Ω -cm or greater (CALTRANS, 2003). FDOT (2007) gives the requirements for coarse and fine aggregates, which are often specified as backfill. According to FDOT (2007), fine aggregate “shall be reasonably free of lumps of clay, soft or flaky particles, salt, alkali, organic matter, loam or other extraneous substances.” In mechanically-stabilized earth walls, current practice is to control the electrochemical properties of backfill to minimize the sacrificial thickness of metallic reinforcement and to reduce uncertainties in reinforcement durability estimates (Elias, 2000). Recommended electrochemical limits for galvanized metallic reinforcements are summarized in Table 2-4, reflecting the considerations indicated above.

Table 2-4
Recommended Electrochemical Limits of Backfill Used with Metallic Reinforcements
(Elias, 2000)

Property	Limit	Standard Test Procedure
Resistivity, Ω -cm	<3,000	AASHTO T-288-91
pH	5<pH<10	AASHTO T-289-91
Organic content	<1%	AASHTO T-267-86
Chloride concentration, ppm	100	AASHTO T-291-91
Sulfate concentration, ppm	200	AASHTO T-290-91

It is noted that these limits apply to galvanized components in reinforced earthwalls, which have been addressed in separate FDOT-sponsored research (Berke and Sagüés, 2009) and will not be further discussed here.

Backfill compaction and segmentation can affect corrosion rates. Air voids are reduced and water retention is improved in backfill during the compaction process. Water added to achieve the desired degree of backfill compaction can consequently increase the corrosiveness of the backfill over its uncompacted

state (Elias, 2000), but the effect may be temporary. Moreover, a buried metal penetrating both a natural soil and an engineered backfill, for example, may create electrochemical conditions ideal for metallic corrosion from a differential aeration cell at the boundary of two soils (Schwerdtfeger and Romanoff, 1972; Beavers and Durr, 1998). A differential aeration cell between two soil strata may have been a contributing factor to severe spring line corrosion of an aluminized steel type 2 culvert pipe emplaced in native soil with a backfilled overburden, as described in Chapter 10, Section 10.4.4 of this report.

2.3.2 Industrial, agricultural, or urban sites

By-products from industrial, agricultural, and urban activities are often corrosive. Examples of activities that release acidic or alkaline wastes to the environment include coal-burning, ore mining, fertilizer manufacturing, metal smelting, concentrated animal feed operations, transportation, and land disposal of solid wastes including construction debris, slag, cinders, or ash. Gerwin and Baumhauer (2000) and Nord et al. (2005) present evidence that the apparent accelerated decay of buried iron and other metallic artifacts, which has been seen on a global scale, is due to a combination of increased acid, salt, and soot deposition to poorly buffered and well-aerated sandy soils, especially near urban areas or along the trajectories of polluted air masses.

2.3.3 Stray current corrosion

Both direct current (DC) and alternating current (AC) can cause corrosion with corrosion damage inversely proportional to frequency when the current “strays” from its intended pathway (Uhlig and Revie, 1985). Sources of stray DC current include electric railways, electric welding machines, cathodic protection systems, electroplating plants, and grounding systems; sources of AC current are electrical transmission lines, grounded AC power lines, or motor generators (McIntosh, 1982; Uhlig and Revie, 1985; Cotton et al., 2005). Stray electric currents in the ground can enter and exit buried metal and cause corrosion of metal at the point of exit (Uhlig and Revie, 1985). Stray currents can also alter electrical potentials within a buried metal or an adjacent electrolyte and thus shift anode-cathode couples, causing unanticipated corrosion (McIntosh, 1982; Metwally et al., 2007). Pipeline design such as bonding, installing anodic and cathodic protection, or adding insulated couplings can mitigate corrosion damage from stray current (McIntosh, 1982; Uhlig and Revie, 1985). Moreover, three-dimensional modeling techniques are available to assess the impact of an existing cathodic protection system (such as might be found on a gas pipeline) on a metallic pipeline or structure installed as part of a road construction project (Metwally et al., 2007). For electrical transit systems, stray DC currents can be minimized by reducing the resistance of rails, increasing the rail resistance to earth, using a floating rail system, or increasing the resistance of the soil around the rails, as examples (Cotton et al., 2005).

2.4 FDOT Environmental Classifications Relevant to the Project Priority Areas

For bridge structures, and more specifically their substructure as that is the portion in contact with soils and waters, and excluding concrete reinforcement per the scope of this project, FDOT (2009b) classifies the aggressiveness of the environment by soil or water pH, chloride concentration, and resistivity as shown in Figure 2-1 and Table 2-5. FDOT (2009b) extends these classifications to the environmental suitability for construction of retaining walls, steel sheet pile walls, and soldier pile/panel walls. It is noted that the classification "Marine Structure" applies to structures located up to 2,500 ft away from a body of brackish water. It is also noted that sulfate content does not enter in defining the classification as that parameter concerns only reinforced concrete. Likewise, consideration of those classifications regarding mechanically stabilized earth walls fall outside the scope of this project.

The resistivity regimes in Table 2-5 are generally consistent with the more recent guidelines (i.e. break points of ~ 1,000 and 5,000 ohm-cm for severely and mildly corrosive designations respectively) noted in Table 2-2 for natural soils. Chloride classification breakpoints are less conservative than those used for reinforced earth wall backfill, but as indicated earlier those applications involve relatively thin metallic cross sections. Moreover, the 5,000 ohm-cm breakpoint for designation of slightly aggressive conditions is quite stringent and compensates to some extent for the more liberal chloride level limits and absence of a sulfate specification.

For drainage piping, the service life estimate of galvanized steel, aluminized steel, and aluminum is not based on global classifications but is instead evaluated according to an empirical model from inputs of soil or water pH and resistivity (FDOT, 2009a; FDOT, 2008). The corresponding forecasting method will be discussed in Chapter 4.

Abbreviations:
 CL = Chloride
 ppm = parts per million

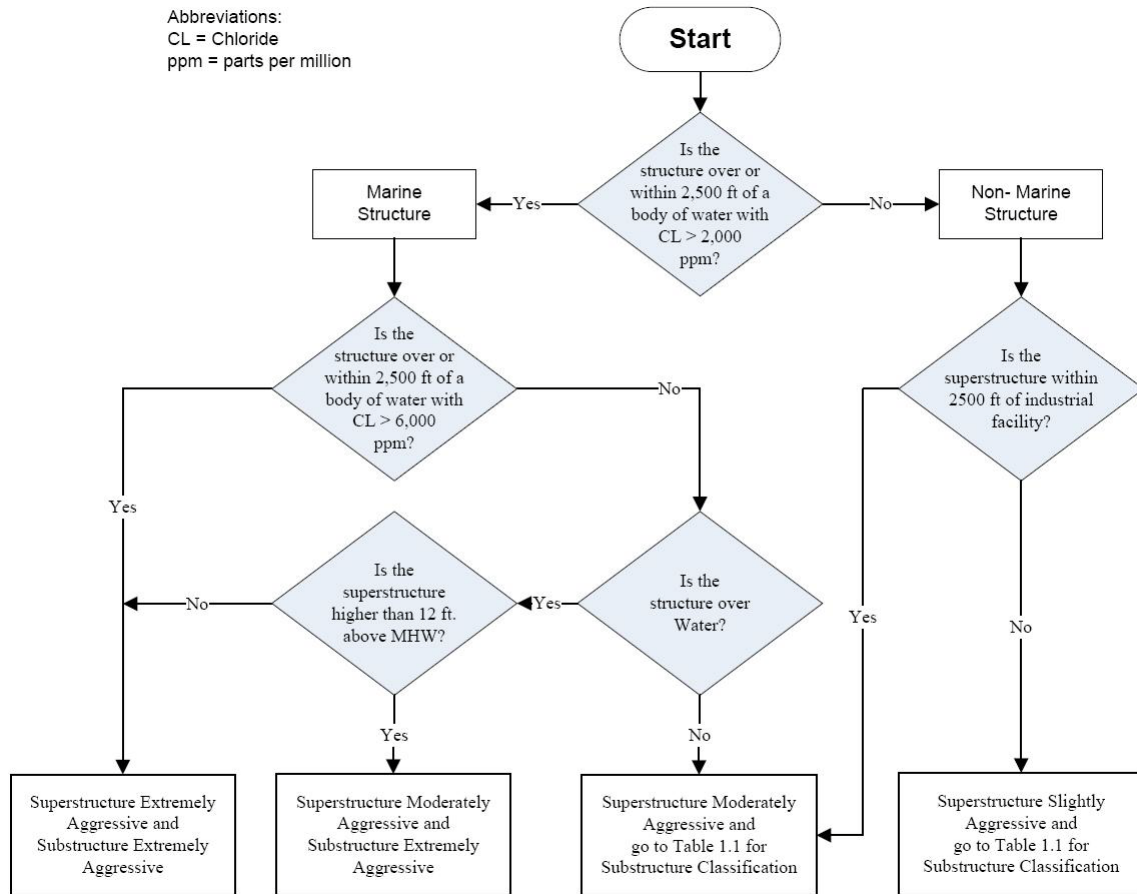


Figure 2.1 FDOT flow chart for definition of environmental classification for bridge structures from the 2009 Structural Design Guidelines Manual (FDOT 2009b). Table 1.1 in the flow chart is reproduced as Table 2-5 of the present report, which is customized for substructures only and excludes reinforced concrete.

Corrosion-Uncoated steel

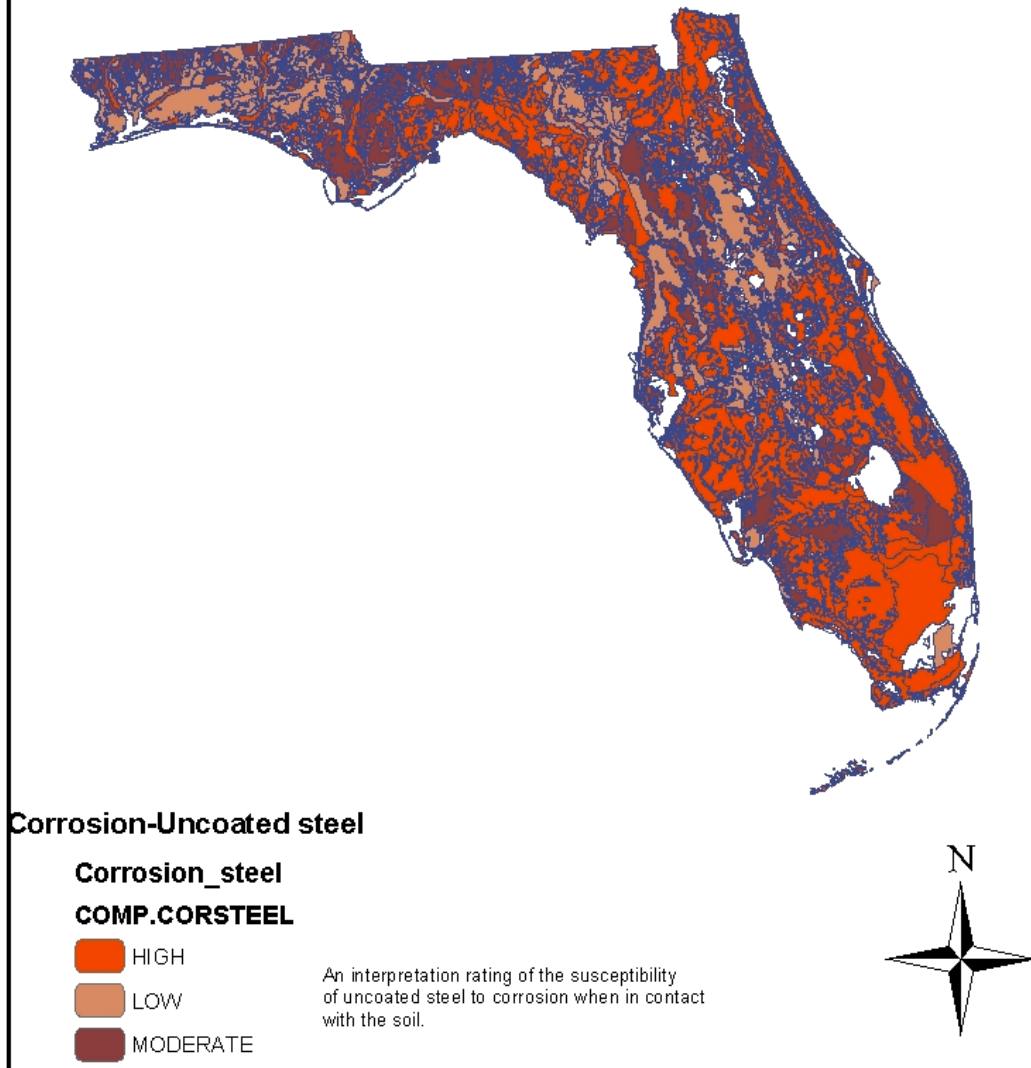


Figure 2-2. Corrosion potential for steel in Florida soil. This spatial plot was prepared from soil property data from the SSURGO database with Geographical Information Systems (GIS) software.

**Table 2-5
Florida DOT Environmental Classifications for Steel Substructures**

Classification	Environmental Condition	Soil or Water
Extremely aggressive (if any of these conditions exist).	pH	<6
	Cl ⁻ , ppm	>2,000
	SO ₄ ²⁻ , ppm	Not applicable
	Resistivity, Ω-cm	<1,000
Slightly aggressive (if all of these conditions exist).	pH	>7
	Cl ⁻ , ppm	<500
	SO ₄ ²⁻ , ppm	Not Applicable
	Resistivity, Ω-cm	>5,000
Moderately aggressive	This classification must be used at all sites not meeting the requirements for extremely aggressive or slightly aggressive	

2.5 Summary and Conclusions

Properties of soil and water that influence corrosion rates of buried metals include temperature, oxygen concentration, resistivity, pH, and scaling tendency; presence of acids, alkalis, and salts; soil particle size distribution, porosity, and water content; microbial activity. The environmental classifications used by FDOT for metallic bridge structures pertaining to the present project are generally consistent with known behavior and practice, and no recommendation for change is made at present.

3 CORROSION MODES AND ESTIMATED SERVICE LIFE PREDICTION METHODS OF METALLIC PILING AND ANCHORS

3.1 Scope

This chapter addresses metallic piling and metallic anchors, the first two of the main component classes that were identified as priority areas in Section 1.4 and listed in Table 1-1. The following items introduce the characteristics of those components and their service conditions. The extents to which present FDOT guidelines and guidelines from alternative sources cover predictive methods are discussed as well. Unless otherwise indicated, the FDOT design service life (DSL) for these components is 75 years (FDOT 2009b). FDOT predictive methods are oriented to using estimated corrosion rates toward calculation of a corrosion allowance (sacrificial) thickness.

3.2 Permanent Steel Piles

Structures and components under the general category of steel piles include steel pipes, H-piles, sheet piles, and wall anchor bars and are designed in accordance with FDOT (2009b) and references therein. Refer to Hannigan et al. (1998) for dimensions and properties of pipe piles and H-piles. Sheet pilings are a relatively expensive alternative for retaining walls and are typically used for a temporary cut application or for a cut application when placement of MSE wall soil reinforcing is difficult (FDOT, 2009b). Steel sheet pilings over 4.5 m are tied back with pre-stressed soil anchors, soil nails, or deadmen (FDOT, 2009b).

Pipe piles are typically constructed of ASTM A-252 steel, while H-piles typically conform to ASTM A36 and A572 Grade 50 steels (Hannigan et al., 1998). Those and most other structural steels have low-alloy compositions (ASM, 1972), and for most service environments of interest to this project the corrosion rate is not strongly dependent on alloy content. Even the so-called weathering steels, which contain typically <1% Cu and show low corrosion rates in atmospheric environments, tend to corrode similarly to the other alloys when buried or in submerged conditions. Therefore, unless otherwise indicated the generalized corrosion rate for a given exposure condition will be assumed to be the same for all structural steel grades.

Examples of protective coatings include coal-tar epoxies, “fusion”-bond epoxies, metalized zinc, metalized aluminum, and phenolic mastics (Hannigan et al., 1998).

3.2.1 FDOT design guidelines

For these components the FDOT Structure Design Guidelines (SDG) (FDOT, 2009b) address the effects of corrosion on durability by means of specified corrosion allowances, as shown in Table 3-1.

Table 3-1
Additional Sacrificial Steel Thickness for All Permanent Steel Substructure
and Wall Components
(FDOT, 2009b)

Steel Component	Substructure Environmental Classification			
	Slightly Aggressive, mm (in)	Moderately Aggressive, mm (in)	Extremely Aggressive, mm (in)	
			Case 1	Case 2 [†]
Pipe and H-piles completely buried in ground without corrosion protection measures	1.9 (0.075)	3.8 (0.150)	Do not use	5.7 (0.225)
Pipe and H-piles on land, partially buried in ground with corrosion protection measures	2.3 (0.090)	4.6 (0.180)	Do not use	6.9 (0.270)
Pipe and H-piles in water, partially buried in ground without corrosion protection measures	3.8 (0.150)	7.6 (0.300)	Do not use	N/A
Pipe and H-piles in water, partially buried in ground with corrosion protection measures	2.3 (0.090)	4.6 (0.180)	Do not use	N/A
Anchored sheet piles	0	0	0	0
Cantilevered sheet piles	1.1 (0.045)	2.3 (0.090)	3.4 (0.135)	3.4 (0.135)
Wall anchor bars with corrosion protection measures	2.3 (0.090)	4.6 (0.180)	6.9 (0.270)	6.9 (0.270)

* Water > 2000 ppm Chlorides or Resistivity < 1000 Ω-cm or pH < 6.0; except for Special Case.

† Special Case for Land Applications: Where Ground Water < 2000 ppm Chlorides and Resistivity > 5000 Ω-cm and 4.9 < pH < 6.0.

Testing for soil or water pH, chloride concentration, sulfate concentration, and resistivity is accomplished on subsurface soil and water samples collected for each relevant stratum at structure locations or along drainage pipe alignments as well as on samples of engineered backfill materials (FDOT, 2009a). Soil

sampling and analysis is done in accordance with standard FDOT methods (FDOT 2000a, 2000b, 2000c, 2000d).

Corrosion rates are explicitly indicated in commentary added to the SDG table where the rationale for the specified corrosion allowance is explained. Thus, for pipe- and H-piles nominal corrosion rates depend on FDOT environmental classification in Table 2-5 (further refined by chemical composition of environment) and on whether the pile is completely or partially buried in ground or immersed in water. The corrosion rate is assumed to be effectively zero for the first 30 years of service if "corrosion protection measures" (CPM) have been adopted. For permanent steel sheet piles, CPM means that the component surface has a shop-applied coating system consisting of an inorganic zinc primer and two coats of coal-tar epoxy per FDOT Specification Section 560-14 (FDOT, 2007). For wall anchor bars CPM is implemented by an epoxy-mastic heat shrink wrap or ducting and grouting but a mastic coating at the connection to the wall. The assumed corrosion rates for either uncoated steel or coated steel after 30 years service are indicated in Table 3-2. The zero sacrificial thickness allowance for anchored steel piles in Table 3-1 is not associated with any assumed corrosion rate value, resulting only from the declaration in the SDG commentary that the structure is structurally redundant and thus requires no corrosion allowance. It is noted that the assumed corrosion rates for extremely aggressive environments may be subject to revision pending an FDOT internal review of consistency with earlier manual versions.

**Table 3-2
Corrosion Rate per Side for Piles and Wall Anchor Bars
(FDOT, 2009b)**

Environmental Classification	Partially Buried mm/yr (in/yr)	Completely Buried mm/yr (in/yr)
Slightly Aggressive	0.03 (0.001)	0.01 (0.0005)
Moderately Aggressive	0.05 (0.002)	0.03 (0.001)
Extremely Aggressive	0.08 (0.003)*	0.05 (0.0015)*

*For pipe- and H-piles these values apply only to piles on land under the mitigating environmental conditions shown in Table 3-1. Corrosion rates for these piles are assumed to be excessively high otherwise in Extremely Aggressive environments.

For partially buried steel pipe or H-piles, corrosion is assumed to take place by two-sided attack at the soil and/or water line. For completely buried steel pipe or H-piles, corrosion is assumed to take place by two-sided attack from soil at both sides or single-sided attack from soil side if the pipe pile is filled with concrete. Corrosion of sheet piles is assumed to be a single-sided attack at soil and/or water line. The corresponding estimated service life (ESL) consistent with the values listed in Table 3-2 (after the CPM duration is reached) is then given for single-sided corrosion by Equation 3-1, where T is the allowable loss of metal thickness and CR is the corrosion rate, with consistent length units. Equations 3-2 and Equation 3-3 applies for the cases where corrosion can proceed from both sides of the metal surface at the same or different corrosion rates, respectively.

$$ESL = \frac{T}{CR} \quad (3-1)$$

$$ESL = \frac{T}{2CR} \quad (3-2)$$

$$ESL = \frac{T}{(CR_1 + CR_2)} \quad (3-3)$$

3.2.2 Potential alternative approaches

3.2.2.1 NCHRP Report 408 (Beavers and Durr, 1998)

In this study, Beavers and Durr (1998) developed a statistical model to explain the variation in piling corrosion rates at eight different sites (Equation 3-4). From their Pearson correlation matrix for measured soil parameters, however, chloride concentration was highly correlated with both weight loss observed in steel piles ($r=0.96$) and with pH ($r=0.84$), thus chloride concentration alone was a reasonable predictor of weight loss.

$$\text{Weight loss (mpy)} = -17.2 + 0.000761 [\text{Cl}^-] \text{ (ppm)} + 2.52 \text{ pH} \quad (3-4)$$

3.2.2.2 NYSDOT Report (Picozzi, et al., 1993)

A corrosion study for steel H-piles according a NYSDOT Technical Report specifies the following alternative corrosion prediction relationships as shown in Equations 3-5 and 3-6, which explain 75% and 73%, respectively, of the variability of the corrosion rates.

$$\text{Section loss (mils)} = 1.2964 \text{ pH} + 0.0025 [\text{Cl}^-] \text{ (ppm)} \quad (3-5)$$

$$\text{Section loss (mils)} = 1.5616 \text{ pH} \quad (3-6)$$

Those relationships above were obtained from weight loss measurements of H-piles exposed to miscellaneous fill and natural soil in the Buffalo Skyway Bridge site, New York. The averaged corrosion rates measured for the different environment conditions were 0.34 mm (13.2 mils) for an exposure time over 35 yr, regardless of the soil type. All measurements correspond to positions below the water table. The soil classification was between corrosive and very corrosive, according the CALTRANS classification of fills used for mechanically stabilized earth walls (MSEW). If the CALTRANS criterion were applied to these soils, a corrosion rate higher than 0.071 mm/yr (2.8 mils/yr) would be expected.

3.2.2.3 FHWA

The FHWA Manual on Design and Construction of Driven Pile Foundations (Hannigan et al., 1998), which is recommended in the FDOT (2000) proposes the following corrosion rate estimates:

- Piles buried in fill or disturbed natural soils: 0.08 mm/year
- Piles immersed in fresh water: 0.05 mm/year; however, corrosion rates at the waterline can be as high as 0.34 mm/year
- Piles in marine environments, where the numbers in brackets represent 95% maximum probable rates

Splash zone: 0.09 mm/year (0.18 mm/year*)

Inter-tidal zone: 0.04 mm/year (0.11 mm/year*)

Low-water zone: 0.09 mm/year (0.18 mm/year*). Abrasion damage may locally increase losses to 0.41 mm/year

Immersion zone: 0.05 mm/year (0.14 mm/year*)

Buried zone: 0.02 mm/year (0.05 mm/year*)

The above are presented in flowchart form in Figure 3-1.

3.2.2.4 CALTRANS

CALTRANS currently uses the following corrosion rates estimates for steel piling exposed to corrosive soil and/or water (CALTRANS, 2003):

- Soil Embedded Zone: 0.025 mm (0.001 in) per year
- Immersed Zone: 0.100 mm (0.004 in) per year
- Scour Zone: 0.125 mm (0.005 in) per year
- Undisturbed soil:

Within the region of the pile down to 1 m (3 ft) below the water table: 0.025 mm (0.001 in) per year

Outside the region of the pile down to 1 m (3 ft) below the water table: no corrosion rate is required.

If a site is characterized as non-corrosive, then no corrosion allowance (sacrificial metal loss) is necessary.

As in the current FDOT methods, the effective corrosion rates are doubled for steel H-pilings, because the two surfaces on either side of the web are exposed to the corrosive environment

A flowchart to determine the environmental classification and the corresponding corrosion rates is shown in Figure 3-2

3.2.2.5 AASHTO

For completeness, it is noted that the AASHTO LRFD Bridge Design Specifications Article 10.7.1.8 (AASHTO, 2007) only cites a FHWA report about corrosion in soil reinforced structures.

3.2.2.6 AWWA

The American Water Works Association (AWWA) includes in Appendix A of AWWA (2005) a 10-point system for assessing the corrosivity of soil for ductile iron pipe. This 10-point system includes terms for soil resistivity, moisture content, groundwater influence, pH, chlorides, sulfides, redox potential, and for the influence of bi-metallics and a known corrosive environment.

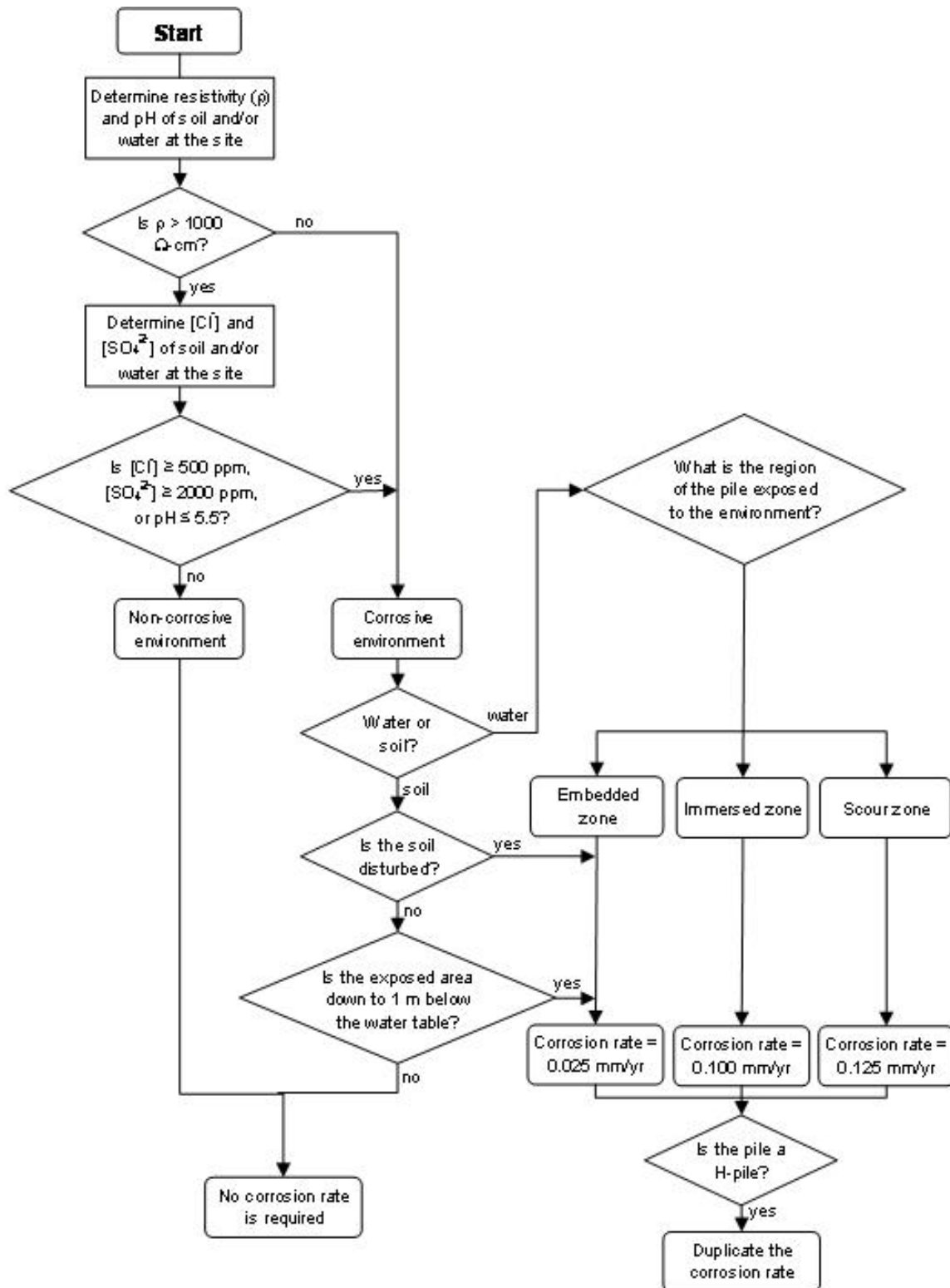


Figure 3-2. Flowchart to determining the environmental classification and the corresponding corrosion rates per CALTRANS (CALTRANS, 2003).

3.2.3 Recent experience with accelerated corrosion of steel pilings

3.2.3.1 Accelerated corrosion of steel pilings in a freshwater environment

Recent observations have documented unusually high corrosion rates of steel used in pilings, fasteners for pier structures, support columns for bridges, and docks at Duluth-Superior Harbor in Minnesota. In this freshwater port, corrosion of steel is characterized by extensive pitting, especially at depths less than 2 m from the surface (Marsh et al., 2005). Marsh et al. (2005) postulated that steel corrosion rates accelerated in the 1970's from 0.012 in/yr to 0.022 in/yr, based on changes in water dissolved oxygen concentrations (Figure 3-3). AMI (2006) obtained corrosion rates at multiple harbor sites by *in-situ* instantaneous linear polarization measurements in combination with measurements of pitting coverage and depth on immersed steel structures. Measurements were made during seasons with both warmer and colder water temperatures and the results were averaged to get a representative annual rate. Corrosion rate estimates ranged from 0.13 to 0.48 mm/yr (0.005 to 0.019 in/yr) (AMI, 2006).

Marsh et al. (2004) listed water quality, dissolved oxygen content, and dissolved chlorides from de-icing salts as the most likely agents of change in observed corrosion rates. Microbiologically Induced Corrosion (MIC) and functional changes in the harbor were not ruled out. Table 3-3 summarizes the range of values for water quality parameters observed across 44 locations within and near the harbor in September 2006 (Alltech, 2007). Hicks (2007) reported that on corroding steel the pattern of corrosion, e.g., red deposits, bio-films and tubercles underlain by pits, the presence of iron-related bacteria, and differences in bacterial communities within the harbor and on less affected steel outside the harbor are consistent with MIC seen in other environments. MIC is further discussed in Chapter 10.

This freshwater harbor is at the boundary of the St. Louis River estuary and Lake Superior, and is separated from Lake Superior by a long spit of land. Waters of the St. Louis River estuary are rich in tannins or natural organic matter. Water and wastewater treatment practices were modified in the 1970's, for example, by treating combined municipal and industrial wastewater flows prior to their discharge to the St. Louis River estuary (Marsh et al., 2005). Improvements in water and wastewater treatment practices and facilities may have lowered oxygen demand in harbor water, thus increasing the dissolved oxygen concentration.

These observations merit attention since based on the water quality parameters summarized in Table 3-3, the Duluth—Superior Harbor water would be classified as slightly to moderately aggressive (Table 2-5), with corresponding predicted corrosion rates of 0.03 mm/yr and 0.05 mm/yr (0.001 in/yr and 0.002 in/yr), respectively (Table 3-2). Thus, corrosion rates of structural steel observed in Duluth—Superior Harbor are 5 to 10 times greater than is predicted by current

FDOT guidelines for steel pilings in similar Florida environments, without consideration of temperature effects.

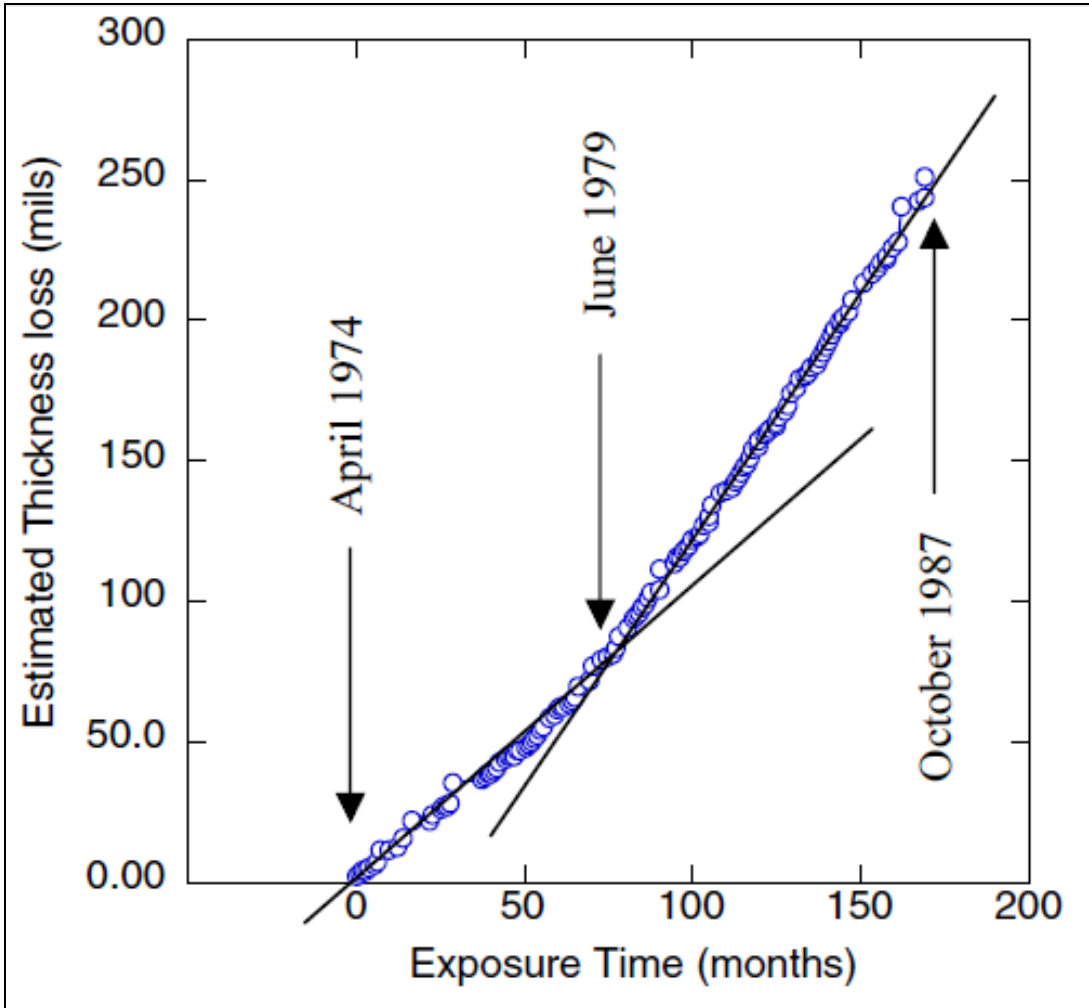


Figure 3-3. Estimated thickness loss as a function of time from April 1974 to October 1987 derived from dissolved oxygen measurements made near the Burlington Northern Bridge in Duluth-Superior Harbor (Marsh et al., 2005).

Table 3-3
Water Quality Within and in the Vicinity of Duluth Superior Harbor
Ranges Based on Measurements Made in September 2006

(Alltech, 2007)

Water Quality Parameter	Range of Values
Temperature	~17 °C
pH	7.67 to 8.44
Dissolved Oxygen	6.85 to 9.32 mg/L
Conductivity (Resistivity)	0.094 to 0.297 mS/cm (11,000-3,400 Ω-cm)
Chloride	<10 to 27 mg/L
Sulfate	4.1 to 35 mg/L
Alkalinity	45 to 110 mg/L
Hardness	45 to 110 (as CaCO ₃) mg/L
Iron	<0.20 to 0.71 mg/L

3.2.3.2 Accelerated corrosion of steel pilings in a marine environment

Beech and Campbell (2008) describe the accelerated corrosion of steel piling in a southern England harbor. On steel pilings at the water level consistent with low tide, localized corrosion rates of steel piling are estimated ~0.5 mm/yr or ~10 times higher than expected for the marine environment. Sulfate-reducing and sulfate oxidizing bacteria appear to play a role in the accelerated corrosion, as well as the concentration of organic carbon in harbor seawater and the mean tidal range (Beech and Campbell, 2008).

For mild steel corroding in unpolluted shallow seawater, Melchers and Jeffrey (2008) provide estimates of temperature dependent terminal uniform and pitting corrosion rates, r_s and r_{sp} , respectively, where T is in temperature in °C (Equations 3-7 and 3-8). These estimates include the effects of anaerobic sulfate-reducing bacteria but with a relatively high uncertainty (Melchers and Jeffrey, 2008).

$$r_s = 0.039\exp(0.0254T) \quad (3-7)$$

$$r_{sp} = 0.353\exp(-0.0436T) \quad (3-8)$$

Assuming an average Florida water temperature of 20°C, the terminal corrosion rates for uniform and pitting corrosion predicted by the above equations are 0.07 mm/yr and 0.15 mm/yr, respectively. For a 75-year design lifetime the rate for the uniform case would correspond to a 5 mm loss. That value exceeds the of sacrificial allowance of 3.4 mm (Table 3-1) in the present FDOT guidelines

3.3 Soil and Rock (Ground) Anchors and Soil Nails

Soil and rock (ground) anchors and soil nails are often used in highway construction of retaining walls that are installed to stabilize excavations or slopes, or structures that require tiedown anchors. Ground anchors or soil nails provide lateral resistance to horizontal pressures acting on vertical members of the wall such as pipe, H-, or sheet piles (Sabatini et al., 1999) and, if permanent, have a design service life of 75 to 100 yrs.

A ground anchor (also called a tieback) consists of pre-stressed bar or strand tendons threaded through a drilled hole or tube filled with grout as shown in Figure 3-4. In Figure 3-4 can be seen the major components of a ground anchor: the anchorage (anchor head, bearing plate, and trumpet), the free stressing (unbonded) length, and the bond length. Refer to Sabatini et al. (1999) for a detailed description of ground anchor design and application, and ASTM A722 and ASTM A416 for material specifications of bar and strand tendons, respectively.

Wall anchor bars (or mild steel tiebacks) are medium strength steel bars components consisting of solid steel rods, with CPM as indicated in Section 3.2.1.

A soil nail consists of a solid steel reinforcing bar that is grouted into place. Soil nails are closely spaced and provide passive reinforcement to the retaining wall. Nails can be installed as construction proceeds from the top of the slope to the bottom of the excavation and are well-suited for near-vertical excavations (Lazarte et al., 2003). Figure 3-5 illustrates a detail of the soil nail components. Lazarte et al. (2003) give detailed design guidance for building retaining walls that are anchored with soil nails.

3.3.1 FDOT design guidelines

With the exception of wall anchor bars, which were addressed as part of the guidelines for piles in Section 3.2.1, no explicit corrosion rate estimates appear to be present for soil and rock anchors and soil nails in FDOT documentation.

Soil nails and post-tensioned anchors are normally grouted and corrosion protection is achieved by passivation of the metal surface in contact with the highly alkaline pore water of the grout. Thus for these components the corrosion protection and durability evaluation methods used for metals in cementitious systems apply, which is outside the scope of this report. Likewise, the corrosion rate expectations for metallic reinforcement in MSEW have been addressed elsewhere (Sagüés, 2000; Berke and Sagüés, 2009).

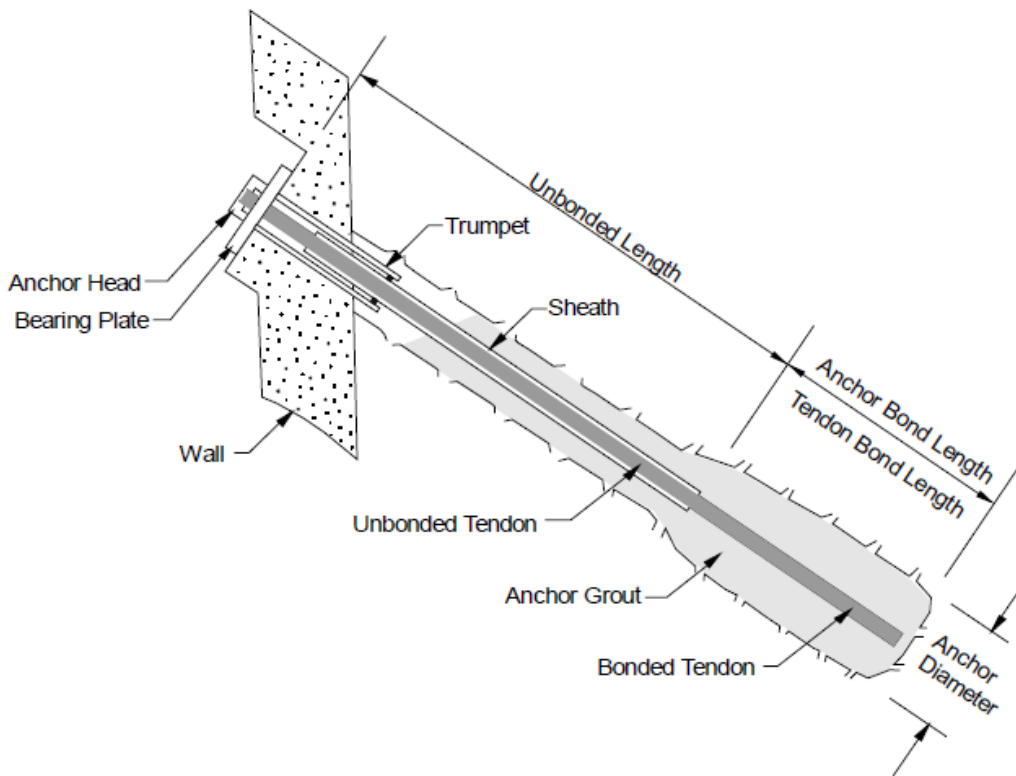


Figure 3-4. Components of a ground anchor (Sabatini et al., 1999).

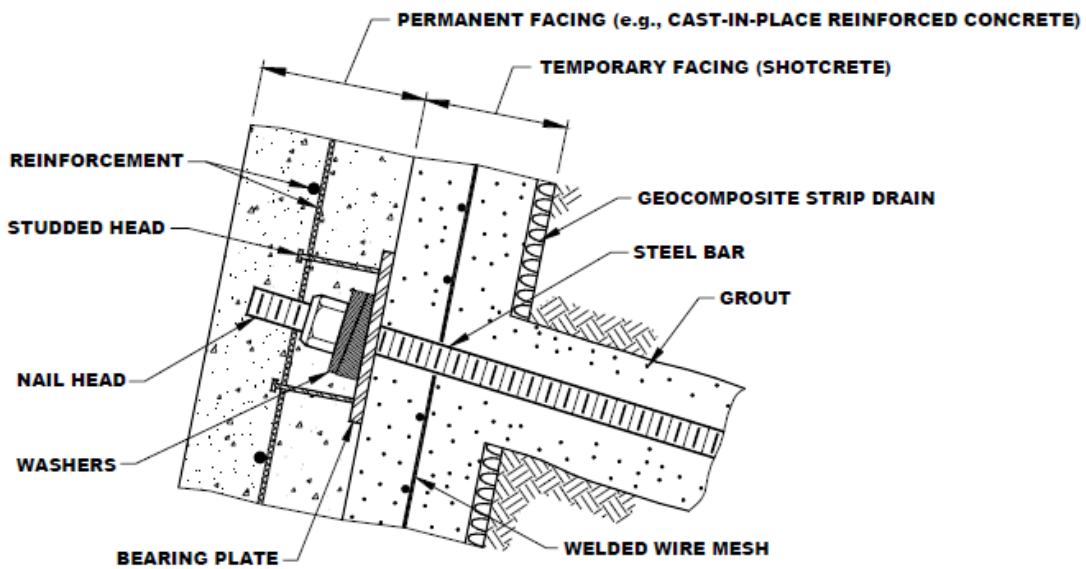


Figure 3-5. Components of a soil nail (Lazarte et al., 2003).

3.3.2 Potential alternative approaches

3.3.2.1 NCHRP Report 477 (Withiam et al., 2002)

In this report, Withiam et al. (2002) gave criteria for assessing groundwater corrosion potential for soil anchors (Table 3-4). Withiam et al. (2002) recommended three additional soil tests: moisture content (AASHTO T265), grain size analysis (AASHTO T88), Atterberg limits (AASHTO T89 and T90). Refer to Chapter 2 for discussion of the influence of soil particle size and moisture content on corrosion rates.

Table 3-4
Criteria for Assessing Groundwater Corrosion Potential^{*,†}
 (Xanthakos, 1991, as cited in Withiam et al., 2002)

Test	Units	Aggressiveness		
		Weak	Strong	Very Strong
pH	--	6.5-5.5	5.5-4.5	<4.5
CO ₂	mg/l	15-30	30-60	>60
NH ₄ ⁺	mg/l	15-30	30-60	>60
Mg ²⁺	mg/l	100-300	300-1500	>1500
SO ₄ ²⁻	mg/l	200-600	600-3000	>3000

*Assign the highest level of aggression from the results of any single test, or, if the results of any two tests are in the upper quarter of any level, assign the next higher level (Withiam et al., 2002).

Withiam et al. (2002) outlined a multi-step model for computing an estimated service life (ESL) of pre-tensioned steel bars buried in soils assuming either uniform or pitting corrosion. They state this model under-predicts the estimated service life because no credit is given for corrosion protection. The first step is to calculate the critical radius of the pre-tensioned steel bar (or strands) from Equation 3-9, where A_0 is the initial cross-sectional area of the bar (μm^2) and r_{crit} is the critical radius (μm). The critical radius is defined as the radius at which the yield stress is reached under constant load (Withiam et al., 2002). The second step is to calculate from Equation 3-10 the allowable loss of bar thickness (X , μm), where r_0 is the original bar radius (μm). For uniform corrosion, the third step is to apply Equation 3-11 to determine the ESL, where K (μm) and n are constants (Table 3-5) that depend on the soil or water corrosion potential, e.g., from Table 2-5 or Table 3-4. For soil conditions that are conducive to pitting corrosion (e.g., low pH), Equation 3.10 is modified by replacement of X with $(X/2)$.

$$r_{\text{crit}} = \sqrt{\frac{0.6A_0}{\pi}} \quad (3-9)$$

$$X = r_0 - r_{\text{crit}} \quad (3-10)$$

$$\ln(\text{ESL}) = \frac{\ln(X) - \ln(K)}{n} \quad (3-11)$$

Table 3-5
Recommended Parameters for Service Life Model
 (Withiam et al., 2002)

Parameter	Normal	Aggressive	Very Aggressive
K (μm)	35	50	340
n	1.0	1.0	1.0

3.3.2.2 FHWA-IF-03-017 (Lazarte, et al., 2003); FHWA-IF-99-015 (Sabatini et al., 1999)

In these reports, Lazarte et al. (2003) and Sabatini et al. (1999) summarized criteria for assessing soil corrosion potential for steel reinforcement used in retaining wall construction (Table 3-6). In comparison with environmental classifications given in Table 2-5, the guidance presented in Table 3-6 for non-aggressive soil conditions extends the lower pH limit down to 4.5 but truncates the upper pH limit at 10, has a lower threshold for chloride concentration, and includes a threshold for sulfate concentration and a check for stray current. Refer to Chapter 2 for a discussion of the corrosion potential of stray current.

Table 3-6
Criteria for Assessing Soil Corrosion Potential
 (Lazarte et al., 2003)

Test	Units	High Potential /Aggressive	Low Potential /Non-Aggressive	ASTM Standard	AASHTO Test Method
pH		<4.5, >10	5.5<pH<10	G51	T-289-91
Resistivity	Ω-cm	<2000	>5000	G57	T-288-91
Sulfates	ppm	>200	<200	D516	T-290-91
Chlorides	ppm	>100	<100	D512	T-291-91
Stray Current	--	Present	--	--	--

Sabatini et al. (1999) and Lazarte et al. (2003) give for aggressive soil conditions the Class I and Class II corrosion protection requirements for permanent installations using ground anchors or soil nails, respectively (Table 3-7). Class I and Class II refer to double and single barrier corrosion protection of the steel tendon in a ground anchor or of a steel bar or soil nail. For permanent structures, selection of the degree of protection depends not only on corrosion potential of the soil (Table 3-6), but also on the consequences of an anchored wall failure and the additional cost of extra corrosion protection (Sabatini et al., 1999; Lazarte et al., 2003).

Table 3-7
Class I and II Corrosion Protection Requirements for Permanent Installation
of Ground Anchors and Soil Nails
(Sabatini et al., 1999; Lazarte et al., 2003)

Anchor	Class	Protection Elements
Ground Anchor	I	Anchorage: Trumpet, cover if exposed Unbonded length: Encapsulate tendons composed of individual grease-filled extruded strand sheaths with a common smooth sheath or a grout-filled smooth sheath, or use smooth bondbreaker over grout-filled bar sheath Tendon bond length: grout-filled encapsulation or fusion bonded epoxy
	II	Anchorage: Trumpet, cover if exposed Unbonded length: Grease-filled sheath or heat shrink sleeve Tendon bond length: grout
Soil Nail	I	Grout and epoxy-coated bar, or grout and PVC sheathing encapsulation
	II	Grout and bare bar

3.4 Discussion of FDOT and Alternative Durability Estimation Methods for Pilings and Anchors

3.4.1 Steel pilings

3.4.1.1 Reliability/usefulness of the present FDOT durability predictive methods

The present method of assessment and related nominal corrosion rates used in the FDOT guidelines represent working assumptions generally justifiable while keeping in mind the large natural variability expected from corrosion rates in the field.

It is noted that CALTRANS has stated corrosion rates (e.g., 0.025 mm for piles buried in disturbed soils or down to 3 ft below the water table in natural soils) that are roughly of the same order as those listed in the FDOT guidelines. It should also be noted that CALTRANS just classifies the environments as non-aggressive or aggressive, and consequently the corrosion rates are conservative estimates to include all the possible degrees of aggressiveness.

No quantitative corrosion related sheet pile failure criteria were found in FDOT guidelines. For foundation piles FDOT uses the AASHTO failure criterion (average loss = 50% of the original cross-sectional area). This criterion does not take in account pitting corrosion since the pilings are usually employed to support structural or lateral loads, so pitting corrosion should not affect considerably the

strength or useful life of pilings as load-bearing structures. Therefore no provision for pitting corrosion is necessary for foundation pilings.

3.4.1.2 Potential alternative approaches

The review of transportation agencies guidelines revealed no alternative methods to evaluate the durability of steel pilings that would represent a clear improvement over those presently used by FDOT. Up to now, attempts to correlate corrosivity of the soil with variables such as pH, resistivity, and the concentration of anions did not have so much success (Schwerdtfeger and Romanoff, 1972). Typically, there is large scatter in the data and the correlation coefficients are low. Usually, U.S. agencies estimate the corrosion rates for pilings by comparison with the ones measured from piles exposed to similar environments (Beavers and Durr, 1989; Hannigan, 1989; AISI, 1999; CALTRANS, 2003).

The alternative prediction method for steel pilings based on pH and chloride content proposed by Beavers and Durr (1998) may hold some promise, but the relationship to estimate the corrosion rates was obtained from weight loss measurements of pilings exposed to a small number of US sites. These sites had a very limited pH range (from 7 to 8) and consequently the proposed equation was formulated only for pH higher than 7. It is noted also that because of the small sample size, strong correlation of model parameters, and lack of independent test data, this model should not be used to predict weight loss in Florida steel pilings.

3.4.1.3 Possible improvements for the existing and/or future durability prediction methods

The following improvements on the present FDOT service life prediction methods may be considered in future versions of the SDG:

Special attention may be given to the region of pile that is located from the surface down to 1 m (3 ft) below the water table in soils, which is well known to have greater corrosion rates. This observation reflects in part the conclusions of Schwerdtfeger and Romanoff (1972), in which the corrosion rates are considered negligible in undisturbed natural soils or 1 m (3 ft) below the water table, regardless of the soil types and soil properties. Additionally, the U.S. case histories of documented incidences of significant steel piling corrosion occurred in disturbed fill soils (Romanoff, 1957; Picozzi, 1993; Beavers and Durr, 1998). Therefore, conservative corrosion rate values may merit adoption in the future. Inspection of piles being decommissioned may provide quantitative indication of the suitability of the present guidelines or need for more conservative criteria.

The possibility of premature failure of corrosion protection measures should be considered for inclusion in new prediction methods. CPM's are at

present effectively considered to be 100% reliable, since guidelines do not seem to consider increased corrosion rates in the case of corrosion protection damage.

3.4.2 Anchors

3.4.2.1 Reliability/usefulness of the present FDOT durability predictive methods

There are no prediction methods of anchors service life based on soil properties in FDOT guidelines, except for wall anchor rods (mild steel tie-back anchors) as noted earlier in slightly, moderately, and extremely aggressive environments, respectively. The present assumed values in that case approach the corrosion rates recommended by Withiam et al. (2002) for similar environments. In contrast to NCHRP recommended practice, no mention was found in the FDOT guidelines on the design criterion for anchors when pitting corrosion may occur, a concern in the case of high strength anchors. No anchors failure criteria were found in FDOT guidelines, possibly because the SDG do not appear to differentiate between the anchors and the pile. It is recommended that future revisions of the guideline clarify the terminology

3.4.2.2 Potential alternative approaches

A service life prediction method for metal-tensioned systems (pre-stressed ground anchors, soil nails, and rock bolts) based on the Romanoff power law was proposed by Withiam et al. (2002). The Romanoff equation was originally proposed to predict uniform corrosion rates of buried metal components. The parameters used in that equation (K and r) depend on the soil properties and material exposed to the environment. The method proposed by Romanoff was improved in the NCHRP report by accounting for the pitting corrosion. Possible extension of this approach to update FDOT guidelines should be considered, but it would be necessary to include the effect of CPM on performance, since the NCHRP recommended practice does not take in account the existence of CPM and the corresponding corrosion rates in case of failure of those measures, for example, undercoating crevice corrosion.

3.4.2.3 Possible improvements for the existing and/or future durability prediction methods

The following improvements on the present FDOT service life prediction methods may be considered in future versions of the SDG.

Pitting corrosion has a greater effect than uniform corrosion on the service life of tensioned metallic elements, and consequently this type of corrosion should be included in the methods to forecast the service life of anchors. The metallic anchors are commonly protected against the corrosion by using several measures (e.g. plastic sheathing, epoxy coating, concrete grout). The failure of these systems should be also considered in the prediction models.

The anchors are made with of various subcomponents and different materials. These components may be in contact with a common electrolyte if damage in the enclosure elements occurs. In this case, galvanic coupling effects should be considered. When appropriate, corrosion control methods against common modes of deterioration found in post-tensioned tendons (Wang and Sagüés, 2005) should translate to the pertinent DSL provisions.

3.5 Summary and Conclusions

- A review of FDOT and alternative design guidelines for steel pipe, H-pile, and sheet pilings, ground anchors (tie-backs), and wall anchor bars revealed the following potential improvements for future versions of the FDOT SDG:
- Depth-specific corrosion rates for steel pilings to a depth greater than 1 m (3 ft) below the water table may merit consideration. Inspection of extracted piles can provide valuable quantitative evidence of suitability of present guidelines or need for modifications.
- Adoption of uniform and pitting corrosion guidelines for ground anchors (tie-backs). The SDG may need to differentiate between piles and anchors for corrosion design purposes; and
- Design service life provisions for corrosion control measures in both pilings and anchors.
- The recent experiences of accelerated corrosion in both freshwater and marine environments with high nutrient levels (with increased potential for MIC) suggest that corrosion rates at the waterline could in some instances be as much as an order of magnitude greater than expected. The operating mechanism is not yet known. Alertness to the possibility of similar incidents during monitoring and inspections of similar structures in the FDOT inventory is recommended.

4 METALLIC DRAINAGE PIPE CORROSION - FOCUS ON ALUMINIZED STEEL

4.1 Scope

This chapter first briefly reviews the general FDOT approach to estimate durability of metallic drainage pipe, and then addresses in detail the development of corrosion guidelines and alternatives for aluminized steel type 2 piping. The emphasis on that material in this section and much of the rest of this report stems from the series of severe corrosion incidents in aluminized steel pipe, first noted in 2005, highlighted in the introduction and project scope (Section 1.1) of this report.

4.2 FDOT Metallic Drainage Pipe - Aluminum Clad and Galvanized

4.2.1 Materials and FDOT guidelines

Metals including clad aluminum (Type 3004 aluminum clad with a 7000 series aluminum alloy, often referred to as Alclad pipe), galvanized steel, and aluminized steel Type 2 (addressed separately in Section 4.3) are optional culvert materials for drain sections when designed in accordance with FDOT (2009a). For jack and bore installations below railroads or high traffic roads, ductile iron is an optional material as well. Metal culvert piping or structures designed as storm drains, cross drains, or French drains have design service lifetimes (DSL) of 50 yr for minor roads and 100 yr for major roads, and 25 yr for side drains and gutter drains (FDOT, 2009a). The estimated service lifetime is based on soil and water resistivity and pH, where soil and water samples are collected and analyzed by FDOT methods (FDOT, 2000a; FDOT, 2000b) from the proposed culvert installation site. For metal culvert piping, the time of first perforation (complete penetration) is considered to be the service life end point.

A computerized culvert service life estimator is available to help with material selection and determination of minimum wall thickness for a given design service lifetime (Cerlanek and Powers, 1993; FDOT, 2008). Inherent in this approach are empirical models that relate observed corrosion rates with environmental conditions (Sagüés, 1989). Design curves for galvanized steel, aluminized steel type 2, and aluminum culvert piping are presented in Figures 4-1, 4-2, and 4-3, respectively. Galvanized steel design curves are used as a starting point for estimating the service life of ductile iron pipe, as described by FDOT (2008). Design engineers are cautioned to consider also previous performance of pipe materials under similar conditions and the possible presence of corrosive effluents from nearby activities (dairy farming, cement manufacturing, or coal burning, as examples) (FDOT, 2008).

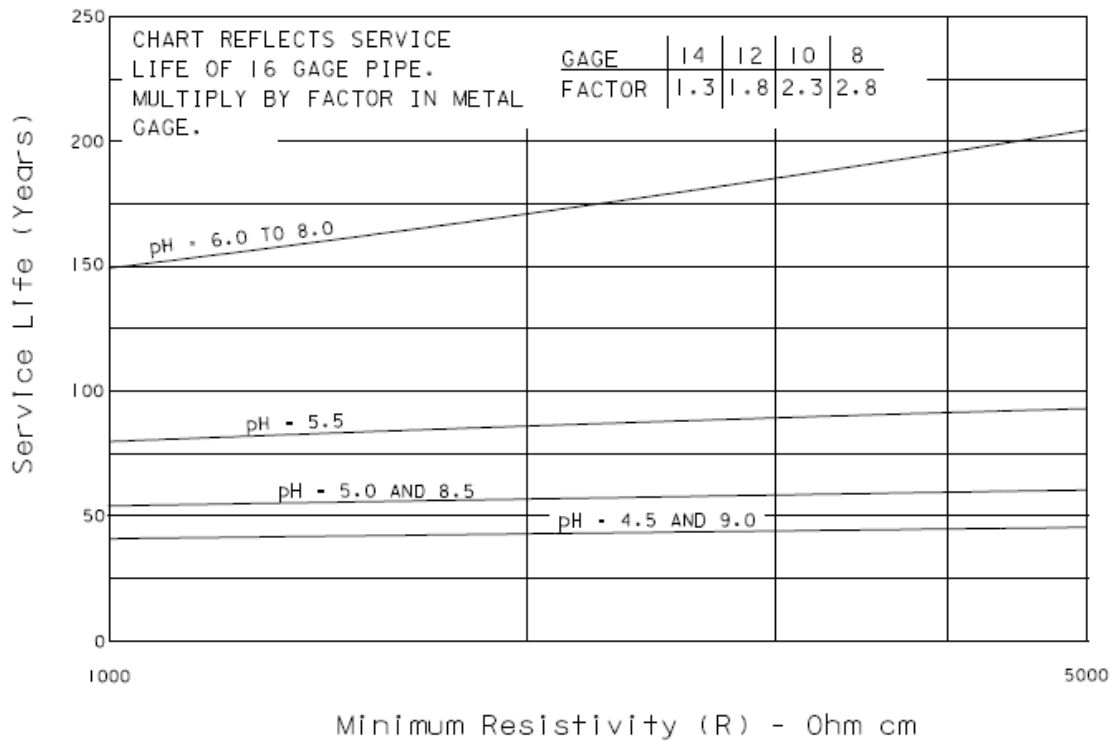


Figure 4-1. Estimated service life versus pH and resistivity for 1.52-mm (16-gage) clad aluminum (FDOT, 2008).

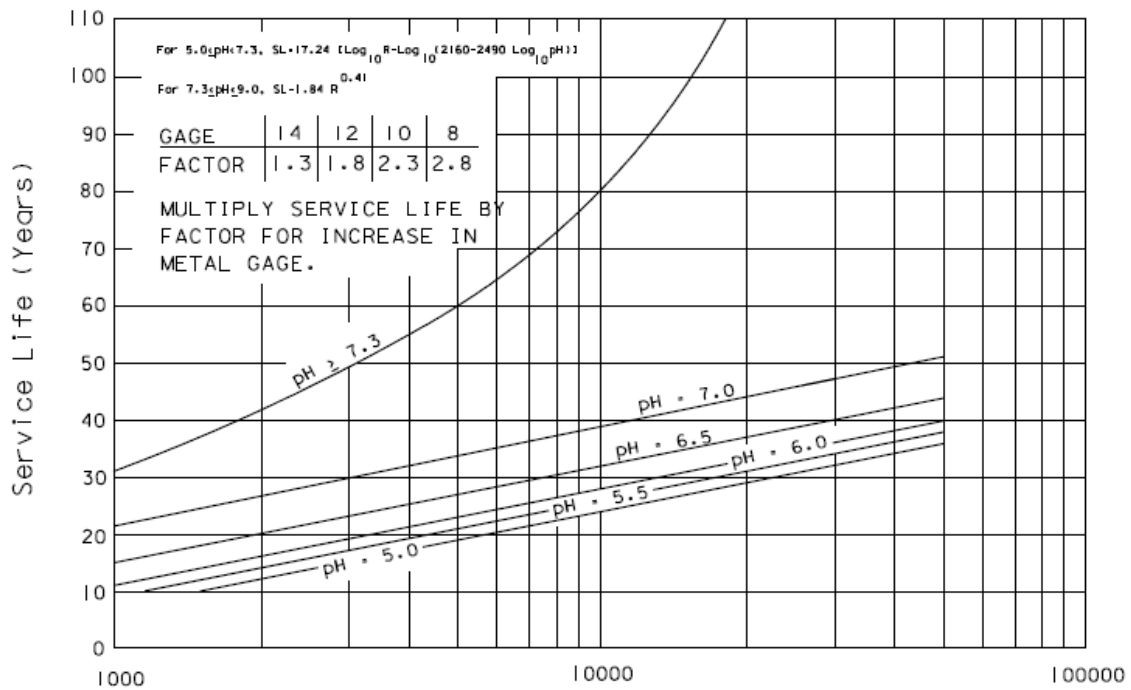


Figure 4-2. Estimated service life versus pH and resistivity for 1.52-mm (16-gage) galvanized steel (FDOT, 2008).

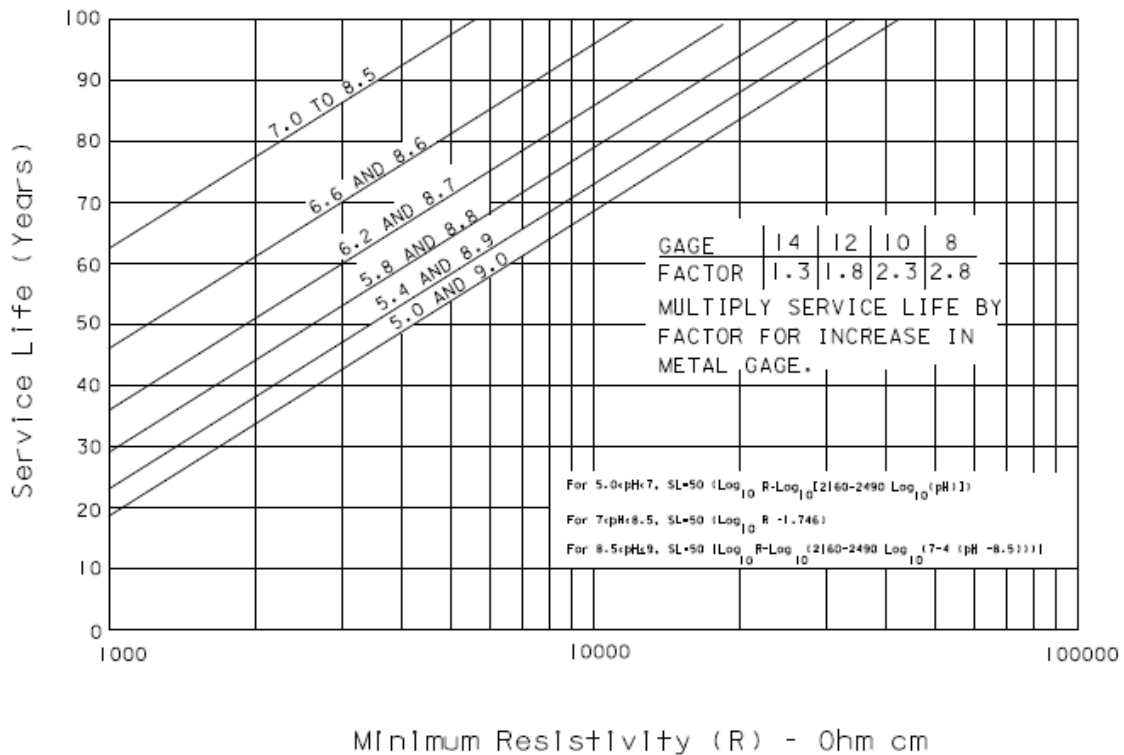


Figure 4-3. Estimated service life versus pH and resistivity for 1.52-mm (16-gage) aluminized steel type 2 (FDOT, 2008).

4.2.2 Potential alternative approaches and recommendation - clad aluminum pipe

The corrosion performance of Alclad drainage pipe has been well established in prior FDOT investigations (Sagüés, 1989; Cerlanek and Powers, 1993 and citations therein) to the extent that no recommendations for alternative methods to those specified in FDOT (2008) are made here. A general discussion of corrosion mechanisms of aluminum is included as part of the detailed analysis for aluminized steel in Sections 4.3.2 and 4.3.3.

4.2.3 Potential alternative approaches and recommendation- galvanized pipe

These alternative approaches are presented here in some detail as they also form the basis (with some modifications) for considerations on the durability of aluminized steel.

4.2.3.1 The California method for galvanized pipe

The California method was developed by the California Department of Transportation (CALTRANS) in the 1950's to assess pipe durability based on the examination of ~7,000 galvanized culvert pipes (Beaton and Stratfull, 1962). A graphical analysis of the environmental parameters gathered versus pipe condition allowed to obtain the most significant parameters affecting the pipe

service life. The service life prediction method has been further refined over the years as a standardized procedure (California Test 643, 1999), which contains detailed information regarding the parameter measuring procedures as well as the use of those parameters to forecast service life of galvanized culvert pipes.

A refined California method uses pH together with the minimum resistivity of both soil side and waterside (interior of a pipe) and metal gauge thickness, as key input parameters to forecast durability of galvanized steel pipe as shown in Figure 4-4. In this refined California method, pipe durability is defined based on the number of years to first penetration of a maintenance-free corrugated metallic component. Per the latest documentation examined (California Test 643, 1999), the refined California method was initially intended for service life predictions of galvanized steel pipes not including provisions for aluminized steel type 2 service life forecast.

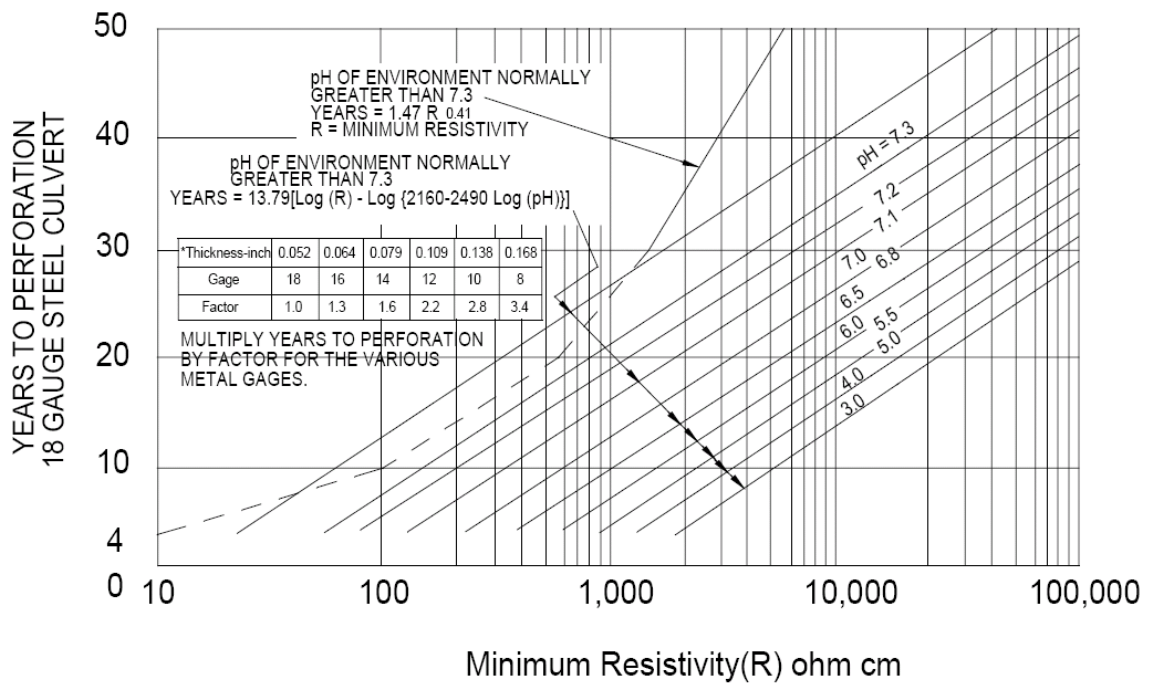


Figure 4-4. Refined California method chart for estimating years to perforation of 1.21-mm (18-gauge) galvanized culvert pipe (California Test 643, 1999).

The refined method establishes that low pH and minimum resistivity values result in reductions in-service life forecasts. However, surface water may have a relatively low pH and still not be very aggressive because other dissolved species (e.g. Ca^{2+} , Mg^{2+} , CO_3^{2-}), not considered in the refined method, may precipitate a protective scale (hard waters) on the metal surface which tends to greatly decrease its corrosion rate. Conversely, high pH by itself may not guarantee extended service life if the water does not promote the formation of the protective scale (soft waters). Performance evidence (Cerlanek and Powers, 1993 and Bednar, 1989) suggests that the refined California method yields highly

conservative predictions in hard waters and liberal results in soft non-scaling waters. Similar limitations exist for the unqualified application of resistivity, which as a parameter cannot differentiate between the presence of beneficial or of detrimental ions in the medium.

With minor variations, the refined version of the California method was the one adopted by FDOT for service life estimation of galvanized pipe.

4.2.3.2 American Iron and Steel Institute (AISI) method for galvanized pipe

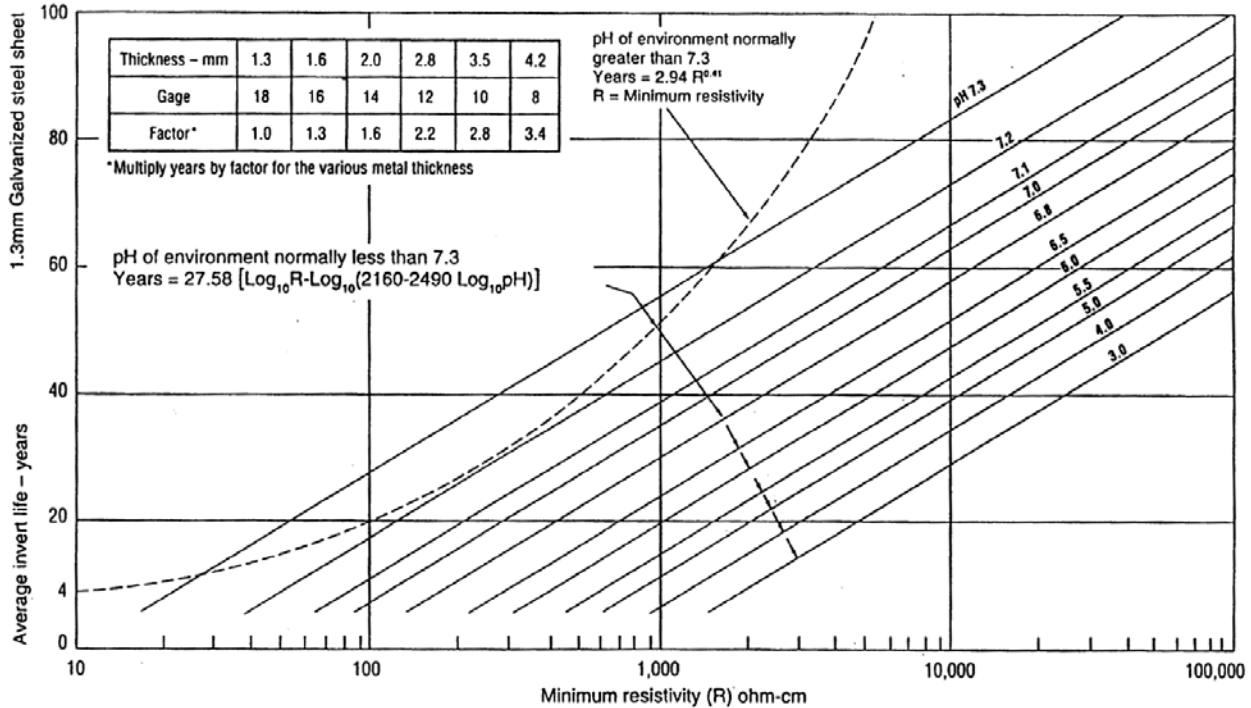


Figure 4-5. The AISI method chart for estimating years to perforation of galvanized steel pipes of 1.21-mm (18-gage) culvert pipe. Computing service life is the same as in the refined California method (AISI, 1994).

The American Iron and Steel Institute (AISI) developed a method, derived from the refined California method, for predicting the service life of corrugated galvanized steel culvert pipes (AISI, 1994). The AISI method uses pH and minimum resistivity values as in the refined California method for service life forecast as shown in Figure 4-5. As noted by Ault and Ellor (2000), in contrast to the refined California method, the AISI method does not consider that small perforations significantly degrade pipe performance, since the consequences of those perforations are deemed to be minimal in a gravity flow pipe such as most storm sewers and culverts installed in non-erodible granular bedding. Instead, the AISI method establishes a 25% total metal loss as the practical limit for estimation of galvanized steel pipe durability, yielding service lives that are approximately twice as much as to those obtained by the refined California method. The AISI method initially applied to galvanized steel and later to

aluminized steel type 2 showed reasonably conservative predictions as reported by the Georgia Department of Transportation (Southeastern Corrugated Steel Pipe Association, 1977).

4.2.3.3 AK Steel method for galvanized pipe

An alternative service life forecasting method based on field observations was proposed by AK Steel (Morris and Bednar, 1998; Bednar, 1989) to incorporate the tendency for water scaling, mainly produced by the formation of adherent CaCO_3 film on the surface of a pipe, into the service life prediction of corrugated galvanized culvert pipes. Instead of pH and minimum resistivity, the AK Steel method (shown in Figure 4-7) uses the scaling tendency parameter equal to the total hardness plus total alkalinity minus free CO_2 , versus the solution conductivity (or its inverse, the resistivity).

In contrast with the other predictive methods, the AK Steel method considers that water scaling protects the metal from subsequent corrosion. If the scaling tendency parameter versus solution conductivity falls on the straight line, a protective scale is expected to be formed on the metal surface and corrosivity of the medium would be minimal. The idealized curves labeled 50 yr, 35 yr, and 20 yr in Figure 4-5 exemplify the effect on durability of increasingly large amounts of aggressive anions such as Cl^- and SO_4^{2-} ions and/or larger amount of free CO_2 , which causes scale dissolution with a consequent increase of the metal corrosion rates.

Preliminary application of this method has shown encouraging results in predicting the performance of galvanized steel in tropical and subtropical environments comparable to those encountered in Florida.

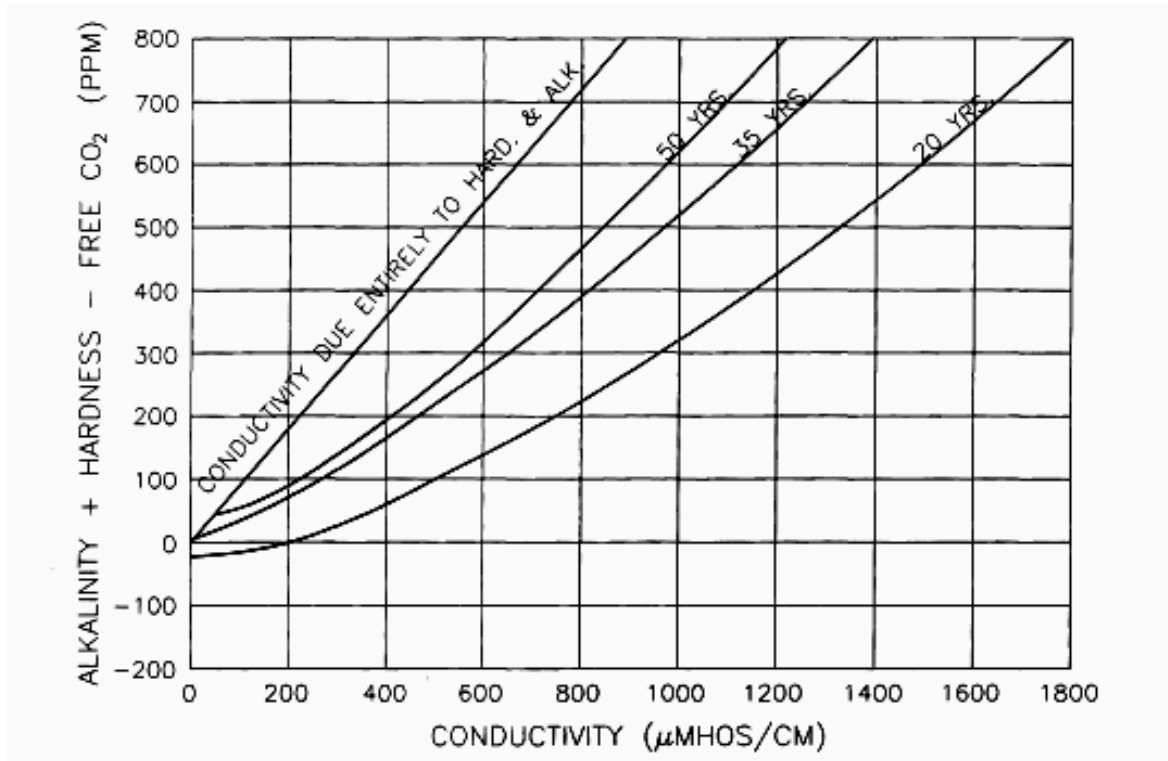


Figure 4-7. The AK Steel method chart for estimating service life of 14-gage galvanized and aluminized steel type 2 culvert pipes (Bednar, 1989).

4.2.3.4 Recommendation - galvanized pipe

In the absence of extensive new evidence, no recommendation is made to consider changing the present California-method based FDOT service life estimation approach. The AISI method may merit consideration in the future if accumulation of performance data from Florida sites indicates that the less conservative criteria for service life provide a more realistic forecast. The performance base for the AK Steel method is still too limited (compared to the California method data base) to warrant recommending considering a change to the AK procedure for galvanized steel.

4.3 Aluminized Steel Type 2 Drainage Pipe

Aluminized steel type 2 pipe showed in prior FDOT evaluations substantially improved corrosion performance compared to that of galvanized steel. As noted in Section 1.1 those observations have been challenged by recent field experience with pipe of this material in Florida. A 2005 FDOT investigation conducted on ~3 yr old spiral rib aluminized steel type 2 culvert pipes in the City of St. Cloud (see Section 5) revealed extensive corrosion damage of aluminized steel even in mild environments with nearly neutral pH and resistivities $>2,000 \Omega\text{-cm}$. Projected nominal service life determined per the FDOT method detailed in Section 4.4.3 (Cerlanek and Powers, 1993) for 1.52-mm (16-gage) aluminized steel type 2 yielded service life estimates between 60 and 115 yr. The alternative AK Steel estimation method (see Section 4.2.3.3) yielded a service life in excess of 50 yr. Clearly, the extensive damage observed early on was not anticipated by either forecasting procedure. The corrosion damage in such short time indicated that the fastest corrosion rates may have locally exceeded $500 \mu\text{m/yr}$, a value significantly higher than those observed for plain steel in similar environments ($\sim 25 \mu\text{m/yr}$). In 2007 similarly severe corrosion of ribbed aluminized steel type 2 pipe was observed at an FDOT site (Curlew Rd., see Section 5.2) after less than 10 years service, also much less than anticipated from normal durability estimates based on environmental variables. It is noted that severe manufacturing defects in the form of rolling distress and helical cuts (see Section 5.1.6.1) were present as well in many of the affected pipes, complicating the task of isolating the factors responsible for the corrosion.

Since aluminized steel is extensively used in FDOT projects, these incidents prompted modification and extension of the original scope of this investigation to address the issue of unexpected corrosion of aluminized steel pipe. The work documented in this report represents the initial phase of a more extended investigation of the problem, and any findings reported here should be regarded as preliminary pending the outcome of continuation work.

This section reviews the material and its corrosion behavior, and the status of service life estimation for aluminized steel pipe prior to the above mentioned incidents.

4.3.1 Manufacture and surface morphology of aluminized steel type 2

Several aluminizing methods suitable for steel coating have been widely used for the past decades (Suzuki, 1989). The methods differ only on the type of protection process of the steel substrate against oxidation before the hot-dipping stage. The Armco Sendzimir method, however, is commonly adopted for the bulk of production of aluminized steel type 2 briefly explained next.

The steel to be hot-dipped is degreased by alkali cleaning or by heating at 450-600 °C followed by water rinsing, pickling, and water rinsing again (pretreatment process). Afterwards, the pretreated steel is cleaned by exposure to a H₂ gas atmosphere at high temperature (activating process). Cleaning the metal strip in a non-oxidizing/reducing atmosphere assures a pristine surface for coating adherence. At the end of the activating process, aluminum coating is continuously applied to the pretreated steel by hot-dipping in a closed environment at ~700 °C. The steel is annealed in the line and the coating thickness is controlled by the line speed, hot-dipping temperature, and air finishing. The reaction rate between molten aluminum and steel is relatively fast, forming a duplex coating on top of the steel substrate. According to the ASTM A929 and AASHTO M274 standard procedures, the final product must comply with a minimum coating weight of 1 oz/ft², which corresponds to a minimum coating thickness of ~40 μm, and minimum tensile and yield strengths of about 310 MPa and 228 MPa, respectively.

Microscopic examination of aluminized steel type 2 in cross section shows a nearly pearlite-free ferrite low carbon steel substrate with regular grains, a partly columnar inner alloy layer ~15 μm thick, and an outer aluminum-rich layer ~30 μm thick. The inner alloy layer is of composition Fe₂Al₅ (An et al., 2001; Li et al., 2003), although others have shown the formation of FeAl₃ in some cases (Serra et al., 1998; Bouche et al., 1998). The inner alloy layer is an essential ingredient of the coating protection system, supplementing the outer aluminum-rich layer and possibly providing a second line of defense against corrosion. The composition of the outer layer is predominantly a matrix of aluminum and Fe-rich inter-metallic precipitates (6-11 wt% Fe) (Cáseres and Sagüés, 2005). During manufacturing, small discontinuities in the aluminized coating, possibly caused by cold working can extend to the substrate steel, creating coating breaks. The potential of those breaks leading to the formation of galvanic macrocells was investigated here.

4.3.2 Overview of aluminum corrosion

Aluminum derives its corrosion resistance from the presence of a thin protective passive oxide layer, which when in contact with air, greatly decreases the rate of metal oxidation. When in contact with water, other forms of protective layers may form being the most common the hydrated aluminum oxide with composition Al₂O₃·3H₂O (Godard et al., 1967). The aluminum oxide film, however, may be subject to localized breakdown resulting in accelerated dissolution of the underlying metal. In particular, aluminum oxides tend to dissolve uniformly in extreme acid or alkaline medium. In non-complexing solutions of ~4<pH<~8.5, aluminum tends to become covered with the protective oxide film as first proposed by Pourbaix (Pourbaix, 1974). Under this condition, the oxide film has very low solubility and its electronic conductivity is also very small. A small but finite current, though, can be measured during metal

polarization as a result of the presence of intrinsic defects in the oxide film. Others (Hunter and Fowle, 1956; Lee and Pyun, 1999) proposed that the oxide film consists of two distinctive layers. The inner oxide layer next to the metal is a compact amorphous barrier layer of thickness determined mainly by the temperature of the environment. Covering the barrier layer is a thicker, more permeable outer layer of hydrated oxide.

As mentioned earlier, in alkaline solutions ($\text{pH} > \sim 8.5$) the initially protective oxide film is expected to uniformly dissolve with the formation of AlO_2^- ions. In acidic solutions ($\text{pH} < \sim 4$), the oxide film decomposes to form Al^{3+} ions also resulting in considerable larger corrosion rates than otherwise. However, the predictions proposed by Pourbaix in these environmental conditions should be taken cautiously as being only general guidelines for estimation corrosion resistance in the absence of contaminants (Pourbaix, 1974).

It has been widely demonstrated that the aluminum oxide film, if present, is covered with a layer of hydroxyl groups (McCafferty, 2003), which has Lewis acid–Lewis base properties that dictate the surface charge of the oxide film when immersed in aqueous solutions. The surface charge has a close connection to the solution pH when compared with the oxide isoelectric point (typically at $\text{pH} \sim 9.5$). If the solution $\text{pH} < 9.5$, the oxide film will acquire positive charges so that, e.g. chloride ions, can be attracted to the oxide surface. If the solution $\text{pH} > \sim 9.5$, the surface will accept negative charges. The attractive forces are mainly coulombic of ion–ion interaction type. The presence of chloride ions on the aluminum surface can induce localized corrosion of aluminum even in the range of aluminum passivity. Notably, chloride ions can cause pitting of aluminum at the region of local breakdown of the passive film as discussed next.

4.3.3 Pitting corrosion of aluminum

In general, pits initiate at some chemical or physical heterogeneities at the metal surface such as inclusions, second phases, grain boundaries, flaws, mechanical damage, or surface dislocations. Pitting of aluminum is considered to be autocatalytic in nature; that is once a pit starts to grow the conditions inside the pit are such that further growth is promoted. The local pit environment becomes depleted in oxygen (assumed to be the main cathodic reactant in well aerated solutions) and enriched in hydrolyzed aluminum cationic and anionic species, maintaining charge neutrality inside the pit. As a result, the pH inside the pit is low (McCafferty, 2003). It is well documented that within aluminum pits, chloride salts exist: aluminum chloride (AlCl_3) and aluminum oxychlorides such as $\text{Al}(\text{OH})_2\text{Cl}$ and $\text{Al}(\text{OH})\text{Cl}_2$. Depending upon the kind of chloride salts, different pH values within the pit can be expected. For instance, in the presence of AlCl_3 the pH may be as low as 1 (Vermilyea, 1971, Hoch, 1974), and a saturated solution of $\text{Al}(\text{OH})_2\text{Cl}$ may exhibit a $\text{pH} \sim 3$ (Vijh, 1973 and Kaesche, 1974).

Considerable understanding of the pitting phenomenon has been achieved but an in-depth description of the steps associated with pitting corrosion is still lacking. The stages of pitting will be discussed below, from passive film breakdown, to metastable pitting, and lastly to pit growth. The first stage of pitting is the passive aluminum film breakdown followed by pit initiation. Typically, aluminum passive films are characterized by extremely high electric fields on the order of $10^6 - 10^7$ V/cm and by being very small in thickness (nm scale). Passive film breakdown and pit initiation can be interpreted by three mechanisms: film penetration, anionic species adsorption, or film breaking. Hoar (1965) established that the film penetration mechanism is associated with the transport by migration of aggressive anions through the passive film to the metal/oxide interface where active aluminum dissolution occurs. The penetration mechanism is supported by the existence of an induction time for pitting after chloride ions are in contact with the oxide film. Nevertheless, a critical chloride concentration in the oxide film at the metal surface has to be attained in order to display film breakdown and pit initiation. In contrast, Berzins et al. (1977), Wood et al. (1978), and Augustynski et al. (1978) found that there is no chloride concentration threshold below which pitting will not occur and that pitting initiation and propagation depends upon the particular properties of the chloride adsorption sites at the aluminum surface.

Another approach to describe pit initiation is by the point defect model developed by Chao and coworkers (Chao et al., 1981). This approach assumes that chloride ions penetrate the outer portion of the oxide film resulting in the formation of cationic vacancies. These vacancies migrate towards the metal/oxide interface where they are consumed by the formation of cations from the metal. However, if there are more vacancies than cations formed, the vacancies remaining may condense at the metal/oxide interface creating a void. The void is presumed to be the first step in the pitting process according to this model. Optical and scanning electron microscopy conducted on ion-implanted aluminum surfaces after polarization above the aluminum pitting potential in 0.1 M NaCl has shown that the propagation of corrosion pits is associated with the formation and rupture of blisters beneath the oxide film due to electrochemical reactions occurring at the oxide/metal interface (Natishan and McCafferty, 1989) validating the postulations of the point defect model.

Foley (1986) proposed in one of his early works that pit initiation involves adsorption of chloride ions at the oxide film surface followed by an oxide film penetration by the adsorbed chlorides, and a later chloride-assisted dissolution, which occurs at the metal/oxide interface (Natishan and McCafferty, 1989; Yu et al., 2000). After initiation, pits propagate following a series of events which lead to changes in internal pit chemistry and to the growth of pits as mentioned above.

Yet another approach, the film breaking mechanism, considers that the passive film is in a continual state of breakdown and repair caused by localized mechanical stresses at weak sites or flaws in the passive film. This mechanism

implies that local breakdown events are followed by a rapid healing process of the passive layer in non aggressive environments. In chloride-containing solutions, the healing process is less likely. According to this mechanism, local passive film breakdown will lead to pitting under conditions that promote pit growth (Sato, 1971; Richardson and Wood, 1970).

4.3.4 Prior field studies on the durability of aluminized steel type 2

One of the most common problems encountered while researching field corrosion findings is that there is very little standardization in the methodology used to test and to evaluate corrosion of culvert pipes. Unfortunately, it is extremely difficult to adequately establish the nature of the test environments (e.g. episodic wetting, abrasion, flow) and to compare corrosion of culvert pipes. Comparison tests typically involve visual inspection to assess pipe deterioration based upon criteria set up by the investigator. In general, visual inspections lack consistency when inspections are carried out by multiple inspectors with differing biases. Despite this ambiguity, several field studies have been conducted on aluminized steel type 2 exposed to numerous environmental conditions. Investigations more relevant to this study are presented in the next paragraphs.

Ault and Ellor (2000) inspected around twenty one corrugated aluminized steel type 2 culvert pipes located in Alabama, Oregon, and Maine. Their field studies suggested that in the absence of significant abrasion, aluminized steel type 2 pipes could reach a service life of up to eight times that of a galvanized steel pipe as predicted by the refined California method (if only waterside corrosion is considered, then the multiplier factor becomes 3.5; see also Section 4.4.1 for the modified factor used presently by FDOT). Similar results were reported by Potter et al. (1991), who suggested that the service life of aluminized steel type 2 is ~6.2 larger than that predicted for galvanized steel. The actual service life multiplier factor varies depending on the specific environment. Under extreme conditions, however, the author stated that these materials would perform in a relatively similar manner (i.e., last a long time or fail rapidly). CALTRANS (2006) indicates that a 1.21-mm (18-gage) aluminized steel type 2 pipe would have a service life equal to that of a 1.52-mm (16-gage) galvanized steel for a pH range between 5.5 and 8.5 and a minimum resistivity of 3,000 Ω -cm. In acid or alkaline environments, however, CALTRANS (2006) asserts that galvanized and aluminized steels would likely show nearly equal performance as indicated by Potter et al. (1991).

A comprehensive evaluation of aluminized and galvanized steel culvert pipes conducted by Bednar (1998) showed that corrugated aluminized steel type 2 would be considerably superior to galvanized steel in environments with resistivities higher than 950 Ω -cm and relatively high free CO₂ content. This scenario would yield a minimum 50-yr service life for aluminized coating, whereas galvanized coating would be limited to up to 20 yr in service. In overly severe environments (resistivities <600 Ω -cm), the study showed that aluminized

steel typically displayed accelerated pitting corrosion and the advantage of aluminized over galvanized coating became minimal. A later field study by Bednar and AK Steel (Bednar, 1998) on the projected service life of aluminized steel type 2 culvert pipes exposed to nearly neutral pH solutions with low chloride concentrations showed deepest pit penetrations of ~0.2 mm and ~0.3 mm after 30 yr and 42 yr in service, respectively, indicative of low/moderate corrosion rates with pit growth of ~6.7 to ~7.2 $\mu\text{m}/\text{yr}$, for a minimum projected service life in excess of 75 yr for a 1.52-mm (16-gage) metal pipe.

Gartland (1987) studied the corrosion behavior of flame-sprayed aluminum coated steel immersed in natural seawater at 9 °C for up to 210 days. A notable difference between the flame-sprayed and the hot-dipped aluminized steels is in the coating thickness (~100 μm for the flame-sprayed procedure, compared to only about half as much for hot-dipping). Open circuit potentials, potentiodynamic polarization, and linear polarization tests in the cathodic direction were conducted at different exposure times. Corrosion rates, determined at the open circuit potentials by extrapolation of the anodic and cathodic polarization curves and by linear polarization, were found to be ~4.9 to ~8.2 $\mu\text{m}/\text{yr}$ at the end of exposure. It is cautioned however that this moderate corrosion rate, if sustained, would mean penetration of the aluminized layer after a decade.

The majority of the field studies reviewed revealed a superior performance of aluminized steel type 2 over galvanized steel for $4 < \text{pH} < 9$ and resistivities $> \sim 2,000 \Omega\text{-cm}$. The unexpected extensive corrosion damage of aluminized steel noted earlier, however, generated serious concerns as to what environmental or mechanical factors, including manufacturing deficiencies, may have been involved in the corrosion mechanism. As a result, laboratory experimentation was needed to elucidate possible modes of metal deterioration, and to study the synergistic influence of the major environmental and material condition variables on durability of aluminized steel type 2.

4.3.5 Galvanic corrosion of aluminized steel type 2

Some prior investigations evaluated the galvanic corrosion performance of aluminized steel type 2 and closely related materials in various atmospheric environments as well as solutions of high chloride concentration. For instance, Legault and Pearson (1978) evaluated the atmospheric corrosion behavior of aluminized steel type 2 test panels with uncoated cut edges (exposing the base steel) in industrial and marine environments. In their five-year investigation the corrosion rates, determined by metal weight loss ($\Delta W = kt^n$, where k and n are constants and t is time), were small (~0.2 $\mu\text{m}/\text{yr}$) and moderate (~0.45 $\mu\text{m}/\text{yr}$) in industrial and marine environments, respectively. Visual inspection of the test panels showed that the aluminized coatings were in excellent condition except for the panels exposed to marine environments, which showed small perforations of the aluminized coating with formation of uniform white corrosion product.

Interestingly, the cut edges were free of corrosion in marine environments and depicted rust formation only in industrial environments indicative of insufficient galvanic protection to the exposed steel.

A similar approach was employed by Townsend and Zoccola (1979) and later by Townsend and Borzillo (1987), who tested aluminized steel type 2 panels with cut edges exposed to severe marine, moderate marine, rural, and industrial environments. After 13 yr of exposure, aluminized steel performed well in all test environments except for the rural atmosphere, where rust staining along the cut edges was observed. For marine environments, the corrosion rates as determined by weight loss measurements decreased with time and approached a terminal corrosion rate of $\sim 0.18 \mu\text{m}/\text{yr}$. In contrast, an increasing corrosion rate trend was noted in rural and industrial atmospheres with also small terminal corrosion rates on the order of ~ 0.25 and $\sim 0.16 \mu\text{m}/\text{yr}$, respectively. The main finding of their work was that aluminized coating had in general good physical barrier properties. If, however, the aluminized layer was partially disrupted, its sacrificial protection to the exposed underlying steel was not sufficient (as visually noted by the growth of rust projections at the pores and cut edges of the specimens) in all environments tested except for the marine environment. The authors stated that in aggressive environments where chloride ions impair the passivity of aluminum, the aluminized coating is anodic to the exposed steel. In industrial and rural atmospheres, however, the aluminized coating is passivated so that little to no galvanic protection to the underlying steel was noted.

Results from other forms of aluminum coating of steel are instructive as well. Creus et al. (2000) investigated the corrosion behavior of aluminum coating ($\sim 10 \mu\text{m}$ thick) deposited on a 3 cm^2 4135 steel base by physical vapor deposition. The coated steels were immersed in a 3% NaCl solution, aerated, and stirred with a rotating working electrode at 500 rpm. Open circuit potentials (E_{oc}) vs saturated calomel electrode (SCE) and electrochemical impedance spectroscopy (EIS) over a frequency range from 4 mHz to 64 kHz with a 10 mV amplitude around the corrosion potential were monitored. E_{oc} stabilized around $\sim -705 \text{ mV}_{\text{SCE}}$ shortly after immersion reaching $\sim -440 \text{ mV}_{\text{SCE}}$ at 75 hr of exposure. Impedance diagrams after 1 hr of immersion showed two distinctive capacitive loops at high and intermediate frequency ranges, and an inductive loop at low frequencies. The authors attributed the high frequency loop to the charge transfer resistance associated with the corrosion rate of the outer aluminized layer. The charge transfer resistance was estimated to be $\sim 2 \text{ k}\Omega\text{-cm}^2$, which is significantly lower than that for pure aluminum.

According to the authors, this difference in resistance values is a result of an enhanced galvanic interaction between the steel substrate and aluminum through coating defects. Based on the charge transfer resistance value reported and assuming Tafel slopes of 160 mV/dec, a nominal aluminum corrosion rate was significantly higher ($\sim 185 \mu\text{m}/\text{yr}$) compared to the results reported by Gartland (1987). Additional tests conducted by the authors to determine the

galvanic behavior of the aluminum/4135 steel system of 3 cm² surface area, for an anode-to-cathode area ratio of unity, exposed to 3% NaCl solution showed a galvanic current of ~300 μA/cm² (aluminum being anodic to steel) at the E_{oc} of ~-712 mV_{SCE}. The authors stated that the aluminum corrosion rate was basically controlled by galvanic coupling to steel.

Shaw and Moran (1985) studied the corrosion behavior of thermally-sprayed aluminum coating specimens (7-14 cm² surface area with ~100 μm thick coating), with and without linear scribe marks exposed to seawater and marine atmosphere at 25 °C for ~6 months. Visual inspection of the specimens without scribe marks immersed in seawater showed small pits with no base metal corrosion. On the other hand, specimens exposed to marine atmosphere exhibited a slight buildup of corrosion products at the scribe marks but no base metal corrosion was found elsewhere on the specimen surface. Additional laboratory tests were conducted on specimens without scribe marks immersed in synthetic seawater. Corrosion potential tests monitored for 30 days stabilized at ~-800 mV_{SCE} after 10 days. During the entire exposure period, no pits were noted. Anodic polarization tests taken after 10 days of exposure showed that the aluminum coating was in passive state in the region from -800 mV_{SCE} to -550 mV_{SCE} with appearance of few well-defined pits at potentials nobler than -550 mV_{SCE}. The authors concluded that aluminum coatings on steel exhibit weak cathodic protection in marine environments, contradicting findings from Townsend and Zoccola (1979) and Creus et al. (2000).

Johnsson and Nordhag (1984) carried out an investigation to compare the sacrificial corrosion performance of several metallic coating on steel exposed to atmospheric environments and seawater for four years. Corrosion rates of uncoated cut edges aluminized steel specimens with and without scribe marks, exposing underlying steel, were determined by weight loss measurement. The atmospheric tests showed that aluminized steel was attacked mainly by pitting even after one year of exposure, especially in the marine atmosphere. The number of pits, however, did not seem to increase with time. Comparing the corrosion performance of the different metallic coatings, aluminized steel without scribe marks had the best performance except in marine environments in which galvanized steel outperformed aluminized steel. The corrosion rates varied from a low 0.2 μm/yr (urban atmosphere considered by the authors a mild environment) to a modest 1.5 μm/yr (marine atmosphere). Comparable tests conducted on the scribed specimens demonstrated the poor galvanic protection of the aluminized coating to the exposed steel in all environments and seawater, displaying heavy red rust formation along the cut edges and at the scribe mark. This finding is in agreement with observations by Shaw and Moran (1985). It is noted that results for seawater are pointed out because of their mechanistic significance, but not from the standpoint of direct application as FDOT does not specify aluminized steel for seawater service.

Most of the prior experimental investigations on the corrosion behavior of aluminized steel are related to visual corrosion assessment and gravimetric techniques. Only limited data were gathered for the evaluation of corrosion of aluminized steel using electrochemical techniques, especially EIS, which can provide a powerful means to elucidate the corrosion mechanisms and corrosion rates of aluminized steel with and without coating breaks. Thereby, laboratory experiments using this evaluation approach were needed. Furthermore, the majority of the studies on galvanic corrosion involving aluminized steel with exposed underlying steel were conducted by atmospheric exposure or by immersion in highly aggressive solutions. Limited information exists on the galvanic behavior of aluminized steel with coating breaks exposed to fresh waters of varying scaling tendencies with moderate chloride contents, where galvanic protection may not take place at all. Studies have demonstrated discrepancies in the galvanic behavior of aluminized steel when exposed to seawater. Work was needed to clarify this issue. Implementation of a computer model of current and potential distribution in the exposed-steel/surrounding coated surface characterized the effectiveness of galvanic protection of the exposed steel under various environmental and geometric regimes.

4.4 Service Life Prediction Methods for Aluminized Steel Type 2

4.4.1 FDOT service life estimation method for aluminized steel pipe

The FDOT State Material Office completed in 1993 a five-year investigation to assess drainage metallic culvert performance in various environmental conditions in Florida (Cerlanek and Powers, 1993). The study concluded that "a relative performance of aluminized steel as being 2.9 better than galvanized steel in the same environment". The study also cited improvements compared to galvanized steel by factors of 2 to 6 times, and 2 times in prior Army Corps of Engineers and FHWA investigations respectively. Other examples of a durability advantage of aluminized over galvanized steel have been noted in Section 4.3.4 in citing Ault and Ellor (1996). Those combined observations resulted in adoption of the current FDOT service life estimate method for aluminized steel type 2 pipe. In this method, the environmental information is used to compute the estimated service life as if the pipes were made of galvanized steel, and the result is increased by a factor of 2.9 for the pH range 5-7. Service for $\text{pH} < 5$ is not recommended. Recognizing the tendency of aluminum to depassivate at high pH values, service life in the range 7-8.5 is computed as if the pH were the same as 7, and service life estimate is rapidly derated for further pH increases until pH 9, beyond which aluminized steel is not recommended. The corresponding equations are shown in Figure 4.6. Service with environmental resistivity below 1,000 ohm-cm is not recommended either for any pH value. As in the refined California method, durability predictions by the FDOT method do not take into account the system complexity and the variety of responses due to the existence of scale-forming waters.

4.4.2 Potential alternative approaches for aluminized steel pipe

4.4.2.1 California and AISI methods

These methods as they apply to galvanized steel have been introduced in Sections 4.2.3.1 and 4.2.3.2. These methods have been applied in the past also to aluminized steel without credit for improved performance. As indicated above, FDOT adopted the California method, but credited by a multiplier for certain environments, to estimate durability of aluminized pipe. Other main characteristics of the California method have been noted in Section 4.3.4 in citing Ault and Ellor (1996). Present CALTRANS service life estimation procedures do provide some additional performance credit for aluminized steel in non-abrasive environments. The credit is in the form of no need for specifying thicker metal gauge or additional coating (relative to galvanized pipe) to meet 50-year service live in the pH 5.5-8.5 range (Caltrans 2009). Given the extent of incorporation and adaptation of the California method into the Florida approach, no substantial advantage for further inclusion is envisioned at this time.

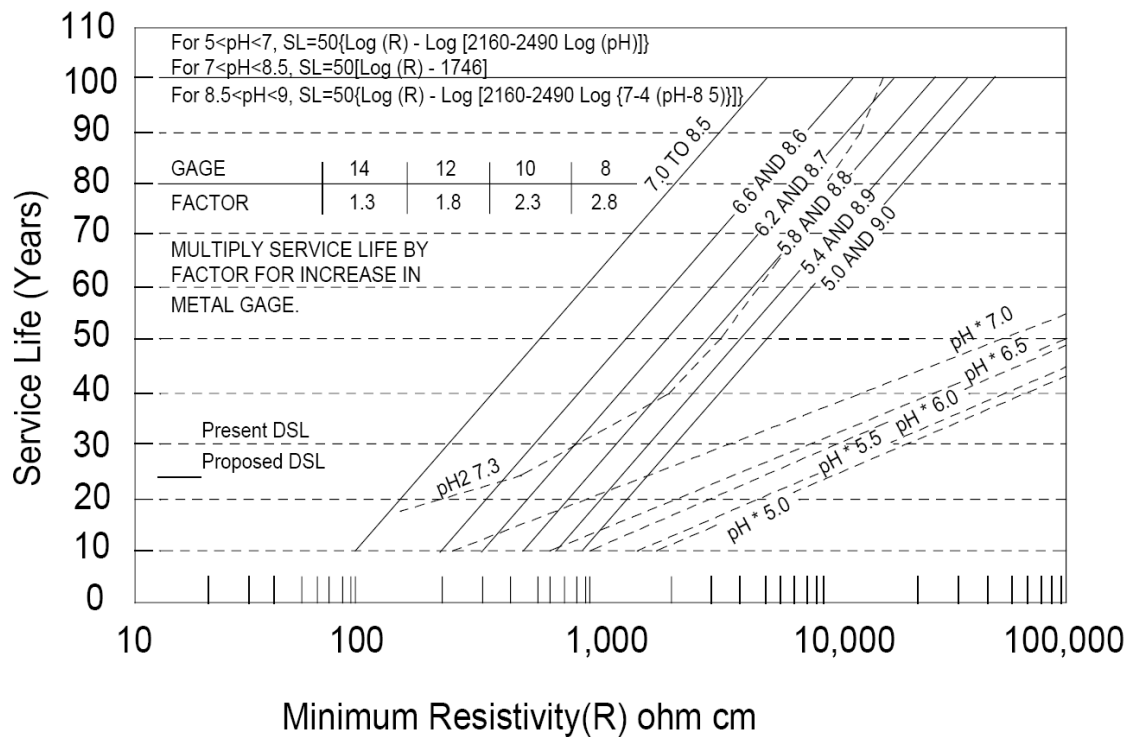


Figure 4-6. The FDOT chart for estimation years to perforation of 16-gage aluminized steel type 2 culvert pipes (solid lines) (Cerlanek and Powers, 1993). Dashed lines correspond to service life estimation using the refined California method for galvanized steel.

4.4.2.2 AK Steel method

The AK-Steel method was introduced in Section 4.2.3.3. As noted in Section 4.3.4 in commenting on the work by Bednar (19998), preliminary application of this method has shown encouraging results in predicting the performance of galvanized steel and aluminized steel type 2 culverts in tropical and subtropical environments comparable to those encountered in Florida. Experimental evidence gathered to support the applicability of this method is nevertheless limited and several important issues remain unsolved that necessitate additional laboratory experimentation. Those issues include the possibility that the aluminized coating could be susceptible to de-passivation if carbonate scales promotes alkaline conditions as indicated by Porter and Hadden (1953).

4.5 Summary and Conclusions

Metals including steel, galvanized steel, aluminized steel, and aluminum are optional culvert materials for drain sections installed in Florida. In non-complexing solutions of $\sim 4 < \text{pH} < \sim 8.5$, aluminum tends to become covered with a protective oxide film; above or below this pH the protective coating can dissolve resulting in high corrosion rates, and the presence of chloride ions on the aluminum surface can induce localized corrosion of aluminum even in the range of aluminum passivity.

Four durability prediction methods were examined: refined California, AISI, FDOT, and AK Steel methods. The first three methods of this list use pH, minimum resistivity of soil or water, and metal gauge thickness as key input parameters to forecast durability of galvanized pipe; the FDOT method extends this approach to aluminized steel type 2 pipe. The AK Steel method incorporates the tendency for water scaling into the service life prediction of corrugated galvanized and aluminized steel type 2 culvert pipes.

Examination of the durability forecasting methods used by FDOT for galvanized and for clad aluminum pipe, and of alternatives to those methods, did not show compelling evidence for changing procedures at this time.

Until recently, the FDOT method to project durability of aluminized steel type 2 was considered to be similarly adequate. Moreover, the majority of the field studies reviewed revealed a superior performance of aluminized steel type 2 over galvanized steel for $4 < \text{pH} < 9$ and resistivities $> \sim 2,000 \Omega\text{-cm}$. The previously mentioned unexpected extensive corrosion damage of aluminized steel in some regions of central Florida, however, generated serious concerns as to the suitability of the present forecasting method. There was uncertainty as to what materials and environmental factors may have been involved in the corrosion mechanism. Mechanical distress and associated coating breaks appeared to have played an important role in the corrosion. The aluminized layer is normally

expected to act as a barrier. Limited information existed prior to this study on the galvanic behavior of aluminized steel with coating breaks exposed to fresh waters of varying scaling tendencies with moderate chloride contents, where galvanic protection may be only a secondary phenomenon or not take place at all.

4.6 Issues for Investigation on Aluminized Steel Performance

Based on the review presented in this chapter, much of the work in this investigation was focused on resolving outstanding issues on the performance of aluminized steel for drainage pipe applications with findings presented in several of the following chapters. Chapter 5 presents detailed assessment of selected instances of premature corrosion of aluminized steel in field applications. Chapter 6 concerns evaluation of the performance of aluminized steel in scaling waters, with attention to the potential for alkaline corrosion of the aluminized film and on the effect of sizable breaks in the film. Chapter 7 addresses the effect of mechanical forming on corrosion, and in Chapter 8 the experimental results are contrasted with the durability expectations from alternative evaluation methods. Findings from evaluation of the cathodic behavior of aluminized steel are presented in Chapter 9.

5 SEVERE CORROSION IN SERVICE OF RIBBED ALUMINIZED STEEL TYPE 2 CULVERT PIPING

5.1 Field Experience and Analyses - St. Cloud, Florida

The first incident of unexpected severe early corrosion of aluminized pipe was noted in 2005 for pipe installed in the City of St. Cloud in Osceola County, Florida. The installation was not an FDOT project but merited extensive attention because of FDOT's large inventory of aluminized pipe. As indicated by Scannell (2005), over 5,000 m in length of spiral rib aluminized steel pipe were installed there in 2002 and 2003. The pipe was manufactured by Contech Construction Products, Inc. and installed by Schuller Contracting, Inc. for the 'El Niño' drainage project. As part of the present investigation, detailed analyses were conducted on soil and water samples as well as on pipe sections extracted from the St. Cloud site. The findings are described in the following sections.

5.1.1 Soil and water samples examined

A total of 5 soil samples placed in airtight plastic containers, 6 water samples received in plastic bottles, and 5 aluminized steel coupons of different sizes were collected by and received from Mr. William Scannell on 08/30/05 and 09/01/05, respectively. The soil samples and coupons were stored in the Corrosion Engineering Laboratory at the University of South Florida (USF) at relative humidity ~ 60-70% and temperature ~23°C. The water samples were kept in a refrigerator. The numbering code of the water and soil samples is consistent with that reported by Scannell (2005). Table 5-1 summarizes information on the origin of the samples. Samples of each soil were dried to a consistent weight and were stored, dried, in amber glass for later chemical analyses.

5.1.2 Water and soil chemistry

Tables 5-2 and 5-3 summarize the chemical analyses and properties of the water and soil samples obtained by the Corrosion Engineering Laboratory and College of Public Health (COPH) facilities at USF except for water sulfate analyses, which were made by PSI, Inc. (Tampa office). Tests of pH and resistivity were performed in accordance with FM 5-550 (FDOT, 2000a), and FM 5-551 (FDOT, 2000b), respectively. The pH was measured with a Corning Model 140 pH meter (Scientific Instruments, Science Products, Corning Glass Works, input impedance $\sim 10^{12} \Omega$) set as a voltmeter. An auxiliary multimeter was connected to the voltmeter output to achieve a resolution of 0.1 mV. Resistivity was measured using a Nilsson Model 400 meter and a soil box from MC Miller. Initial water and soil sample preparation for chloride and sulfate detection was conducted in accordance with FM 5-552 (FDOT, 2000c) and FM 5-553 (FDOT, 2000d), respectively. Testing for chloride and sulfate ions as well as nitrate, nitrite, total alkalinity, and total hardness was performed following the procedures

detailed in APHA (1998). Ion chromatography of the soil extract was done with a Dionex DX-600 ion chromatography unit equipped with an EG40 eluent generator, a GP50 dual-piston pumping system, a CD25 conductivity detector connected to an online computer for data acquisition, and an AS40 automated sampler. An IonPac® AS9-HC analytical column (4-mm diameter and 50-mm long) was used.

**Table 5-1
Description of Samples Tested**

Sample Type	ID Number	Date Obtained	Sample Origin
Water	1	08/29/05	Pump discharge hose at Indiana Ave.
	2	08/29/05	Pump discharge hose at Indiana Ave.
	3	08/31/05	Inside pipe at manhole #S-548 on Indiana Ave.
	4	08/31/05	Inside concrete overflow at the east retention pond just east of Illinois Ave.
	5	08/31/05	Lake Tohopekaliga at the Dan Tarrell Memorial Point
	6	08/31/05	West retention pond just west of Massachusetts Ave.
Soil	1	08/31/05	Excavation site at 1 ft. deep from roadway surface and ~11.5 ft. south of manhole #S-548
	2	08/31/05	Adjacent to concrete overflow at the east retention pond just east of Illinois Ave. and at the depth just below grass level
	3	08/31/05	West retention pond just west of Massachusetts Ave.
	4	08/31/05	Adjacent to the east side of pipe section #1 at the depth just below springline and ~7 ft. south of manhole #S-548
	5	08/31/05	Adjacent to the west side of pipe section #2 at the depth just below springline and ~16 ft. south of manhole #S-548
Metal Coupon	1	08/31/05	See Figure 5-2 for details
	2 (2A and 2B)	08/31/05	
	3	08/31/05	
	4	08/31/05	

**Table 5-2
Water Sample Results**

Sample ID	Cl ⁻ , ppm	SO ₄ ²⁻ , ppm*	Hardness, ppm as CaCO ₃	Alkalinity, ppm as CaCO ₃	pH	Resistivity, Ω-cm	Nominal Service life**, yr
#1	34.7	62.9	44	13	5.56	5,200	62
	35.6				5.53		61
#2	34.1	62.9	44	10	5.51	5,100	60
	34.8				5.47		60
#3	14.5	28.8	44	36	6.50	8,200	89
	15.9				6.31		84
#4	12.2	30.0	44	41	6.61	7,400	90
	14.2				6.65		91
#5	15.0	17.2	36	20	6.93	11,100	111
	15.5				6.92		111
#6	16.7	35.2	80	50	6.83	6,400	95
	17.3				6.73		91

*Values reported by PSI, Inc. (Tampa office) performed in accordance with FM 5-553.

**Per FDOT Drainage Culvert Service Life Estimator (Cerlanek and Powers, 1993).

**Table 5-3
Soil Sample Results**

Sample ID	*Cl ⁻ , μg/g	NO ₂ ⁻ , μg/g	NO ₃ ⁻ , μg/g	SO ₄ ²⁻ , μg/g	pH	As-received resistivity, Ω-cm	Minimum resistivity, Ω-cm	Nominal Service life**, yr
#1	7.1	0.6	11.5	72	7.84	12,350	5,050	98
					7.80			98
#2	7.2	0.2	5.5	165	6.30	3,950	3,500	66
					6.09			61
#3	14.7	1.0	6.8	118	7.40	5,500	5,500	100
					7.03			100
#4	6.6	0.2	6.3	15	7.04	12,100	7,500	106
					7.06			106
#5	6.5	0.2	5.5	19	7.08	12,700	11,200	115
					7.10			115

*The results for Cl⁻, NO₂⁻, NO₃⁻, and SO₄²⁻ are expressed in μg of anion per gr. of dry soil.

**Per FDOT Drainage Culvert Service Life estimator (Cerlanek and Powers, 1993).

The environmental chemistry data were used to estimate nominal durability per the FDOT Drainage Culvert Service Life Performance and Estimation document (Cerlanek and Powers, 1993) for 16-gage aluminized steel type 2. The results, incorporated in Tables 5-2 and 5-3, were between 60 and 115 years. An alternative scaling index durability estimation method proposed by

Bednar (Bednar, 1989; Morris, 1998) was applied as well with the results shown in Figure 5-1. With one exception (~20 years), the alternative method indicates durability ~50 years or more. Clearly, the extensive damage observed in the field after only ~3 years of service was not anticipated by either forecasting procedure.

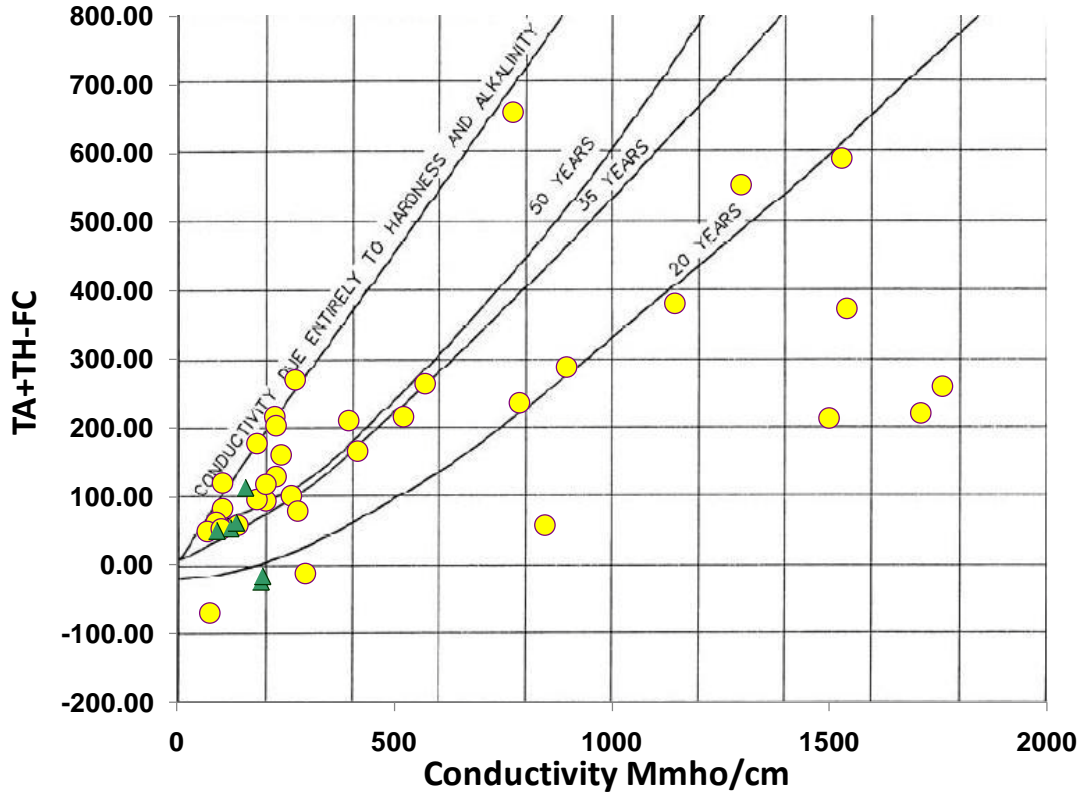


Figure 5-1. Alternative scaling index durability projection (Bednar 1989; Morris 1998) using water data from St. Cloud (triangles) and other Florida fresh waters (circles).

5.1.3 Visual assessment of the pipe metal coupons

Figure 5-2 shows the actual coupon locations cut out of metal pipe sections #1 and #2 described in detail in the Draft Report – Phase 1 dated on 09/08/05 reported by Mr. William Scannell. In general, the metal coupons exhibited heavy red-like corrosion products accumulated mainly at the spiral ribs and lock seams from the water and soil sides, except for coupon #3 which depicted slight waterside corrosion and little corrosion from the soil side as shown in Figure 5-3.

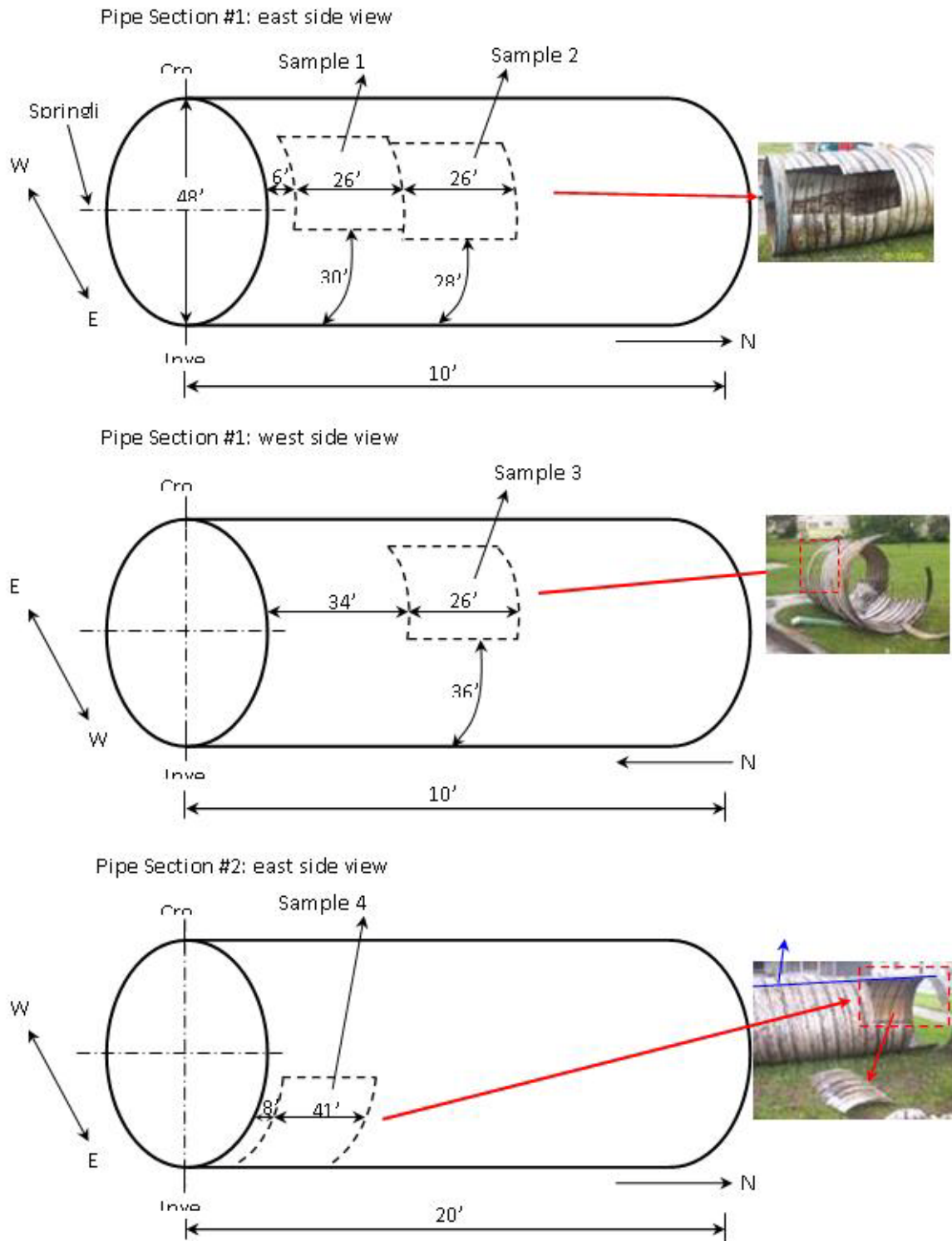


Figure 5-2. Schematic and pictures of the metal coupons taken from sections of aluminized steel type 2 culvert piping removed from service in St. Cloud, Florida.



Figure 5-3. Coupon #3 corrosion before cleaning on water side (left) and soil side (right).

After initial visual assessment, the metal coupons were carefully cleaned on both sides and corrosion morphology was investigated in detail. At the time of visual inspection, there was clear indication that corrosion at the ribs and seams started in the form of pits and then propagated along the rib curvatures as more uniform corrosion on both metal sides. At the flat portions of the metals away from the seams and ribs several well-defined pits were noticed with red-like corrosion products surrounding pit mouth.

Close examination of the outside rib section of the coupons showed several spots with nearly complete aluminum/intermetallic coating loss along the ribs. Corresponding coating thickness measurements made with a magnetic thickness gage meter indicated a remaining coating thickness of ~0.7 mils. Where coating loss was not prominent, coating thickness was typically ~2.6 mils as found also in the metal portions away from ribs and seams. That coating thickness is as expected from normal aluminized steel type 2.

In metal coupons #1 and #4 there were full penetration elongated openings ~1.3 to 11 cm long and ~3 mm wide located in the center of the coupons at the rib base (Figures 5-4a and 5-4b). From the placement of the sharp opening edges and overall shape, it is inferred that penetration started from the waterside and propagated towards the outside of the metal. For metal coupon #1, the elongated opening was positioned a few inches above the pipe springline whereas all cracks observed in coupon #4 were close to the pipe invert. Overall visual assessment of the pipe condition at the time of excavation revealed a waterline location just below the pipe springline. As a result, all cracks present in coupon #4 were presumed to be immersed in water at all times, whereas the position of the crack in coupon #1 was apparently above the waterline. The above statement, however, does not consider temporal variations of the water table position and/or water present in the pipe.



Figure 5-4a. Coupon #1 outer rib after cleaning.



Figure 5-4b. Coupon #1 inside rib before cleaning.

Approximately 2 g of corrosion products from coupon #1 were extracted from the rib inside ~30 cm from the opening and mixed with a small volume of distilled water in a small glass vial to form a mud-like mix. The resulting leachate had pH ~6.34, value comparable to those obtained from water pH tests (Table 5-2).

During the cleaning process several small holes, ~1 to 7 mm diameter and located at the rib bends, were revealed in coupons #1 and #4 (Figure 5-5). Table 5-4 summarizes the features that were observable after cleaning. A sum of the total length of all full penetration linear openings plus diameters of all holes was made individually for coupons #1 and #4. Dividing that length by the area of each coupon yielded 0.064 m/m^2 (0.21 ft/ft^2) and 0.024 m/m^2 (0.08 ft/ft^2), respectively. For the elongated openings or holes that were revealed by cleaning no clear indication was found as to whether penetration started from the water or soil side, or both combined. It is noted that linear penetrations following the helical rib pattern were consistent with the severe mechanical distress from manufacturing defect origin mentioned earlier and discussed further in Section 5.1.6.1.



Figure 5-5. Coupon #4 outer rib after cleaning.

Figure 5-6 shows a close-up view of the spiral rib from coupon #1 after cleaning. Some degree of mechanical disturbance noticeable, in the form of fine parallel marks ~5 mm long located perpendicular to the rib base extended along the ribs. These features were observed at several locations and are consistent with the normal manufacturing process as they were also seen in newly produced pipe. Later examination showed that the alteration is mostly superficial and not necessarily associated with severe deficiency..

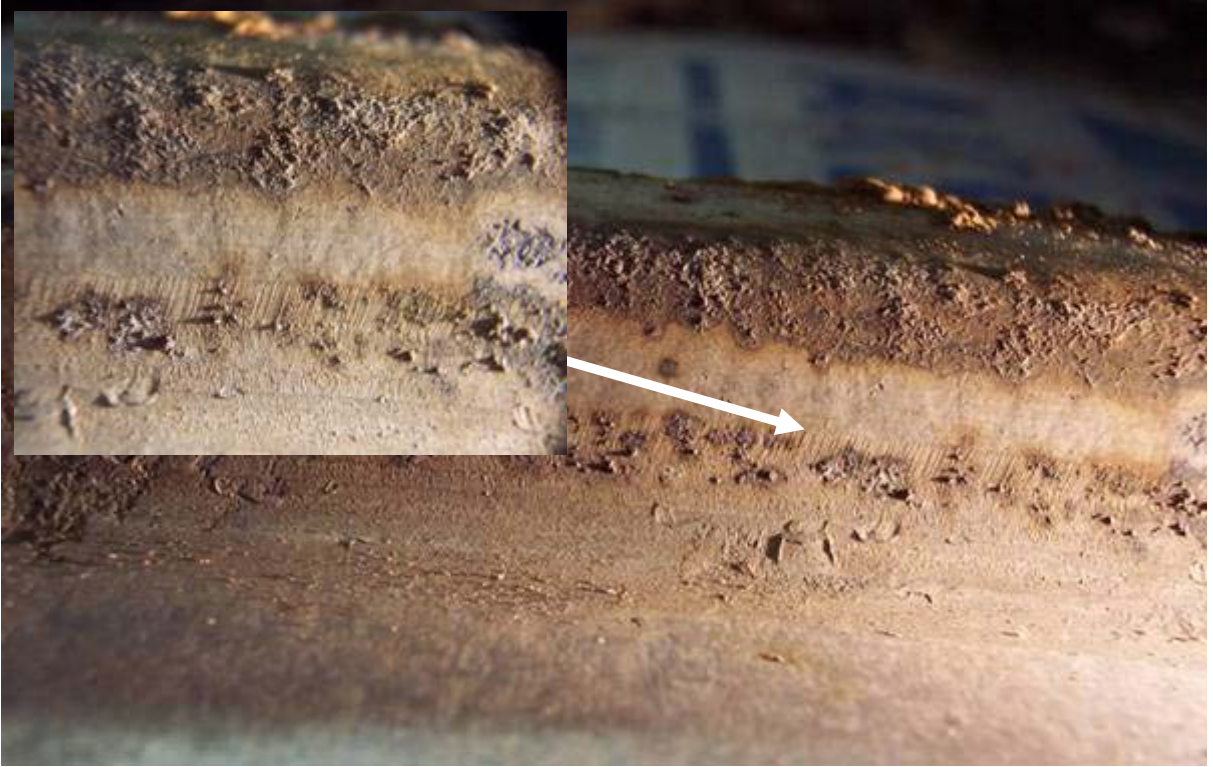


Figure 5-6. Coupon #1 close-up view of an outer rib.

**Table 5-4
Description of Pipe Coupons after Cleaning**

Coupon ID	Dimension	Number of penetrations	Penetration Dimensions	Number of Elongated Openings	Elongated Opening Dimensions	Overall Condition
#1	51x66 cm	1	$\phi \approx 0.3$ cm at rib base	1	~11 cm long, ~0.3 cm wide at rib base	Extensive damage at ribs (waterside was in worse condition). Full coating loss in several locations
#2A	30x43 cm	None	None	None	None	Corrosion at ribs (most noticeable in waterside). Several spots with full coating loss
#2B	36x46 cm	None	None	None	None	Corrosion at ribs (most noticeable in waterside). Several spots with full coating loss
#3	51x66 cm	None	None	None	None	Good condition with minor corrosion at ribs on the inside
#4	71x107 cm	7	$\phi \approx 0.2$, ~0.3 (three holes), ~0.5, and ~0.7 cm at rib base	2	~4 cm long, ~0.3 cm wide. ~1.3 cm long, ~0.2 cm wide	Severe corrosion at ribs with several full penetrations at upper rib bends

5.1.4 Microscopic examination

Two ~5 to 7 cm wide and 10 cm long metal pieces (one obtained at a spiral rib and the other at a lock seam) were cut out of coupon # 3 (see Figure 5-7 and 5-8) for metallographic analysis. Each metal piece was then transversely cut into three samples and mounted in epoxy. The samples were polished down to 0.05 micrometers, cleaned with ethanol and etched with Nital solution.



Figure 5-7. Spiral rib sample cut out from coupon #3 used for metallographic analysis.



Figure 5-8. Lock seam sample cut out from coupon #3 used for metallographic analysis.

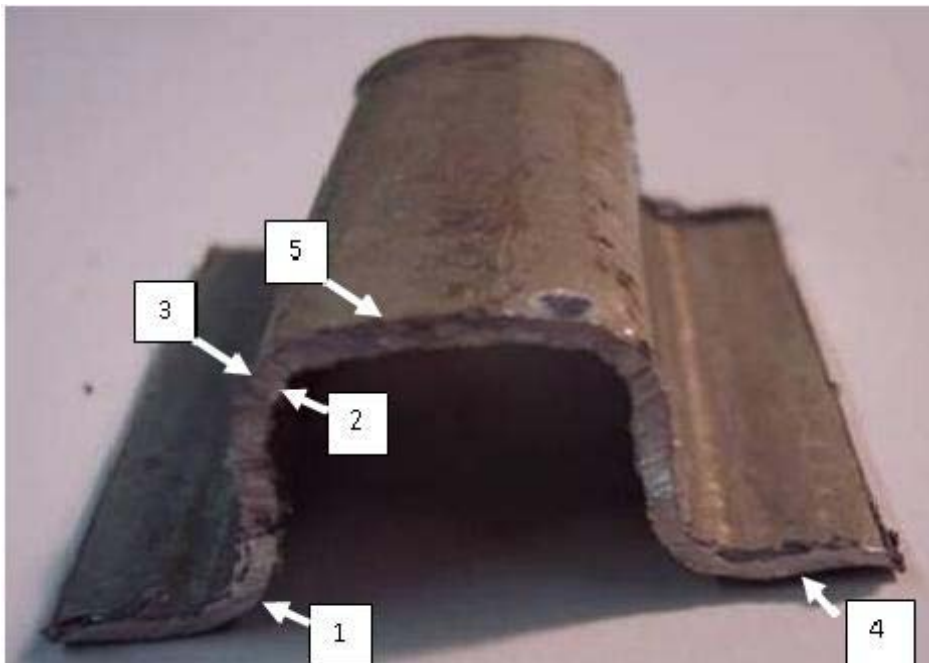


Figure 5-9a. Sample of the cross section of the coupon #3 spiral rib. Feature key.

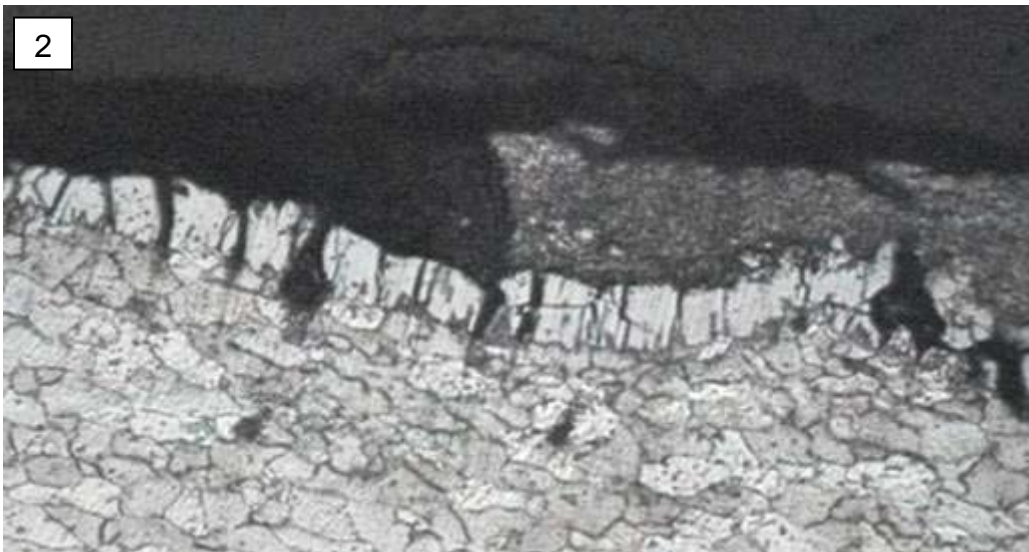
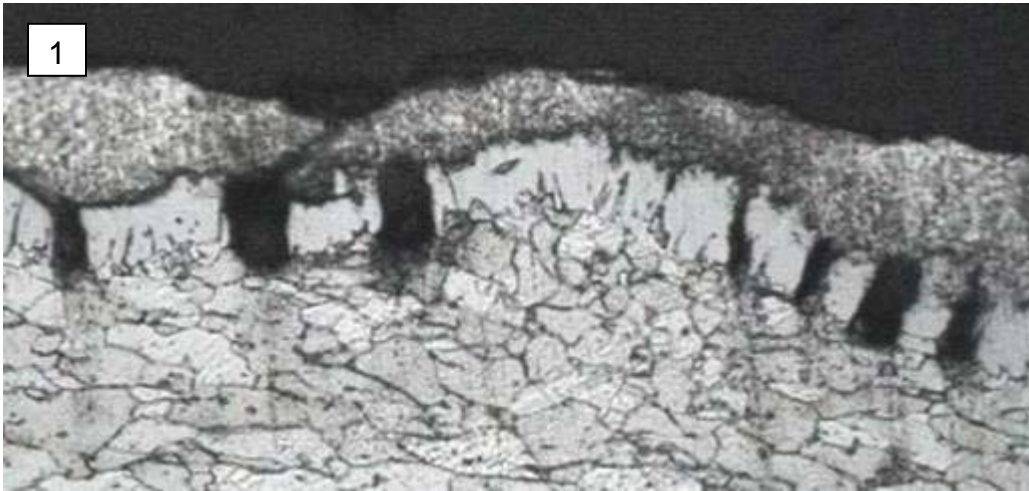


Figure 5-9b. Cross sections for features 1 to 3. Inner layer is ~10 μm thick.

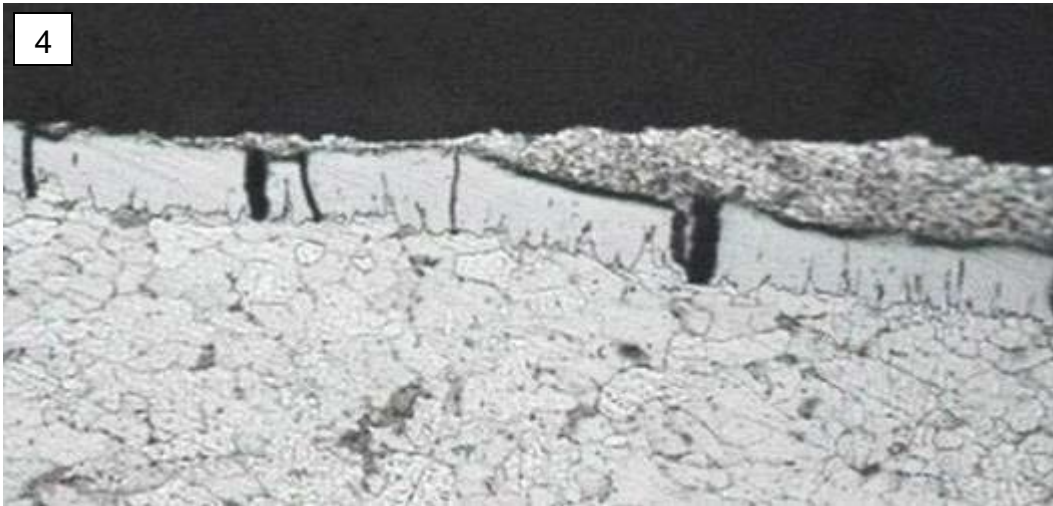


Figure 5-9c. Cross section for features 4 and 5. Inner layer is $\sim 10 \mu\text{m}$ thick.

Microscopic examination of the samples showed a nearly uniform outer coating ~ 15 to $20 \mu\text{m}$ thick and an inner intermetallic layer $\sim 10 \mu\text{m}$ thick, consistent with normally produced aluminized steel type 2. However, the outer layer was missing at several locations at the rib and seam bends as shown in Figures 5-9 and 5-10. There was no conclusive evidence as to whether the missing outer layer was missing because of corrosion during service or if it was absent beforehand.

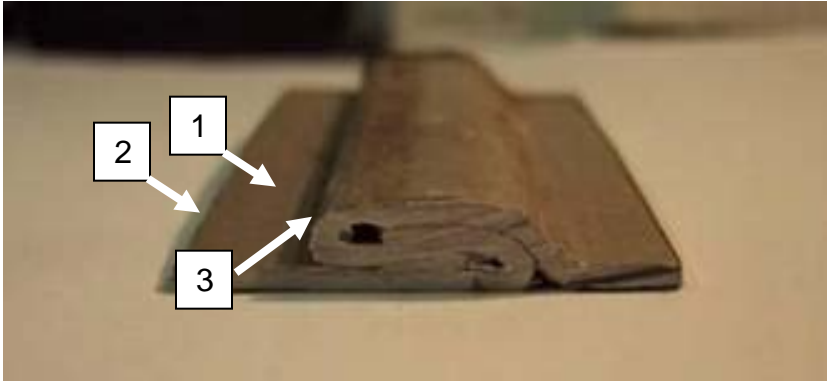


Figure 5-10a. Sample of the cross section of the coupon #3 lock seam. Feature key.

No evidence was observed in these field samples of aluminized coating cracking or spalling due to differential deformation during sharp-radius bending. It is noted however that severe distress was observed in sharply bent samples from nominally the same type of aluminized steel obtained from other sources (Chapter 7) so some variability in tolerance to bending appears to exist. Coating distress did appear to be associated with sharp shearing near some of the rib bends, as illustrated in Figure 5-11. The corrosion spot (semicircular region underneath the break) seems to be due to base steel having been exposed at the shear line.

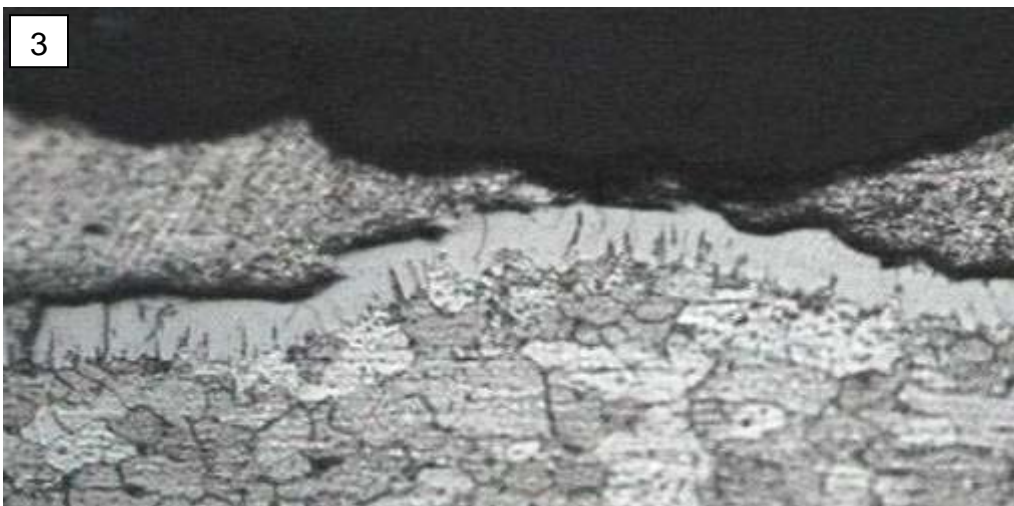
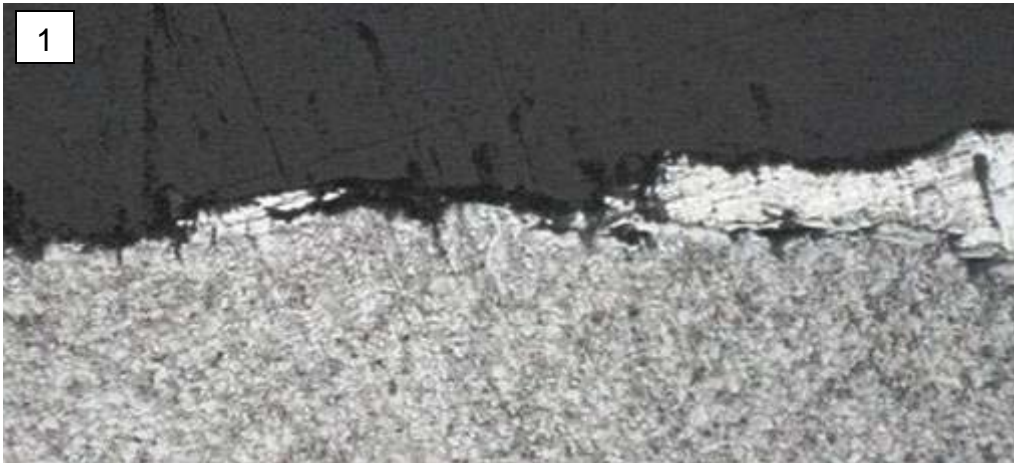


Figure 5-10b. Cross sections for features 1 to 3. Inner layer is $\sim 10 \mu\text{m}$ thick.

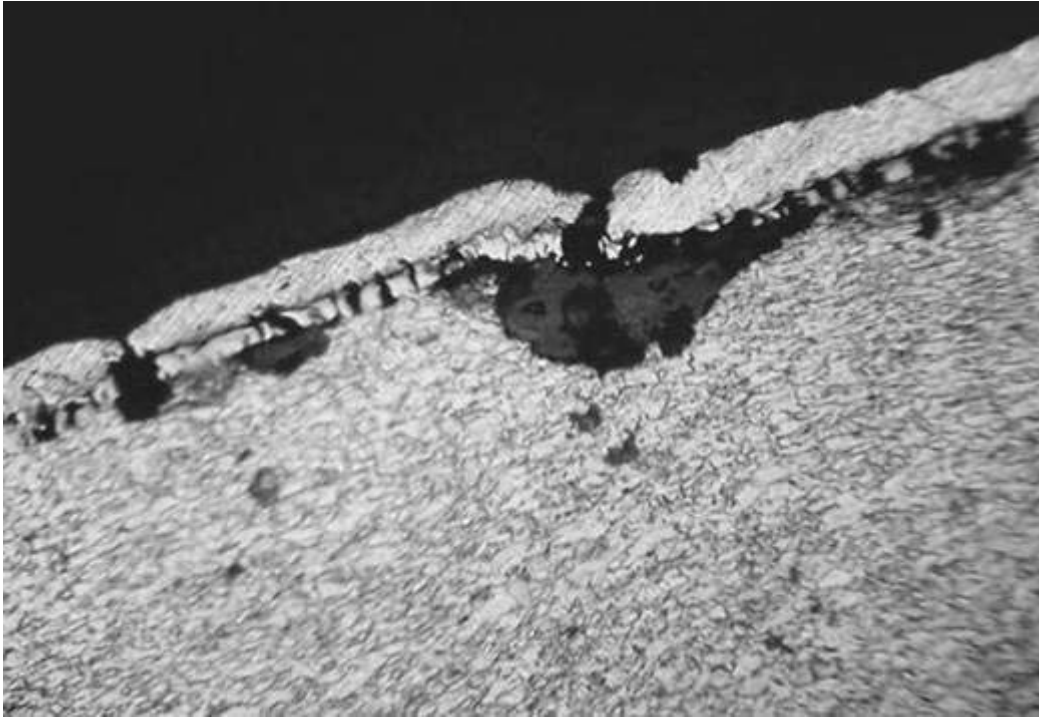


Figure 5-11. Microstructure of a sample cut out of coupon #3 inside rib bend. Inner layer is ~10 μm thick.

5.1.5 Measurements of half-cell potentials in the field

Additional visits to the City of St. Cloud were conducted on 09/16/05 and 09/20/05 coincident with extraction of additional soil and water samples. Tables 5-5 and 5-6 summarize the field site locations visited as well as the single open circuit potentials (OCP) obtained from the water and soil sides for each aluminized steel pipe sample, where available. The OCP values are referred to a copper sulfate reference electrode (CSE) unless stated otherwise. An MC Miller voltmeter with 200 M Ω input resistance was used. The waterside OCP measurements were obtained by briefly immersing the CSE tip into the water stream. The soil side OCP measurements, except for the location #1, were obtained by inserting the CSE into the bore hole ~1 to 2 m deep drilled ~0.6 m away from the pipe. The soil side OCP reading for the location #1 was taken at the bore hole at ~10 cm depth. Typically, stable OCP readings were recorded in less than a minute.

**Table 5-5
Single OCP Measurements and Pipe Characteristics**

Location	Pipe diameter cm (in)	Pipe depth m	Water table m	OCP, V vs. CSE	
				Waterside	Soil side
#1	122 (48)	2.1	0.8	-0.381*	-0.633
#2	91 (36)	2.0	0.9	-0.599	-0.620
#3	91 (36)	2.1	1.0	N/A	N/A
#4	61 (24)	1.1	1.1	-0.607	-0.617
#5	91 (36)	2.0	1.2	-0.601	-0.536
#6	137 (54)	2.7	0.9	N/A	N/A
#7	137 (54)	2.7	N/A	-0.596	-0.619
#8	137 (54)	2.3	N/A	N/A	N/A
#9	137 (54)	2.7	N/A	-0.697	-0.601

*Unstable reading even after 5 min. N/A: not accessible

**Table 5-6
Pipe Locations and Site Description**

Location	Address	Observations
#1	400 Indiana Ave.	Pipe half full with water
#2	438 Indiana Ave.	Pipe half full with water
#3	612 Indiana Ave.	Pipe not accessible
#4	806 Indiana Ave.	Pipe with little water
#5	701 Cypress St.	Pipe half full with water
#6	200 Illinois Ave. (SW corner of Cypress & IL)	Pipe totally immersed in water
#7	348 Illinois Ave.	Pipe 2/3 full of rain water run off
#8	522 Illinois Ave.	Pipe not accessible
#9	722 Illinois Ave.	Pipe nearly empty

Measurements of open circuit potentials suggested that little galvanic protection was provided to any steel that may have been exposed where coating damage existed initially. Laboratory experiments described in Chapter 6 have indicated that effective galvanic protection takes place when the environment is sufficiently aggressive to de-passivate the aluminized layer (e.g. in the presence of high chloride levels) but not under the relatively mild conditions encountered at the St. Cloud locations examined.

5.1.6 Discussion of significance of findings from the St. Cloud, Florida site

The following sections summarize the field observations from this site and present initial speculations as to the causes of the observed deterioration. Much

of the research work presented starting in Chapter 6 was aimed at elucidating the issues discussed here.

5.1.6.1 Forms of pipe distress

Distress of the aluminized steel pipes was manifested by severe initial mechanical damage (SIMD) created during manufacturing, by severe corrosion, or both.

SIMD was sufficient sometimes to result by itself in pipe breach or collapse even in the absence of corrosion. SIMD was present in two forms. The most consequential form of SIMD consisted of helical cuts usually running at one of the bases of a rib, for lengths ranging from a few cm to several meters. Cuts were associated with partial or massive pipe collapse and intrusion of soil into the pipe. A lesser form of SIMD took place as isolated (e.g. some meters apart) longitudinal cracks running the width of a rib (about 1 inch). The cracks are wide enough to allow easily inserting a knife blade. Examination of one of those cracks, that had little associated corrosion, revealed sharp edges suggestive of little residual ductility possibly from excessive local triaxial stress during forming. This damage often allowed conspicuous intrusion of soil into the pipe.

At two locations (Illinois Ave. and 6th St., and Indiana Ave. at 7th St) SIMD occurred with very little associated corrosion; the aluminized surface was generally bright and clean with only minor and infrequent rust spots. In other instances SIMD, mostly in the form of helical cuts, was accompanied and aggravated by severe corrosion as indicated below. At some pipe collapse/massive leaking locations the SIMD may not have quite cut through the full aluminized sheet metal thickness. Instead, perforation was likely completed by subsequent corrosion of the base steel exposed by the mechanical damage.

Corrosion penetrating into the base steel, occurring at a relatively fast rate, took place in several of the pipes with SIMD. The corrosion was severe not only at the base metal exposed at the cut or crack edges, but often also decorated the sharp bend regions of the ribs and sometimes extended for one inch or more into the flatter metal onto each side of the rib. When a rib exhibited SIMD in the form of a cut for part of its length, the rest of that rib tended to show more corrosion than adjacent ribs that did not have any cuts. Sometimes small pits (penetrating the pipe wall) were observed in the flatter zone near corroding ribs. Both the soil side and waterside of the pipe were affected. The fastest corrosion rates may have exceeded 0.5 mm/yr (based on typical pipe thicknesses and 3 years service time to breach).

Corrosion was also observed separate from SIMD. This was the case for the 183 cm diameter pipe that did not exhibit SIMD but showed extensive corrosion of the base metal (both on the waterside and soil side surfaces), especially at the rib bends and with morphology comparable to that observed in

pipes with SIMD away from the actual cuts or cracks. The pipe was of thicker gage (#8) than at the other locations and no full wall penetration took place. Nevertheless, the deepest penetrations were on the order of ~1 mm, which corresponds to about 0.33 mm/yr, comparable to corrosion rates at the SIMD-affected pipes.

5.1.6.4. Possible causes

SIMD appears to have resulted from tooling problems during the bending/forming process, possibly as a result of worn or stuck, mis-aligned or over-tightened rollers and/or insufficient lubrication. The findings did not indicate any obvious aluminized steel sheet stock deficiencies.

For corrosion associated with SIMD, it is noted that plain low carbon steel as that used in the base metal for the aluminized sheet stock has very little inherent corrosion resistance. In the absence of any galvanic protection, such steel if devoid of any protection may corrode in even mild environments (neutral naturally aerated water with little aggressive anion contamination) at a relatively fast rate, comparable to those noted above. Small-sized components may experience relatively faster corrosion because of more efficient local oxygen transport.

Cuts and cracks in SIMD expose small amounts of bare base steel to the environment. Under some environmental circumstances the surrounding aluminum coating may act as a galvanic anode, which would protect such small amounts of exposed base steel from corrosion. Laboratory experiments (see Chapters 6 and 7) as well as the field measurements of pipe potential, however, indicate that the environmental conditions at St. Cloud were not conducive to strong protective galvanic action by the surrounding aluminized coating. Thus, the bare steel in the small exposed areas would tend to behave as if it were not protected by the rest of the sheet and high corrosion rates are possible, as observed in several cases. Notably, if conditions were more aggressive (for example, high chloride concentrations) than those present, the galvanic protective action of the aluminum might have been activated, as discussed in Chapter 6 and following.

For this site, there were no clear indications from environmental analyses as to why corrosion was severe at some SIMD locations and mild at others. Analyses indicated that environmental aggressiveness (from the standpoint of attacking normally produced aluminized pipe) was relatively low at all locations sampled. Environmental factors not commonly considered in metallic pipe durability (e.g. microbiologically-influenced corrosion, MIC) could have been unrecognized aggravating agents at some locations. Chapter 10 includes an extensive discussion of that possibility, which will need additional investigation in the future to be resolved.

The severe corrosion in some SIMD cases at ribs, etc., away from the cuts or cracks but intensified at the ribs associated with cuts, suggests that whatever caused SIMD also adversely distressed the coating (and bared sufficient base metal) at the other observed corrosion spots. It would seem that the coating distress had to be more than that resulting from normal forming, since some sharp bending spots (e.g. seams) in the same pipes showed little corrosion. Thus, coating damage (e.g. microcracks) if any from regular mechanical action appeared not to have bared enough base metal to trigger severe corrosion. Subsequent work presented in Chapter 7, however, showed instances in which forming strains without surface abrasion did create conditions for severe corrosion under otherwise moderate to mild exposure conditions.

It is also possible that the hypothesized distress associated with corrosion reflected some form of surface scratching by the same rollers and related components that cause SIMD. Metallographic examination of bent areas suspected of corrosion-inducing distress did not identify the form of that distress. It is possible that the affected regions corroded away early on, leaving no useful indications of the hypothesized damage.

Corrosion was also observed separate from SIMD. Because of similarity of corrosion morphology with the SIMD cases, corrosion on the 183 cm diameter pipe may have reflected coating distress that would have been associated with SIMD in a thinner gage pipe. As in the other cases, telltale distressed regions might have already disappeared by the time of the investigation. As noted above, regular forming could have explained at least some of the corrosion apart from SIMD and that was investigated as detailed in Chapter 7.

5.2 Field Experience and Analyses - SR 586 Project, Curlew Road, Pinellas County

5.2.1 Observations and interpretation

Extensive corrosion of ribbed aluminized steel type 2 culvert pipe installed along Curlew Road in Clearwater, Florida, was discovered in late 2006, when the installation was about 10 years old. A subsequent investigation and full report was made for FDOT by Concorr Florida, Inc. (CONCORR Florida, 2007). Additional examinations of the site were conducted by the pipe manufacturer (Burnette, 2007).

The pipes showed widespread presence of circumferential and horizontal splits and corrosion, often clearly associated with mechanical distress that included helical splits similar to those noted at the St. Cloud site. Pipe segments at Curlew Road site appeared to be contaminated from a nearby sewer line. The additional investigation by the pipe manufacturer revealed the presence of sulfur compounds in some of the corrosion products, indicating that MIC may have been a factor (see Chapter 10.4.1).

It can be concluded that the particularly severe corrosion observed at the Curlew Road site and the severe corrosion at the St. Cloud site share in common the presence of substantial metal-forming defects and corrosion concentration in the rib areas, indicating that forming distress was the primary cause of early pipe failure. Differences in corrosion severity may be ascribed to longer service age at the Curlew Road site, and possibly to some variation in environmental aggressiveness (such as MIC) as a secondary issue.

5.3 Forming Strain

It was of interest to determine whether mechanical strain in production of the pipe ribs (as opposed to SIMD in the form of helical cuts or similar severe damage) may have been unusually high at the Curlew Road site. To that end, a portion of a Curlew Road pipe was sectioned at spots not showing significant corrosion and the outer (tension side) radius of curvature of the bends was measured in four different cross sections. Each cross section yielded four radius measurements (Figure 5-12 shows schematic with the circle fit for each) for a total of 16 values. A similar sampling took place for five cross sections from a newly produced pipe from the same manufacturer, produced under strict quality control. The results in Figure 5-12 revealed no statistical difference between both products considering the natural dispersion of the measured radii in both cases.

At present there is not enough service time experience to directly determine if, even under ideal fabrication conditions, the sharp bending radius inherent to the rib shape would appreciably de-rate long term performance compared to that of plain corrugated pipe of the same material. That question is of importance since much of the longer-term experience with aluminized pipe cited in the previous chapter (e.g., Ault and Ellor (1996), Bednar (1998)) is for regular corrugated pipe. Regular corrugation requires a much gentler bending radius (e.g. >50 mm) compared with a few mm for ribbed pipe, with consequently a lesser degree of breaks in the coating layer due to bending. Further examination of the effects of regular forming on corrosion is presented in Chapter 7.

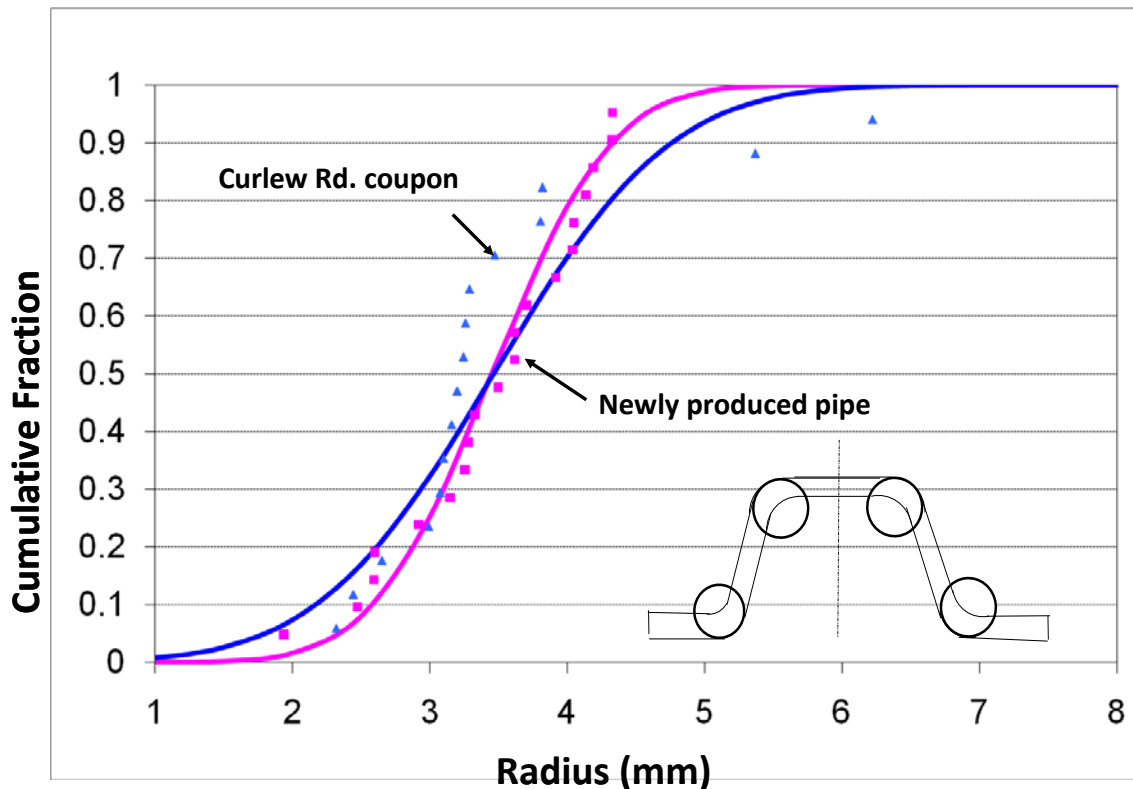


Figure 5-12. Comparison of cumulative distributions of rib outer radius of curvature (mm) between samples from a newly produced aluminized steel type 2 pipe and from a pipe once installed at the Curlew Road site. The schematic shows the position of the circles fit to each bend for each cross section.

5.4 Summary and Conclusions

- Environmental conditions at field sites showing severe aluminized pipe corrosion fell under relatively mild regimes per conventional classifications. Projections based on current FDOT service life estimations or an alternative procedure greatly underestimated the extent of damage observed in the field.
- Corrosion damage took place mostly at the pipe ribs and seams. Corrosion appears to have been more severe at the waterside than at the soil side. The aluminized coating in the portions of the field samples where it was sound enough to be examined metallographically did not show evidence of having been severely damaged by the small bending radii used in normal fabrication. The most severe damage may have resulted instead at ribs and seams from scrapping by die/tool contact. Further assessment (as started in Chapter 7) of the effect of normal fabrication bending on corrosion is needed.

- Field OCP measurements on the order of ~ -600 mV (vs. CSE) indicated little galvanic protection of any spots (such as those at the deformations noted above) where base steel may have been exposed during fabrication. It would appear that much of the observed corrosion took place at prior coating damage spots.
- The service life estimation methods in present use by FDOT and possible alternatives considered in the previous chapter were largely based on regular corrugated pipe, and do not have provisions for the effect of substantial localized aluminized coating damage as it may occur in ribbed pipe production. Such consideration would need, among other issues, assessment of the extent of galvanic protection available under various environmental conditions.

6 CORROSION OF ALUMINIZED STEEL TYPE 2 IN SCALE FORMING WATERS

6.1 Introduction

As indicated in Chapter 4, detailed examination of the factors responsible for the corrosion resistance of aluminized steel type 2 is needed to elucidate that source of the deterioration encountered in the field experience discussed in the previous Chapter. In addition, information is needed on whether the service life of aluminized steel may be better predicted by methods alternative to those presently used by FDOT. In particular, methods based on the proposition (Morris and Bednar, 1998; Bednar, 1989) that calcium carbonate scales formed from natural waters are protective to aluminized steel merit investigation. It is noted too that the outer aluminized coating can maintain passivity for extended exposure times in scale-forming environments so that long service lives of unblemished aluminized steel components could be expected. The aluminized coating, however, may be mechanically partially disrupted in common use exposing the underlying base steel. In such case, it is important to know if the aluminized coating could provide a measure of galvanic protection to the exposed steel, and to what extent the size of the exposed steel portion would be important when exposed to environments relevant to those encountered in Florida.

As discussed in Chapter 2, a common indicator of scaling tendency is the Langelier Saturation Index (LSI), where positive values of LSI imply a tendency for CaCO_3 precipitation. The LSI parameter, however, does not consider the reserve of species in the solution responsible for a given pH. Based on extensive field data collection, Bednar (1989) proposed that the corrosion performance of aluminized steel type 2 in aerated media may be better predicted by the combination of an index indicating carbonate scaling tendency (scaling index (SI) = total alkalinity (TA) plus total hardness (TH) minus free CO_2 (FC)) and the conductivity σ of the solution in contact with the metal. There is concern, however, that the aluminum-rich layer of the aluminized steel could be susceptible to de-passivation if the carbonate scale promotes alkaline conditions. Porter and Hadden (1953), for example, stated that corrosion of pure aluminum was most severe in natural waters with a high scaling tendency. This concern is addressed in the present Chapter, where experiments to examine the corrosion behavior of aluminized steel type 2 in synthetic waters of varying scaling tendencies at the room temperature are reported.

This Chapter has as its focus the stability of the aluminum-rich coating layer of aluminized steel type 2 in the as-received condition without any further forming or mechanical distress, and in a mechanically distressed condition with exposed underlying steel substrate, when immersed in waters of varying scaling tendencies with moderate and high chloride contents. These conditions are of

interest as the environmental may be sufficiently aggressive to cause significant corrosion of the exposed steel, but not enough to promote adequate galvanic current delivered by the outer aluminized coating. Of importance is to determine the amount of current delivered by the outer aluminized coating when coupled to steel of different areas, and the mechanisms associated with the galvanic corrosion processes that are relevant to forecasting durability in critical highway applications. The following sections describe the methodology and findings of experiments conducted toward answering those issues.

6.2 Experimental Procedure

6.2.1 Composition of aluminized steel type 2

As-received aluminized steel type 2 tested came from a flat sheet stock manufactured per ASTM A929, from low carbon steel (Table 6-1) coils rolled to 16-gage (~1.59 mm thick) and hot-dipped in a bath of commercially pure aluminum. The microstructure (Figure 6-1) had a nearly pearlite-free ferrite substrate with regular grains. The aluminized coating layer resulting from the hot dip process included a partly columnar inner layer ~15 µm thick, of approximate intermetallic composition Fe₂Al₅ (Li et al., 2003) as determined by scanning electron microscopy (SEM) with energy dispersive x-ray analysis (EDS), and an outer layer ~25-30 µm thick (Figure 6-1). The compositions of the gray outer layer matrix and the small lighter features were predominantly aluminum with ~2.4 wt% Fe and 6-11 wt% Fe, respectively. The small light features resemble Fe-rich precipitates identified elsewhere (ASM, 1972).

Table 6-1
Chemical Composition of Steel Substrate (% weight)*

C	Mn	P	S	Si	Cu	Al	Cb	Ni	Cr	Ti	N	Mo	Fe
0.05	0.2	0.006	0.012	0.01	0.03	0.04	0.002	0.017	0.03	0.002	0.004	0.003	Bal.

*Mill test report transmitted by Contech Construction Products Inc.

6.2.2 Test solutions

Four test solutions were used. Three of the solutions simulated conditions encountered in non-marine Florida environments but with modifications to enhance the differences between degrees of precipitating tendency. Those solutions also incorporated an appreciable chloride content to create aggressive baseline conditions where the potential beneficial effects of scale precipitation could be easily differentiated. Consequently, those three solutions had relatively low resistivity values (below the 1,000 ohm-cm recommended limit) and would yield limited service life for aluminized steel under the present FDOT guideline formulas. The fourth solution was simulated seawater, which is not a recommended service environment under present FDOT guidelines but served as a highly aggressive extreme reference. The test solutions corresponded to a carbonate precipitating condition (solution P), a mildly alkaline but non-precipitating condition (solution NP), a neutral pH of non carbonate precipitating

condition and negligible alkalinity (solution C), and a substitute ocean water (solution SW) prepared according to ASTM D1141-90 standard procedure. Table 6-2 shows the composition of the test solutions, all made from reagent-grade chemicals and de-carbonated de-ionized water of resistivity $>10^6 \Omega\text{-cm}$. Combinations of NaOH and NaCl (C), NaHCO₃, NaCl, and HCl (NP), NaHCO₃, NaCl, HCl, and Ca(OH)₂ (P), and chemical compounds commonly found in ocean water (SW) were used. The ionic constituent composition of the simulated ocean solution, reported by the manufacturer, is shown in Table 6-3. To make up for depletion of O₂, the test solutions were aerated for 30 sec at a rate of $\sim 0.03 \text{ cm}^3/\text{sec}$ twice a day using CO₂-free air for solution C, and ambient air for solutions NP, P, and SW, and isolated from external air the rest of the time. Values of FC were calculated based on the total alkalinity and pH of the solution per Equation 6-1 (Snoeyink and Jenkins, 1980).

$$FC = \frac{TA \cdot 10^{-\text{pH}}}{10^{-6.35}} \quad (6-1)$$

**Table 6-2
Synthetic Solution Compositions and Properties**

Solution	TA	TH	FC	BI	pH _L (pH _H)	Ca ²⁺ mg/L	Cl ⁻ mg/L	σ μmho/cm
C (control)	6	2	0	8	~7.4 (~9.0)	0	372	1,140
NP (non precipitating)	480	2	11	471	~7.8 (~8.7)	0		1,850
P (precipitating)	184	52	13	223	~7.4 (~7.8)	200		1,390
SW (precipitating-high chloride)	210	8,280	12	8,480	~7.3 (~7.9)	†	†	40,000

Legend: TA: total alkalinity expressed as mg/L CaCO₃; TH: total hardness expressed as mg/L CaCO₃; σ: solution conductivity; pH_L, pH_H: lowest and highest pH values for exposed as-received aluminized steel specimens, respectively.

†See Table 6.3 for detailed simulated ocean water composition.

**Table 6-3
Chemical Composition of Simulated Ocean Water***

Ionic species	Cl ⁻	Na ⁺	SO ₄ ²⁻	Mg ²⁺	Ca ²⁺	K ⁺	HCO ₃ ⁻	Br ⁻	Sr ²⁺	B ³⁺
Concentration, ppm	19,846	11,024	2,768	1,326	419	400	145	67.1	13.8	4.72

*as reported by manufacturer

Test solutions C and NP had LSI = -5.9 and -0.6, respectively. Test solutions P and SW had LSI = +1.5 and +0.4, respectively. Indeed, solution P precipitated to yield a $\sim 0.5 \text{ mm}$ thick powdery layer over the entire specimen surface shortly after initiation of the test exposure. To examine possible effects

of thick precipitate formation in solution P tests, an additional 10 grams CaCO_3 reagent grade powder was poured into two of the three test cells after 312 hr and again after 480 hr to form ~5 mm and ~9 mm thick layers, respectively. In test solution SW, precipitate deposited uniformly in a very thin layer of on the metal surface. The composition of that layer was expected to be mainly CaCO_3 since CaCO_3 has a lower solubility product than $\text{Mg}(\text{OH})_2$ and is supersaturated in seawater (Mantel et al., 1992). Typically, $\text{Mg}(\text{OH})_2$ is undersaturated at nearly neutral pH and precipitating in considerable amounts at $\text{pH} > 9.3$ (Barchiche et al., 2003). The deposits in both P and SW solutions were washed off readily during cleaning.

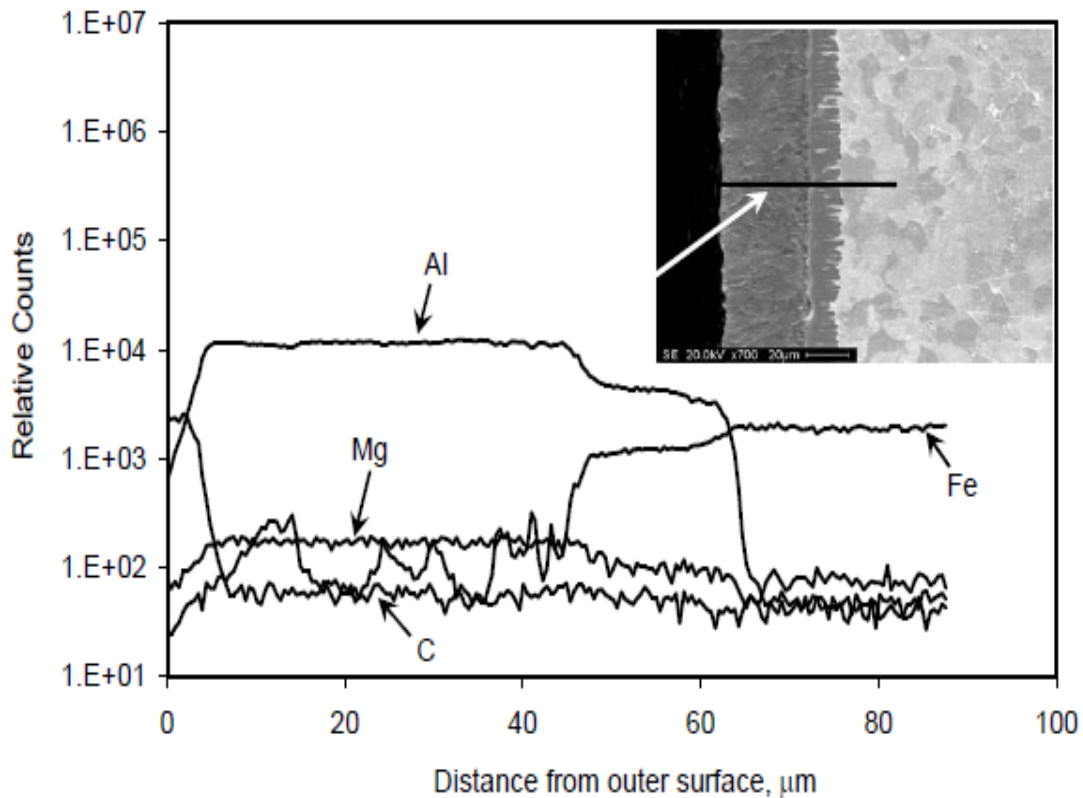


Figure 6-1. Scanning electron microscope (SEM) line scan conducted on a cross section of aluminized steel type 2 (perpendicular to rolling direction) showing the main constituents in the dual coating layer and the base steel. Insert: cross section perpendicular to rolling direction of a 16-gage (~1.59 mm) thickness flat aluminized steel type 2 after etching with 2% Nital solution showing the outer and inner coating layers on base steel. Light features in the outer coating are Fe-rich inclusions per SEM-EDS analysis.

6.2.3 Test cell configuration and electrochemical impedance spectroscopy (EIS)

A three-electrode test cell configuration (Figure 6-2) was used, exposing horizontally one of the specimen faces. A metal-metal oxide activated titanium

mesh placed parallel ~6 cm from the specimen surface was used as a counter electrode, while a low impedance activated titanium pseudo-reference electrode 0.3 cm diameter and 5 cm long (Castro et al., 1996) was placed ~1 cm from the specimen surface and periodically calibrated against a saturated calomel reference electrode (SCE). All potentials reported here are in the SCE scale unless otherwise stated. Electric contact to the specimen (working electrode) was made through a copper wire soldered to a copper sheet in contact with the bottom surface of the specimen not exposed to test solution. Each test cell was filled with 500 mL of solution and the cells were never replenished during the entire length of the experiment. The relatively small electrolyte volume/specimen area ratio was intended to be representative of worst-case culvert pipe conditions with stagnant water on a pipe invert, or of occluded conditions for pore water on the soil side of a pipe.

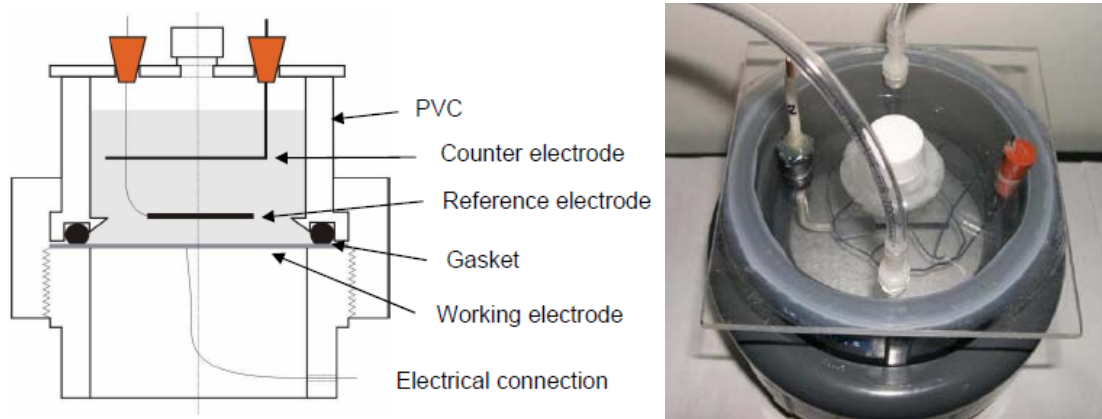


Figure 6-2. Schematic (left) and photograph (right) of test cell arrangement to monitor impedance behavior of as-received and blemished specimens of aluminized steel type 2.

6.2.3.1 As-received test specimens

Circular test specimens of 95 cm² nominal surface area were cut out from the as-received stock, cleaned with ethanol and acetone, and stored in a desiccator prior to immersion. Specimen exposure test began typically within 24 hr after storage. Immersion tests were conducted for up to ~3,100 hr at 22 ± 2°C in duplicate for solutions C, NP, and SW and in triplicate for solution P. Solution pH and electrical conductivity, and open circuit potential (E_{oc}) for each specimen were monitored at selected times. Electrochemical impedance spectroscopy (EIS) measurements were obtained at the E_{oc} with a Gamry® PCI4-300 potentiostat in the frequency range from 100 kHz to 1 mHz using a sinusoidal signal of 10 mV_{RMS} amplitude. At the end of the immersion test, the specimens were removed, cleaned by washing with water and ethanol, and visually examined. Additional sets of duplicate specimens placed in solutions P and NP were used for Mott-Schottky (M-S) tests (De Gryse et al., 1975) to determine nominal capacitance-potential behavior with a Solartron 1260/1287 potentiostat/electrochemical interface in the potential range from 0 to -300 mV vs,

E_{oc} at a scan rate of 10 mV/sec, a fixed test frequency of 10 Hz, and a 10 mV_{RMS} amplitude. Nominal capacitance evaluation was refined by correction for the effect of the presence of a charge transfer resistance as shown later.

6.2.3.2 Blemished test specimens

Circular unblemished specimens of 95 cm² nominal surface areas were cut out from the as-received aluminized steel sheet, and coating breaks 2 cm and 0.2 cm diameters and 300 μm deep were machined in the center of one of the specimen faces exposing the underlying steel. The blemished specimens are identified hereon as LCB and SCB for the large and small coating breaks, respectively. The exposed steel/ aluminized coating area ratio A_R was ~ 0.03 for the LCB specimens and $\sim 3 \cdot 10^{-4}$ for the SCB specimens. Traces of metal shavings were removed from the machined breaks with a razor blade. A magnetic coating thickness gauge was used to verify that the exposed steel was free of aluminized coating.

Immersion tests were conducted in duplicate and in some cases in triplicate for up to $\sim 3,500$ hr at 22 ± 2 °C. Solution pH and electrical conductivity were monitored at selected times. Open circuit potentials (E_{oc}) were periodically measured as a function of exposure time with a multimeter of 200 MΩ input resistance. To map the potential profile with radius a Luggin capillary placed at ~ 1 mm from the metal surface was manually scanned over the surface in duplicate LCB specimens exposed to solutions P and NP. In addition, EIS measurements were regularly conducted at the E_{oc} with a Gamry® PCI4-300 potentiostat in the frequency range from 100 kHz to 1 mHz taken 5 data points per decade using sinusoidal signals of 10 mV_{RMS} amplitude.

6.2.4 Macrocell configuration and galvanic current measurements

To determine the electrochemical behavior of the underlying steel, additional experiments were conducted in duplicate on uncoupled steel specimens of ~ 3 cm² nominal surface areas, made by mechanically stripping the aluminized coating from the same aluminized steel stock and wet ground to a 320-grit surface finish, placed in a companion cell. For those experiments, a SCE electrode was placed momentarily in each test solution for the duration of the electrochemical measurements. To monitor galvanic currents between the exposed steel and the surrounding aluminized coating as well as the electrochemical impedances of the individual macrocell components, a test cell as shown in Figure 6-3 was used. The test cell consisted of an as-received unblemished aluminized steel specimen of 95 cm² nominal surface area placed at the bottom of the cell and a separate but normally interconnected (except during EIS and galvanic measurements) 3 cm² nominal surface area steel specimen positioned ~ 2 cm parallel to the aluminized surface. The macrocell assemblies had an $A_R \sim 0.03$. The steel component was made by mechanically stripping the aluminized coating from the same aluminized steel stock, and wet

ground to a 320-grit surface finish. Electrical connection was made using a stainless steel wire spotted welded to the back side of the steel. Afterwards, the back side and the edges of the steel were coated with epoxy. Both the aluminized and the steel components were cleaned with acetone and ethanol and stored in a desiccator prior to immersion.

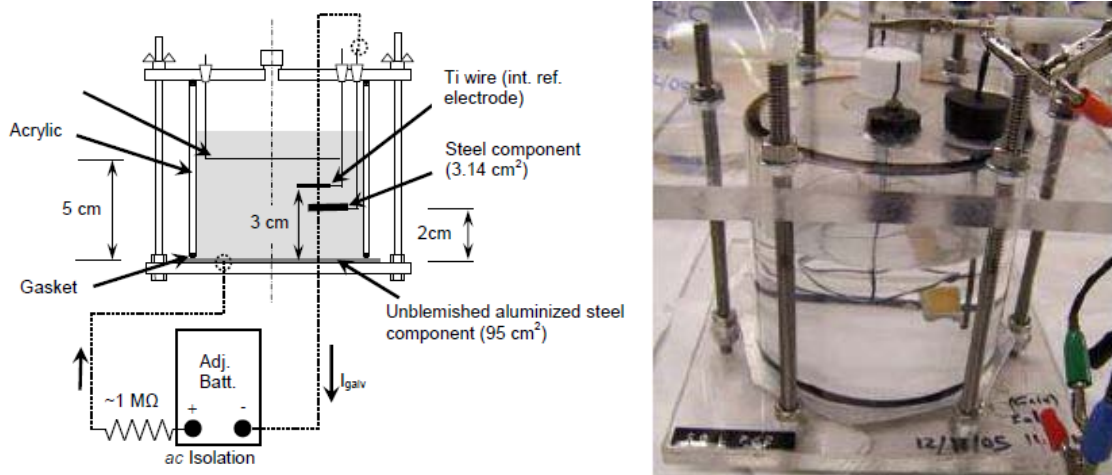


Figure 6-3. Schematic and photograph of macrocell arrangement used to monitor galvanic currents and impedance behavior of as-received aluminized steel type 2 and steel components.

Galvanic currents between the aluminized and steel components were periodically measured with a 0.1Ω input resistance ammeter (HP Model 34401A). By convention, net anodic currents were assigned positive signs. Measurements of E_{oc} of the interconnected components were recorded right before measurements of galvanic currents. To evaluate the individual impedance response of the two macrocell components in the galvanic couple, the components were disconnected and a battery-operated dc current source of impedance at least one order of magnitude above the impedance of each component of the couple was connected across the components, to preserve the individual static polarization conditions (Figure 6-3). The component to be tested was then connected to the EIS system as usual. The other component of the couple remained dc-polarized but nearly free of ac excitation current during the test. At the end of long term exposure, all specimens were removed, cleaned, and examined by 40X optical microscopy.

6.2.5 Direct assessment of corrosion rates

Direct assessment of the corrosion rate of the aluminized portion conducted in selected specimens shown in Table 6-4 was accomplished by performing coating thickness measurements after the end of exposure using a magnetic coating thickness gauge (model Mikrotest® III by ElektroPhysik), reported by the manufacturer to have an accuracy of $\pm 5\%$ of the reading. The

measuring protocol included the selection of six locations on the aluminized surface distributed as follows: three locations at the unexposed rim of the specimen that approximated conditions before exposure, and three locations on the exposed aluminized surface where it had retained deposits in the form of corrosion products or other precipitates. Afterwards, the deposits at those three locations were stripped from the aluminized surface by lightly hand rubbing with 600-grit abrasive paper until revealing the bare aluminized surface underneath.

Similar rubbing on the unexposed locations was found to result in no detectable metal loss per magnetic gauge indications. A total of three measurements were taken at each location by three independent operators, each selecting different spots in each specimen following the measuring protocol above. Coating thickness results were then combined for each location, and averages and standard deviations were calculated. Nominal average coating loss was roughly estimated by subtracting the remaining coating thickness (after removing deposits) from that measured at the unexposed metal, and then converted to nominal average corrosion rate by dividing by the corresponding test duration. The nominal average coating loss was then compared to the integrated material loss computed from EIS measurements as shown in Section 6.4.4.2.

Table 6-4
Average Thickness Measurements, per Magnetic Coating Thickness Test, and Corresponding Nominal Corrosion Rates for Selected Specimens

Specimen	Thickness µm		Exposure time hr	Nominal corrosion rate µm/yr
	Before exposure	After exposure		
LCB Solution SW (2)	45.7	45.5	2,800	2
SCB Solution NP(2)	45.0	40.9	3,400	10
LCB Solution NP(1)	47.8	38.1	2,600	33
LCB Solution NP(3)	47.0	40.9	2,600	21
LCB Solution P(1)	51.8	49.8	2,650	7
LCB Solution P(2)	49.0	47.5	2,650	6
Macrocell assembly P(1)	52.3	48.3	2,700	13
Macrocell assembly P(2)	50.8	45	1,900	25
Macrocell assembly NP(1)	48.5	43.4	2,700	16
Macrocell assembly NP(2)	48.8	43.2	2,500	20

Thickness measurements are the average values obtained by three independent operators. Thickness measurements were determined with a standard deviation of ± 7.6 µm.

6.3 Results

No under-gasket crevice corrosion developed in any of the specimens for which results are reported. The results reported in this Chapter are those of the

specimens #1 in each test solution unless otherwise indicated. The results of the replicate specimens were similar to that of the example unless indicated otherwise (Cáseres, 2007). In addition to the information provided next, the reader is referred to Table A-1 in Appendix A, which summarizes the visual assessment and E_{oc} evolution trends.

6.3.1 As-received specimens

6.3.1.1 Direct observations of corrosion and E_{oc} trends

Refer to Figure 6-4 for the E_{oc} evolution of replicate specimens. Immediately after immersion, values of E_{oc} were ~ -630 mV, ~ -650 mV, ~ -800 mV, and ~ -750 mV for the solutions C, NP, P, and SW, respectively.

After ~ 180 hr of exposure, the E_{oc} in solution C started to drop abruptly to reach ~ -920 ~ -950 mV. After ~ 310 hr (and after ~ 115 hr for specimen #2), stable isolated pits (a few per specimen) became visible to the naked eye; typical pit diameters were < 0.1 mm and a uniform dark grayish layer that covered the entire surface of the specimen. SEM-EDS analysis of a dried portion of that layer in the specimen #1 showed results consistent with the presence of aluminum hydroxide. The appearance of the strong surface discoloration was associated with a momentary increase in solution pH as explained later. Afterwards, the E_{oc} for both specimens slowly evolved toward a terminal value of ~ -830 mV.

In solution NP, the E_{oc} decayed to ~ -910 mV after ~ 500 hr of exposure and remained nearly constant afterwards. The appearance of moderate surface discoloration in solution NP did not start concurrent with the beginning of the E_{oc} drop but instead was noted after $\sim 2,250$ hr for #1 and $\sim 1,200$ hr for #2 in agreement with a moderate solution pH increase as shown later. Post exposure optical 25X examination revealed few small pits.

In solution P, the first addition of excess CaCO_3 to specimens #1 and #2 caused short term negative and then positive E_{oc} excursions by ~ 80 mV followed by a slow recovery to a terminal E_{oc} ~ -770 mV, little affected by the next CaCO_3 addition. The specimen #3 (with no extra CaCO_3 addition) showed E_{oc} values ~ 50 mV more negative than those of the replicate specimens for exposure times ranging from 190 hr to 1,400 hr reaching ~ -800 mV after 2,250 hr of exposure. In all specimens, the aluminized surface remained bright throughout the test. Post exposure optical 25X examination revealed no pit formation. In solution SW (Figure 4-8), E_{oc} of the specimen #1 started to drop steeply immediately after exposure reaching ~ -900 mV after ~ 165 hr. The duplicate specimen showed noble E_{oc} values for ~ 265 hr followed by a slow drop to ~ -840 mV after ~ 865 hr. Afterwards, the E_{oc} remained nearly constant for both specimens increasing to ~ -805 mV for #1 and ~ -835 mV for #2 after $\sim 1,500$ hr of exposure. The aluminized surface stayed bright for up to ~ 525 hr for #1 and ~ 585 hr for #2 with small isolated pits < 0.1 mm diameter (a few per specimen) visible to the naked eye.

Then, light uniform surface discoloration was noted on both specimens not concurrent with the start of Eoc drop.

When present, the pit depths appeared to be limited only to the outer aluminized coating layer since no reddish deposits were noted at the pit mouths. In addition, metallographic examination showed that in all cases, the damage associated with uniform aluminized surface discoloration, during the time frame investigated, appeared to be limited only to the outer coating layer.

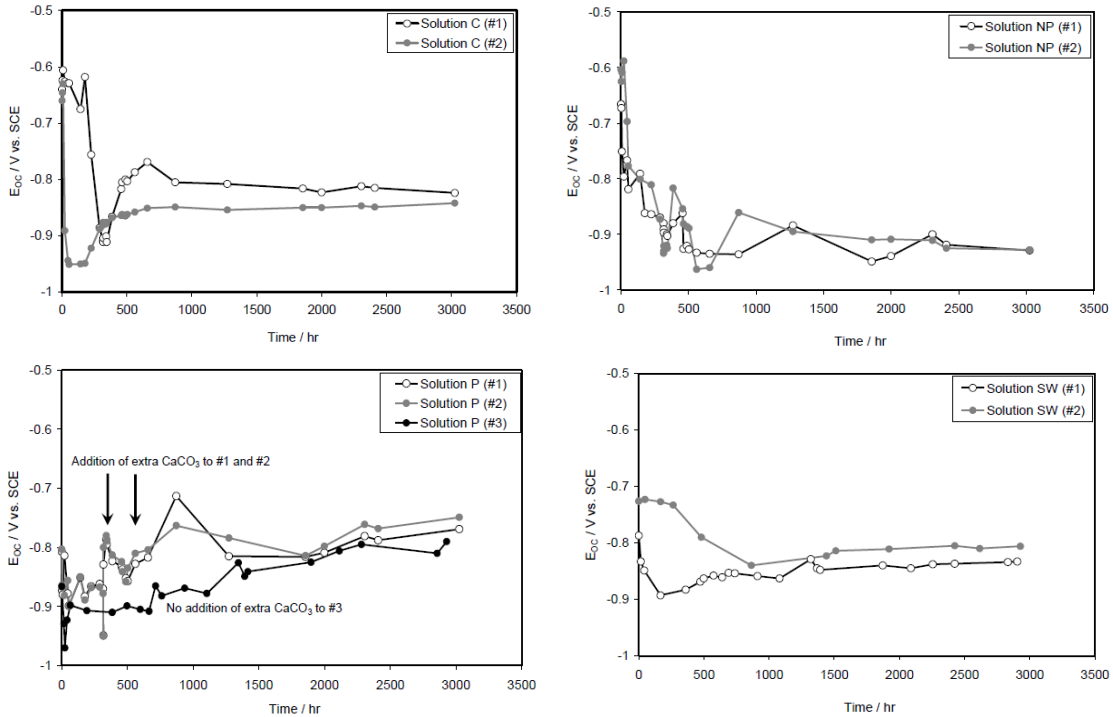


Figure 6-4. Eoc evolution of as-received aluminized steel type 2 replicate specimens in solution C (top left), solution NP (top right), solution P (bottom left) (arrows indicate two CaCO₃ additions to test cells #1 and #2), and solution SW (bottom right). Exposure ended at the time that the last datum was taken.

6.3.1.2 Solution composition

Figure 6-5 shows that immediately after immersion, the bulk pH of all test solutions closely approached the lowest values reported in Table 6-2. However, after equilibrium with the surrounding air was reached, the bulk pH of the solutions NP, P, and SW was expected to naturally evolve toward alkaline values despite the given buffering capacity of those solutions. In solutions P and SW, the bulk pH remained quite stable for the entire exposure increasing to only ~7.8 and ~7.9, respectively. In solution NP, however, the bulk pH increased to ~8.5 after 24 hr and reached ~8.7 near the end of the test. In solution C, the bulk pH was ~7.7 after 3,000 hr attaining a maximum of ~9.0 at ~310 hr. The brief pH

increase and later decrease was not anticipated and the cause of this trend remains unclear at present.

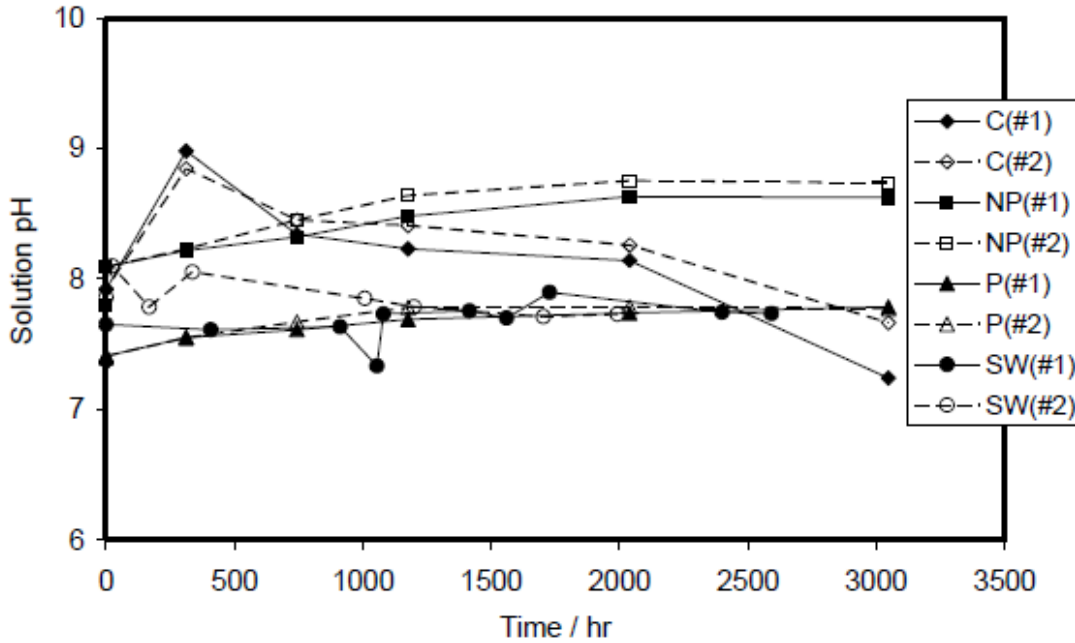


Figure 6-5. Evolution of the solution bulk pH for as-received aluminized steel type 2 specimens exposed to waters with varying scaling tendencies.

Total hardness and total alkalinity, determined by titration following procedures indicated in the APHA (1992), as well as the solution conductivity are reported in Table 6-2. The Fe^{2+} content in all four solutions, measured by atomic absorption spectroscopy after ~2,000 hr of immersion, was <0.01 ppm.

6.3.1.3 Impedance behavior

After solution resistance subtraction, the impedance responses for solutions P, NP, and SW at the high frequency end of the impedance diagram revealed capacitive behavior with frequency dispersion that could be reasonably approximated by means of a constant phase angle element (CPE) at frequencies above a compromise cutoff of ~100 Hz. A CPE has an impedance $Z_{\text{CPE}}=1/Y(j\omega)^n$ where $\omega=2\pi f$, Y is the admittance parameter of dimensions $\Omega^{-1} \text{ cm}^{-2} \text{ sec}^n$ (if area normalized), and n (dimensionless) is the dispersion coefficient (Hsu and Mansfeld, 2001, Lasia et al, 1999). Data for higher test frequencies showed more pronounced dispersion (possibly reflecting surface roughness, uneven macroscopic current distribution (De Levie, 1967) or spurious wiring effects) and were not used for quantitative impedance evaluation for these solutions (Figure 6-6).

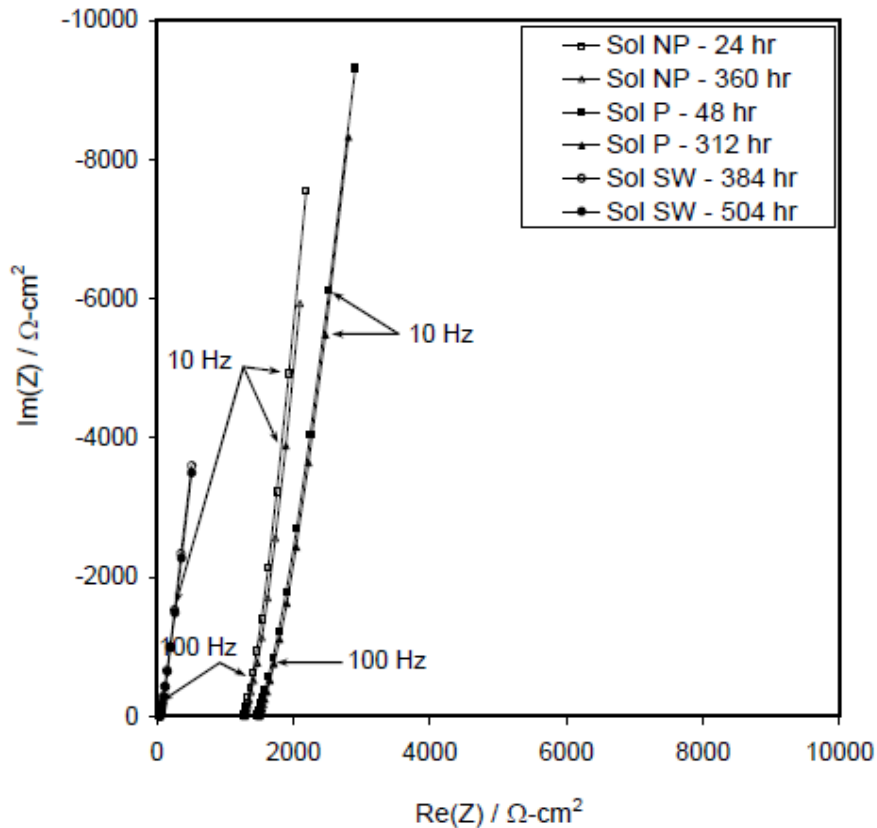


Figure 6-6. Typical electrochemical impedance spectroscopy (EIS) plot of the high-frequency limit for solutions NP, P, and SW.

The impedance results for solution NP (Figure 6-7) showed an impedance diagram where the 1 mHz impedance modulus initially increased with time, consistent with generally passive behavior and absence of visual evidence of active aluminized corrosion. The 1 mHz impedance modulus decreased later to values smaller than at the beginning, but even then its magnitude was large ($\sim 380 \text{ k}\Omega\text{-cm}^2$) after $\sim 3,000$ hr of exposure. The decrease in the impedance modulus coincided with the appearance of moderate surface discoloration.

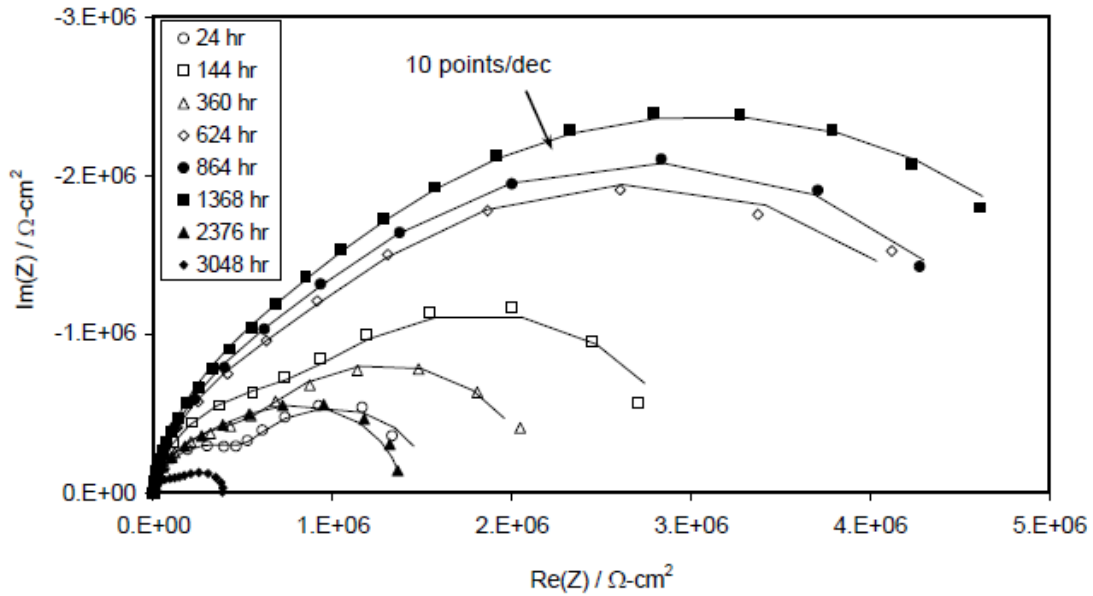


Figure 6-7. EIS behavior of as-received aluminized steel type 2 specimen #1 in solution NP (100 KHz-1 mHz - 5 points/decade unless indicated otherwise).

In solution P (Figure 6-8), the 1 mHz impedance magnitude of the specimen #1 (and #2 as well) was large ($>6,000 \text{ k}\Omega\text{-cm}^2$) and showed an increasing trend with time. Upon each CaCO_3 addition, however, the 1 mHz impedance modulus showed a pronounced momentary decrease to $\sim 1,450 \text{ k}\Omega\text{-cm}^2$ and a slow recovery later on to attain $\sim 10,000 \text{ k}\Omega\text{-cm}^2$ after $\sim 3,000 \text{ hr}$.

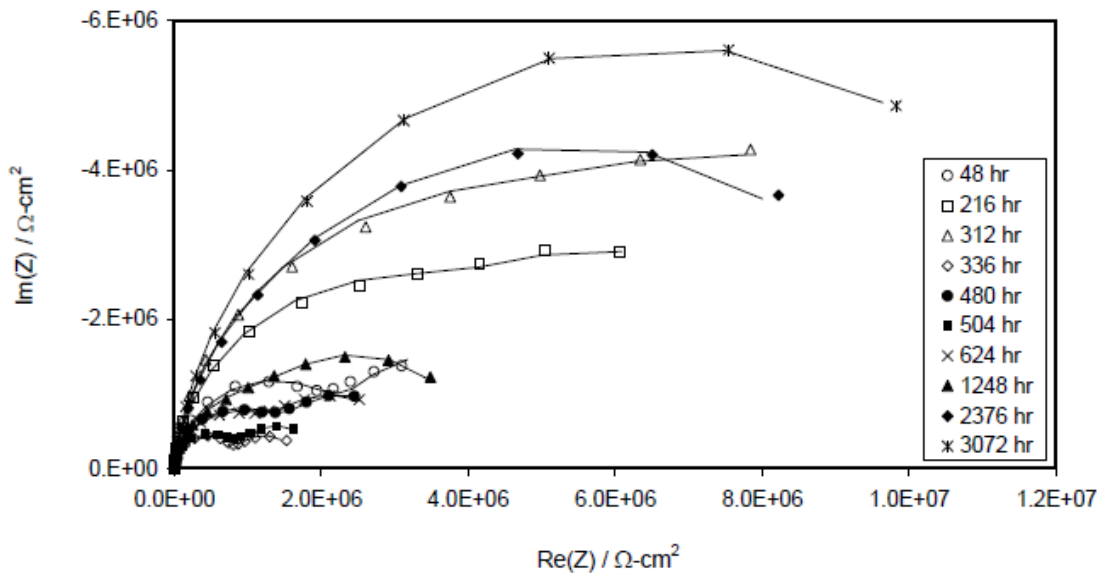


Figure 6-8. EIS behavior of as-received aluminized steel type 2 specimen #1 in solution P (100 KHz - 1 mHz – 5 points/decade).

For the specimen #3 in solution P (Figure 6-9), the 1 mHz impedance magnitude was increasingly large as well reaching $\sim 10,000 \text{ k}\Omega\text{-cm}^2$ after $\sim 3,000$ hr, consistent with generally passive behavior and absence of visual evidence of active aluminized corrosion throughout the exposure in all specimens. For the frequency range analyzed, the impedance diagrams were usually describable by two overlapping loops, both approaching ideal capacitive behaviors. The M-S behavior is keyed to the analysis of the impedance response.

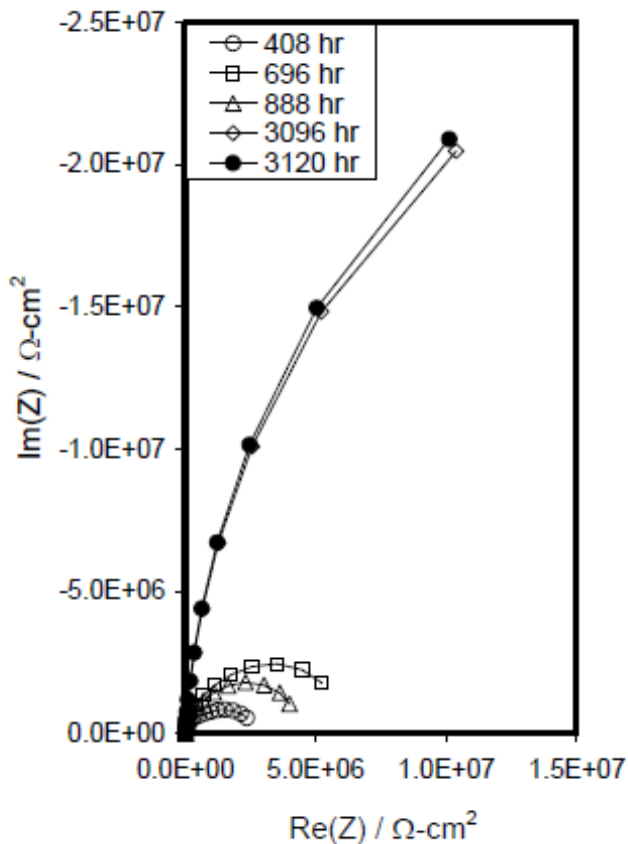


Figure 6-9. EIS behavior of as-received aluminized steel type 2 specimen #3 in solution P (100 KHz - 1 mHz – 5 points/decade).

The impedance results for solution SW (Figure 6-10) show an impedance diagram where the 1 mHz impedance modulus initially increased with time attaining $\sim 365 \text{ k}\Omega\text{-cm}^2$ at ~ 504 hr of exposure followed by a decreasing trend to $\sim 270 \text{ k}\Omega\text{-cm}^2$, consistent with the start of light surface discoloration. Afterwards, the 1 mHz impedance moduli started to increase again to attain values comparable to those recorded at the beginning. The impedance diagrams can be describable by two distinctive loops, each approaching ideal capacitive behavior.

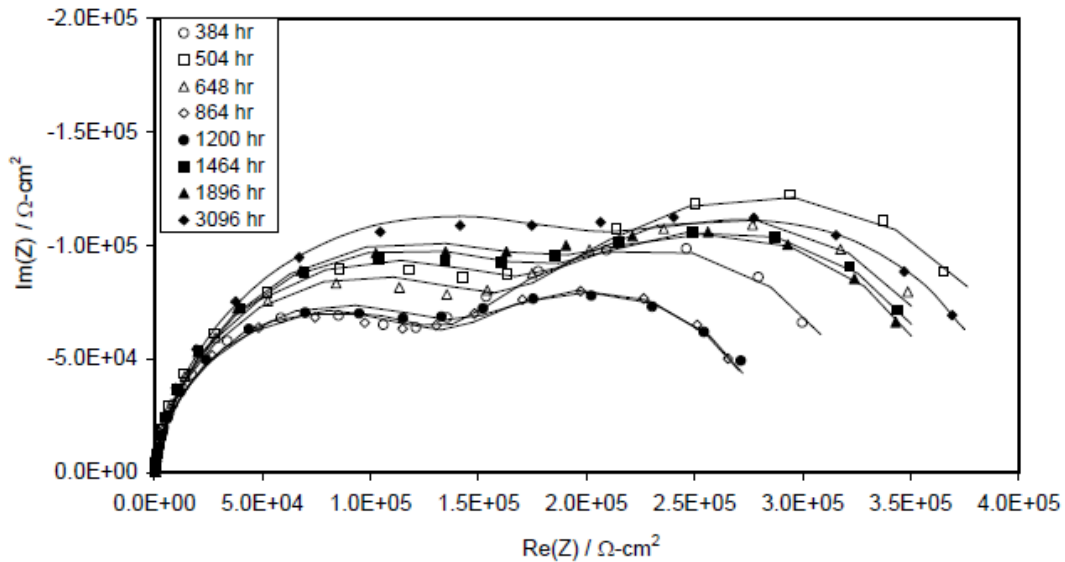


Figure 6-10. EIS behavior of the specimen #1 in solution SW (100 KHz - 1 mHz - 5 points/decade).

As will be shown below, the C system had a large Faradaic admittance component that was strongly manifested already at the highest test frequencies. Thus, for solution C the complete impedance spectra were used for the analysis with the understanding that using a CPE for simulation purposes would involve a coarser approximation than in the NP, P, and SW systems. The impedance response at the low frequency end (Figure 6-11) was initially much smaller than in the NP, P, and SW solutions, and for a short initial period there was also a low frequency inductive loop. After some exposure time the 1 mHz impedance modulus decreased even further (to $\sim 68 \text{ k}\Omega\text{-cm}^2$), coinciding with the appearance of strong surface discoloration, but there was a long term recovery trend toward larger 1 mHz impedance moduli. The diagrams were usually describable by two overlapping loops. Partly as a result of using the entire frequency spectrum, the high frequency loop deviated from ideal capacitive behavior more than in the cases of NP, P, and SW solutions.

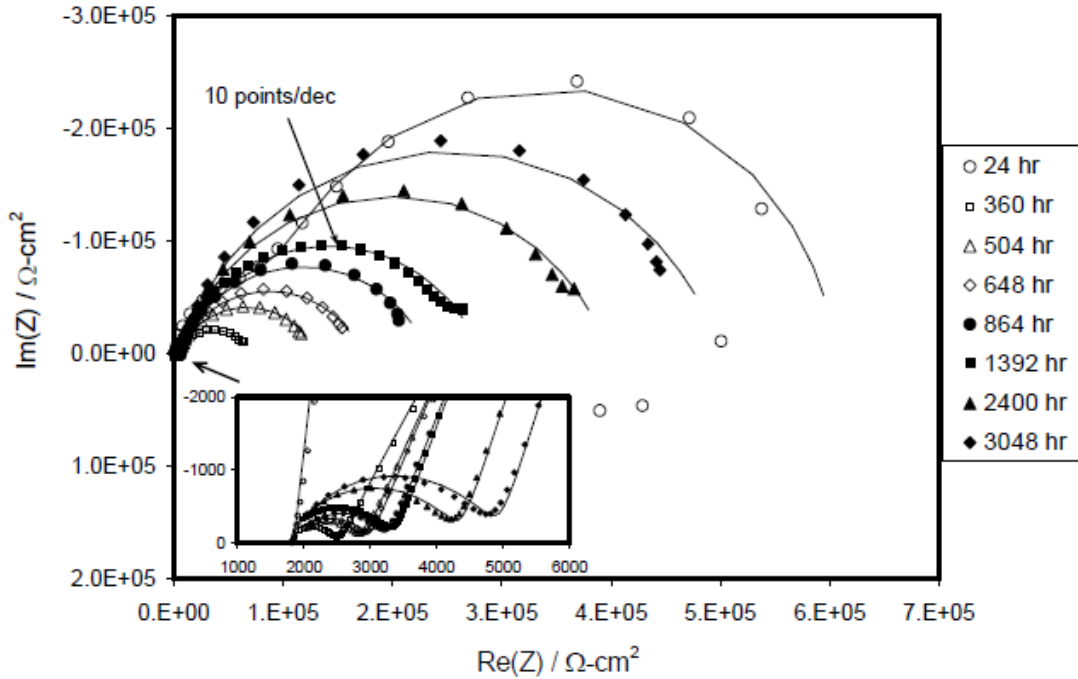


Figure 6-11. EIS behavior of as-received aluminized steel type 2 specimen #1 in solution C (100 KHz - 1 mHz – 5 points/decade unless indicated otherwise).

6.3.2 Blemished specimens

Results for the LCB specimens exposed to solution C and for the macrocell assemblies in solutions C and SW are not available because significant crevice corrosion developed underneath the sealing gasket in all replicate specimens such that the results were discarded.

6.3.2.1 Direct observations of corrosion

In LCB specimens exposed to solutions NP and P the beginning of the E_{oc} drop was concurrent with the appearance of grayish discoloration of the aluminized surface around the perimeter of the exposed steel spot. The discoloration, moderate in P and darker in the NP system, later covered uniformly the entire aluminized surface forming an adherent layer $\sim 10\text{-}15\ \mu\text{m}$ (NP) and $<1\ \mu\text{m}$ (P) thick as measured by a magnetic thickness gauge after the end of the exposure. Specimen autopsy showed that corrosion damage associated with uniform discoloration appeared to be mainly associated with changes in the outer coating layer as confirmed by metallographic analysis. Metallographic examination conducted on a cross section near the aluminized/steel edge of the LCB specimen #1 (and the specimen #2 as well) exposed to solution NP (Figure 6-12) showed an annulus $\sim 70\ \mu\text{m}$ wide surrounding the exposed steel spot of severe corrosion, not noted in any of the specimens in solution P. As a result, the outer aluminized coating layer in NP was completely consumed exposing the inner layer which appeared to remain intact for the time frame examined.

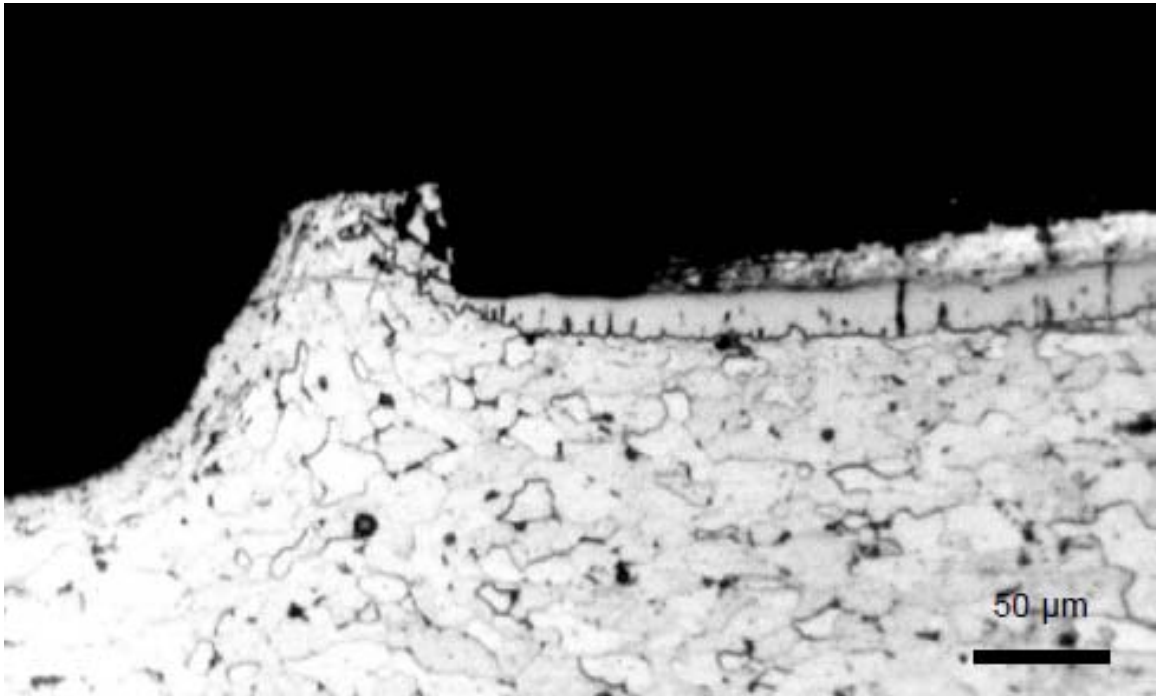


Figure 6-12. Cross section of blemished aluminized steel type 2 LCB specimen #1 exposed to solution NP showing complete outer coating loss surrounding the exposed steel.

A SEM image (Figure 6-13) of the discolored surface of the LCB specimen #1 in solution NP taken at the end of exposure showed a tight, compact layer covering uniformly the aluminized surface. Further SEM-EDS analysis (Figure 6-13) of a dried portion of that layer was consistent with the presence of aluminum hydroxide $\text{Al}(\text{OH})_3$ in agreement with the results seen for as-received specimens and the results shown elsewhere (Davis, 1999). Few isolated small pits were observable only under magnification (indicative of pit diameter <0.1 mm) in both solutions NP and P.

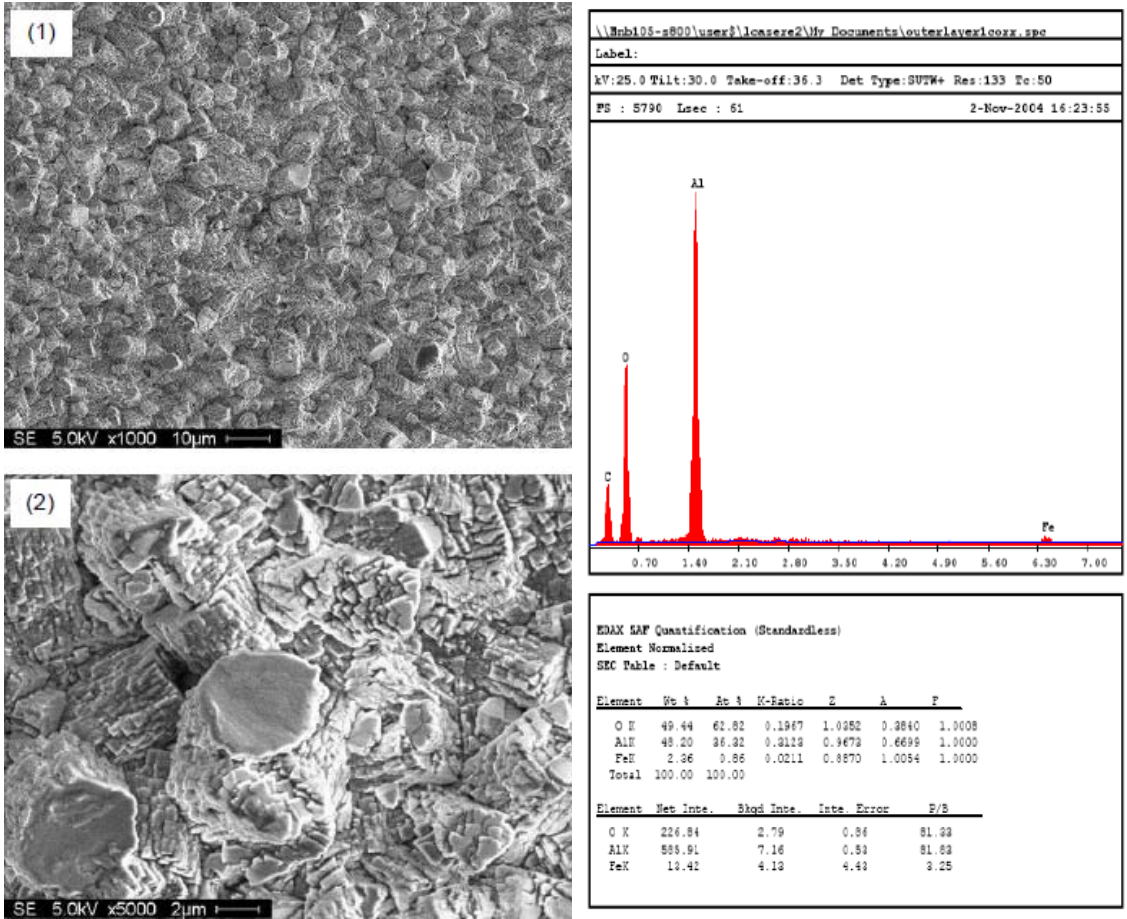


Figure 6-13. SEM image (left): (1) 1000x magnification and (2) 5000x magnification of the surface morphology of blemished aluminized steel type 2 LCB specimen #1 in solution NP taken after the end of exposure. SEM-EDS analysis (right) of corrosion deposits on the aluminized surface.

LCB specimens exposed to solution SW showed isolated small visible pits (indicative of pit diameter ~0.1 mm) on the aluminized surface early on followed by the appearance of uniform light discoloration, forming an adherent layer <1 μm thick, but the appearance of that layer (at ~360 hr of exposure) was not coincident with the start of the Eoc decay. The light surface discoloration in SW did not start near the exposed steel perimeter but instead at several locations on the aluminized surface. Interestingly, metallographic examination conducted on specimen #1 in SW (Figure 6-14) showed that the aluminized coating surrounding the exposed steel did not display signs of severe corrosion with both outer and inner coating layers in place.

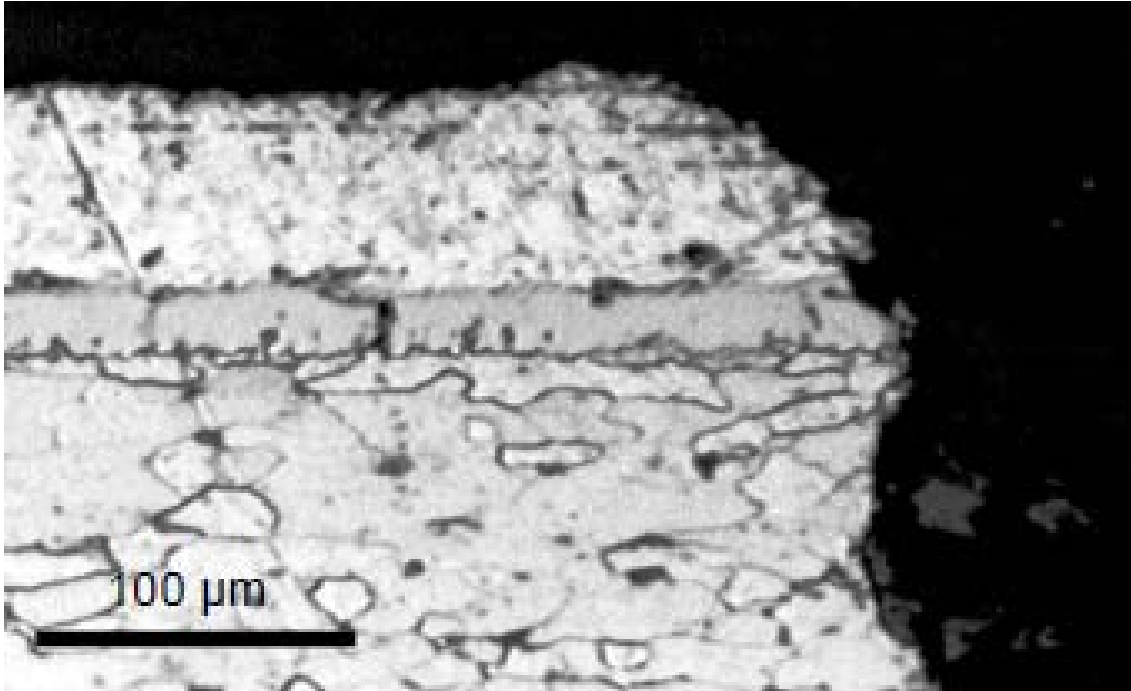


Figure 6-14. Cross section of the LCB specimen #1 exposed to solution SW near the edge of the exposed steel.

During exposure, a similar grayish discoloration was noted starting at the aluminized surface in the vicinity of the exposed steel of all SCB specimens in solutions NP and C, and at various spots on the aluminized surface in SW. The discoloration, dark for solutions C and NP and lighter for SW, progressed until covering uniformly the entire aluminized surface, forming an adherent layer ~5-10 μm (NP), <2 μm (C), and <1 μm (SW) thick. The appearance of initial discoloration was concurrent with the Eoc drop for solution C (~545 hr after immersion). For solutions NP and SW, the appearance of initial discoloration was not concurrent with the beginning of the Eoc drops (which took place after short exposure times) but instead were noted (for the specimens #1) at ~1,030 hr and ~275 hr for NP and SW, respectively. In contrast, the aluminized surface of the SCB specimens exposed to solution P did not show discoloration or pits throughout the entire test period.

Autopsy of the SCB specimens showed that corrosion damage associated with uniform discoloration appeared to be mainly associated with changes in the outer coating layer as confirmed by metallographic examination. In addition, few pits visible to the naked eye (~0.1 mm diameter) in solutions C and SW were noted on the aluminized surface shortly after exposure. Some of those pits in solution C appeared to have reached the underlying steel since reddish deposits were detected at some pit mouths as shown in Figure 6-15. Few isolated small pits were observable only under magnification (indicative of pit diameter <0.1 mm) in solution NP.

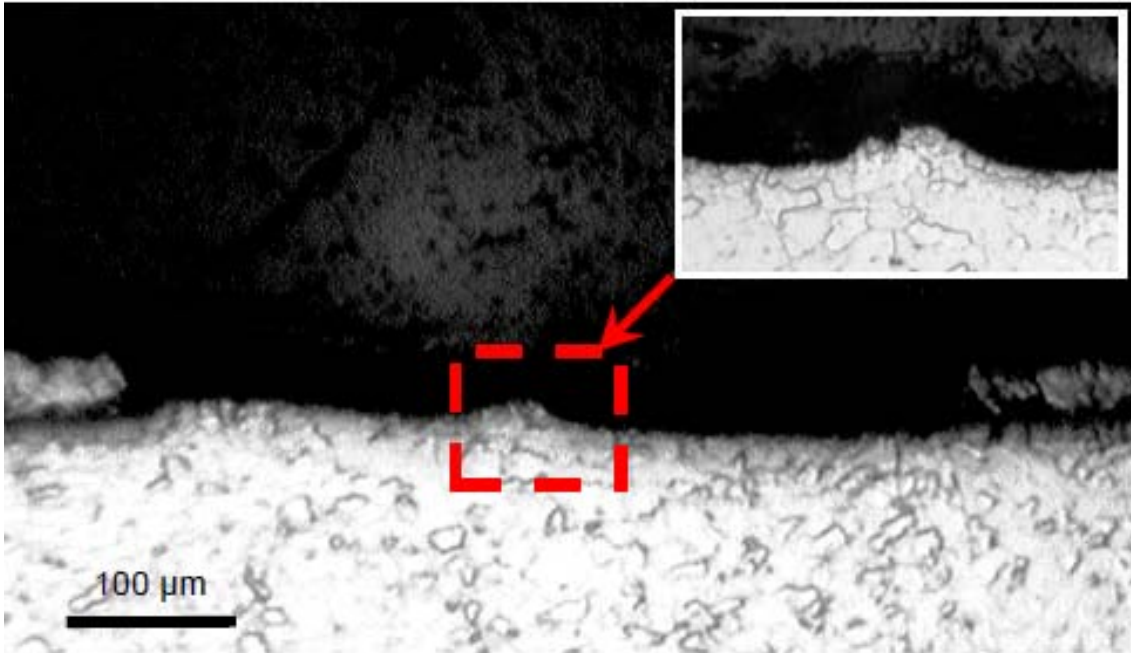


Figure 6-15. Cross section of the blemished aluminized steel type 2 SCB specimen #1 exposed to solution C showing that a pit ~0.5 mm diameter that reached the underlying steel.

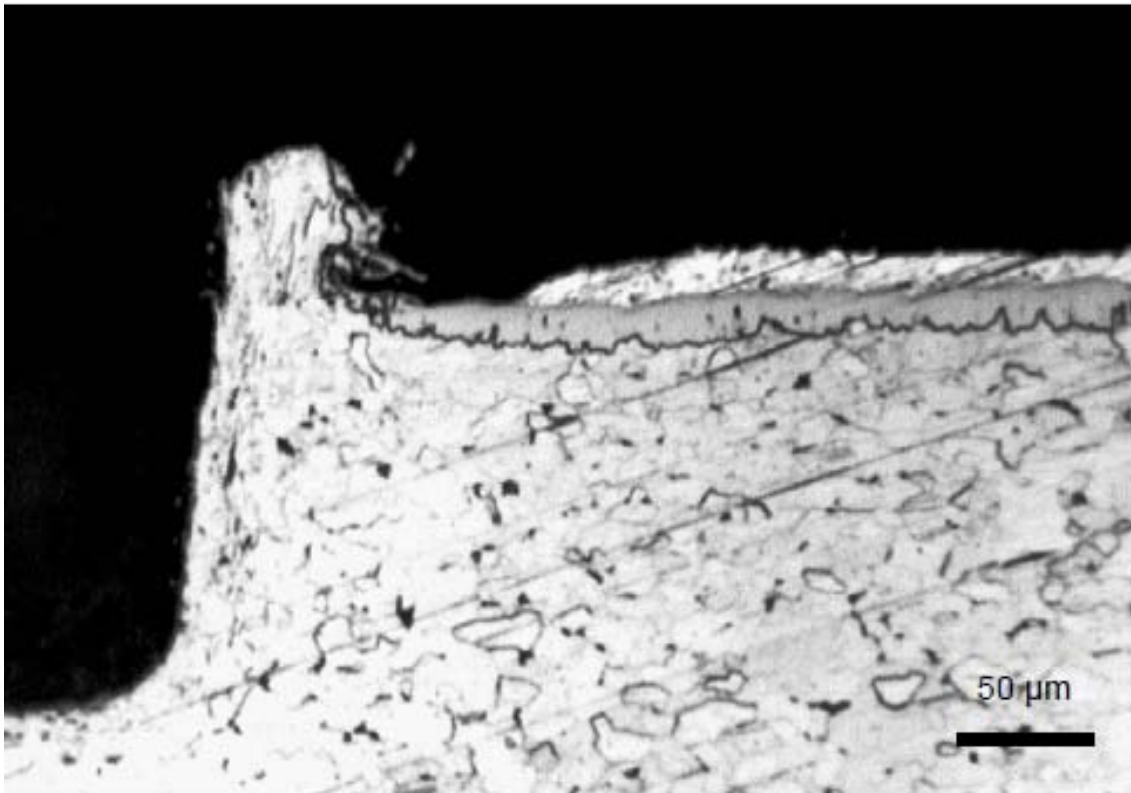


Figure 6-16. Cross section of blemished aluminized steel type 2 SCB specimen #1 exposed to solution NP showing complete outer coating loss surrounding the exposed steel.

As in the LCB specimens in the NP system, the SCB specimens in solutions NP and C as well showed a ~50 μm wide annulus of severe corrosion surrounding the exposed steel as shown in Figure 6-16. It can be noted that the outer aluminized layer was completely consumed exposing the inner coating layer, which appeared to have remained intact throughout the exposure. Contrarily, the SCB specimens in SW and P did not show severe corrosion around the exposed steel as exemplified in Figure 6-17 for the SW solution.

A few hrs after immersion, visual examination conducted on the exposed steel of the LCB and SCB specimens exposed to solutions P and NP (and the individual steel specimens in P and NP solutions as well) showed a uniform reddish/black scale (likely rich in $\text{Fe}^{2+}/\text{Fe}^{3+}$) formed over the entire steel surface. Later on, the scale in those specimens developed until forming a layer ~300 μm thick. At ~450 hr of exposure, the central ~0.3 cm^2 of the exposed steel area of all LCB and individual steel specimens in solutions P and NP developed a 1-3 mm thick porous reddish growth. There was noticeable additional steel metal loss underneath the central growth in the LCB and individual bare steel specimens in NP, but less so in P. A metallographic examination (Figure 6-18) carried out in the LCB specimen #1 exposed to solution NP showed that the metal loss at the exposed steel was estimated to be ~0.1 grams. No such central growth was observed in the SCB specimens exposed to those solutions. At ~500 hr, formation of small crystals appeared on top of the Fe-rich scale in both LCB, SCB, and individual steel specimens immersed in solution P. SEM-EDS analysis of a few crystals obtained from the LCB specimens in P was consistent with the presence of CaCO_3 . During post exposure cleaning, the scales on the exposed steel of the LCB, SCB, and uncoupled steel specimens in solution NP were easily removed, but were better adhered to the steel in solution P.

The exposed steel of the SCB specimens in solution C showed corrosion in only one (#1) of the triplicate specimens, an early formation of a thin reddish scale (likely rich in Fe^{2+}) that later developed to form a layer ~<300 μm thick on top of the steel. No signs of corrosion were observed in either replicate #2 or #3, where the steel spot remained bright over the entire test period. The replicate individual steel specimens in solution C showed early formation of corrosion deposits distributed over the entire surface of similar appearance to that noted in the SCB specimen #1. The exposed steel of the SCB specimens in solution SW was bright and free of corrosion scale throughout the entire exposure, and there was only very light steel discoloration with no corrosion deposits of the LCB specimens in solution SW. Selected photographs of the LCB and SCB specimens taken after exposure and after cleaning are shown in Figure 6-18.

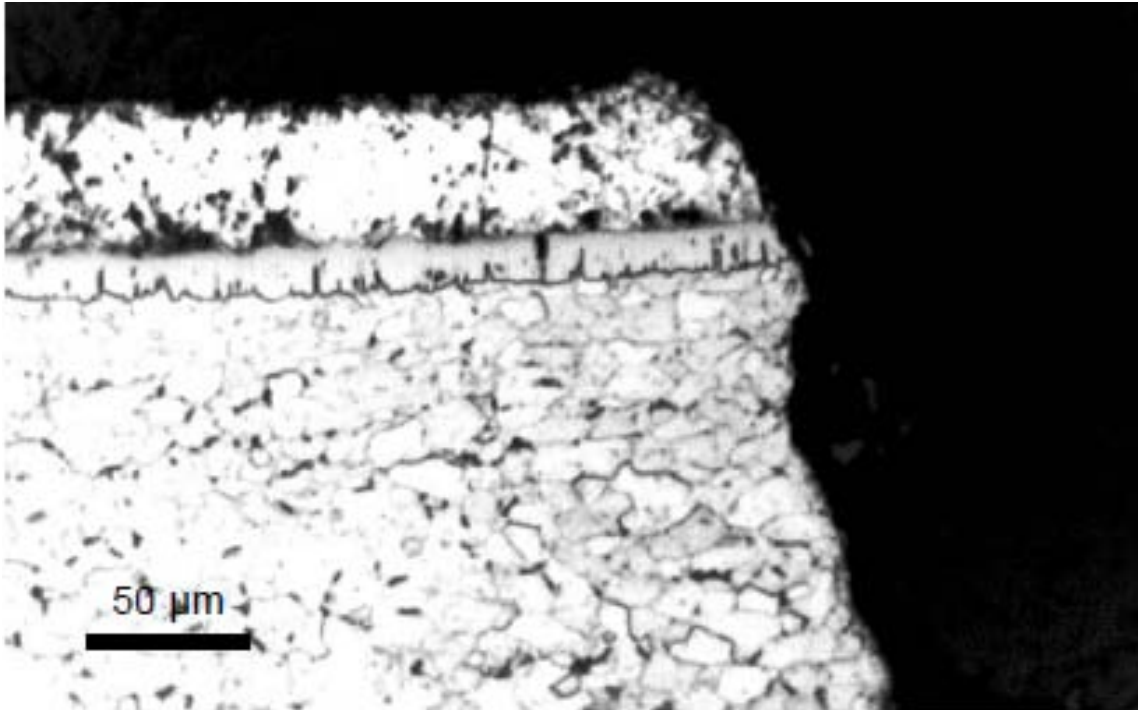


Figure 6-17. Cross section of of blemished aluminized steel type 2 SCB specimen #1 exposed to solution SW near the exposed steel region.

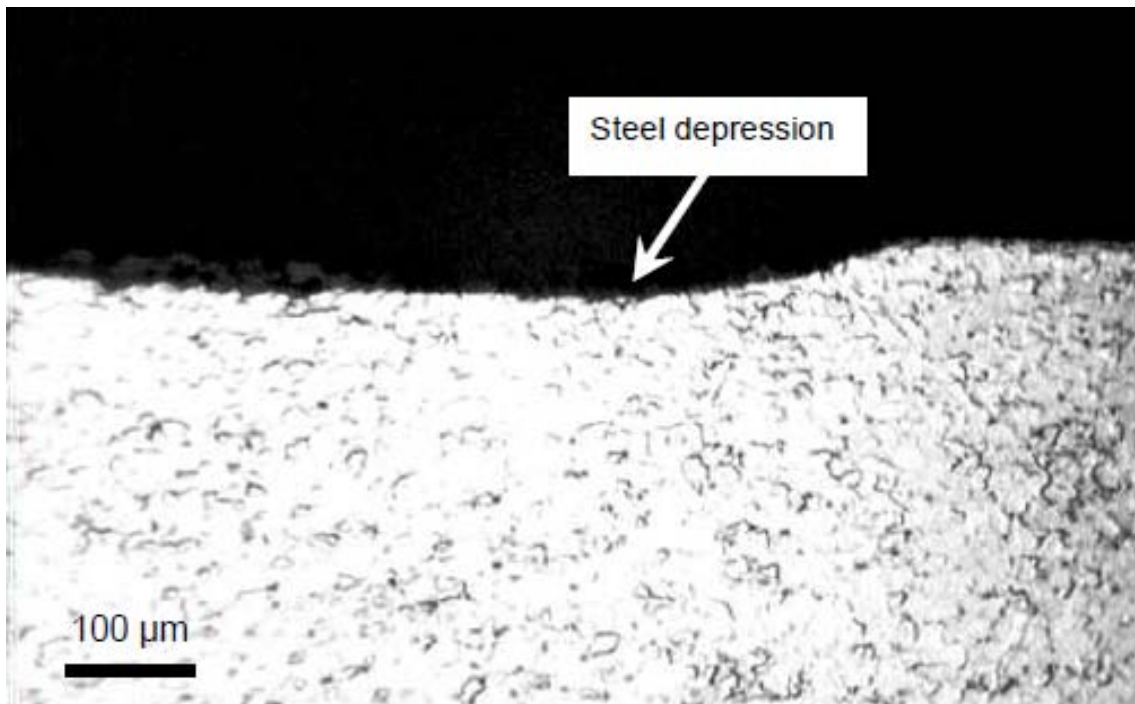
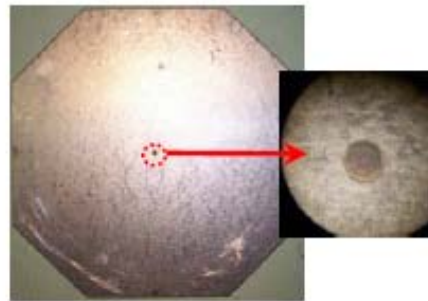


Figure 6-18. Cross section of of blemished aluminized steel type 2 LCB specimen #1 exposed to solution NP showing additional metal loss at the central region of the exposed steel.

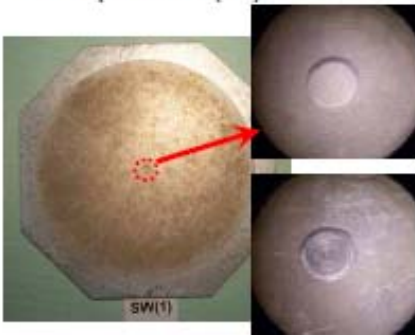
SCB specimen (#1) in Sol NP



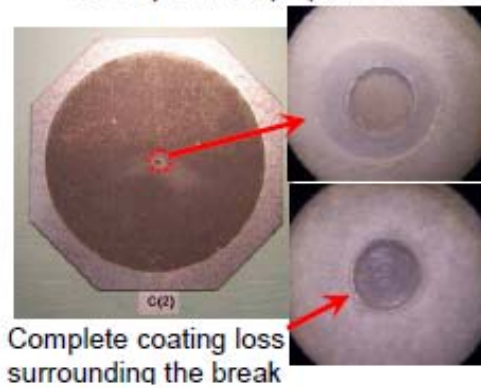
SCB specimen (#1) in Sol P



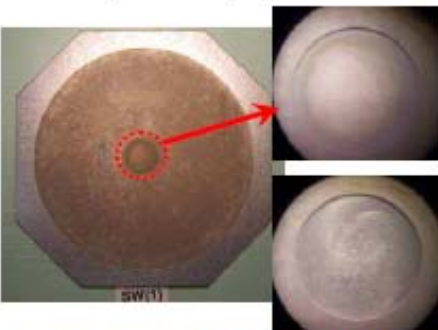
SCB specimen (#1) in Sol SW



SCB specimen (#2) in Sol C



LCB specimen (#1) in Sol SW



LCB specimen (#2) in Sol P



LCB specimen (#1) in Sol NP

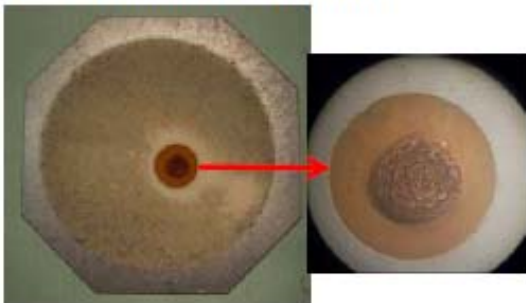


Figure 6-18. Post-exposure photographs of selected blemished aluminized steel type 2 specimens.

6.3.2.2 E_{oc} trends

Figures 6-19 and 6-20 show the E_{oc} evolution for up to ~3,000 hr for the LCB and SCB specimens, respectively. The LCB specimens exposed to solution P showed E_{oc} values of ~-780 mV immediately after immersion, increasing to nearly constant values of ~-745 mV for a period ranging from ~1,200 hr to ~1,700 hr of exposure. At the end of that stage, E_{oc} started a gradual decrease to attain terminal values of ~-910 mV after ~2,000 hr. The SCB specimens exposed to solution P showed E_{oc} values of ~-760 mV immediately after immersion, then decreased to ~-900 mV after ~180 hr and slowly recovered to ~-820 mV near the end of the test. Values of E_{oc} obtained with a Luggin probe placed at ~1 mm above the surface at various radial locations of replicate LCB specimens in solution P at ~72 hr and ~200 hr of exposure, were nearly constant only ~1-2 mV more positive over the exposed steel than over the aluminized surface. The E_{oc} distribution next to the metal surface for the LCB configuration, calculated using a dc computational model (Cáseres, 2007) was in agreement with the E_{oc} profiles observed here.

The LCB specimens exposed to solution NP showed E_{oc} values of ~-770 mV immediately after immersion, increasing to ~-730 mV for periods ranging from ~500 hr to ~1,600 hr. At the end of that period, E_{oc} decayed to ~-930 mV for periods ranging from ~900 hr to ~2,000 hr. For up to ~1,200 hr, the LCB specimen #2 did not display a decrease in E_{oc} possibly associated with a premature test termination. The SCB specimens showed E_{oc} values of ~-750 mV immediately after exposure to solution NP, decreasing to ~-900 mV for periods ranging from ~50 hr to ~200 hr. The SCB specimen #1 showed long term (days-weeks) E_{oc} fluctuations for up to ~1,500 hr followed by a stabilization period around the terminal E_{oc}. Long-term E_{oc} fluctuations were unnoticeable in the duplicate specimen.

The LCB and SCB specimens exposed to solution SW showed comparable E_{oc} trends. For a very few hrs after immersion, E_{oc} values were ~-750 mV followed by a sharp decrease to a terminal E_{oc} around ~-880 mV. The SCB specimens exposed to solution C showed E_{oc} values of ~-620 mV a few hrs after immersion followed by a gradual drop to ~-810 mV after ~1,000 hr, and then recovered slowly reaching ~-710 mV by the end of exposure.

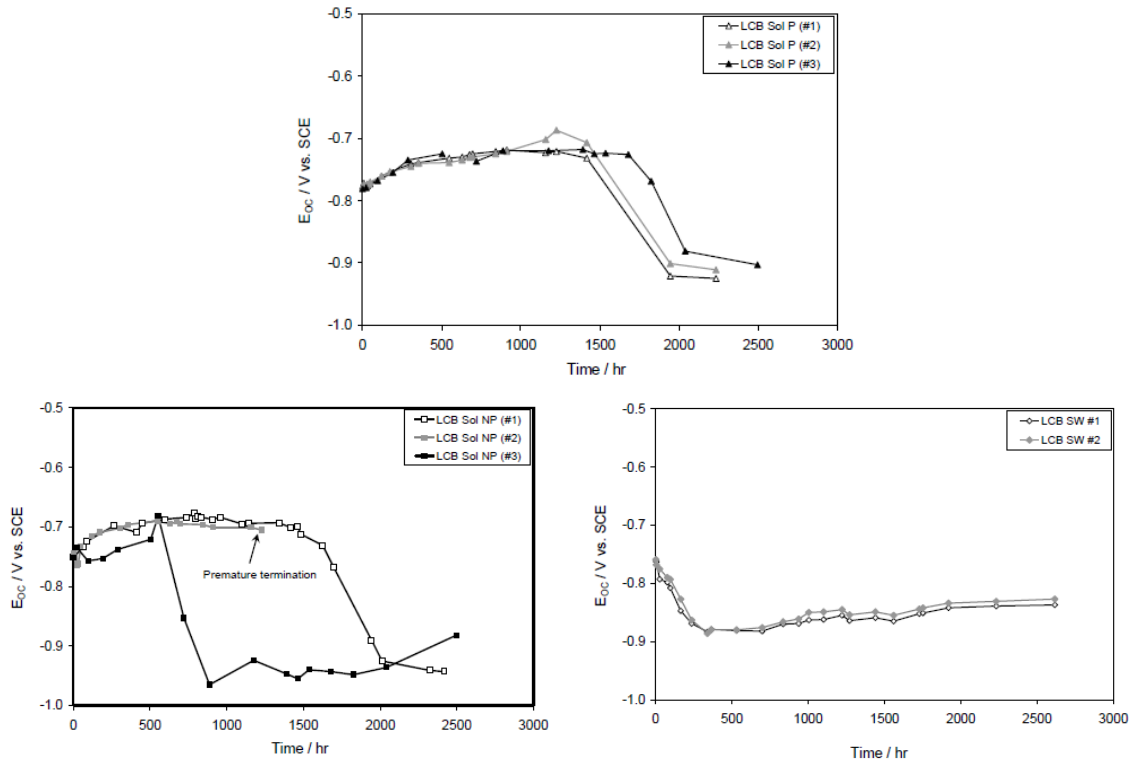


Figure 6-19. E_{OC} evolution in blemished aluminized steel type 2 LCB specimens in solution P (top), solution NP (bottom left), and solution SW (bottom right). Exposure ended at the time that the last datum was taken.

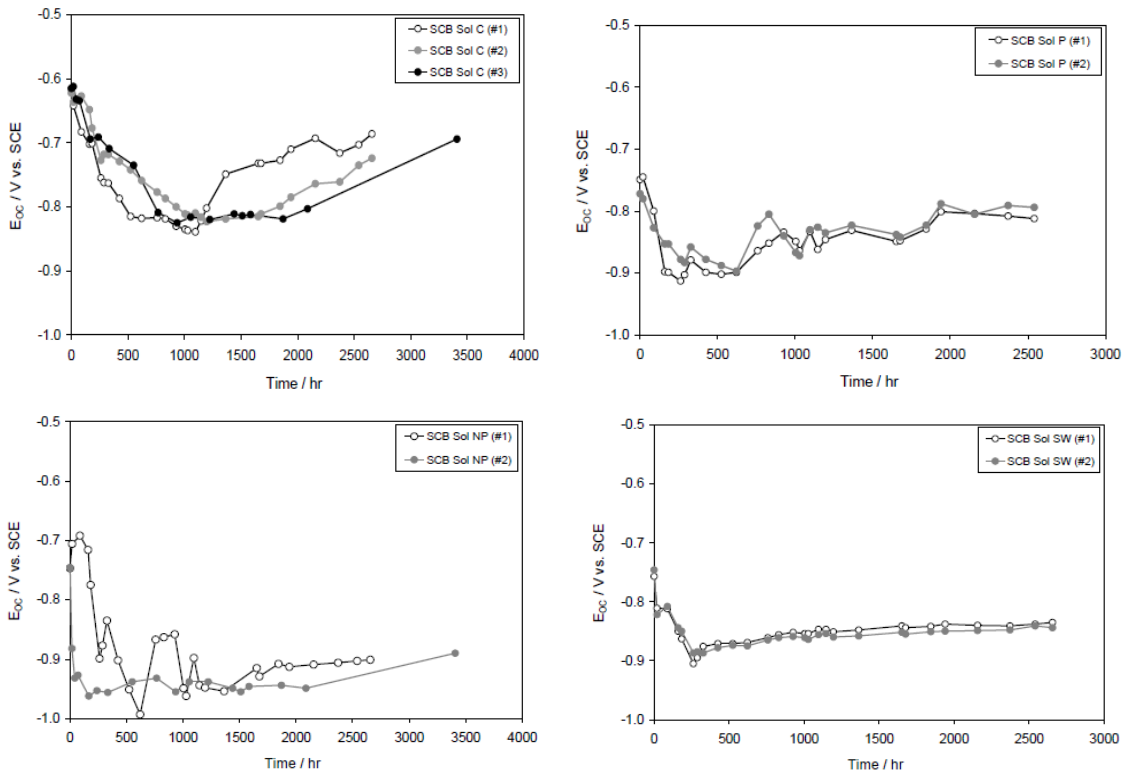


Figure 6-20. E_{OC} evolution as a function of time in blemished aluminized steel type 2 SCB specimens exposed to solution C (top left), solution P (top right) (test exposures were terminated ~450 hr after the last datum), solution NP (bottom left), and solution SW (bottom right). Exposure ended at the time that the last datum was taken, except as noted.

6.3.2.3 Solution compositions

Figures 6-21 and 6-22 show the pH evolution for up to 3,000 hr for the LCB and SCB specimens, respectively. Immediately after immersion, bulk pH values were ~7.8 for NP, ~7.5 for P, ~7.3 for C, and ~7.6 for SW, close to the values reported in Table 6.2 for “as received” specimens. As time progressed, the bulk pH for solution P steadily increased to ~7.7 and ~8.2 for the LCB and SCB configurations, respectively, up to ~1,200 hr and remained nearly constant afterwards. The bulk pH for solution NP showed an increase to terminal pH values of ~9.0 (SCB) after ~200 hr and ~8.8 (LCB) near the end of the exposure. The bulk pH for the solution SW for both SCB and LCB configurations increased to ~8.0 by the end of the test. In solution C, the bulk pH showed pH fluctuations (around a pH unit) around the terminal pH of ~7.5. Comparable pH trends were also observed for the macrocell assemblies exposed to solutions NP and P.

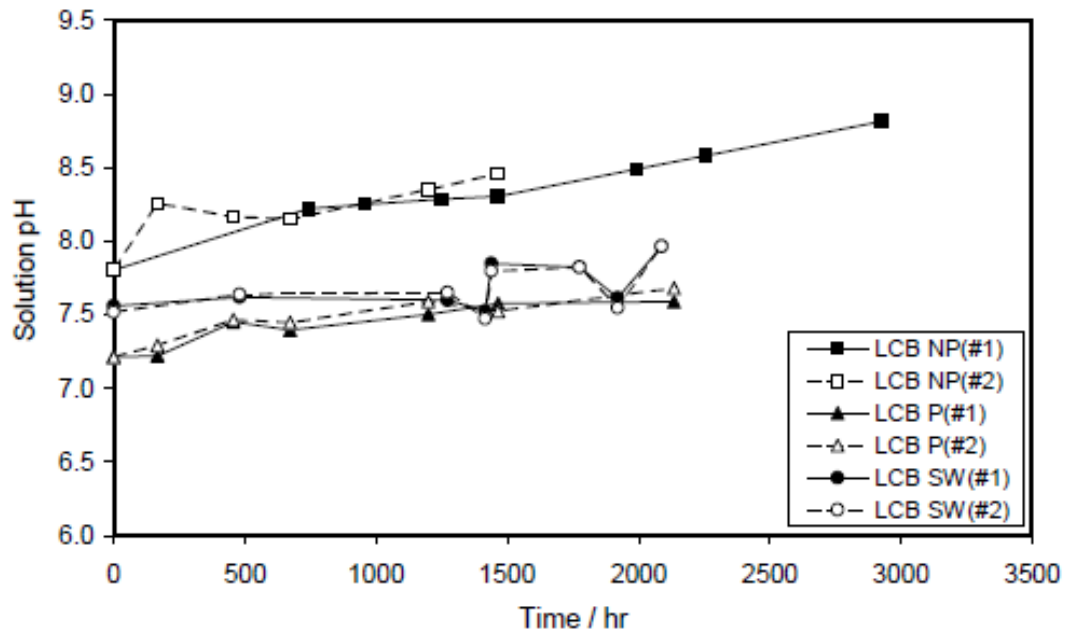


Figure 6-21. Evolution of solution bulk pH for the blemished aluminized steel type 2 LCB configuration.

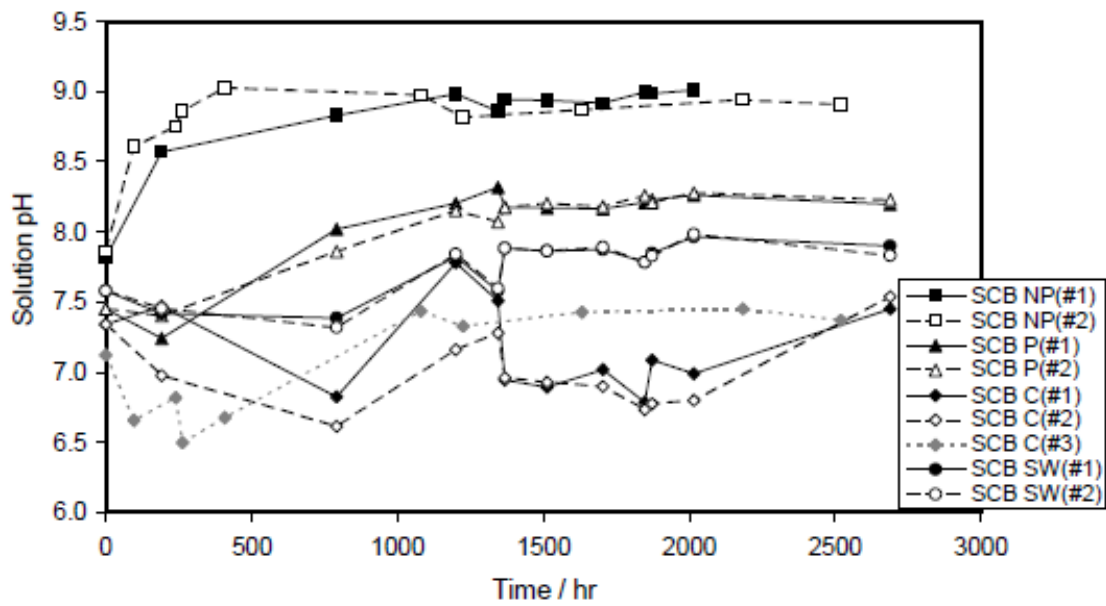


Figure 6-22. Evolution of solution bulk pH for the blemished aluminized steel type 2 SCB configuration.

Total hardness and total alkalinity, determined by titration following procedures indicated in APHA (1992), as well as the solution conductivity are reported in Table 6-2. The Fe^{2+} concentration in all solutions, measured by atomic absorption spectroscopy after ~2,000 hr, was below the minimum detection limit of the instrument (0.01 ppm).

6.3.2.4 Impedance behavior

Figures 6-23 through 6-25 show the non area normalized impedance evolution for up to ~2,400 hr for the LCB specimens exposed to solutions P, NP, and SW. Figures 6-23 and 6-24 show the EIS results for solutions NP and P, respectively, before and after the onset of the E_{oc} drop. For the period before the onset of the E_{oc} drop, the 1 mHz impedance moduli in both solutions were small ($\sim < 1.5 \text{ k}\Omega$ for NP and P) for up to ~1,300 hr of exposure. Per visual assessment of the specimen surface, the impedance behavior during that period was expected to be dominated mainly by the impedance of the steel portion by itself since corrosion scales there were notable, indicative of significant corrosion rates and correspondingly large integrated admittance. In contrast, the aluminized surface remained bright, suggesting passive behavior with consequent very small integrated admittance despite the large aluminized surface. After the onset of the E_{oc} drop, the 1 mHz impedance moduli decreased even further to $\sim 150 \Omega$ (NP) and $\sim 250 \Omega$ (P), consistent with active corrosion of the aluminized surface in both solutions. At that stage, the impedance behavior was expected to be dominated mainly by the impedance of the uniformly corroding aluminized portion, whereas the exposed steel was cathodically protected by the surrounding aluminized surface. That expectation was supported by evidence presented in the subsequent sections. Figure 6-25 shows the EIS results for solution SW for the period after the onset of E_{oc} drop. The 1 mHz impedance moduli ranged from $\sim 2.5 \text{ k}\Omega$ to $\sim 4.5 \text{ k}\Omega$ throughout the test, expected to be dominated by localized corrosion of the large aluminized portion. As before, the exposed steel was cathodically protected by the surrounding aluminized surface as discussed in the subsequent sections.

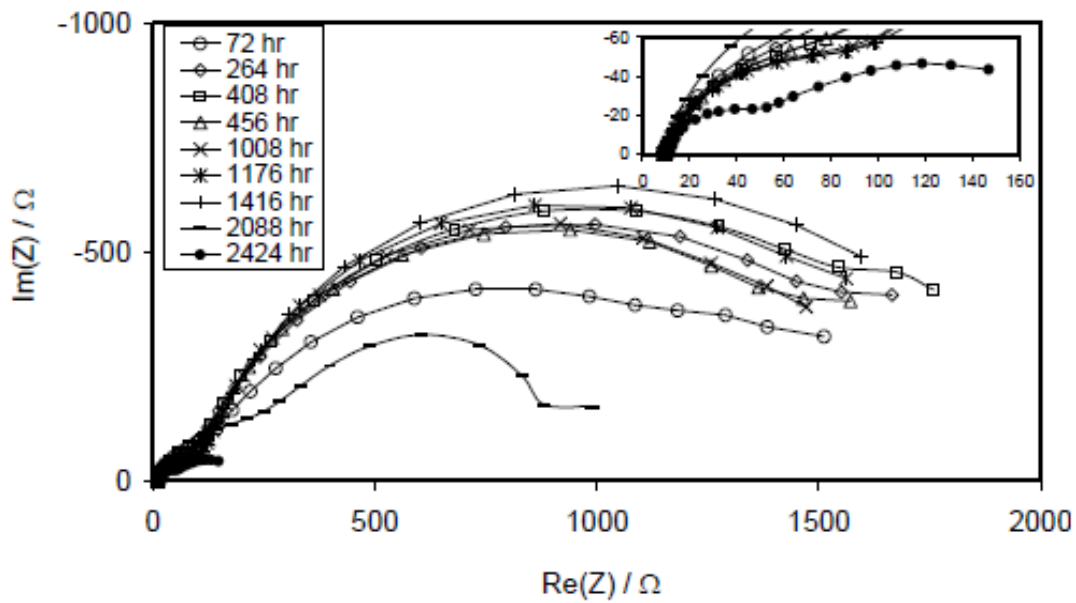


Figure 6-23. Nyquist plot of the impedance response of the LCB specimen #1 in solution NP (100 KHz - 1 mHz - 5 points/decade).

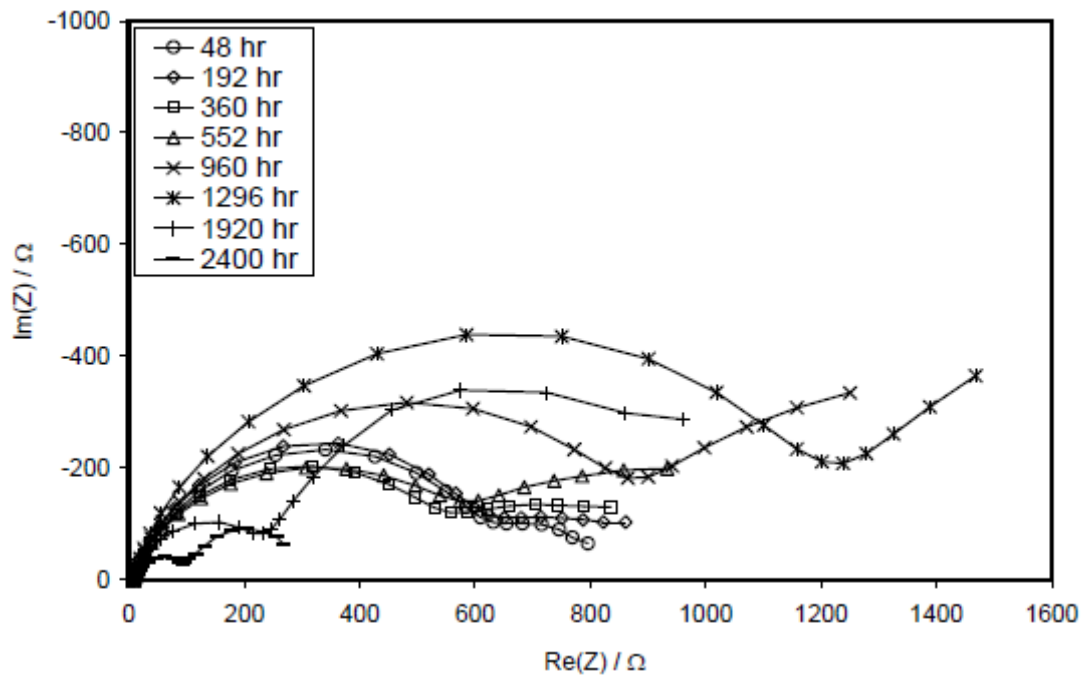


Figure 6-24. Nyquist plot of the impedance response of the LCB specimen #1 in solution P (100 KHz - 1 mHz - 5 points/decade).

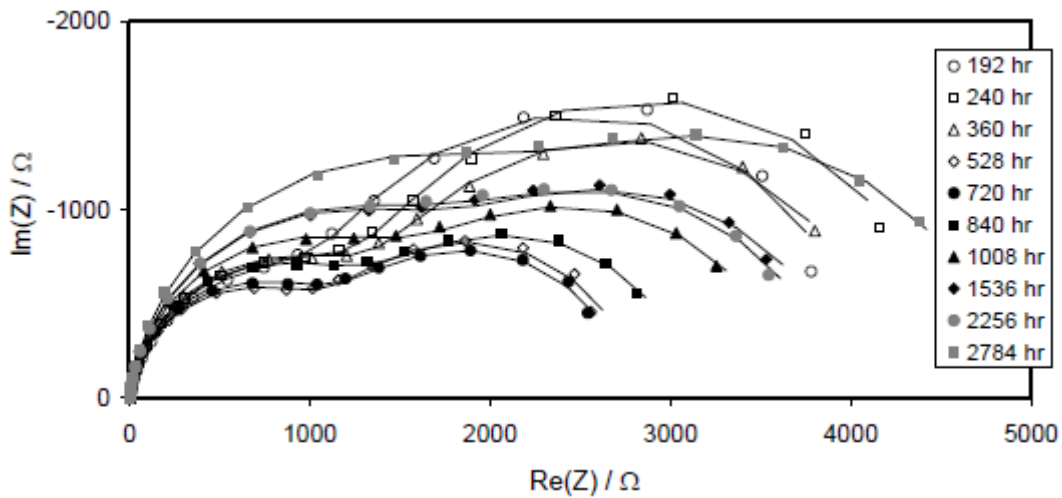


Figure 6-25. Nyquist plot of the impedance response of the LCB specimen #1 in solution SW (100 KHz - 1 mHz - 5 points/decade).

Figures 6-26 through 6-30 shows the non area normalized impedance (EIS measurements conducted on the SCB specimens in all solutions were obtained after the onset of the EOC drop took place) evolution for up to ~2,700 hr for the SCB specimens exposed to solutions NP, P, SW, and C. Figure 6-26 shows the EIS results for solution NP where the 1 mHz impedance moduli initially increased with time to reach ~30 kΩ for up to ~1,000 hr, despite the early corrosion scales deposited on the exposed steel. After ~1,000 hr, the 1 mHz impedance moduli started to decrease, consistent with the start of aluminized discoloration, to values smaller than at the beginning (~600 Ω). Figure 6-27 shows the EIS results for solution P where the 1 mHz impedance moduli increased with time from ~30 kΩ to ~80 kΩ after ~2,500 hr, consistent with generally passive behavior and the absence of visual evidence of active corrosion of the aluminized surface over the entire test exposure. Figure 6-28 shows the EIS results for solution SW where the 1 mHz impedance moduli ranged from ~3 kΩ to ~5 kΩ throughout the exposure. Figures 6-29 and 6-30 show the EIS results for the specimens #1 and #2 in solution C. The EIS results for the triplicate specimen were comparable to those of the duplicate. The 1 mHz impedance moduli in those cases were initially large approaching ~12 kΩ for #1 and ~50 kΩ for #2 at ~120 hr of exposure. Afterwards, the 1 mHz impedance moduli started to decrease to reach ~2 kΩ for #1 and ~4.5 kΩ for #2 after ~650 hr, coinciding with the appearance of the dark grayish layer on the aluminized surface in both specimens. After ~1,000 hr, there was a long-term recovery toward larger 1 mHz impedance moduli for both specimens.

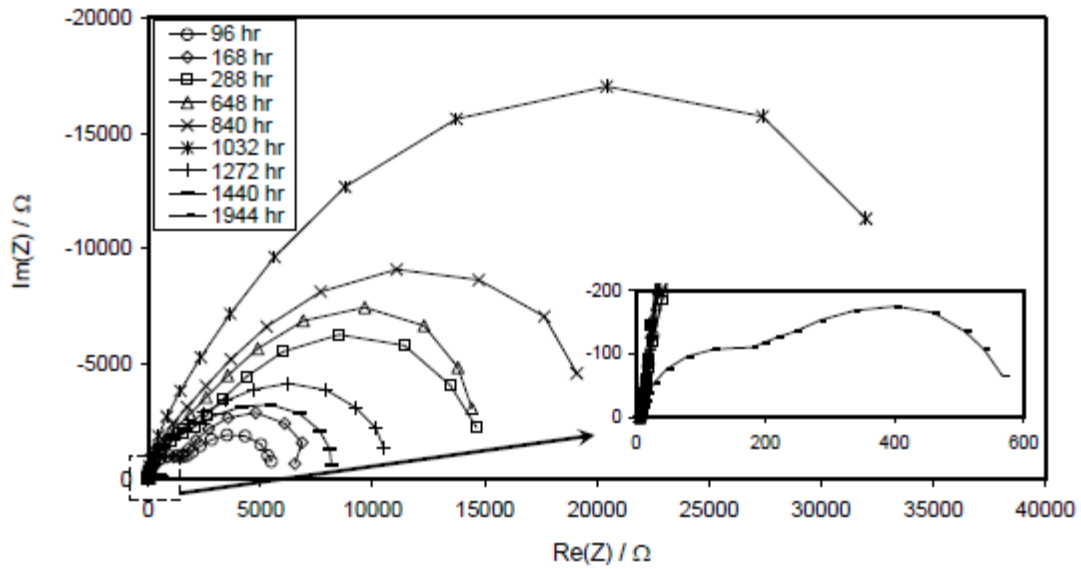


Figure 6-26. Nyquist plot of impedance response for blemished aluminized steel type 2 SCB specimen #1 in solution NP (100 KHz - 1 mHz - 5 points/decade).

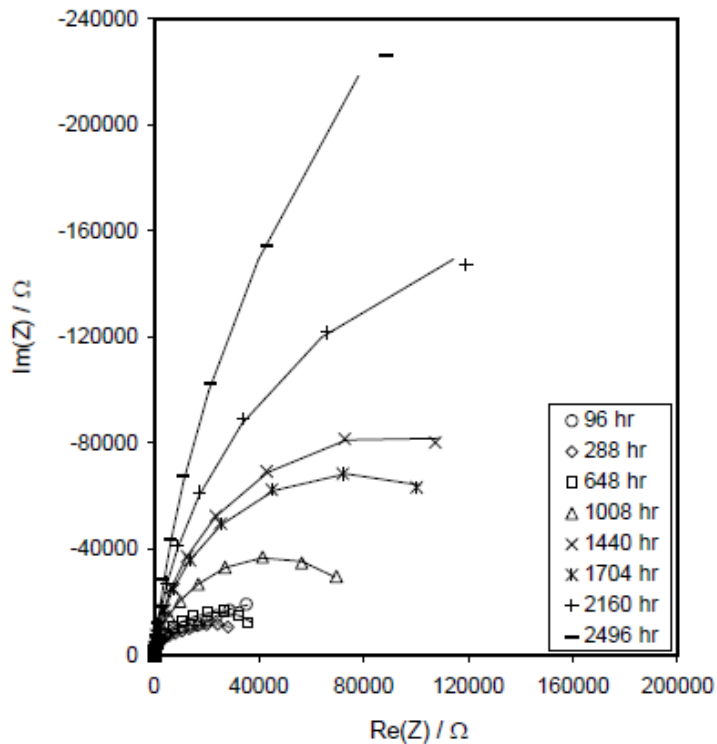


Figure 6-27. Nyquist plot of impedance response for blemished aluminized steel type 2 SCB specimen #1 in solution P (100 KHz - 1 mHz - 5 points/decade).

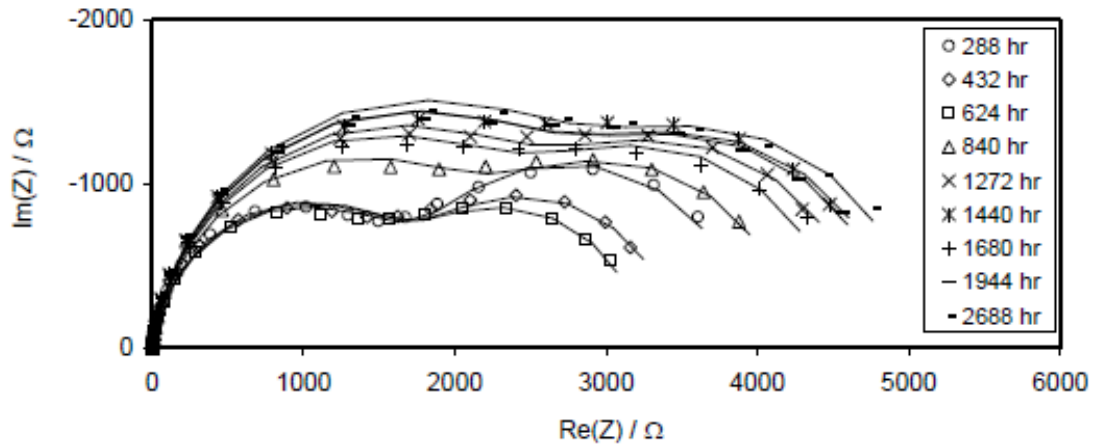


Figure 6-28. Nyquist plot of impedance response for blemished aluminized steel type 2 SCB specimen #1 in solution SW (100 KHz - 1 mHz - 5 points/decade).

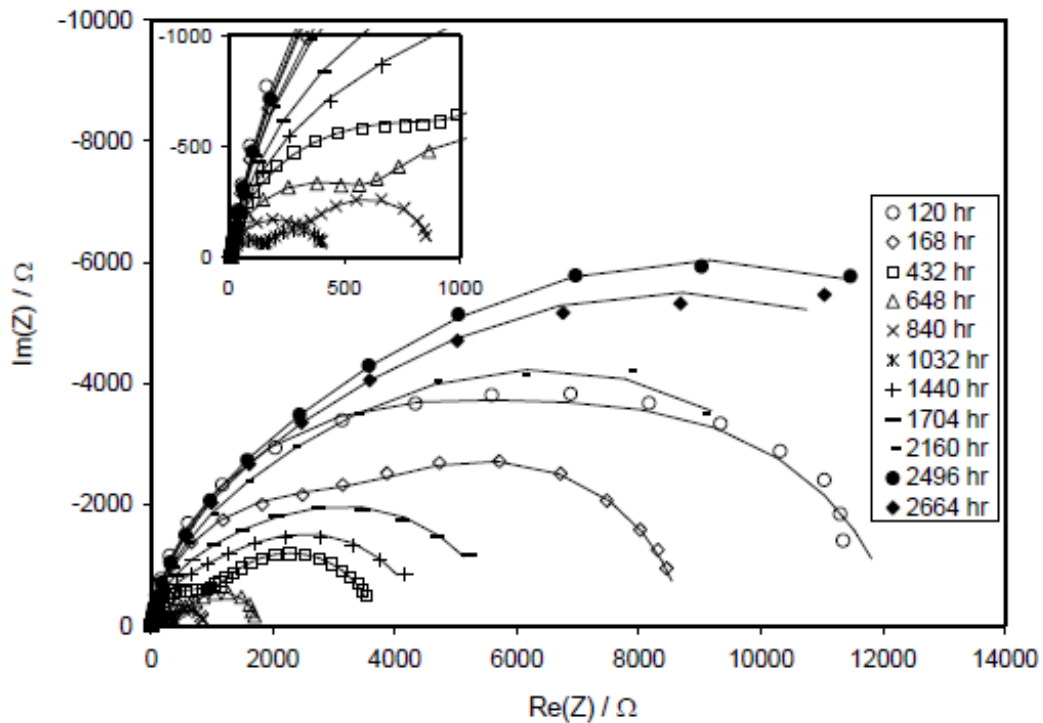


Figure 6-29. Nyquist plot of impedance response for blemished aluminized steel type 2 SCB specimen #1 in solution C (100 KHz - 1 mHz - 5 points/decade).

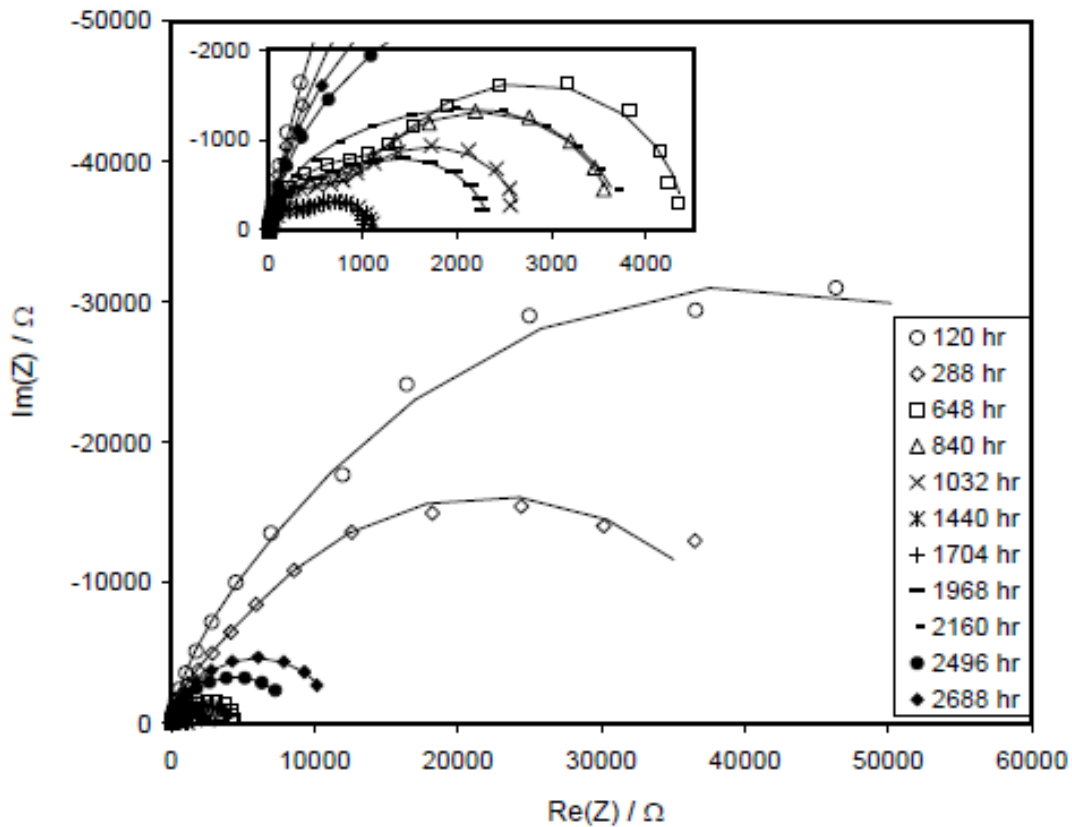


Figure 6-30. Nyquist plot of impedance response for blenished aluminized steel type 2 SCB specimen #2 in solution C (100 KHz-1 mHz - 5 points/decade).

In all cases, the EIS behavior was expected to be dominated mainly by the impedance of the active (NP, SW, and C systems) and passive (P system) aluminized surface. The exposed steel in all cases remained cathodically protected so its impedance was expected to be comparably large to that of the aluminized coating and that expectation was supported by the evidence presented in the subsequent sections. In the LCB specimens in NP and the SCB specimens in C and NP, the amount of electric charge consumed by the corrosion of the annulus region calculated by the Faraday's law was <2.7 Coulombs which represents a local impedance of >170 kΩ. This value was considerably larger than the 1 mHz impedance moduli determined after aluminized discoloration (~150 Ω for NP and ~2-4.5 kΩ), thus, its contribution to the overall anodic dissolution of the aluminized surface can be neglected.

6.3.3 Macrocell assemblies

6.3.3.1 E_{OC} and macrocell current trends

Visual appearance and E_{OC} trends for the macrocell assemblies are summarized in Table A-1 (Appendix A). The E_{OC} trends, rust evolution at the steel component, and changes in the appearance of the aluminized coating

generally paralleled those of the LCB specimens exposed to the same environments. In addition to that information, measurements in these macrocell assemblies provided the galvanic current (I_{galv}) between the steel and aluminized components. The evolution of I_{galv} , as well as the mixed E_{oc} is shown in Figure 6-31 for up to ~2,700 of exposure (data available only for P and NP). In both solutions, the unblemished aluminized steel component of the couple was always a net anode while the steel component was a net cathode. The initial I_{galv} values were ~14 μA and ~1.5 μA for solutions NP and P, respectively. Upon the later start of E_{oc} drop, the I_{galv} values in both solutions started to increase reaching terminal values of ~60 μA and at ~35 μA for solutions NP and P, respectively.

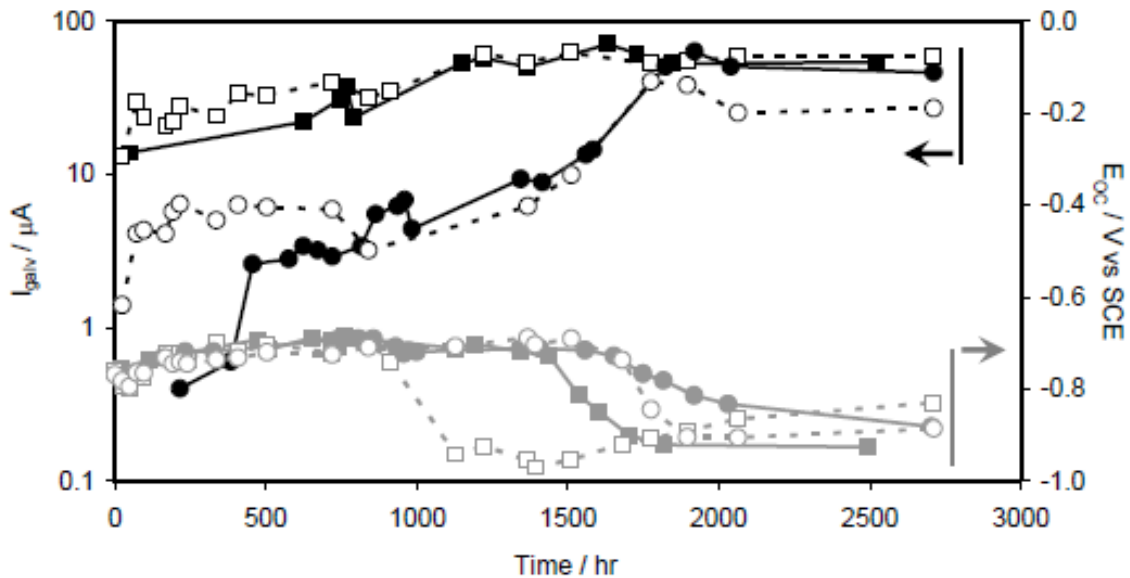


Figure 6-31. E_{oc} and galvanic current I_{galv} measurements for the macrocell assemblies exposed to solutions P (circles) and NP (squares). The steel components were always net cathodes.

6.3.3.2 Impedance behavior

The impedance responses of the coupled macrocell assemblies and the individual components exposed to solutions P and NP before (~900 hr) and after (~1,780 hr) the onset of the low E_{oc} regimes are illustrated in Figures 6-32 through 6-35. Before the E_{oc} drop (Figures 6-32 and 6-34), the 1 mHz impedance moduli of the aluminized component were large (~55 k Ω for P and ~13 k Ω for NP), consistent with generally passive behavior and the absence of visual evidence of active corrosion. The 1 mHz impedance modulus for the steel component was ~1 k Ω for both solutions, in agreement with the observation of early corrosion deposits on the steel surface in both environments. Notably, the overall impedance responses of the coupled macrocell assemblies in both solutions nearly equaled that of the steel component by itself, indicating that the steel ruled the impedance behavior of the coupled system. After the onset of the low E_{oc} regime (Figures 6-33 and 6-35), the 1 mHz impedance moduli of the

aluminized component greatly decreased to $\sim 1 \text{ k}\Omega$ in solution P and to $\sim 2 \text{ k}\Omega$ in solution NP, consistent with the appearance of uniform discoloration (strong for NP and moderate for P) and light pitting indicative of ongoing corrosion in both solutions. In addition, the impedance diagrams of the steel component in both solutions resembled a nearly straight line rather than the earlier depressed semicircular appearance. The 1 mHz impedance magnitudes of the coupled assemblies nearly matched those of the aluminized component by itself, indicating that the aluminized coating dominated the impedance behavior of the coupled system for the low E_{OC} regime.

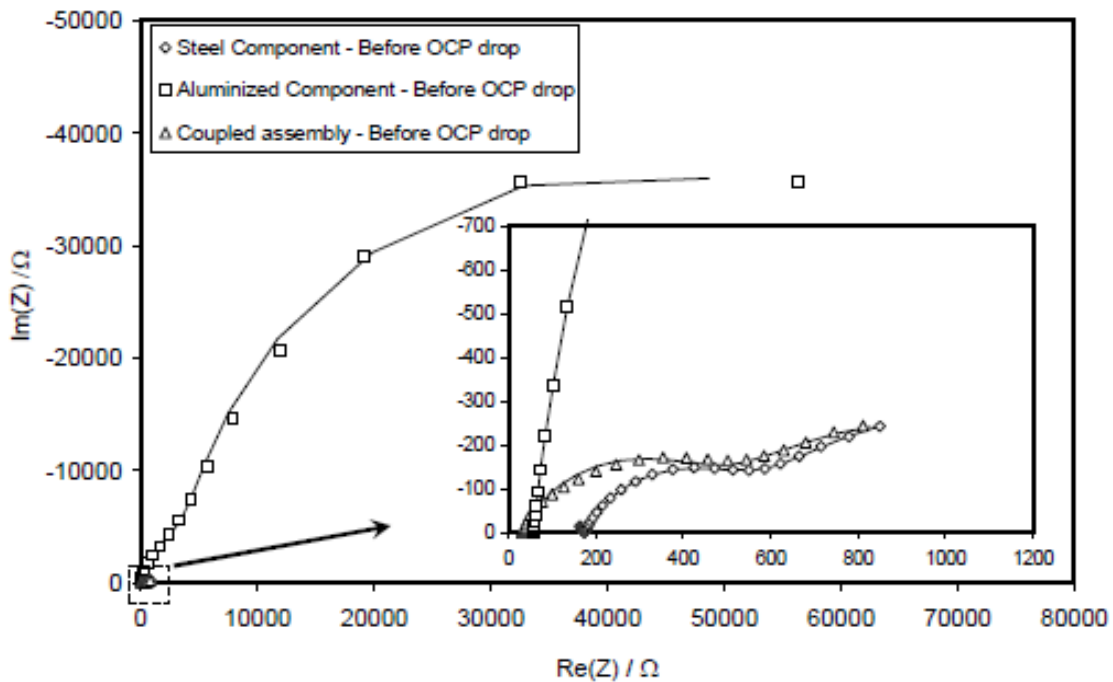


Figure 6-32. Nyquist plot of the impedance response of the macrocell assembly and the individual components exposed to solution P (100 kHz–1 mHz, 5 points/decade) before ($\sim 900 \text{ hr}$) the E_{OC} drop.

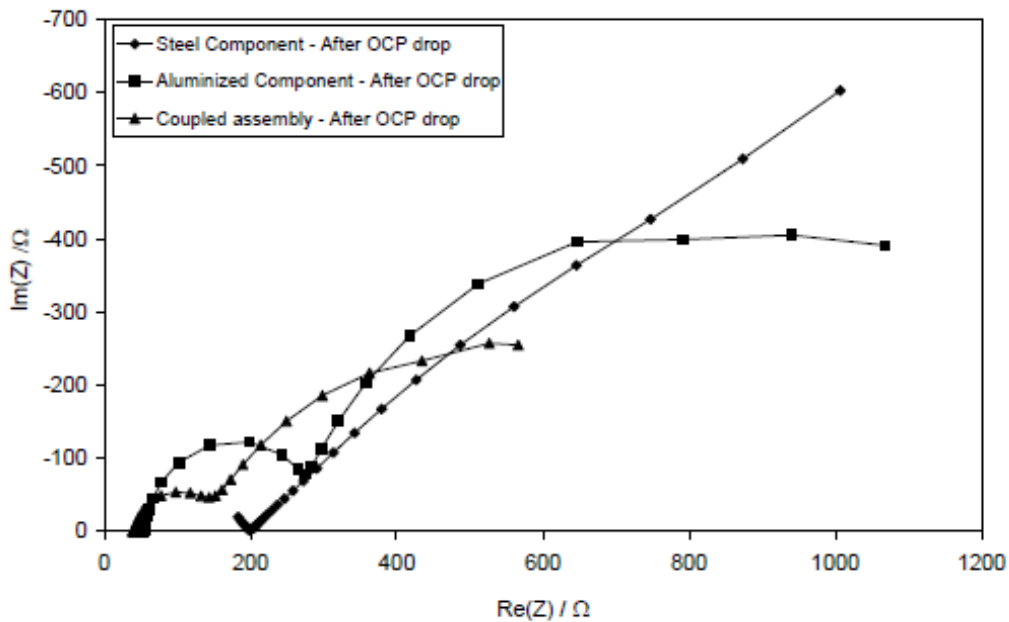


Figure 6-33. Nyquist plot of the impedance response of the macrocell assembly and the individual components exposed to solution P (100 kHz–1 mHz, 5 points/decade) after (~1,780 hr) the E_{OC} drop.

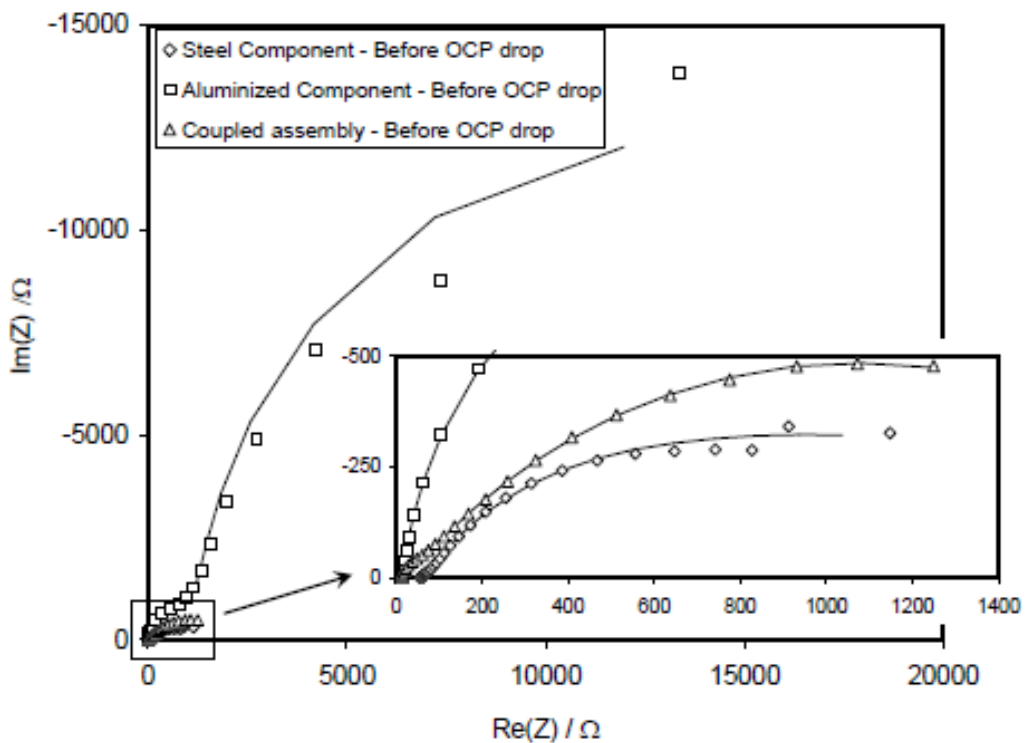


Figure 6-34. Nyquist plot of the impedance response of the macrocell assembly and the individual components exposed to solution NP (100 kHz–1 mHz, 5 points/decade) before (~900 hr) the E_{OC} drop.

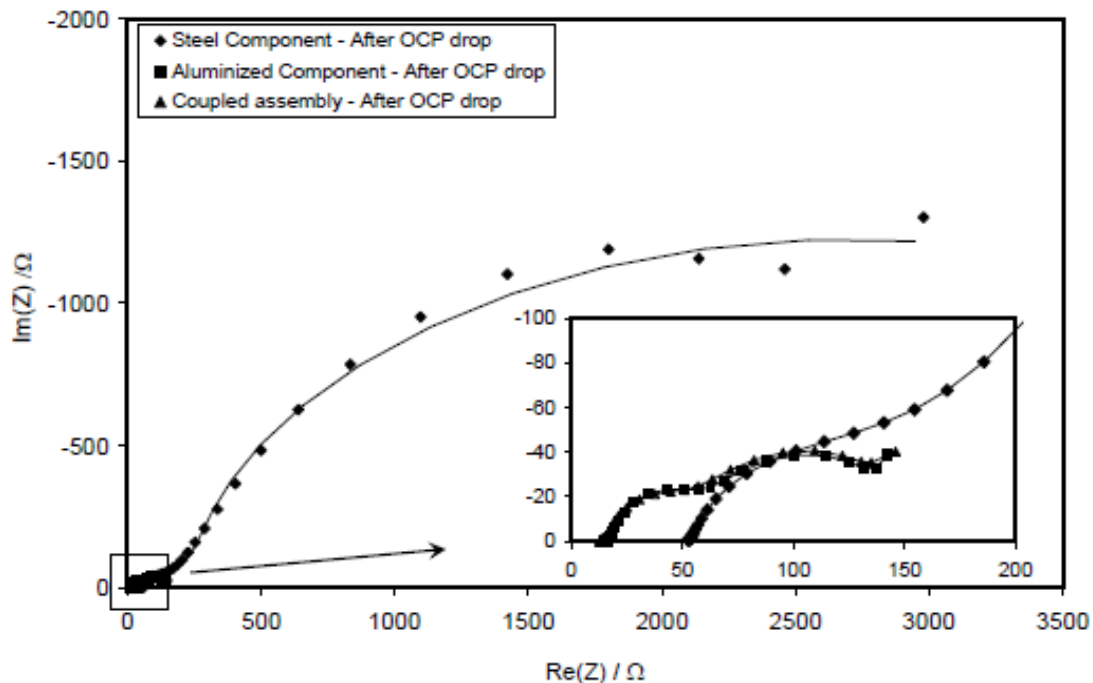


Figure 6-35. Nyquist plot of the impedance response of the macrocell assembly and the individual components exposed to solution NP (100 kHz–1 mHz, 5 points/decade) after (~1,780 hr) the E_{oc} drop.

6.3.4 Uncoupled steel specimens

Figure 6-36 illustrates the E_{oc} evolution for up to ~500 hr for the uncoupled steel specimens exposed to solutions C, NP, and P. Immediately after exposure, the E_{oc} was ~-380 mV for solution NP and ~-430 mV for C and P. A few hrs after immersion, the E_{oc} decayed steeply to nearly constant terminal values around ~-720 mV for solutions NP and P and ~-630 mV for solution C. These terminal E_{oc} values were comparable to those recorded for the LCB and SCB specimens in the same solutions before the start of the E_{oc} decay.

Figure 6-37 shows the non area normalized impedance of the uncoupled steel specimens recorded after ~216 hr of exposure to solution NP and ~72 hr to P. The 1 mHz impedance modulus for the steel component was ~500-800 Ω for both solutions, in agreement with the observation of early corrosion deposits on the steel surface in both environments. The overall impedance trends in both solutions were in good agreement with those recorded for the LCB specimens and the coupled macrocell assemblies exposed to the same solutions for the period before the E_{oc} drop despite the larger solution resistances R_s observed for the uncoupled steel specimens attributed to the larger separation between the metal surface and the reference electrode sensing point. Again, this observation confirms that the impedance response for the aluminized/steel system for the period before the E_{oc} drop is largely dominated by that of the steel.

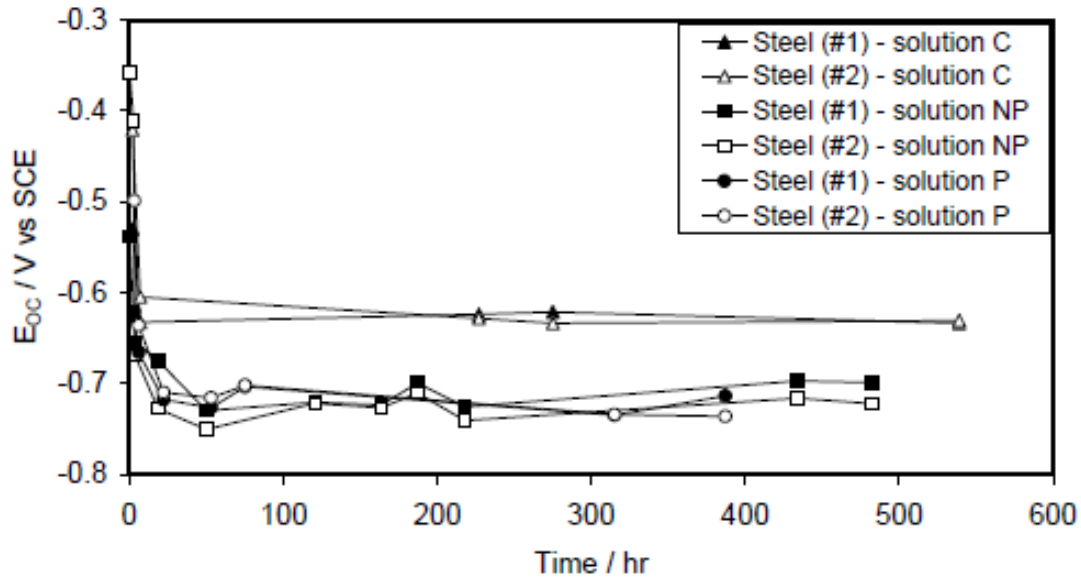


Figure 6-36. E_{OC} evolution as a function of time of in macrocell replicate uncoupled steel specimens. Exposure ended at the time that the last datum was taken.

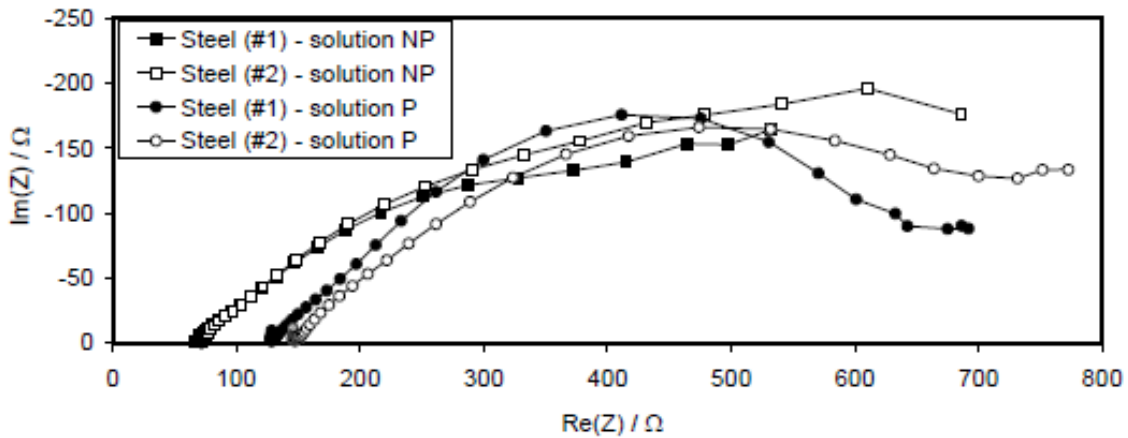


Figure 6-37. Nyquist plot of the impedance response of the replicate uncoupled steel specimens exposed to solutions NP and P (100 kHz–1 mHz, 5 points/decade).

6.3.5 Coating thickness measurements

Figure 6-38 exemplifies schematically a typical aluminized coating cross section of an aluminized steel type 2 that has been exposed for extended periods of time. Table 6-4 summarizes the average coating thickness measurements (comprising both inner and outer layers) obtained from three independent operators for the conditions before and after exposure obtained for selected specimens. Thickness measurements were measured with a standard deviation of $\sim \pm 7.6 \mu\text{m}$. Table 6-4 also includes estimates of the nominal corrosion rates for

the aluminized portion obtained per methodology described in Section 6.2.5. For instance, nominal corrosion rates of the aluminized components for the macrocell assemblies in solutions NP and P were large ($\sim 16\text{-}20\ \mu\text{m}/\text{yr}$ in NP and $\sim 13\text{-}25\ \mu\text{m}/\text{yr}$ in P) in agreement with the visual observation of uniform surface discoloration noted on those specimens. Nominal corrosion rates were also large for the LCB specimens in NP ($\sim 21\text{-}33\ \mu\text{m}/\text{yr}$) and smaller but modest for the LCB specimens in P ($\sim 7\ \mu\text{m}/\text{yr}$) also consistent with visual observation of surface discoloration in those cases. The LCB specimens in SW showed the smallest nominal corrosion rates ($\sim 2\ \mu\text{m}/\text{yr}$) of all specimens examined, in agreement with light uniform corrosion.

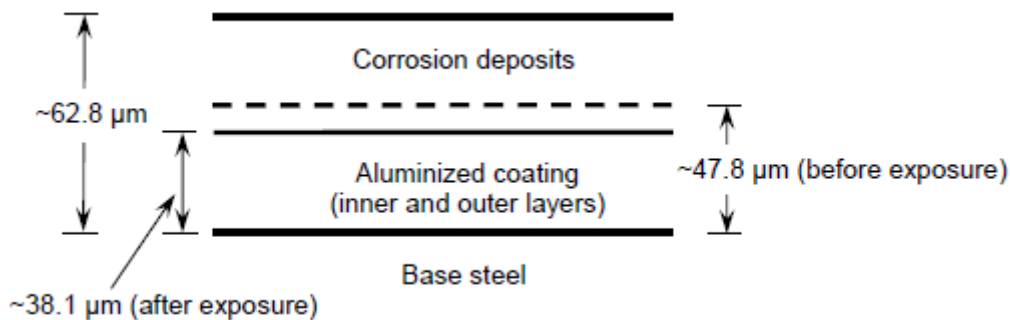


Figure 6-38. Schematic of a typical aluminized coating cross section of a LCB specimen #1 exposed to solution NP.

6.4 Discussion

6.4.1 As-received specimens

6.4.1.1 Direct evidence of corrosion performance

The detailed direct evidence of corrosion in the various systems presented in the previous section may be summarized as follows. Visual examination of the specimen surfaces indicated no corrosion distress in solution P (which included high carbonate precipitating tendency and moderate chloride content) throughout the entire test exposure, suggesting good corrosion performance in these environments. The addition of extra powdered CaCO_3 to solution P did not appear to have had harmful consequences despite momentary electrochemical disturbances as explained below. There was moderate surface discoloration with formation of few small isolated pits in solution NP (which included high total alkalinity without carbonate precipitating tendency and moderate chloride content).

A few small isolated pits followed by strong aluminized surface discoloration were noted early on in solution C, which had low alkalinity, negligible CaCO_3 precipitating tendency, and moderate chloride content. A few small isolated pits but only light discoloration appeared also early on in the

exposure to solution SW, that had moderate alkalinity, high precipitating tendency, and high chloride content/very low resistivity. The corrosion distress and pit penetration in all solutions was not found to extend beyond the outer aluminized layer for the time frame examined.

6.4.1.2 Corrosion mechanisms and analysis of the impedance response

In Chapter 4, a general introduction to corrosion phenomena in aluminum was presented. In the rest of this report, the terminology used to refer to the various corrosion features and events will be used more specifically as in the following.

The term inclusion will indicate the Fe-rich intermetallic precipitate particles present in the outer aluminized surface layer. The inclusions have been identified as preferential sites for both cathodic reactions and effective pit initiation (Nisancioglu, 1990; Johnson, 1971). Acidic oxidation of aluminum will be referred to as a process where aluminum dissolves into an acidic electrolyte according to the reaction $\text{Al} \rightarrow \text{Al}^{3+} + 3\text{e}^-$ where Al^{3+} ions are soluble. Alkaline oxidation of aluminum refers to a process of corrosion of aluminum in an alkaline environment, postulating that a film is always present on the aluminum surface (Pyun et al, 1999). As indicated in Chapter 4, such event may take place when the solution pH near the metal surface normally exceeds ~ 8.5 (Pourbaix, 1974). In such a case, the initially protective aluminum passive film covering most of the aluminized surface is in the form of amorphous $\text{Al}(\text{OH})_3$ (or a comparable intermediate compound as part of the film) and becomes unstable and is expected to be readily chemically attacked at the film-solution interface by OH^- ions with formation of soluble aluminate ions $\text{Al}(\text{OH})_4^-$ (Doche et al, 1999). The resulting enhanced dissolution of aluminum ensues through enhanced transport of the relevant species through a much thinned or more defective passive film (Kolics et al., 2001; Sullivan et al., 2000). Under those conditions in the highly alkaline limit, a likely sequence of aluminum dissolution proposed by MacDonald et al. (1988) and later by Chu et al. (1991) is as shown in Equations 6-2 through 6-5, where Al_{ss} represents aluminum sites at the metal-film interface, the subsequent steps indicate metastable film formation, and the last step is the chemical dissolution at the film-electrolyte interface.



It is noted that since alkaline conditions tend to develop around cathodic sites, alkaline oxidation of aluminum can be enhanced around inclusions, especially if

the solution is not buffered. Such enhanced dissolution has been extensively documented in the literature (Szklańska-Smiałowska, 1999; Suter and Alkire, 2001).

A pit will be referred to as an occluded acidic zone where acidic oxidation of aluminum takes place (Sasaki and Isaacs, 2004; Wiersma and Herbert, 1991; Nguyen and Foley, 1979). As mentioned in Chapter 4, several mechanisms have been proposed to describe pitting corrosion of aluminum in chloride solutions (McCafferty, 2003; Foley, 1986; McCafferty, 1995). There is common agreement that chloride ions migrate to the interior of the pit cavity once a pit initiation event takes place. To maintain charge neutrality inside the cavity, H^+ ions also accumulate in the cavity and decrease the pH there to values below the passivity range of aluminum, resulting in a self-sustaining pit (Seri and Furumata, 2002; Frankel, 1998; Verhoff and Alkire, 2000). The pit geometry needs to be such to maintain active regime inside by efficiently separating the environment inside from that outside, and/or to providing enough ohmic potential drop between the outside and inside regions (Pickering, 2003). Inside the pit cavity acidic oxidation of aluminum takes place.

The corrosion mechanisms proposed below will be evaluated by and used in the interpretation of the results from the EIS experiments. Over the past decades, the EIS technique has been increasingly used to elucidate corrosion mechanistic issues of aluminum exposed to various environments (Mansfeld et al., 1990; Shao et al., 2003). From the numerous investigations reviewed for this study, it can be concluded that there is little consensus on the explanation of the dominant corrosion mechanisms and the models used to simulate the impedance data of aluminum alloys (De Wit and Lenderink, 1996; Aballe et al., 2001; Emregul and Abbas Aksut, 2000; Sherif and Park, 2005; Sasaki and Isaacs, 2004). It is thus noted that the mechanisms and the associated analog equivalent circuit chosen to represent the impedance response for the present case may not be unique, and that alternative mechanisms and analog equivalent circuits may explain equally well the observed impedance behavior. Indeed, other corrosion mechanisms and their corresponding analog equivalent circuits were explored as well, but the ones presented here were chosen mainly for overall simplicity and having provided a reasonable account of the observed impedance spectra. The approach used here is summarized by the analog equivalent circuit shown in Figure 6-39, which serves all the cases considered but with the meaning of some of the individual components depending on the case as detailed in the next sections.

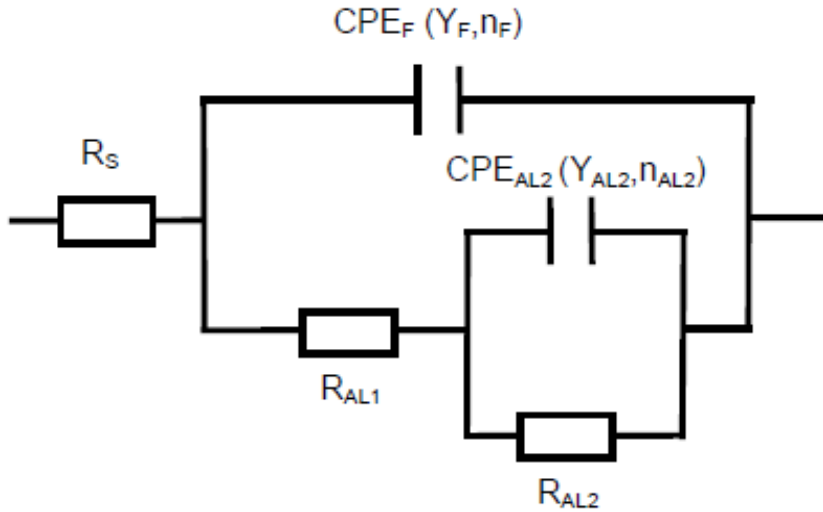


Figure 6-39. Analog equivalent circuit used to simulate the EIS responses.

It is noted that all the corrosion mechanisms considered in this study involve abiotic systems, but the absence of microbiologically induced corrosion (MIC) has not been ruled out, other than by the lack of indications of any conspicuous biofilm in the surfaces of the test specimens.

6.4.1.2.1 Solution P and solution NP before surface discoloration

The following analysis applies to solution P over the entire exposure time and solution NP for the regime before the appearance of moderate aluminized surface discoloration. In those cases, the initial system E_{oc} was quite negative reflecting the coupled potential of the inclusions with the slow passive dissolution of the larger area aluminum solid solution phase surrounding the inclusions. As time progresses, a more mature passive film is expected to experience slower dissolution with potentials drifting to moderately nobler values as observed. The impedance response for the present passive systems is interpreted with the aid of the analog equivalent circuit shown in Figure 6-39. The resistor R_s represents the ohmic solution resistance. All components in Figure 6-39 are expressed as surface-normalized elements by dividing/multiplying as appropriate by the nominal specimen area (95 cm^2).

The working assumption is made that the impedance response of the passive film (which occupies most of the specimen surface), when combined with the Helmholtz layer capacitance C_H , is predominantly capacitive and may be represented by the constant phase angle element CPE_F in the upper branch of the circuit. The film surface is taken to be the locus of a slow, nearly uniform anodic dissolution reaction as stated above, which is also only mildly potential dependent so its admittance is neglected. As mentioned earlier, the matching cathodic reaction at E_{oc} is expected to occur primarily at the inclusions (Nisancioglu, 1990; Johnson, 1971) represented by the lower branch of the

circuit. The buffering capacity of these solutions is expected to neutralize the OH⁻ ions formed by the cathodic reaction so that increase in the local pH is minimized at least at the beginning of the exposure. To account for the observation of a low frequency loop in the impedance diagrams, the cathodic reaction is proposed to proceed in coupled steps of the type where surface coverage by an intermediate adsorbate alters the rate of the next step (Bessone et al., 1992; de Wit and Lenderink, 1996; Armstrong and Edmondson, 1973; Epelboin and Keddam, 1970). The resulting response is pseudo-capacitive, (approximated by the element CPE_{AL2}) with a high-frequency limit resistance R_{AL1}, and a low frequency limit resistance R_{AL1}+ R_{AL2} (Armstrong and Edmondson, 1973). Consequently, the pseudo-capacitive element CPE_{AL2} is placed across the resistance R_{AL2} as shown. Refer to Cáseres (2007) for a detailed explanation of the proposed modeling of the impedance behavior for this mechanism.

The analog equivalent circuit in Figure 6-39 with EIS parameters reported in Tables 6-5 and 6-6 yielded good best-fit simulations of the impedance responses of both solutions, shown by the solid lines in Figures 6-7 through 6-11. Although CPEs were used in the circuit, the best fit values of n_F and n_{AL2} for both solutions were close to unity, indicating little deviation from ideal capacitive behavior. Sometimes best fit values of n_F and n_{AL2} slightly >1 were obtained for one of the CPEs. In those cases, there was little sensitivity of the fit to the choice of which element approached ideal behavior more closely. For those cases a value n_{AL2}=1 was imposed and n_F was allowed to vary resulting in n_F values >0.93 (subscripts are keyed to the element designations in Figure 6-39). Figures 6-40 and 6-41 show examples of the time dependence of the admittance parameters and resistive components thus calculated (the figures contain also the results for the NP system after aluminized surface discoloration and for the other solutions as well, to be discussed later).

Table 6-5
Values of Equivalent Circuit Components for Circuit Shown in Figure 6-39
Estimated from EIS Data Fit for As-Received Aluminized Steel Type 2
Specimen #1 Exposed to Solution P

Time Hr	R _S Ω	R _{AL1} kΩ	Y _F s ^{n_F} /Ω	n _F	R _{AL2} kΩ	Y _F s ^{n_{AL2}} /Ω	n _{AL2}	i _{corrAL} μA cm ⁻²
48	17.8	27	3.19E-04	0.94	27	3.83E-03	1	0.034
216	17.7	55.5	3.49E-04	0.94	37.6	3.83E-03	1	0.016
312	18.3	79.6	3.51E-04	0.94	47.8	3.24E-03	1	0.011
336	17.1	10.1	4.00E-04	0.94	7.6	1.25E-02	1	0.091
480	19.5	18.4	4.11E-04	0.94	16.5	7.75E-03	1	0.05
504	20.2	10.7	4.28E-04	0.94	9.9	9.78E-03	1	0.085
624	20.7	17.2	4.36E-04	0.94	15.9	6.31E-03	1	0.053
1248	22.1	22.5	5.09E-04	0.94	20.7	2.75E-03	0.98	0.041
2376	20.9	74.8	5.41E-04	0.93	32.5	1.84E-03	1	0.012
3072	21.6	110.4	5.39E-04	0.93	25.4	2.08E-03	1	0.008

Nominal specimen area A_{AL} = 95 cm²

Table 6-6
Values of Equivalent Circuit Components for Circuit Shown in Figure 6-39
Estimated from EIS Data Fit As-Received Aluminized Steel Type 2
Specimen #1 Exposed to Solution NP

Time Hr	R_S Ω	R_{AL1} k Ω	Y_F s^{n_F}/Ω	n_F	R_{AL2} k Ω	Y_F $s^{n_{AL2}}/\Omega$	n_{AL2}	i_{corrAL} $\mu A\ cm^{-2}$
24	14.8	6.6	3.69E-04	0.95	9.6	4.42E-03	1	0.14
144	15.3	13.9	4.20E-04	0.95	17.5	2.44E-03	1	0.07
360	14.9	8.7	4.85E-04	0.94	13.6	2.86E-03	0.99	0.1
624	15	20.4	4.98E-04	0.94	30.5	1.14E-03	0.95	0.04
864	14.9	24.4	5.06E-04	0.94	27.9	1.31E-03	0.99	0.04
1368	15.3	28.1	5.59E-04	0.94	31.2	1.29E-03	0.99	0.03
2376	14.7	7.9	7.03E-04	0.94	6.6	2.74E-03	1	0.07
3048	14.5	2.1	9.62E-04	0.94	2	9.92E-03	1	0.22

Nominal specimen area $A_{AL} = 95\ cm^2$

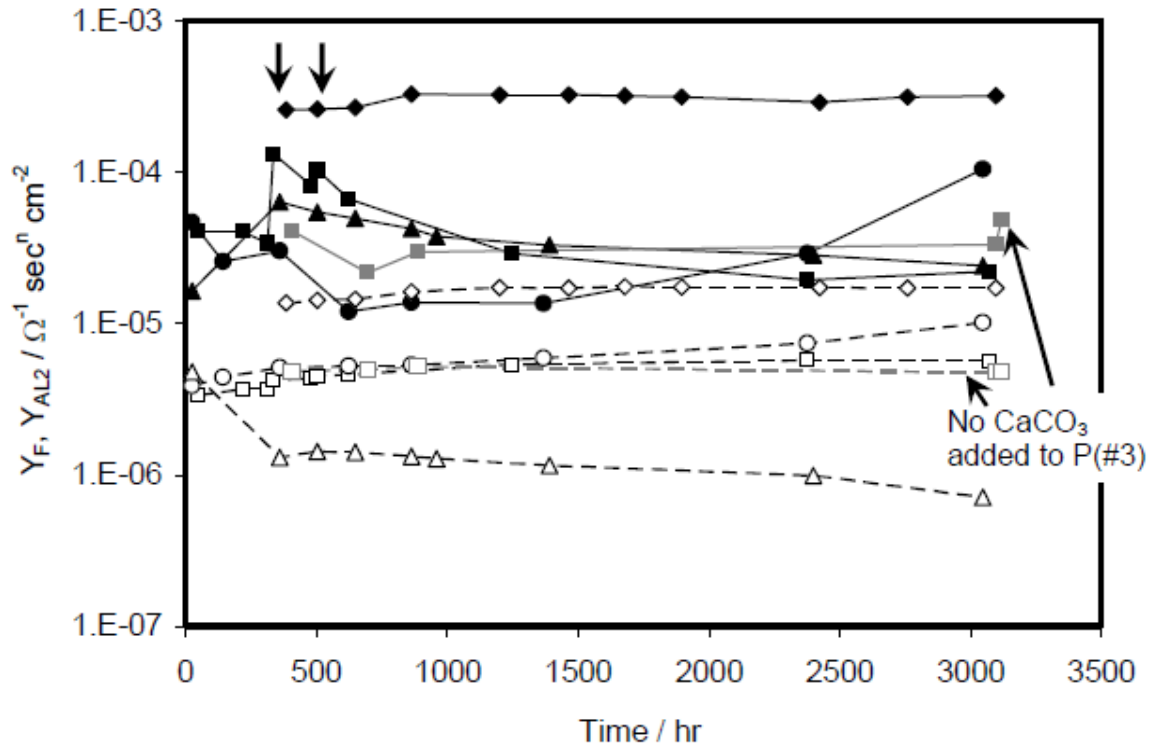


Figure 6-40. Evolution of the admittance parameter as a function of time for as-received aluminized steel type 2 specimens #1 in solutions NP (circles), P (squares), C (triangles), and SW (diamonds) (--- Y_F , — Y_{AL2}). Arrows indicate $CaCO_3$ additions to solution P (#1).

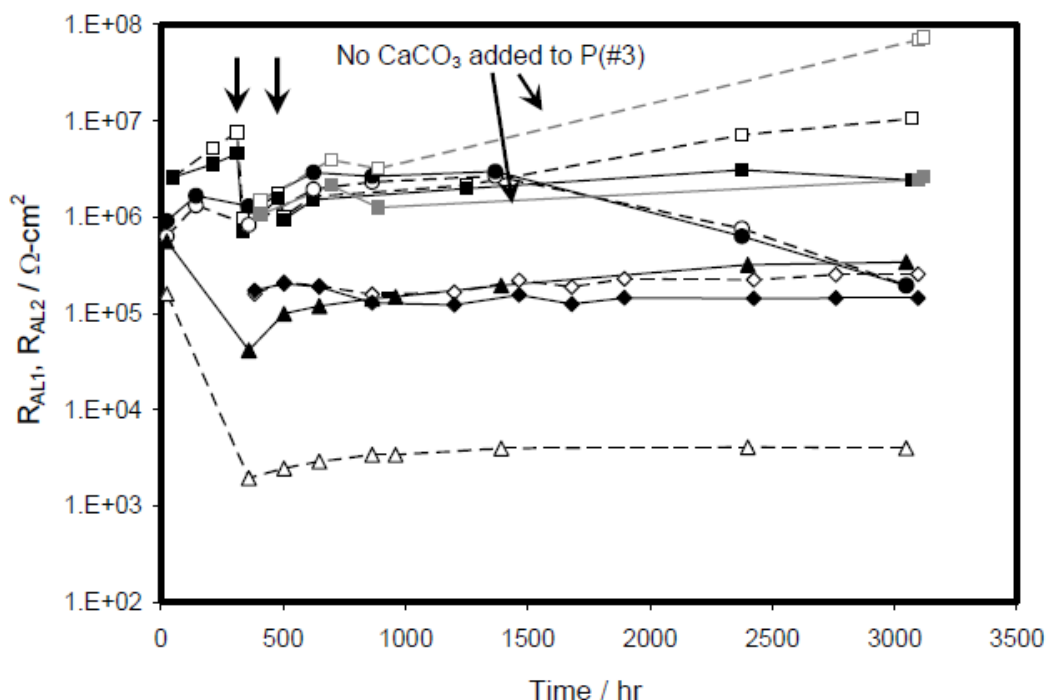


Figure 6-41. Evolution of the resistive components as a function of exposure time for for as-received aluminized steel type 2 specimens #1 in solutions NP (circles), P (squares), C (triangles), and SW (diamonds) (--- R_{AL1} , — R_{AL2}). Arrows indicate CaCO_3 additions to solution P (#1).

Throughout the test, the values for $R_{AL1} + R_{AL2}$ for solution P were large ($\sim 2.5 \cdot 10^6 \Omega\text{-cm}^2$ and $\sim 1.5 \cdot 10^7 \Omega\text{-cm}^2$, respectively), and tracked roughly together as exposure time progressed, in keeping with the above assumption of coupled steps of the associated cathodic reaction. Similar trends were noted for solution NP with large values of R_{AL1} and R_{AL2} , both reaching $\sim 3 \cdot 10^6 \Omega\text{-cm}^2$ before the start of aluminized surface discoloration.

The Y_{AL2} values in both solutions were much larger and variable with time than Y_F , consistent with the assumed origin for CPE_{AL2} other than film capacitance. In solution P, Y_{AL2} values were initially $\sim 4 \cdot 10^{-5} \text{sec}^{n_{AL2}}/\Omega\text{-cm}^2$ followed by a strong momentary increase to $\sim 1.3 \cdot 10^{-4} \text{sec}^{n_{AL2}}/\Omega\text{-cm}^2$ only noticeable upon the first addition of extra powdered CaCO_3 to specimens #1 and #2 and a later decrease to a terminal value of $\sim 2.2 \cdot 10^{-5} \text{sec}^{n_{AL2}}/\Omega\text{-cm}^2$. Y_{AL2} was nearly constant ($\sim 3.3 \cdot 10^{-5} \text{sec}^{n_{AL2}}/\Omega\text{-cm}^2$) for specimen #3 in P, which had no addition of powdered CaCO_3 . The Y_{AL2} values for the duplicate specimens in solution NP were initially $\sim 4.6 \cdot 10^{-5} \text{sec}^{n_{AL2}}/\Omega\text{-cm}^2$ decreasing to $\sim 1.4 \cdot 10^{-5} \text{sec}^{n_{AL2}}/\Omega\text{-cm}^2$ recorded before the start of the appearance of aluminized surface discoloration.

The association of CPE_F with the passive film capacitance is further supported by the following considerations. The Y_F values were similar in both

solutions ($\sim 3.4 \cdot 10^{-6}$ to $\sim 1 \cdot 10^{-5} \text{ sec}^{n_{AL2}}/\Omega\text{-cm}^2$) and changed relatively little with exposure time. In the following, the charge storage function associated with CPE_F will be quantified by a nominal capacitance C_F that has the same imaginary impedance component as CPE_F at a suitable frequency f_N . For ease of comparison with the M-S results, f_N was chosen to be 10 Hz. In fact, the sensitivity of C_F to the choice of f_N was expected to be small since n_F approached unity. Thus, Equation 6-6, which yielded C_F values from ~ 2.6 to $\sim 7.9 \mu\text{F}/\text{cm}^2$, was numerically close to Y_F since $n_F \sim 1$.

$$C_F = \frac{Y_F \cdot (2\pi \cdot f_n)^{n_F - 1}}{\sin\left(n_F \cdot \frac{\pi}{2}\right)} \quad (6-6)$$

These values are comparable to those reported in the literature for passive aluminum (Pyun, 1999; Bockris and Kang, 1997). If the passive film behaved as an ideal capacitor of thickness L and dielectric constant ϵ , its area-normalized capacitance C_i would be given by Equation 6-7, where ϵ_0 is the permittivity of vacuum.

$$C_i = \frac{\epsilon \cdot \epsilon_0}{L} \quad (6-7)$$

Assuming $L \sim 5 \text{ nm}$ and $\epsilon \sim 9$ (typical of thickness of naturally grown passive films on aluminum (Bessone et al., 1983; Diggle, 1972) and of solid or hydrated aluminum oxides, respectively) yields $C_i \sim 1.60 \mu\text{F}/\text{cm}^2$. That value is much less than typical values of C_H (Bockris and Kang, 1997) so the combined series interfacial capacitance is still $\sim C_i$, which approximates well the low end of the C_F value range obtained above. The approximation could be even better if it included natural surface roughness which would increase the effective value of C_i above that of the ideally flat surface assumed for Equation 6-7. Similar general behavior on passive aluminum has been observed often (Lee and Pyun, 1999) and supports the interpretation that the high frequency loop in the spectra corresponds to the passive film.

Capacitive behavior in a semiconducting passive film often reflects the presence of a space charge zone that may extend through the entire film thickness L (the entire film thickness then acting effectively as a dielectric), or have a depth $d_{SC} < L$. The M-S experiments sought to elucidate that issue for the present systems since in the first case the film capacitance is not potential dependent upon brief cathodic excursions from the E_{oc} . In the latter case, however, the differential capacitance of the film is still approximately given by Equation 6-7 but replacing L with d_{SC} , which varies with potential E . For example, if the film is an n-type semiconductor as generally observed in aluminum (Bockris and Kang, 1997; Fernandes et al, 2004) and the polarization conditions are adequate, then $d_{SC} \sim (2 \epsilon \epsilon_0 q^{-1} (E - E_{fb}) N_d^{-1})^{0.5}$, where q is the

electron charge, N_d is the net density of electron-donor defects (assumed to be constant for simplicity), and E_{fb} is the flatband potential (Morrison, 1980).

Assuming $C_F(E) \ll C_H$, $C_F(E)$ was estimated from the 10 Hz M-S impedance measurements at 100 mV intervals by Equation 6-8, where $Z''(10\text{Hz})$ is the imaginary component of the impedance and $k_C(E)$ is a correction factor close to unity.

$$C_F(E) \approx \frac{-k_C(E)}{2\pi \cdot f_n \cdot Z''(10\text{Hz})} \quad (6-8)$$

The factor $k_C(E)$ corrected for the obscuring effect of R_{AL1} , which at the lowest potentials (with R_{AL1} small) could cause the value of $Z''(10\text{Hz})$ to be significantly smaller than what would have resulted from the capacitive element alone. To obtain $k_C(E)$, impedance measurements spanning the range 100 Hz⁻¹ Hz were conducted at a few selected potentials over the same potential range as the M-S tests. Those measurements yielded at each selected potential values of Y_F and n_F , which were used to calculate accurate values of $C_F(E)$ using Equation 6-6. Therefore at the selected potentials $k_C(E) = -C_F(E) 2\pi f_N Z''(10\text{Hz})$. Values of $k_C(E)$ at intermediate potentials were then assigned by polynomial interpolation.

Figure 6-42 shows the M-S results in duplicate in solutions NP and P for ~330 hr of exposure obtained per the above procedure. At the time of the tests, no apparent corrosion was observed in any of the specimens. The results show nearly constant capacitance with potential (from ~3.4 to ~5.9 $\mu\text{F}/\text{cm}^2$), which is therefore consistent of a space charge zone spanning the entire film thickness.

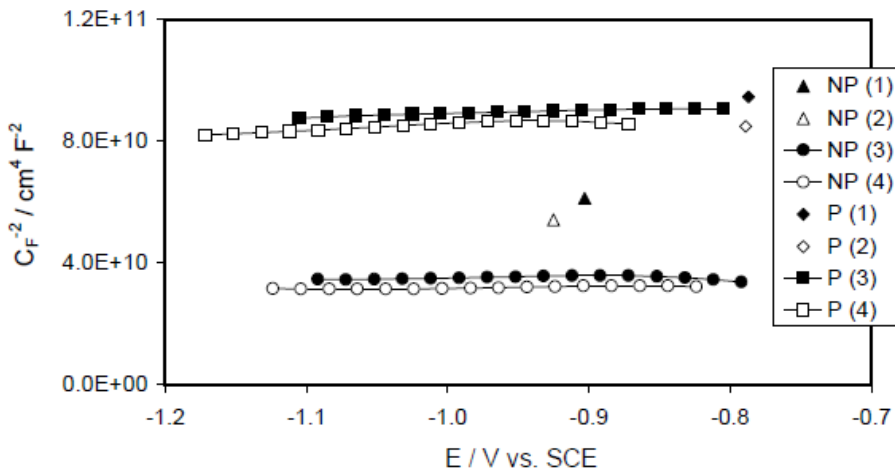


Figure 6-42. Mott-Schottky plot of the oxide film capacitance recorded for as-received NP and P systems (specimens #3 and #4) at ~330 hr of exposure. C_F^{-2} values obtained by EIS at E_{oc} of the duplicate specimens #1 and #2 at comparable exposure age are plotted as well (specimen # is denoted in parenthesis).

6.4.1.2.2 Solutions C, SW, and solution NP after surface discoloration

The information collected in this investigation does not permit to clearly identify the corrosion mechanisms associated with the activation of the aluminized surface manifested by uniform discoloration and the appearance of few small macroscopic pits. Thus, additional experiments will be needed in the future to elucidate such mechanisms.

It can be speculated, however, that the cases of development of aluminized surface discoloration (moderate in NP later on in the test and strong in C early on) may be attributed to macroscopically uniform alkaline oxidation on the aluminized surface. High pH conditions developed spontaneously in the bulk of solutions C (early in the exposure) and in solution NP (later on). The pH increase in C was not expected and it remains unsolved at present. The pH increase in NP was as predicted by the solution chemistry evolution toward equilibrium with the surrounding air in the pseudo-closed test cells. Those conditions coincided with aluminized surface discoloration, and with marked changes in the specimen corrosion rates (as shown later), indicative of activation of the aluminized surface. Thus, dissolution (with formation of soluble Al(OH)_4^- ions per Equation 6-5) of the aluminum oxide film due to alkaline conditions appears to be the main corrosion process in these cases.

It is likely that, especially in the case of solution C, which is unbuffered, alkaline oxidation was more intense around the rim of the inclusions due to the increase in pH there from local O_2 reduction. Thus, while macroscopically uniform, the corrosion may have been more localized at the microscopic, inclusion-scale level. As time progressed, the Al(OH)_4^- concentration near the metal surface may have reached a critical value so precipitation of aluminum corrosion products in the form of hydrated Al(OH)_3 , by the reaction $\text{Al(OH)}_4^- \rightarrow \text{Al(OH)}_3 + \text{OH}^-$, is expected to occur (Nisancioglu and Holtan, 1979). That event would explain the observed corrosion deposits and consequent discoloration of the entire aluminized surface in the solutions C and NP. In those solutions the observed few macro pits are deemed to be relatively inconsequential because of their small number and dimensions. The resulting large combined associated ohmic resistance of the macro pits would result on a total macro pit anodic current that would be only a small fraction of the total (Oltra and Keddum, 1988). It is emphasized that the above scenario is speculative and that, in the absence of additional experimental data, other corrosion modalities cannot be completely ruled out. In particular, there could be significant micro pit activity with internal acidic corrosion, at the inclusion-scale level. Such condition is explored later in this Chapter, where instances of discoloration of the aluminized surface in the absence of an increase in pH of the bulk solution are addressed for some of the test solutions.

The situation noted for NP and C was reversed in the case of solution SW where surface discoloration was light but the presence of a few macro pits, likely nucleated around inclusions, was notable. This condition can be explained by the strong aluminum pitting tendency in highly concentrated chloride solutions as in the solution SW (~20,000 ppm chloride concentration as opposed to only ~370 ppm in the other media used in this work). A common indicator of the pitting tendency of a particular metal in a given solution is the pitting potential E_{pit} at which pits can be initiated and sustained. As a general rule, the lower the value of E_{pit} , the easier is the development of pits as less oxidizing power is required from the electrolyte. For pure aluminum, E_{pit} is a function of chloride concentration as originally determined by Kaesche (1962) and reproduced by Bohni and Uhlig (1969) of the form:

$$E_{\text{pit}} (\text{V vs SCE}) = 0.124 \cdot \log(\text{Cl}^-) - 0.745 \quad (6-9)$$

For solution SW, the initial relatively positive E_{oc} was dictated by the active corrosion of the inclusions in the high chloride environment and had a value on the order of E_{pit} for pure aluminum (~-750 mV for 20,000 ppm) so pit initiation was promoted. Indeed, for aluminum alloys as in the case of the outer aluminized layer, the presence of inclusions may lower the value of E_{pit} relative to pure aluminum (Furuya and Soga, 1990) further facilitating initiation of pits under the initial exposure conditions. In unbuffered solutions inclusions may additionally facilitate pitting by local alkalization and subsequent corrosion of the aluminum creating a groove around the perimeter of the inclusion (Nisancioglu et al., 1981; Rynders et al., 1994; Van de Ven and Koelmans, 1976). This mechanism may not have been dominant in the strongly buffered SW solution. Upon pit formation, E_{oc} drops due to enhanced electron release by aluminum corrosion within the active pits and to some extent by aluminum alkaline oxidation (again, limited in this buffered solution). The potential drop proceeded until the current for oxygen reduction at inclusions plus hydrogen evolution inside pits matched the overall rate of aluminum oxidation (oxidation of the inclusions considered to be negligible at the more negative potential). Upon the potential drop some pits may have become inactive, eventually leading to a terminal density of pits per unit area that was sustained over long periods.

Thus, in the SW medium anodic action on the aluminized surface was likely limited to the active pits and the observed light discoloration indicated only secondary global distress in the form of vestigial alkaline oxidation. In the other solutions, having only ~370 ppm chloride concentration, the value of E_{pit} for pure aluminum is ~-650 mV. While that value was reached in some cases early on (possibly accounting for the observation of some pits in those cases), the long term E_{oc} values for NP and C were much lower (-900 mV and -830 mV) so pit growth was less likely to be sustained. In solution P, the long term E_{oc} value was ~-760 mV, but early potentials were significantly more negative so initiation was likely inhibited throughout consistent with the lack of observation of macroscopic pits in that solution.

The impedance responses for solutions C, SW, and NP (after the start of active aluminized corrosion) were also simulated using the analog equivalent circuit in Figure 6-16 with R_S and CPE_F having essentially the same meaning as before. However, the proposed meaning of the components of the circuit of the lower branch is quite different to that presented for passive aluminized steel as explained next. Per the above discussion, it is tentatively proposed that the macroscopically uniform corrosion manifested by discoloration is localized to micro sites at the inclusion scale level. Corrosion is proposed to proceed simultaneously also at macro active sites in the scale of the observed macro pits. While it is recognized that alternative scenarios are also plausible, these assumptions resulted in reasonable approximations of the overall impedance behavior, and will be considered as a first step in understanding a complex system, pending future development of experimental evidence. Per the assumptions, the local electrolytic current distribution around each micro and macro active site can be associated with a local ohmic resistance component, $R_{SL} = \sigma^{-1}/4 r_{PS}$, where r_{PS} is the radius of the active zone (Oltra and Keddam, 1988). At high enough frequencies R_{SL} will, at each active site, be significantly larger than the modulus of the capacitive impedance of the site. At those high frequencies, the resistive effects from all the sites can be approximated by a simple parallel combination given by Equation 6-10, where A_{AL} is the nominal aluminized area, N_{PS} is the number of microsities (assumed for simplicity to be all of radius r_{PS}) per cm^2 , and N_{PL} is the number of pits (assumed all to have radius r_{PL}) per cm^2 .

$$R_{AL1}^* = \sigma^{-1} (4 A_{AL})^{-1} [r_{PS} N_{PS} + r_{PL} N_{PL}]^{-1} \quad (6-10)$$

The relative contribution of macro and micro sites cannot be uniquely ascertained from the impedance response alone. However, the fit values of the impedance response for R_{AL1} , reported in Tables 6-5 through 6-8 for solutions C, NP, and SW, are in reasonable agreement with the values of R_{AL1}^* calculated for the σ values shown in Table 6-2, and $r_{PS} \sim 2 \mu m$ typical of the Fe-rich particle size, $r_{PL} \sim 100 \mu m$ for typical macropit radius, $N_{PL} < 5/cm^2$, and assuming $N_{PS} \sim 10^3/cm^2$. Within the context of the model assumptions, such value of N_{PS} suggests that only a fraction of all possible sites were active, a situation not unusual in cases of localized corrosion (Seri and Masuko, 1985).

Table 6-7
Values of Equivalent Circuit Components for Circuit Shown in Figure 6-39
Estimated from EIS Data Fit for As-Received Aluminized Steel Type 2
Specimen #1 Exposed to Solution SW

Time Hr	R_S Ω	R_{AL1} k Ω	Y_F s^{n_F}/Ω	n_F	R_{AL2} k Ω	Y_F $s^{n_{AL2}}/\Omega$	n_{AL2}	i_{corrAL} $\mu A\ cm^{-2}$
384	0.48	1.7	1.30E-03	0.92	1.8	2.46E-02	0.97	0.25
504	0.51	2.2	1.35E-03	0.92	2.1	2.47E-02	0.98	0.21
648	0.48	2	1.37E-03	0.92	2	2.54E-02	0.98	0.23
864	0.48	1.7	1.53E-03	0.92	1.4	3.10E-02	0.98	0.34
1200	0.49	1.7	1.64E-03	0.91	1.3	3.07E-02	0.97	0.35
1464	0.51	2.3	1.63E-03	0.91	1.6	3.06E-02	0.99	0.28
1680	0.5	1.9	1.67E-03	0.91	1.3	3.01E-02	0.98	0.35
1896	0.51	2.4	1.65E-03	0.91	1.5	2.98E-02	0.99	0.3
2424	0.49	2.4	1.64E-03	0.91	1.5	2.73E-02	0.97	0.3
2760	0.51	2.6	1.62E-03	0.91	1.5	2.96E-02	0.99	0.3
3096	0.51	2.7	1.63E-03	0.91	1.5	3.03E-02	0.99	0.3

Nominal specimen area $A_{AL} = 95\ cm^2$

Table 6-8
Values of Equivalent Circuit Components for Circuit Shown in Figure 6-39
Estimated from EIS Data Fit for As-Received Aluminized Steel Type 2
Specimen #1 Exposed to Solution C

Time Hr	R_S Ω	R_{AL1} k Ω	Y_F s^{n_F}/Ω	n_F	R_{AL2} k Ω	Y_F $s^{n_{AL2}}/\Omega$	n_{AL2}	i_{corrAL} $\mu A\ cm^{-2}$
24	19.5	150	4.36E-04	0.93	4.9	1.94E-03	0.93	0.09
360	17.6	9.4	9.59E-05	0.57	0.7	6.59E-03	0.69	0.63
504	18.6	12.1	6.57E-05	0.6	1.3	4.29E-03	0.72	0.34
648	18.4	13.5	5.24E-05	0.62	1.8	3.43E-03	0.74	0.26
864	19.0	15.9	4.24E-05	0.63	2.4	2.70E-03	0.76	0.19
960	18.1	15.6	4.00E-05	0.64	2.2	2.65E-03	0.76	0.21
1392	16.9	19.1	3.78E-05	0.62	2.9	2.21E-03	0.77	0.16
2400	17.5	28.9	2.89E-05	0.63	4.1	1.81E-03	0.79	0.11
3048	17.6	35.2	2.74E-05	0.63	5.2	1.65E-03	0.8	0.09

Nominal specimen area $A_{AL} = 95\ cm^2$

At high enough frequencies, the impedance is dominated by the parallel combination of R_{AL1} and the film capacitance represented by CPE_F as discussed earlier. Each active site is assumed to have a Faradaic polarization resistance and an interfacial capacitance with some degree of non ideality. Assuming that this combination has a relatively large time constant relative to that of the resistive-film capacitance considered before, the combined behavior can be represented by the discrete parallel combination of all the polarization resistances R_{AL2} and the corresponding interfacial capacitances CPE_{AL2} . The equivalent circuit fit calculations for solution C yielded small values (~ 0.89 to $\sim 3.2\ k\Omega\text{-cm}^2$) for R_{AL1} . Accordingly, R_{AL2} was in the order of the low frequency

impedance modulus ($\sim 68 \text{ k}\Omega\text{-cm}^2$ early on, $\sim 495 \text{ k}\Omega\text{-cm}^2$ near the end of the test). Both capacitive elements Y_F and Y_{AL2} had significant frequency dispersion: $n_F \sim 0.57$ to 0.63 (consistent with the highly distorted appearance of the high frequency loops in Figure 6-11) and $n_{AL2} \sim 0.69$ to 0.80 . The values of Y_F were on the order of $\sim 4.6 \cdot 10^{-6}$ to $\sim 2.9 \cdot 10^{-7} \text{ sec}^{n_F}/\Omega\text{-cm}^2$ at the end of the test and, considering the uncertainty inherent to the high frequency dispersion, the C_F values were consistent with the values obtained in the other solutions. Even though there is considerable deviation from ideally capacitive behavior, the values obtained for Y_{AL2} ($\sim 6.9 \cdot 10^{-5}$ early on to $\sim 1.7 \cdot 10^{-5} \text{ sec}^{n_{AL2}}/\Omega\text{-cm}^2$) were comparable to those obtained for solutions P and NP.

The equivalent circuit fit calculations for solution SW yielded values for R_{AL2} ranging from $\sim 173 \text{ k}\Omega\text{-cm}^2$ early on to $\sim 143 \text{ k}\Omega\text{-cm}^2$ near the end of the test), and R_{AL1} values from $\sim 160 \text{ k}\Omega\text{-cm}^2$ at the beginning to $\sim 255 \text{ k}\Omega\text{-cm}^2$ at the end of exposure. The capacitive elements Y_F and Y_{AL2} had little frequency dispersion ($n_F \sim 0.91$ and $n_{AL2} \sim 0.98$) as shown in Figure 6-10. The values for Y_F ranged from $\sim 1.4 \cdot 10^{-5}$ to $\sim 1.7 \cdot 10^{-5} \text{ sec}^{n_{AL2}}/\Omega\text{-cm}^2$ by the end of the test. The nominal capacitance C_F calculated per Equation 6-8 for a frequency $f_N = 10 \text{ Hz}$ was $\sim 10.5 \mu\text{F}/\text{cm}^2$ fairly invariant with time comparable to those obtained for the P system. For the period of aluminized surface discoloration, the values of R_{AL2} and R_{AL1} for solution NP decreased to $\sim 2 \cdot 10^5 \Omega\text{-cm}^2$ near the end of exposure. Both capacitive elements Y_F and Y_{AL2} increased after aluminized discoloration to $\sim 10^{-5} \text{ sec}^{n_{AL2}}/\Omega \text{ cm}^2$ $\sim 10^{-4} \text{ sec}^{n_{AL2}}/\Omega\text{-cm}^2$, respectively, with little frequency dispersion ($n_F \sim 0.94$ and $n_{AL2} \sim 1.00$).

6.4.2 Blemished specimens

6.4.2.1 E_{oc} trends and corrosion mechanisms

Figure 6-43 is a schematic of the typical E_{oc} evolution trends shown in Figures 6-23 through 6-29 for the LCB and SCB specimens. Macrocell assemblies, where available for the corresponding environments, had E_{oc} trends essentially identical to those of the LCB specimens and will not be discussed separately here. Shortly after exposure, the E_{oc} values of the specimens with large A_R (LCB and macrocell assemblies) in solutions P and NP ($\sim -700 \text{ mV}$ $\sim -730 \text{ mV}$) were nobler ($\sim 100\text{-}150 \text{ mV}$) than those with smaller A_R (SCB) exposed to the same solutions and comparable to those measured for the uncoupled steel specimens ($\sim -720 \text{ mV}$) exposed to solutions P and NP. Inasmuch as the active steel showed a small degree of polarizability compared with the more polarizable passive aluminized coating early on in the test, the resulting E_{oc} trends were then dominated largely by the E_{oc} of the large exposed steel corroding at a moderate rate. For the specimens with small A_R in solutions NP, P, and SW and with large A_R in SW, nobler E_{oc} values were maintained for a few hrs after immersion before the E_{oc} decay took place.

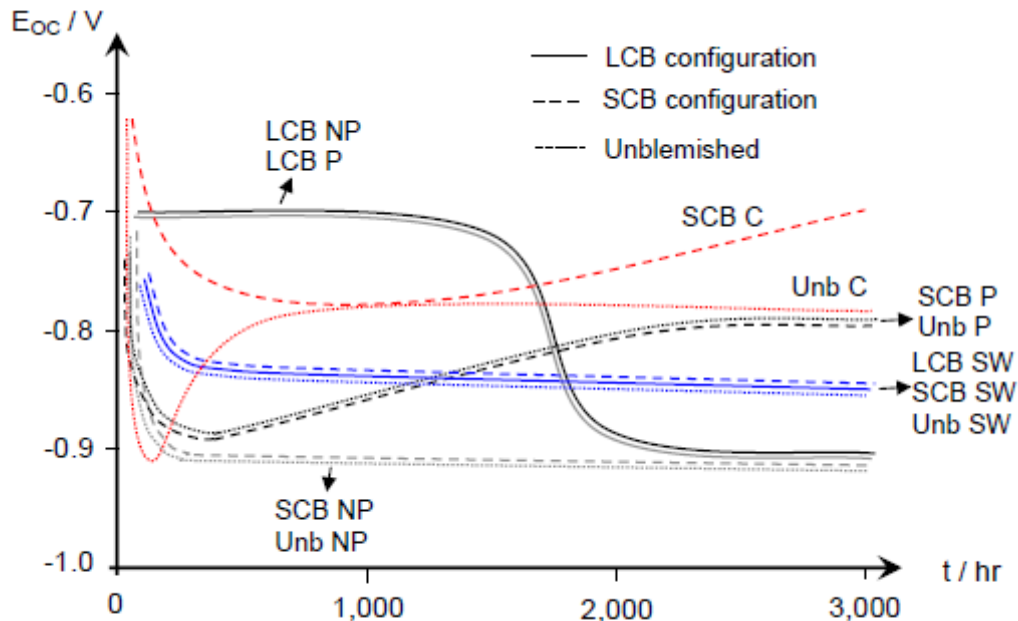


Figure 6-43. Schematic of the E_{OC} trends shown in Figures 6-23 through 6-29.

In the following paragraphs, the corrosion mechanism of blemished aluminized steel will be discussed, keeping in mind the mechanisms proposed in for the baseline unblemished material condition. The discussion is keyed to each of the solutions that were evaluated.

6.4.2.1.1 Solution P

The behavior of the small coating break (SCB) specimens was similar to that of the unblemished specimens, except that at the very beginning (first day or so) the E_{OC} was relatively positive, likely dominated by that of the small exposed base steel, which initially developed rust as mentioned above. After that period, the E_{OC} dropped to that of the unblemished system, suggesting that the rust layer on the steel acted as an obstacle to O_2 reduction there. From there on, the E_{OC} was such that the exposed steel was cathodically protected by the rest of the system (likely only a very small current is needed for that). The aluminized surface remained passive thereafter.

In specimens with a larger amount of exposed steel (LCB and macrocell assemblies), the E_{OC} was initially quite positive, dictated by the corrosion potential of the large exposed steel spot corroding at a moderate rate in the low Cl^- , scale-forming solution as mentioned above. The most striking feature of these systems was that after an interval of typically $\sim 1,500$ hr the aluminized surface experienced macroscopically uniform activation and the potential dropped dramatically, with the aluminized surface acting as a strong protecting anode to the exposed steel. The bulk solution pH remained neutral, and about $2 \mu m$ of the outer aluminized layer were macroscopically uniformly consumed in

the next 2,000 hr or so. The activation of the aluminized surface was manifested by light gray discoloration and the appearance of a few small macroscopically apparent pits. As observed for similar conditions in as-received specimens, the few active macro pits are deemed to be inconsequential because of their small number and dimensions, and their consequently large combined associated ohmic resistance, which would yield only a small fraction of the observed macrocell current. Thus, the macro pits will not be further discussed.

It is tentatively proposed that this macroscopically uniform corrosion reflects the combined presence of many micro pits distributed on a spatial scale comparable to that of the inclusions. Some alkaline dissolution is expected to have taken place as well, but likely to be of secondary importance (except during the initial activation stages as speculated further below) because of the relatively large buffering capacity of solution P. The discoloration is viewed as the result of precipitation of hydrated alumina outside the mouths of those pits. The large cathodic current at the exposed steel plus additional cathodic action at inclusions (minus the current needed to balance any alkaline dissolution) sustains the combined anodic processes at the micro pits. The extent of these effects would be expected to increase with the effective ratio of the area the blemished zone to that of the surrounding sound aluminized surface. If there is a small blemish in a large aluminized surface and the electrolytic coupling is efficient (as in the SCB specimens), then the effect on the aluminized coating would be expected to be less.

The above proposal is speculative in that the conditions needed to support that modality of pitting in a 0.01 M Cl⁻ solution such as solution P would need to be ascertained in future work. In that connection, the following questions could be formulated: (1) Why are the proposed micro pits so uniformly distributed and stable? (2) Why was there a long incubation period (effectively unlimited in the case of small coating breaks) before activation of the aluminized surface? A possible answer to (1) is that since the exposed steel zone was a strong cathode, competitive action between adjacent pits was less important than otherwise and larger pits will have less of the cathodic protection action in immediate neighbors that would have tended to lower active pit density. The cathodic action in the small break case is deemed not to be large enough to provide the required cathodic sustaining action. With regards to (2), it is speculated that some degree of alkaline dissolution is needed to start the micro pits (likely nucleated around the inclusions as previously discussed for as-received specimens). That process is initially slow due to the high potentials prevalent early in the test. The necessary degree of dissolution takes place first at the rim of the exposed steel where pH is mildly elevated through a mechanism (Evans, 1926) where the rim is a net cathode, hence more alkaline, and the center is a net anode, as confirmed by the presence of a central depression on the steel (Figure 6-18). The alkalization is mild and etching around the inclusions in the ring around the exposed steel is slow. After a long time (e.g. 1,500 hr) micro pit activation of the aluminized surface immediately around the steel finally takes place. As those

micro pits develop and local potential drops further, the active zone slowly expands away from the exposed steel, with consequent expansion of the mildly alkaline zone (but with likely enhanced local action around inclusions at the lower prevalent potentials), until micro pits affect the entire aluminized surface.

Experiments to test the validity of this speculative scenario in future research may include (and not be limited to) the following: (a) detailed local pH measurements to ascertain that mild alkalinization is a pre-micro pitting step; (b) verification that micro pits have etching around inclusions as precursors; (c) exploring solution chemistry spontaneous changes (for example due to exhaustion of buffering capacity because of interaction with air or with products of steel corrosion) as an alternative trigger to the aluminum excitation and (d) exploration of the potential for microbiology induced corrosion in the system.

6.4.2.1.2 Solution NP

In these solutions, there was also delayed onset of macroscopically uniform active corrosion in blemished specimens, although it is recalled that enhanced corrosion also developed in the as-received specimens late in the test. Some of the processes proposed above for specimens with large coating breaks in solution P are likely to be present here too, with the important difference that this solution evolves spontaneously with time to increasingly higher bulk pH values (~9.0) as result of interaction with open air. The onset of the high corrosion regime then appears to be associated with the pH increase, and alkaline oxidation is probably the dominant form of deterioration as it was in the case of the unblemished specimens but aggravated by the coupling with the strongly cathodic steel surface. Consistent with this interpretation, in both small and large coating break systems there was severe aluminized surface corrosion (with complete consumption of the outer coating layer) immediately around the perimeter of the exposed steel region as expected from the local increase in pH from O_2 reduction at the rim of the exposed steel.

Corrosion of the aluminized surface next to the rim is also expected to be aggravated by macrocell coupling since the resistive path is lowest there. As noted previously, while macroscopically uniform, the corrosion of the aluminized surface may have been more localized at the microscopic level, likely involving aluminum surrounding inclusions, where increasingly higher pH takes place because of O_2 reduction, or because of some extent of micro pit formation around those inclusions following the initial alkaline oxidation undercutting. Solution NP has significant buffering strength, but the effects of local alkalinization around inclusions may be still important because they would be additional to that of the already enhanced high bulk pH of the solution. Macro pits were few in these systems and appear to be secondary per the arguments mentioned earlier.

Finally, it is noted that in the small coating break specimens, the E_{OC} dropped long before the onset of surface discoloration and associated fast

corrosion. It is thought that the early E_{OC} drop reflected less efficient O_2 reduction at the small central steel spot, because of the early buildup of a compact steel corrosion product scale there. Since the steel area was small compared with the rest of the system, local steel polarization and consequent overall E_{OC} drop were expected to be substantial. In the large coating break specimens, the steel surface was larger, and occluding effects would have been proportionally less important.

6.4.2.1.3 Solution C

In this solution, only small coating break specimens could be evaluated, but delayed onset of active aluminum corrosion took place as well. Unlike the other solutions, solution C has negligible buffering power and the effects of local alkalization at inclusions are likely to be important. In the case of the blemished specimens the bulk solution pH remained nearly neutral, so widespread alkaline oxidation as proposed for solution NP does not appear to be the main cause of the observed discoloration. Instead, localized alkalization may have been responsible for generation of finely dispersed micro pits at the inclusion size scale, which would then represent the main form of aluminum attack. Such mechanism is subject to the same caveats noted above for the case of solution P. In solution C, however, the initiation of micro pits is facilitated by the lower buffering capacity, which may explain why activation took place even though the coating break was small. It is noted that in the case of unblemished specimens the mechanism responsible for the activation of the aluminized surface in solution C was probably a result of a temporary early surge in solution pH in the pseudo closed cell conditions used there. Those experiments should be repeated under open cell conditions for relevant comparison with the blemished specimen test results.

For completeness, the process of alkalization and undercutting of inclusions is described here in more detail, keyed to the pictorial description in Figure 6-44 adapted from sources that include Nisancioglu (1990) and Park et al. (1999). The increase in local pH from the cathodic reactions tends to elevate the OH^- ion concentration in the vicinity of the cathodic reaction locus (Figure 6-44A). Furthermore, the aluminum activation surrounding the inclusions may cause an increase in the effective area of the inclusions which further catalyses the cathodic reaction, enhancing aluminum dissolution there (Figure 6-44B). If conditions are propitious, some of the inclusions can eventually become non faradically separated as free particles from the aluminum matrix, due to undercutting enhanced-pH corrosion of the surrounding aluminum as proposed by Vukmirovic et al. (2002) (Figure 6-44C). The free particles would corrode more readily as they are not cathodically protected by the surrounding corroding matrix (Figure 6-44D), forming Fe^{2+} ions. Those ions can be electrochemically re-deposited (by $Fe^{2+} + 2e^- \rightarrow Fe$) on the surface either uniformly or, more likely, around the perimeter of the inclusions. The Fe deposition phenomenon is described in detail in Chapter 4. The plated Fe, which is a strong cathode, may

promote further aluminum corrosion if high local pH develops around the plated Fe (Figure 6-44E). As time progresses, more undercutting corrosion of aluminum and the subsequent plating of Fe is expected at many finely dispersed locations with macroscopically uniform appearance.

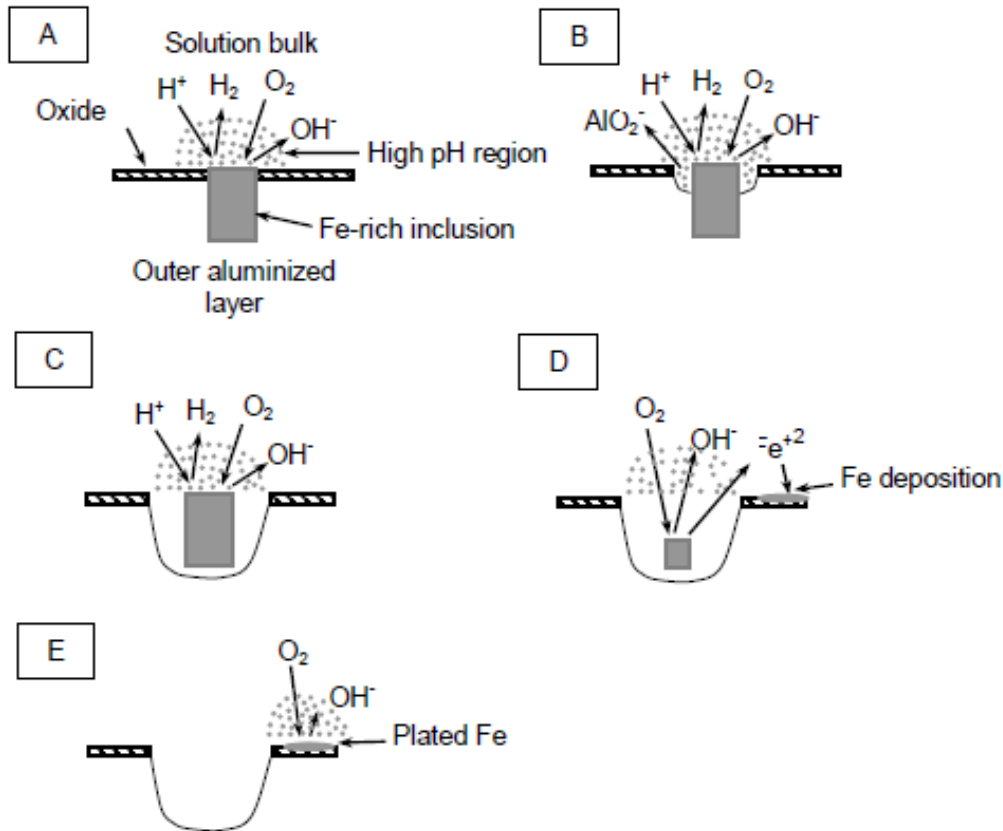


Figure 6-44. Schematic description of the corrosion mechanism of aluminized steel around the Fe-rich inclusion present in the outer aluminized layer: (A) development of high pH region around the inclusion due to the cathodic reaction, (B) corrosion initiation of the surrounding aluminum exposing larger inclusion area with consequent enhancement of the cathodic reaction, (C) detachment of the inclusion as a free particle from the aluminum matrix, (D) dissolution of the free particle and plating of Fe on aluminized surface, (E) development of a high pH region around the plated Fe (after Vukmirovic et al. (2002)).

6.4.2.1.4 Solution SW

The main aspects for the unblemished condition apply also to the blemished specimens. In the blemished condition, the E_{oc} , initially dictated by corroding inclusions and the central exposed steel zone, is thought to meet or exceed E_{pit} . The rest of process should be qualitatively the same as in the unblemished condition, except that because of coupling with the exposed steel one would have expected an even faster initiation of the pitting regime and a more positive terminal E_{oc} here. However, that was not the case in either count. That observation suggests that even for large coating breaks the cathodic current

from the exposed steel spot (3% of total area) at the operating potentials was not large compared with the total cathodic current at inclusions (initially) and inclusions plus pits (later on) on the aluminized surface. Protection of the exposed steel was excellent because activation of the aluminized surface was prompt, so the steel surface remained virtually free of corrosion products.

6.4.2.2 Interpretation of the impedance response

The analog equivalent circuit for macrocells (Figure 6-45) was simplified to be applicable to LCB and SCB configurations. The simplified equivalent circuits shown in Figure 6-46 were consistent with the assumptions presented in Section 6.4.1.2 and the observations made earlier. For the period before the E_{oc} drop, the impedance response (dominated largely by the anodic and cathodic reactions at the exposed steel as stated earlier) of the LCB specimens in solutions P and NP was modeled using solely the upper branch of the equivalent circuit in Figure 6-45 but by replacing CPE_1 by the parallel combination of CPE_1 and CPE_F (keyed as CPE^*) as shown in the simplified equivalent circuit in Figure 6-46A. This simplification is valid only if the passive aluminized portion has cathodic and anodic admittances significantly smaller than those of the active exposed steel as it is observed for the period before the E_{oc} drop. After the E_{oc} drop, however, the impedance response for all the cases was modeled using the simplified equivalent circuit in Figure 6-46B. The anodic polarization resistance R_{AL2} in Figure 6-46B represents the active aluminized corrosion (either by pitting in solution SW or by uniform corrosion in the other solutions) in parallel with the diffusional cathodic impedance of the exposed steel, under the assumption that the majority of the cathodic reaction took place there as mentioned earlier and considering that the value of the resistance R_{AL1} (representing the parallel combination of the local electrolytic current distribution around each pit associated with an ohmic resistance component) is expected to be considerably smaller than R_{AL2} so that R_{AL1} can be neglected. The element CPE^{**} in Figure 6-46B encompasses the parallel combination of CPE_1 , CPE_F , and CPE_{AL2} . After the E_{oc} drop took place, the anodic admittance of the exposed steel in all solutions were nearly zero as a result of the proximity of the system potential to that of the Fe/Fe^{2+} equilibrium reaction as mentioned earlier, thus R_{a1} is infinity.

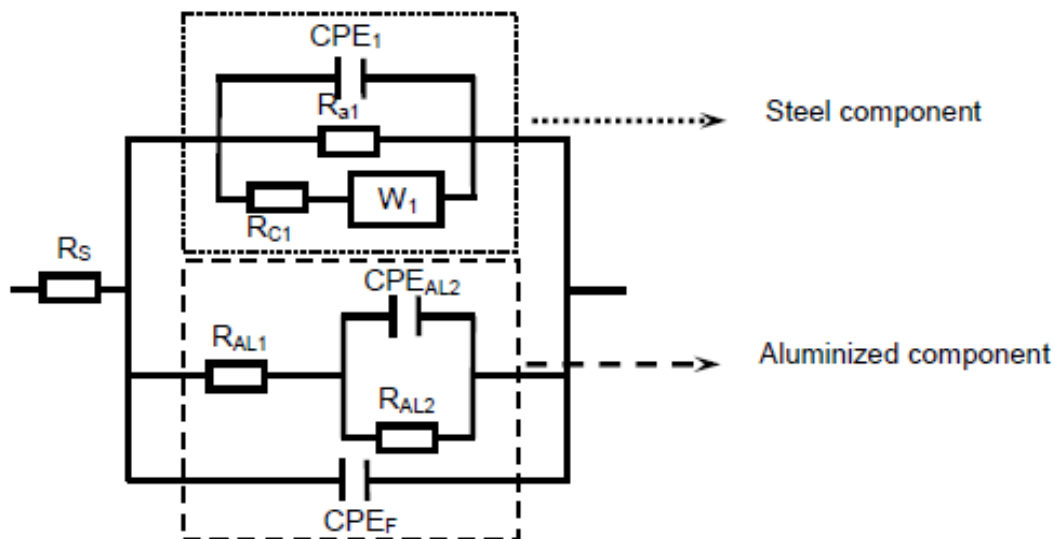


Figure 6-45. Analog equivalent circuit used to simulate the impedance response of the macrocell assemblies in solutions NP and P for the regimes before and after the Eoc drop.

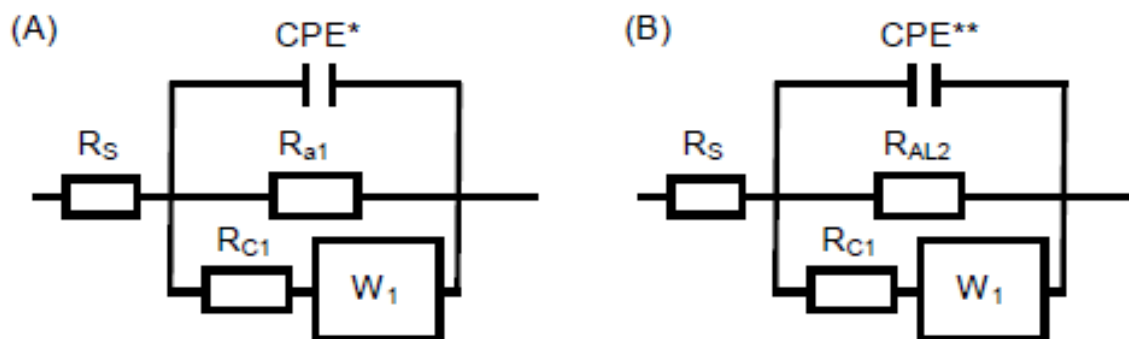


Figure 6-46. Simplified equivalent circuit used to simulate the impedance response of the LCB and SCB specimens. The circuit (A) was employed solely for the LCB specimens exposed to solutions NP and P before the Eoc drop. The circuit (B) was used for all solutions after the Eoc drop.

EIS interpretation, however, used for the macrocell assemblies and the blemished specimens do not account for the presence of non-uniform ac current distribution commonly encountered in arrangements involving interconnected dissimilar metals (Kranc and Sagüés, 1993). This experimental artifact may lead, if not properly quantified, to an incorrect EIS interpretation and therefore to inaccurate corrosion rate estimates. The results from the ac computational model indicate that negligible non uniform ac current distribution can be expected in these systems even though there is a substantial difference in the polarization

resistance of the steel and the aluminized components, especially early on in the exposure (Cáseres, 2007). Thus, the use of the analog equivalent circuits proposed in this Chapter to fit the EIS data is valid.

6.4.3 Galvanic macrocells

The E_{oc} trends and the appearance of aluminized surface discoloration of the LCB specimens in solutions NP and P were consistent with the macrocell galvanic current trends recorded for the coupled macrocell assemblies exposed to the same solutions. Measurements of galvanic currents for which data are available (P and NP, Figure 6-31) demonstrated that the outer aluminized coating layer behaved always as net anode upon contact with steel. However, the amount of macrocell current delivered by the outer coating layer in those solutions was insufficient to prevent rust formation on the steel surface early on in the exposure. This observation was also noted in the specimens with small A_R exposed to the same solutions. This weak early galvanic action could be attributed to a predominantly passive condition of the outer aluminized coating layer, as manifested by its large impedance moduli in both solutions early on.

Larger galvanic currents were expected in both solutions for the A_R examined upon signs of corrosion of the outer aluminized coating later on in the test. There were no macrocell current measurements available for solution SW, but the steel in the specimens with small A_R in that solution did not show signs of corrosion over the entire exposure time, and the steel in the specimens with large A_R in solution SW showed only very light discoloration. Those results indicate strong galvanic protection by the surrounding aluminized coating in the SW solution as well, consistent with observation of pitting of the aluminized surface and some secondary macroscopically uniform corrosion. In solution SW, the protective regime was established soon, as manifested by the drop of E_{oc} into protective potentials after only about two days of exposure for specimens with both small and large A_R .

The galvanic behavior of the specimens with small A_R in solution C showed variability, in that one of three specimens showed signs of steel corrosion but in all cases an annulus of aluminized outer layer corrosion wastage around the steel was noted. It is intriguing, however, that the relatively positive E_{oc} (~ -620 mV) in all replicate specimens existed for at least ~ 1 hr up to ~ 100 hr and clearly protective potentials did not develop until about ~ 600 hr, yet the steel showed no signs of corrosion in two cases. For those cases, however, it should be recalled that aluminized corrosion was limited to the aforementioned annulus of severe coating loss around the steel. With such tight macrocell configuration, the local steel potential could have been significantly more negative than that measured by the reference electrode several diameters away, so the recorded E_{oc} values may have been misleading.

Figure 6-47 shows the time for the initial appearance of discoloration of the aluminized surface as a function of A_R for the unblemished, blemished specimens, and the macrocell assemblies. The time to initial discoloration, obtained by averaging the results of replicate specimens for each A_R , was largest for the specimens with $A_R=0$ (unblemished specimens) in solutions NP, P, and SW and did not show significant difference when varying A_R from 3×10^{-4} (SCB specimens) to 0.03 (LCB and macrocell specimens) in solutions NP and SW. For solution P arrows in Figure 6-47 indicate minimum values since no discoloration was observed for the specimens with smaller A_R . The trends obtained for solution P, NP, and SW are not unexpected since for large A_R (large cathode/anode area ratio), enhanced macrocell action between the large exposed steel and the small aluminized coating could be established, and hence, large corrosion rates of the aluminized coating would be expected with consequent earlier appearance of aluminized surface discoloration. However, the trend for solution C is opposite to those obtained for the other solutions in that smaller time to discoloration was attained when going from unblemished condition to a finite A_R . This discrepancy for the C system can be explained by recalling that while there was a high bulk pH excursions (to ~ 9.0 , Figure 6-5) shortly after immersion for the unblemished specimens, the specimens with $A_R=3 \times 10^{-4}$ maintained a nearly neutral solution pH throughout the exposure (Figure 6-21). The early pH elevation in the unblemished specimens triggered early global de-passivation with consequent strong uniform surface discoloration of the unblemished specimens but not for the blemished specimens.

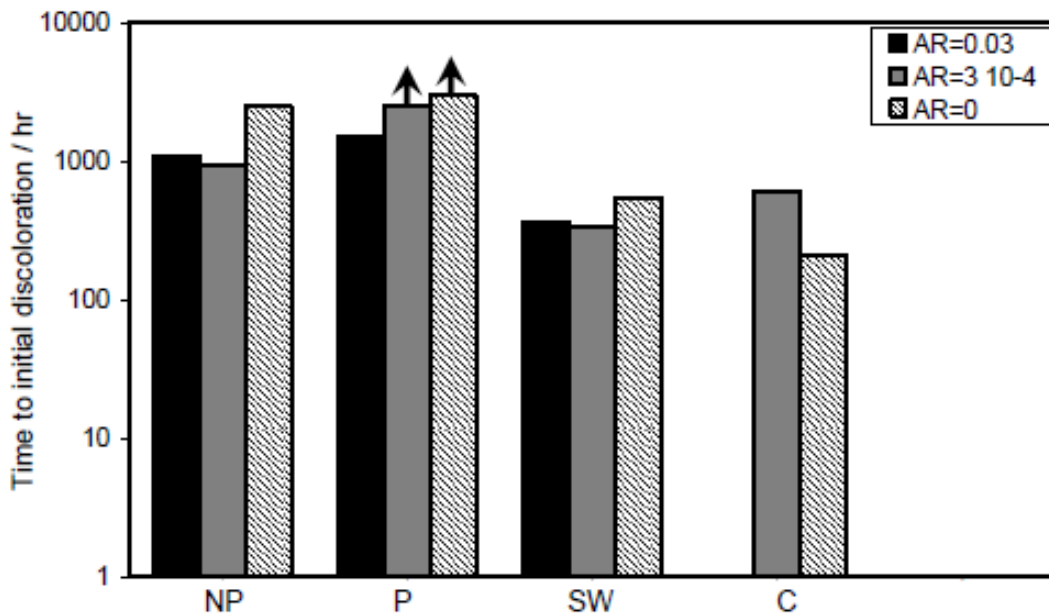


Figure 6-47. Average of the time to initial discoloration of blemished aluminized steel type 2 replicate specimens as a function of A_R . Results for $A_R = 0$ and $A_R = 3 \times 10^{-4}$ in solution P are minimum values as indicated by the arrows.

The analog equivalent circuit chosen to simulate the impedance response of the macrocell assemblies is shown in Figure 6-45. It is assumed that the overall interfacial admittance can be divided into two branches as explained below.

The upper branch in Figure 6-45 is for the exposed steel (and the individual steel specimens as well) and describes scenarios for both before and after the E_{oc} drop. For the period before the E_{oc} drop, the circuit consists of polarization admittance (R_{a1}^{-1}) for the activation polarization of the anodic reaction ($Fe \rightarrow Fe^{2+} + 2e^-$ in parallel with a constant phase angle element CPE_1 representing the interfacial charge storage at the steel surface, and an admittance (series combination of the polarization admittance $R_{c1}^{-1} = 2.3 i_{c1}/\beta_{c1}$ and the diffusional component W_1) governed by activation/concentration polarization of the cathodic reaction. The latter is likely to be $O_2 + 2H_2O + 4e^- \rightarrow 4OH^-$ and it is assumed to be so and, for simplicity, to occur under simple one dimensional condition. The resulting impedance for the exposed steel has the form $Z_1(\omega) = [1/R_{a1} + 1/Z_{C1}(\omega)]^{-1}$ where $R_{a1}^{-1} = 2.3 i_{a1}/\beta_{a1}$ and $Z_{C1}^{-1}(\omega) = 2.3 i_{c1}/\beta_{c1} + 2.3 (i_L - i_{c1}) \beta_{c1}^{-1} (j\omega \delta^2 D^{-1})^{0.5} (\tanh(j\omega \delta^2 D^{-1})^{0.5})^{-1}$ (Bard and Faulkner, 2000), where i_{a1} and i_{c1} are the anodic and cathodic current densities, respectively. After the E_{oc} drop, the exposed steel (which may or may not have corrosion products on the surface depending on the case) is polarized down to a potential level where the Fe/Fe^{2+} reaction is near equilibrium (Pourbaix, 1974).

The corresponding equilibrium current density is expected to be small with correspondingly small admittance. The remaining reaction of importance is expected to be O_2 reduction, occurring at a diffusion-limited, potential-independent value. The lower branch of the equivalent circuit in Figure 6-45 is for the aluminized component and describes scenarios for both before and after active corrosion of the outer aluminized coating layer.

6.4.4 Computation of the nominal corrosion current density

6.4.4.1 As-received specimens

The following nominal corrosion current density i_{corrAL} estimates are consistent with the proposed corrosion mechanisms and the associated analog equivalent circuit presented earlier. Figure 6-48 illustrates the i_{corrAL} evolution as a function of exposure time. Comparable results were recorded for the duplicate specimens (Cáseres, 2007).

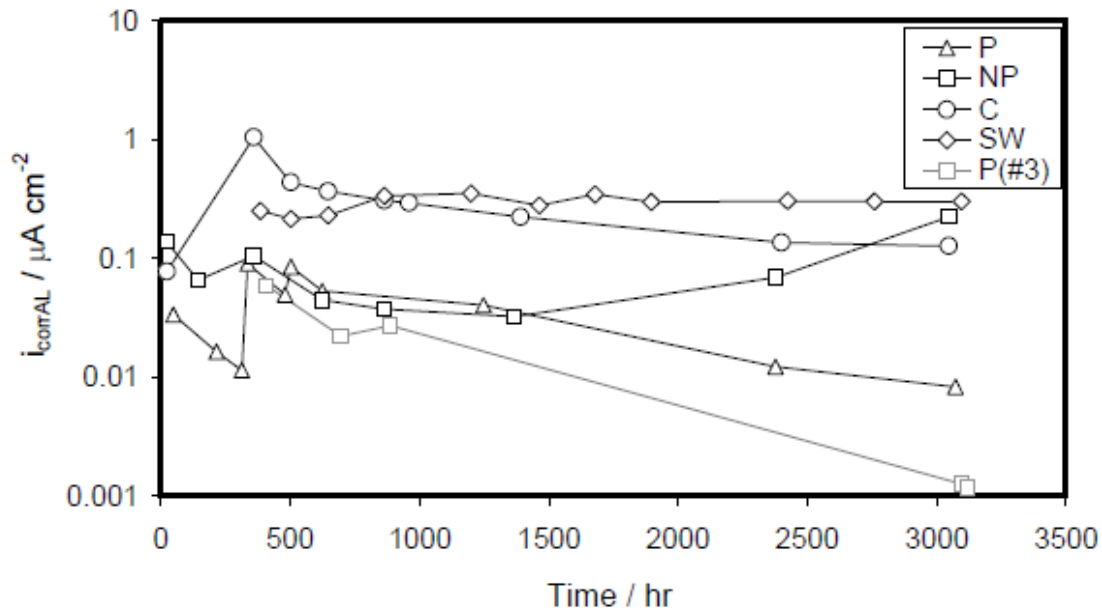


Figure 6-48. Nominal corrosion current density evolution for as-received aluminized steel type 2 specimens (#1) in all media. No extra powdered CaCO_3 was added to the triplicate specimen in solution P (#3).

For specimens in solution P over the entire test exposure and for the specimens in solution NP for the period before the appearance of uniform discoloration, a working assumption is made that the high frequency limit resistance (R_{AL1}) is approximately the same as that of a cathodic reaction under purely activation control, having a Tafel slope value $\beta_{C2} \sim 200$ mV. The value of β_{C2} is representative to those reported for likely coupled cathodic reactions on aluminum (Armstrong and Braham, 1996) and also comparable to those obtained from cyclical polarization tests for unblemished aluminized steel exposed to solution P. Since the rate of the anodic reaction was considered to be nearly potential-independent, and hence its admittance negligible, the nominal corrosion current density i_{corrAL} can then be obtained from the Stern-Geary relationship applied to the cathodic reaction only (Stern and Geary, 1957):

$$i_{corrAL} \sim \beta_{C2} (2.3 R_{AL1})^{-1} \quad (6-11)$$

To estimate i_{corrAL} for solutions C and SW, and for solution NP after the start of aluminized active corrosion, the same working assumptions were made as before but using only the value of R_{AL2} and considering for simplicity that both anodic and cathodic reaction polarizability have the same anodic and cathodic Tafel slopes $\beta_{C2} = \beta_{a2}$ and equal to 200 mV as stated previously. Thus, the i_{corrAL} under those conditions is (Lorenz and Mansfeld, 1981):

$$i_{corrAL} \sim 0.5 \beta_{C2} (2.3 R_{AL2})^{-1} \quad (6-12)$$

The values of i_{corrAL} were extremely small for solution P ($\sim 0.03 \mu\text{A}/\text{cm}^2$ early on to $\sim 0.008 \mu\text{A}/\text{cm}^2$ by the end of exposure). However, the first addition of excess CaCO_3 to specimens #1 and #2 caused a momentary i_{corrAL} increase to $\sim 0.1 \mu\text{A}/\text{cm}^2$ not observable after the next CaCO_3 addition. Similarly, i_{corrAL} values for the specimen #3 in P (no extra CaCO_3 added) were extremely small ~ 0.06 early on to $\sim 0.001 \mu\text{A}/\text{cm}^2$ by the end of the test. The values of i_{corrAL} of the duplicate specimens in solution NP before the start of aluminized discoloration were $\sim 0.15 \mu\text{A}/\text{cm}^2$ for both at the beginning, decreasing to $\sim 0.03 \mu\text{A}/\text{cm}^2$ after $\sim 1,400$ hr. The i_{corrAL} values for solution P and for solution NP for the period before the onset of aluminized discoloration were consistent with visual observation of corrosion-free aluminized steel surface.

For solution NP for the period after the onset of active aluminized corrosion, the i_{corrAL} of the duplicate specimens showed an increasing trend to reach by the end of the test a modest i_{corrAL} of $\sim 0.2 \mu\text{A}/\text{cm}^2$, in agreement with moderate uniform aluminized discoloration. For solution C, the duplicate specimens had i_{corrAL} values ranging from $\sim 1.05 \mu\text{A}/\text{cm}^2$ early on to $\sim 0.13 \mu\text{A}/\text{cm}^2$ after $\sim 3,000$ hr. As expected, the highest corrosion current density coincided with the appearance of uniform strong surface discoloration. The smaller i_{corrAL} values in C recorded later on are in agreement with the decrease of the solution pH back to the range of aluminum passivity. The i_{corrAL} values for the duplicate specimens in solution SW were nearly constant with time reaching $\sim 0.3 \mu\text{A}/\text{cm}^2$ at the end of exposure, in reasonable agreement with the results reported by Johnsson and Nordhag (1984) for aluminized steel type 2 exposed to natural seawater at room temperature.

It is important to note that the above estimates reflect the application of a tentative interpretation of the impedance response, and that alternative scenarios should be examined in future research. Efforts should be aimed in particular at ascertaining to which extent the macroscopically uniform corrosion may be localized at the inclusion scale level.

6.4.4.2 Blemished

Per the assumptions above and the observations made earlier, for the period before the onset of the E_{OC} drop a rough estimation of the nominal corrosion current density for the exposed steel i_{corrFE} was made by computing the charge transfer resistance $R_{\text{CT}} = [R_{\text{a1}}^{-1} + R_1^{-1}]^{-1}$, where the resistors R_{a1} and R_{C1} were obtained by fitting the EIS data using the analog equivalent circuits shown in Figures 6-45 (upper branch for the macrocell assemblies and the individual steel specimens) and 6-46A (for the LCB specimens in NP and P systems). (For before the E_{OC} drop regime, values of i_{corrFE} for the LCB specimens in SW and the SCB specimens in all test solutions are not available, since all EIS measurements in those cases were taken after E_{OC} had reached an arbitrary potential < -800 mV. In that case, the values of i_{corrFE} were expected to be nearly

zero as a result of the proximity of the system potential to that of the Fe/Fe²⁺ equilibrium reaction as mentioned earlier.)

From the Stern-Geary relationship (Stern and Geary, 1957), the values of i_{corrFE} are computed from Equation 6-13, where A_{FE} is the nominal steel area and the parameter B is called the Stern-Geary constant equal to $\beta_{a1}\beta_{c1}[2.3(\beta_{a1}+\beta_{c1})]^{-1}$ for the assumed values of the Tafel slopes $\beta_{a1}=60$ mV/dec and $\beta_{c1}=120$ mV/dec (Kaesche, 1985).

$$i_{\text{corrFE}} \sim B (A_{\text{FE}}R_{\text{CT}})^{-1} \quad (6-13)$$

For the macrocell assemblies in solutions NP and P for the period before the E_{OC} drop, the nominal corrosion current density for the aluminized component i_{corrAL} was computed using Equation 6-11 following the assumptions presented for passive unblemished aluminized steel. Values of R_{AL1} computed here were obtained by fitting the EIS data using solely the lower branch of the analog equivalent circuit in Figure 6-45. Values of i_{corrAL} for the LCB and the SCB specimens in all test solutions before EOC drop are not available, since all EIS measurements in those cases were taken either after EOC had reached an arbitrary potential <-800 mV or the overall impedance response was largely dominated by the small impedance of the active steel compared to the much larger impedance of the passive aluminized portion.

For the period after active aluminized surface corrosion, the values of i_{corrAL} in all cases were computed using Equation 6-12 with values of R_{AL2} obtained by fitting the EIS data using the corresponding simplified analog equivalent circuits shown in Figures 6-45 and 6-46B. The time evolutions of i_{corrFE} and i_{corrAL} for the blemished specimens and the macrocell assemblies is shown in Figures 6-49 through 6-52 with the EIS parameters shown in Tables 6-9 through 6-11.

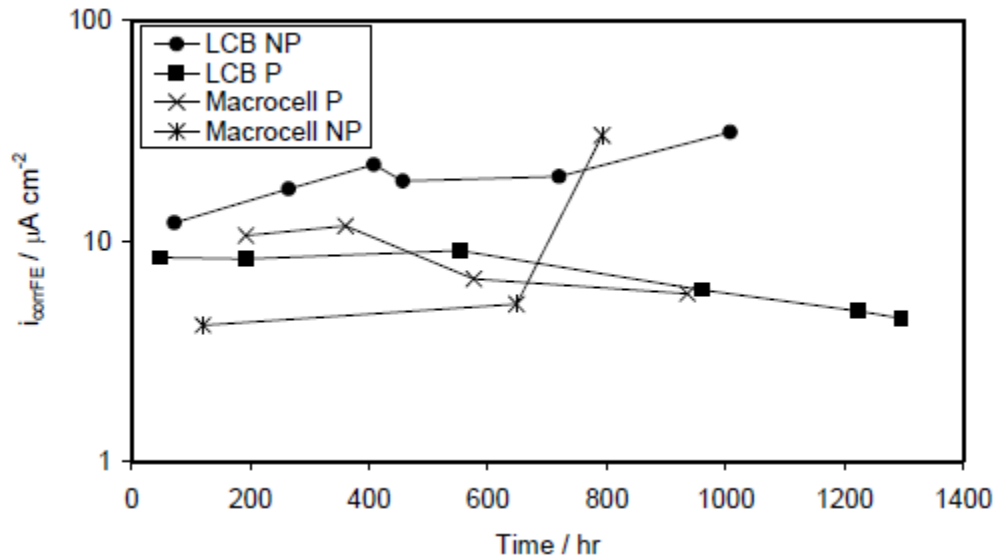


Figure 6-49. Evolution of i_{corrFE} of the exposed steel portion for the LCB specimens (#1) in solutions NP and P obtained per analog equivalent circuit shown in Figure 6-46A and the steel component in the macrocell assemblies obtained per the upper branch of the analog equivalent circuit in Figure 6-45.

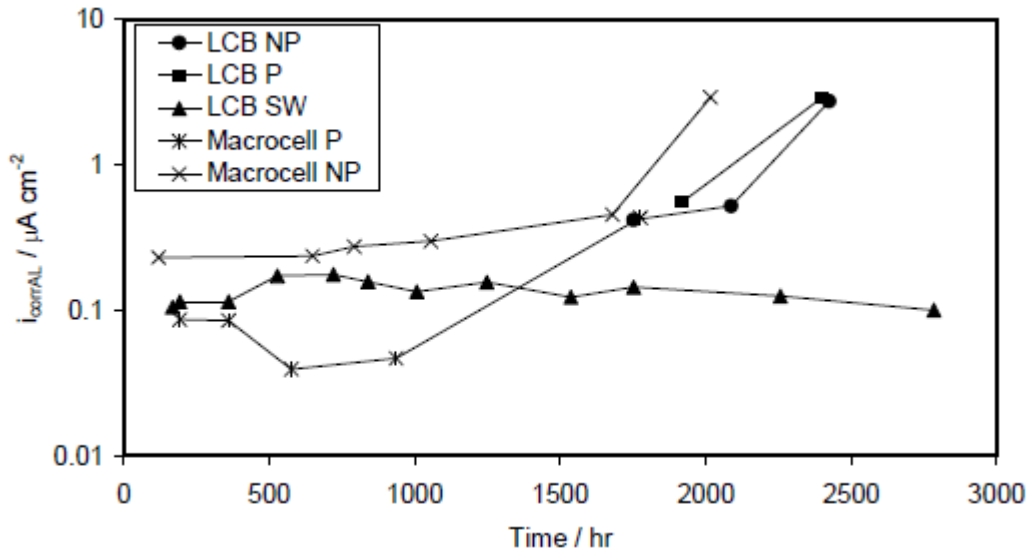


Figure 6-50. Evolution of i_{corrAL} of the aluminized portion for the LCB specimens (#1) obtained using the analog equivalent circuit shown in Figure 6-46B and the aluminized component in the macrocell assemblies using the lower branch of the analog equivalent circuit shown in Figure 6-45.

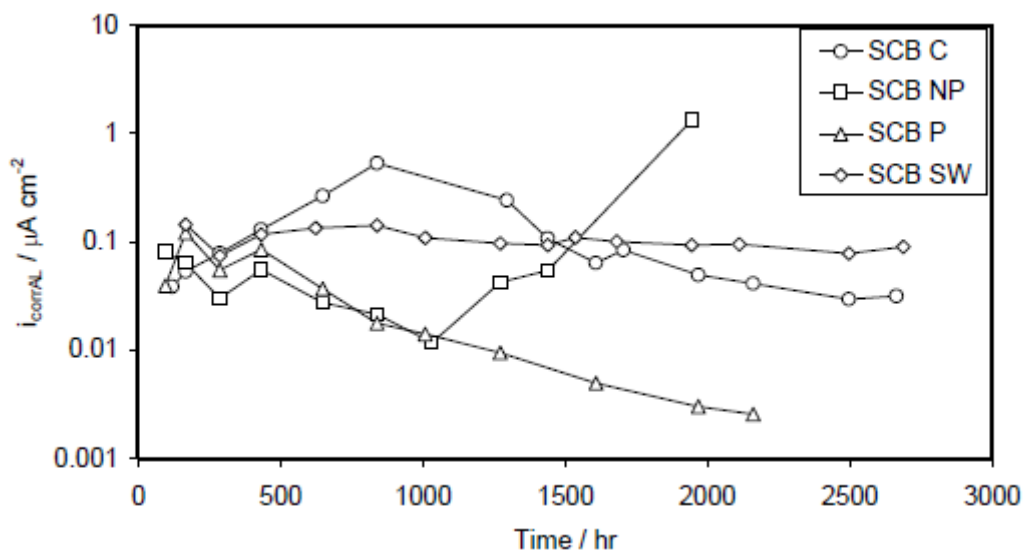


Figure 6-51. Evolution of i_{corrAL} of the aluminized portion for the SCB specimens (#1) obtained using the analog equivalent circuit shown in Figure 6-46B.

For the steel portion in the LCB specimens (Figure 6-49), the values of i_{corrFE} ranged from $\sim 10 \mu\text{A}/\text{cm}^2$ early on to $\sim 30 \mu\text{A}/\text{cm}^2$ by the end of the positive E_{OC} trend for NP, and from $\sim 10 \mu\text{A}/\text{cm}^2$ early on to $\sim 5 \mu\text{A}/\text{cm}^2$ for solution P. Those values were roughly in agreement with the results of the steel component in the macrocell assemblies and the individual steel specimens exposed to the same solutions and also consistent with the observed corrosion deposits over the steel surface in both solutions early on in the exposure.

For the regime after the E_{OC} drop, the i_{corrAL} values of the LCB specimens (Figure 6-50) were modest for solutions P and NP ($\sim 3 \mu\text{A}/\text{cm}^2$) and smaller for solution SW ($\sim 0.1 \mu\text{A}/\text{cm}^2$), consistent with the appearance of moderate/strong aluminized surface discoloration for P and NP, and light in SW. The i_{corrAL} values for the aluminized component in the macrocell assemblies (Figure 6-50) were $\sim 0.5 \mu\text{A}/\text{cm}^2$ and $\sim 5.1 \mu\text{A}/\text{cm}^2$ for solutions P and NP, respectively, also consistent with moderate in P and strong aluminized surface discoloration in NP. For the SCB specimens (Figure 6-51), the i_{corrAL} value obtained by the end of exposure was extremely small for P ($\sim 0.003 \mu\text{A}/\text{cm}^2$), consistent with absence of aluminized corrosion throughout the entire test exposure. Values of i_{corrAL} by the end of exposure were $\sim 1.5 \mu\text{A}/\text{cm}^2$, $\sim 0.1 \mu\text{A}/\text{cm}^2$, and $\sim 0.03 \mu\text{A}/\text{cm}^2$, for NP, SW, and C, respectively.

Table 6-9
Evolution of the Nominal Corrosion Current Density for LCB Specimens

Solution NP (#1) – Before the E _{OC} drop								
Time hr	R _S Ω	W ₁ Ω	R _{C1} Ω	R _{a1} Ω	Y* sec ^{n*} Ω ⁻¹	n*	I _{corrFE} μA cm ⁻²	I _{corrAL} μA cm ⁻²
72	8.30	44.4	682.5	1378	1.65E-03	0.68	12.13	Passive
264	8.48	79.2	401.2	1631	1.67E-03	0.70	17.20	
408	8.42	55.6	294.5	1636	1.71E-03	0.70	22.19	
456	6.11	11.1	358.6	1689	2.04E-03	0.64	18.72	
720	7.01	10.9	345.3	1556	1.83E-03	0.68	19.60	
1008	8.75	14.4	203.2	1430	1.50E-03	0.75	31.13	
Solution NP (#1) – After the E _{OC} drop								
Time hr	R _S Ω	W ₁ Ω	R _{C1} Ω	R _{a1} Ω	Y* sec ^{n*} Ω ⁻¹	n*	I _{corrFE} μA cm ⁻²	I _{corrAL} μA cm ⁻²
1752	9.05	9.0	499	1123	2.36E-3	0.81	Immune	0.42
2088	9.03	8.8	470	902	2.34E-3	0.83		0.52
2424	9.05	8.7	456	172.4	2.13E-3	0.86		2.75
Solution P (#1) – Before the E _{OC} drop								
Time hr	R _S Ω	W ₁ Ω	R _{C1} Ω	R _{a1} Ω	Y* sec ^{n*} Ω ⁻¹	n*	I _{corrFE} μA cm ⁻²	I _{corrAL} μA cm ⁻²
48	6.8	74.5	3508	808	1.05E-3	0.78	8.44	Passive
192	7.5	55.6	2832	873	9.77E-4	0.80	8.30	
552	7.3	5.0	1634	980	1.13E-3	0.77	9.04	
960	7.4	4.8	2418	1496	1.01E-3	0.78	5.99	
1224	7.7	3.3	3177	1805	8.99E-4	0.80	4.81	
Solution P (#1) – After the E _{OC} drop								
Time hr	R _S Ω	W ₁ Ω	R _{C1} Ω	R _{a1} Ω	Y* sec ^{n*} Ω ⁻¹	n*	I _{corrFE} μA cm ⁻²	I _{corrAL} μA cm ⁻²
1920	8.1	3.3	546	843	3.23E-03	0.85	Immune	0.56
2400	8.1	3.3	436	163	7.22E-03	0.85		2.91

Table 6-9 (Continued)
Evolution of the Nominal Corrosion Current Density for LCB Specimens

Solution SW (#1) – After the E _{OC} drop								
Time hr	R _S Ω	W ₁ Ω	R _{C1} Ω	R _{a1} Ω	Y [*] sec ^{n*} Ω ⁻¹	η [*]	I _{corrFE} μA cm ⁻²	I _{corrAL} μA cm ⁻²
168	0.23	19.5	2602	4452	1.39E-03	0.90	Immune	0.11
192	0.23	33.6	2796	4108	2.02E-03	0.87		0.12
360	0.23	18.6	2824	4080	1.41E-03	0.92		0.12
528	0.22	13.6	2509	2718	1.54E-03	0.92		0.17
720	0.23	14.0	2828	2669	1.61E-03	0.92		0.18
840	0.24	14.1	3448	2988	1.66E-03	0.92		0.16
1008	0.24	14.6	4199	3499	1.68E-03	0.92		0.14
1248	0.24	11.9	3933	3012	1.70E-03	0.92		0.16
1536	0.25	12.5	5224	3819	1.68E-03	0.92		0.12
1752	0.24	12.6	4450	3267	1.70E-03	0.92		0.14
2256	0.24	13.8	5534	3761	1.67E-03	0.92		0.13
2784	0.24	14.2	7125	4704	1.64E-03	0.91		0.10

For specimen #1 exposed to solutions NP, P, and SW. The parameters of the simplified analog equivalent circuits shown in Figure 6-46 are also included. Immune condition for the exposed steel was assumed when the system EOC reached <-800 mV. Passive condition for the outer aluminized coating was assumed when the aluminized surface was bright with no visible pits.

Table 6-10
Evolution of the Nominal Corrosion Current Density for the SCB Specimens

Solution NP (#1)								
Time hr	R _S Ω	W ₁ Ω	R _{C1} Ω	R _{AL2} Ω	Y ^{**} sec ^{n**} Ω ⁻¹	n ^{**}	I _{corrFE} μA cm ⁻²	I _{corrAL} μA cm ⁻²
96	6.8	274	4080	5694	5.97E-04	0.91	Immune	0.08
168	6.7	211	3236	7159	6.39E-04	0.91		0.06
288	6.8	456	7244	15250	6.78E-04	0.91		0.03
432	7.0	333	3898	8293	7.72E-04	0.91		0.06
648	6.9	974	11570	16650	7.81E-04	0.91		0.03
840	7.2	1196	16520	21460	8.16E-04	0.91		0.02
1032	7.3	1819	37620	38930	8.15E-04	0.91		0.01
1272	7.0	1046	12820	10820	8.91E-04	0.91		0.04
1440	7.2	780	10510	8455	9.32E-04	0.92		0.05
1944	7.2	846	1231	343	1.30E-03	0.93		1.33
Solution P (#1)								
Time hr	R _S Ω	W ₁ Ω	R _{C1} kΩ	R _{AL2} kΩ	Y ^{**} sec ^{n**} Ω ⁻¹	n ^{**}	I _{corrFE} μA cm ⁻²	I _{corrAL} μA cm ⁻²
96	7.1	74.5	44.5	55.4	3.59E-04	0.92	Immune	0.017
168	7.5	62.2	16.1	15.8	4.25E-04	0.92		0.058
288	7.9	121.1	38.7	35.1	4.67E-04	0.93		0.026
432	7.9	64.7	27.2	20.3	5.03E-04	0.92		0.045
648	8.2	100.6	79.7	43.6	5.15E-04	0.91		0.021
840	8.1	170.4	288.9	71.9	5.18E-04	0.92		0.013
1008	8.1	157.4	533.4	86.9	5.09E-04	0.92		0.011
1272	8.3	291.3	2921	112.5	5.06E-04	0.92		0.008
1440	8.5	539.1	1.5E5	189.1	4.94E-04	0.92		0.005
1704	7.9	292.6	1.7E5	156.4	4.98E-03	0.92		0.006
2160	8.2	335.2	1.9E5	372.2	4.83E-04	0.93		0.002

Table 6-10 (Continued)
Evolution of the Nominal Corrosion Current Density for the SCB Specimens

Solution SW (#1)								
Time hr	R _s Ω	W ₁ Ω	R _{C1} Ω	R _{AL2} Ω	Y** sec ^{n**} Ω ⁻¹	n**	I _{corrFE} μA cm ⁻²	I _{corrAL} μA cm ⁻²
96	0.32	18.1	2216	3144	8.29E-04	0.92	Immune	0.15
168	0.35	11.6	3718	6144	9.27E-04	0.92		0.07
288	0.35	5.9	4251	3895	1.20E-03	0.91		0.12
432	0.35	6.2	5031	3419	1.39E-03	0.90		0.13
624	0.35	6.8	5256	3208	1.49E-03	0.90		0.14
840	0.37	7.8	7455	4202	1.51E-03	0.90		0.11
1272	0.37	9.0	9400	4698	1.48E-03	0.90		0.10
1440	0.39	9.4	10420	4907	1.45E-03	0.90		0.09
1536	0.35	9.1	8856	4148	1.47E-03	0.90		0.11
1680	0.35	8.9	8838	4539	1.45E-03	0.90		0.10
1944	0.37	9.6	10590	4871	1.40E-03	0.90		0.09
2112	0.37	9.7	10560	4816	1.40E-03	0.90		0.10
2496	0.37	9.7	14450	5881	1.37E-03	0.90		0.08
2688	0.37	4.7	11350	5062	1.38E-03	0.90		0.09
Solution C (#1)								
Time hr	R _s Ω	W ₁ Ω	R _{C1} Ω	R _{AL2} Ω	Y** sec ^{n**} Ω ⁻¹	n**	I _{corrFE} μA cm ⁻²	I _{corrAL} μA cm ⁻²
120	11.3	827.1	28220	11910	3.67E-04	0.91		0.04
168	10.6	553.1	11440	8569	4.14E-04	0.91		0.05
288	10.4	278.7	3489	5792	6.05E-04	0.91		0.08
432	10.2	182.5	2137	3519	8.64E-04	0.92		0.13
648	10.1	120.2	1290	1715	1.29E-03	0.93		0.27
840	10.3	54.9	660	858	1.80E-03	0.94		0.53
1296	10.4	71.0	1853	1892	2.61E-03	0.90		0.24
1440	10.4	113.7	4506	4228	2.35E-03	0.91		0.11
1608	10.7	108.6	8494	7126	2.21E-03	0.91		0.06
1704	10.3	70.5	7674	5444	2.25E-03	0.91		0.08
1968	10.9	170.4	13860	9269	2.18E-03	0.91		0.05
2160	10.6	181.8	13180	11060	2.16E-03	0.91		0.04
2496	10.9	226.3	16780	15450	2.09E-03	0.91		0.03
2664	10.5	219.9	16640	14470	2.09E-03	0.91		0.03

For specimen #1 exposed to solutions NP, P, SW, and C. The parameters of the simplified analog equivalent circuits shown in Figure 6-46 are also included. Immune condition for the exposed steel was assumed when the system E_{OC} reached <-800 mV. Passive condition for the outer aluminized coating was assumed when the aluminized surface was bright with no visible pits.

Table 6-11
EIS Parameters from Analog Equivalent Circuit and Nominal Corrosion
Current Density for Aluminized and Steel Components in the Macrocell
Assembly

Specimen	Time hr		Sol	R _S Ω	R _{a1} kΩ	R _{C1} kΩ	W ₁ Ω sec ^{-0.5}	Y ₁ sec ^{n*} Ω ⁻¹	n ₁	I _{corrFE} μA cm ⁻²	
Steel component	Before E _{oc} drop	900	P	175.1	0.9	0.6	17.9	3.2E-03	0.75	16.1	
		900	NP	59.8	1.2	0.3	51.1	5.0E-03	0.55	21.2	
	After E _{oc} drop	1780	P	210.6	3.8	0.1	5.1	6.4E-03	0.75	Immune	
		1780	NP	50.1	3.3	0.2	54.4	1.1E-03	0.55		
Specimen	Time hr		Sol	R _S Ω	R _{AL1} kΩ	Y _{AL2} sec ⁿ² Ω ⁻¹	n _{AL2}	R _{AL2} kΩ	Y _F sec ^{nF} Ω ⁻¹	n _F	I _{corrAL} μA cm ⁻²
Aluminum component	Before E _{oc} drop	900	P	57.4	9.9	9.8E-04	0.98	71.2	5.2E-04	0.94	0.09
		900	NP	16.5	6.9	3.4E-03	0.99	24.6	7.9E-04	0.94	0.13
	After E _{oc} drop	1780	P	55.7	0.2	3.2E-02	0.84	1.0	1.3E-03	1.00	0.46
		1780	NP	16.7	0.05	1.3E-01	0.80	0.09	1.2E-02	0.85	5.08

For analog equivalent circuit shown in Figure 6-45.

The integrated aluminized coating loss, during the exposure period from t=0 to t_f where t_f is the time for the end of the test, was evaluated by using the time evolution of i_{corr}(t_i) obtained from the EIS measurements where i=1 to n represents each EIS measurement. The integrated material loss was then calculated from the charge density according to Equation 6-14.

$$Q = \sum_{i=1}^{n-1} i_{\text{corri}} \cdot (t_{i+1} - t_i) + i_{\text{corr1}} \cdot t_1 + i_{\text{corrn}} \cdot (t_f - t_n) \quad (6-14)$$

The integrated coating loss during exposure is L_{INT} = Q A_W (nFρ)⁻¹, where A_W is the aluminum atomic weight and ρ is the aluminum density. Figure 6-52 compares the integrated coating loss obtained by EIS and the nominal coating thickness loss determined by magnetic coating thickness measurements in a log-log representation. The comparison shows reasonable agreement between both estimates, in support of the assumptions made for interpretation of the EIS data. Figure 6-53 shows a metallographic analysis conducted on the LCB specimen #1 exposed to solution NP. Corrosion deposits noted on top of the outer aluminized layer were ~10-15 μm thick which yields a nominal corrosion rate of ~40 μm /yr, using the appropriate exposure time. This result is in good agreement with that determined by magnetic coating measurements and EIS measurements. The magnetic coating thickness measurement, however, does not have the capability

to detect pitting loss in the case of e.g. the solution SW, where pitting was the main form of corrosion. As a result, measurements of magnetic coating thickness may underestimate the actual corrosion rates in those cases.

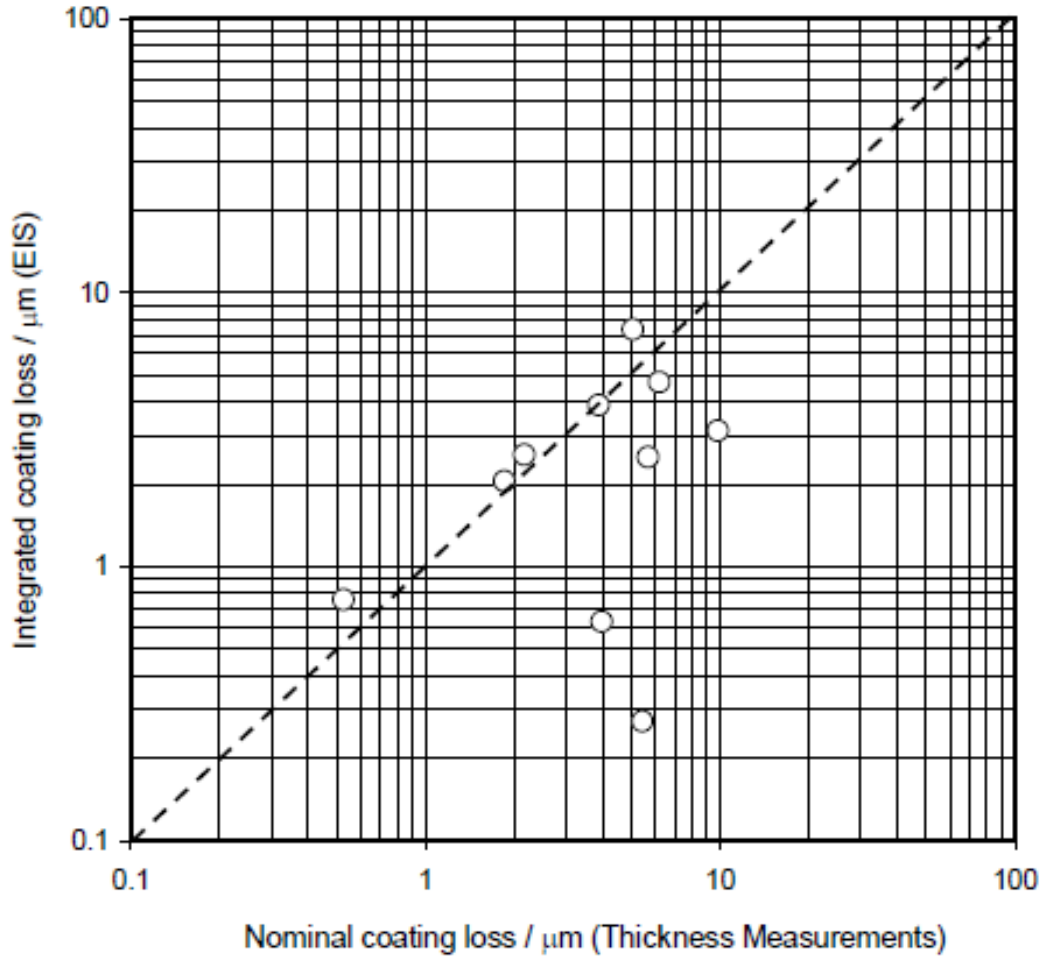


Figure 6-52. Correlation between the integrated coating loss obtained by EIS and the nominal coating thickness loss determined by magnetic coating thickness measurements for selected specimens shown in Table 6-4.

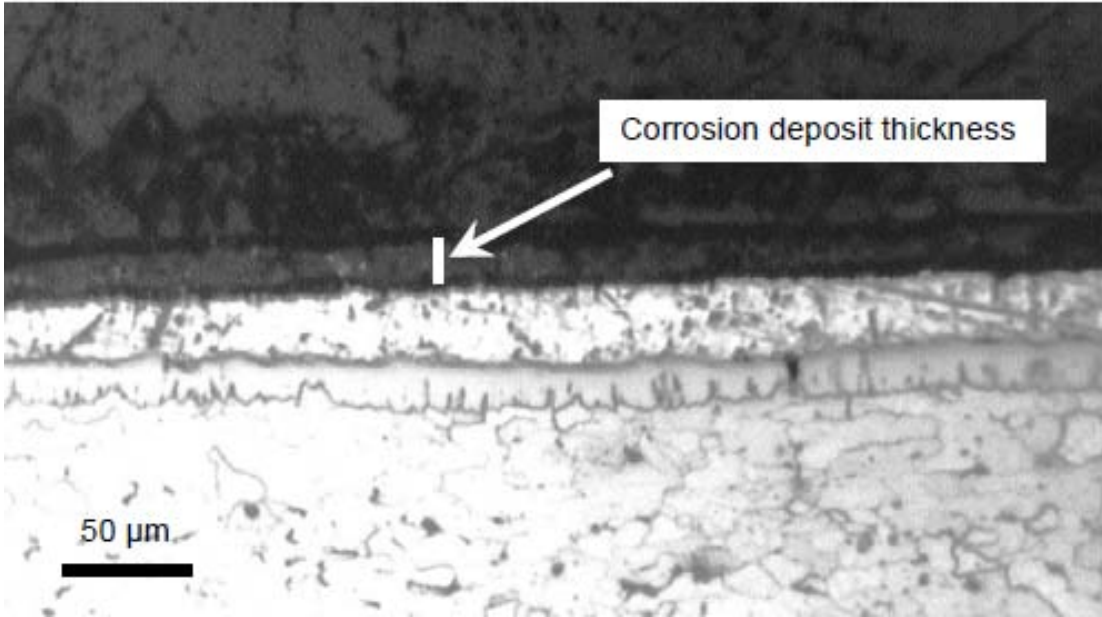


Figure 6-53. Cross section of the LCB specimen #1 exposed to solution NP. The dark outer layer covering the entire outer aluminized coating layer corresponds to corrosion deposits of ~10-15 μm thick.

6.5 Summary and Conclusions

- In >3,000 hr tests, as-received aluminized steel type 2 showed extremely low nominal corrosion rates ($<\sim 0.008 \mu\text{A}/\text{cm}^2$) by the end of the test period in an environment with moderate chloride content but of high carbonate precipitating tendencies (the solution P), supporting prior evidence in favor of a carbonate scale tendency criterion to predict corrosivity.
- In a high total alkalinity, but non-scale forming medium with moderate chloride content (the solution NP), as-received aluminized steel type 2 showed low/moderate nominal corrosion rates ($<\sim 0.10 \mu\text{A}/\text{cm}^2$) for most of the test exposure. However, electrochemical impedance measurements revealed higher nominal corrosion rates ($\sim 0.22 \mu\text{A}/\text{cm}^2$) by the end of exposure concurrent with the appearance of uniform discoloration, indicative that corrosion may be of importance over longer periods upon evolution of solution pH to higher values.
- Exposure of as-received aluminized steel type 2 to moderate chloride content but in the absence of total alkalinity and carbonate scaling tendency (solution C) led to strong uniform aluminized surface discoloration and the appearance of few macro pits early on, consistent with early development of high solution pH likely responsible for the severe initial corrosion. Early on, nominal corrosion rate was large ($\sim 1 \mu\text{A}/\text{cm}^2$) but it decreased to $\sim 0.15 \mu\text{A}/\text{cm}^2$, consistent with a decrease in solution pH to nearly neutral values.
- Exposure of as-received aluminized steel type 2 to high chloride content and high carbonate scaling tendency (solution SW) led to early formation of few small macro pits as well as light uniform discoloration of the aluminized surface with nearly constant nominal corrosion rates of $\sim 0.3 \mu\text{A}/\text{cm}^2$ throughout the test exposure.
- Macro pits and surface discoloration of as-received aluminized steel type 2 appeared to be limited to the outer aluminized coating layer at least for the time frame examined in all solutions. The macro pits were usually small and infrequent on the corroding aluminized surface so they appeared to play a secondary role for the solutions C and NP and a primary form of corrosion for solution SW. The macroscopically uniform nature of the corrosion may be a manifestation of micro pits at the scale of the finely distributed Fe-rich inclusions present in the outer aluminized coating layer.
- It is tentatively proposed that the mechanism of activation of the aluminized surface in solutions NP and C may involve alkaline dissolution of aluminum as a result of a high pH of the solution bulk (early on for C

and later in the test for NP), which would cause aluminum dissolution possibly more localized at the microscopic, inclusion-scale level, and later precipitation of aluminum corrosion products, covering the entire specimen surface, consistent with visual evidence of uniform surface discoloration.

- For solution P over the entire test time and solution NP before the appearance of aluminized surface discoloration, impedance response was described assuming coupled cathodic reactions acting on the inclusions where surface coverage by an intermediate adsorbate alters the rate of the next step. That proposed mechanism results in pseudo-capacitive behavior consistent with that observed experimentally in the EIS diagrams. .
- For solutions C and SW, and solution NP after the appearance of aluminized surface discoloration, the impedance response was assumed to be dominated at high frequencies by the parallel combination of the local ohmic resistance of all micro and macro active sites and the aluminum oxide film capacitance, and at low frequencies by the discrete parallel combination of the Faradaic polarization resistance and an interfacial capacitance at all active sites.
- Galvanic protection was provided by the surrounding aluminized surface to base steel exposed at coating breaks in all the environments tested. In the less aggressive media (e.g., solution P), however, protection developed only after a period of thousands of hours at which the open circuit potential was ~ -720 ~ -750 mV (comparable to those of the steel), when some corrosion of the base steel had already taken place.
- At the end of that positive potential trend period, the aluminized surface of specimens with exposed steel (except for the specimens with small A_R in solution P) showed signs of developing a macroscopically uniform active condition. The open circuit potentials at that stage were ruled by the aluminized coating.
- The positive potential period was shorter for the more aggressive media (NP, C, and SW), where the base steel remained bright throughout the test period in SW. Positive potential period was also shorter when the area ratio of exposed steel to aluminized surface was greater.
- Impedance spectroscopy estimates of the long-term corrosion rates of the outer aluminized layer in the active conditions for the LCB configuration (largest steel/aluminized area ratio) were ~ 30 $\mu\text{m}/\text{yr}$ for solutions P and NP and ~ 1.5 $\mu\text{m}/\text{yr}$ for SW. For the SCB configuration (small steel/aluminized area ratio), long-term corrosion rates of the outer aluminized layer in the active conditions were ~ 15 $\mu\text{m}/\text{yr}$ for NP, ~ 0.03 $\mu\text{m}/\text{yr}$ for P, ~ 1 $\mu\text{m}/\text{yr}$ for SW, and 0.4 $\mu\text{m}/\text{yr}$ for C. Those estimates were

approximately consistent with direct measurements of thickness loss. Notably, the most nominally aggressive solutions did not result in the highest outer aluminized layer corrosion rates.

- Results for blemished/macrocell specimens have trends that extrapolate reasonably to the limit case of as-received aluminized surfaces (zero steel/aluminized area ratio). In that limit, the active aluminized surface condition was never reached in the least aggressive medium (P) during the 3,000 hr test. However, active conditions developed on the as-received aluminized surfaces in the more aggressive media after incubation times comparable to those encountered for blemished specimens with the smallest area ratio ($\sim 3 \cdot 10^{-4}$). Long-term corrosion rates in that condition were $\sim 3\text{-}5 \mu\text{m/yr}$.
- Corrosion macro pits were usually small and infrequent on the corroding aluminized surface so they appeared to play a secondary role for the solutions C, NP, and P, and a primary form of corrosion for solution SW. The macroscopically uniform appearance of the corrosion indicates that aluminum corrosion products may have deposited uniformly on the aluminized surface.
- The mechanism of activation of the aluminized layer may involve local alkalinization from enhanced cathodic reaction at the inclusions (especially in the low buffering capacity solution C), which would activate aluminum in the form of micro pits at the scale of the finely distributed inclusions present in the outer aluminized coating layer. Alkalinization may have been greater next to the steel region due to faster O_2 reduction rates there, consistent with the observation of a discoloration front radiating from the central exposed steel area.
- Plating of Fe (from inclusion particles separated from the matrix by undercutting corrosion and/or from initial corrosion of the exposed steel) on the aluminized surface may have further enhanced cathodic action in an autocatalytic manner that could account for the observation of the positive open circuit potential period, especially in solutions with low buffering capacity (solution C).

7 CORROSION ASSESSMENT OF MECHANICALLY FORMED ALUMINIZED STEEL

7.1 Introduction

Chapter 5 documented the severe corrosion observed in ribbed type 2 culvert pipes exposed to Florida inland waters for only a few years. Both localized and generalized corrosion tended to be associated with the pipe ribs and seams (where extended material bending occurred), and less so with the other portions of the pipe. The work described in this chapter aimed at determining the corrosion behavior of mechanically formed aluminized steel type 2. The microstructural aspects of mechanical distress upon bending as a potential precursor to corrosion development were characterized. Specimens were extracted from actual production pipe, and other specimens were prepared from flat stock subjected with various degrees of deformation. The specimens were exposed to waters of different compositions and assessed visually and electrochemically during exposure as well as by microscopic examination afterwards.

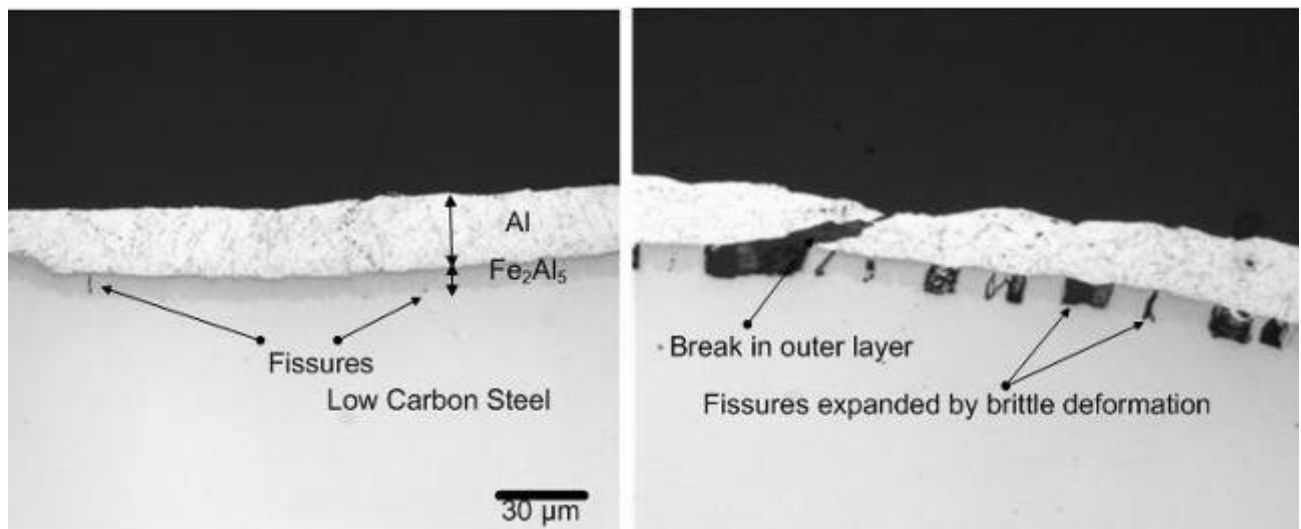


Figure 7-1. Flat specimen (left), bent specimen (right).

7.2 Experimental Procedure

7.2.1 Mechanical treatment and test configuration

Micro structural assessment of mechanical distress due to bending has been performed to date with 1.52 mm thick (16-gage) aluminized steel type 2 sheets simply bent to various extents. The bent region was mounted metallographically and digitized low magnification images of the outer bent region were examined to determine local radius of curvature (Figure 7-1). The same

regions were then examined at high magnification to determine the type and extent of local distress.

For electrochemical evaluation of the effect of deformation in corrosion tests were conducted with specially prepared specimens starting from flat stock, and with coupons cut out of actual production pipes.

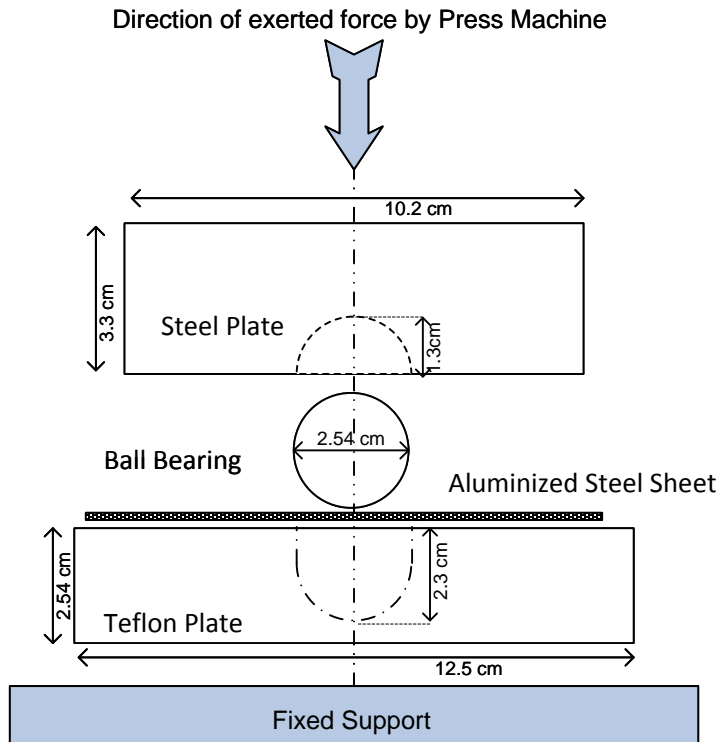


Figure 7-2. Schematic of indentation arrangement (not to scale).

The specially prepared specimens were made of octagonal portions of 1.52-mm (16-gage) aluminized steel sheet with minimal as-received surface distress. These specimens were indented at the center to a roughly hemispherical dimple shape using steel ball-bearing balls with diameters of 2.54 cm (1 in) , 1.90 cm (3/4 in), and 1.43 cm (9/16 in) (Figure 7-2). The indentation was made by pressing the bearing ball, socketed in a steel plate, into the initially flat specimen. Guide rods in the press assembly assisted in centering the indentation. An indented Teflon plate was used to protect the convex face of the sample until nominally full hemispheric penetration was achieved. Figure 7-3 shows the

appearance of the dimpled specimens. The convex face was the one later exposed to the test solution. After forming, the specimens were cleaned with ethanol and acetone, and stored in a desiccator prior to immersion exposure to the test solution with a circular exposed area of 82 cm^2 (12.6 in^2) centered on the dimple. The dimple configuration with flat surroundings permitted placement in the test cell with a flat gasketed joint that avoided leaking and minimized risk of crevice corrosion at an unevenly sealed joint. Control flat specimens without surface indentation and similar exposed surface area were used for comparison. Specimens were tested in duplicate.



Figure 7-3. Duplicate specimens indented to (left to right) 2.54 cm (1 in), 1.90 cm, (3/4 in), 1.43 cm (9/16 in), and flat.

A three-electrode test cell (Figure 7-4) was designed for exposing horizontally the convex side of the specimen, where distress is expected to be worst because of the tensile stresses. A metal-metal oxide activated titanium mesh placed parallel ~ 6 cm from the specimen surface was used as a counter electrode, while a low impedance activated titanium pseudo reference electrode 0.3 cm diameter and 5 cm long was placed ~ 1.5 cm above the specimens' indentation and periodically calibrated against a saturated calomel reference electrode (SCE). All potentials reported here are in the SCE scale. Each test cell was filled with 500 mL of a solution, which was not replenished during the test as explained below.

7.21 Test Solutions, and measurements, first series of experiments

Two test solutions, C and P as described in Chapter 6, Table 6-2, were prepared from de-carbonated de-ionized water of resistivity $>10^6 \Omega\text{-cm}$ combining

reagent grade NaCl and NaOH (solution C of negligible carbonate precipitating tendency) and NaHCO₃, HCl, and Ca(OH)₂ (solution P of high carbonate precipitating tendency). The Langelier Index was -5.9 for solution C and +1.50 for solution P, consistent with the observation of a ~0.5 mm thick powdery precipitate layer of CaCO₃ uniformly distributed on the specimen surface shortly after initiation of exposure. The test solutions in the test cells were quiescent and naturally aerated through a small opening. The relatively small electrolyte volume/total specimen area ratio was intended to be representative of, for instance, worst-case culvert pipe conditions with stagnant water on the pipe invert, or of occluded conditions for pore water on the soil side of a pipe.

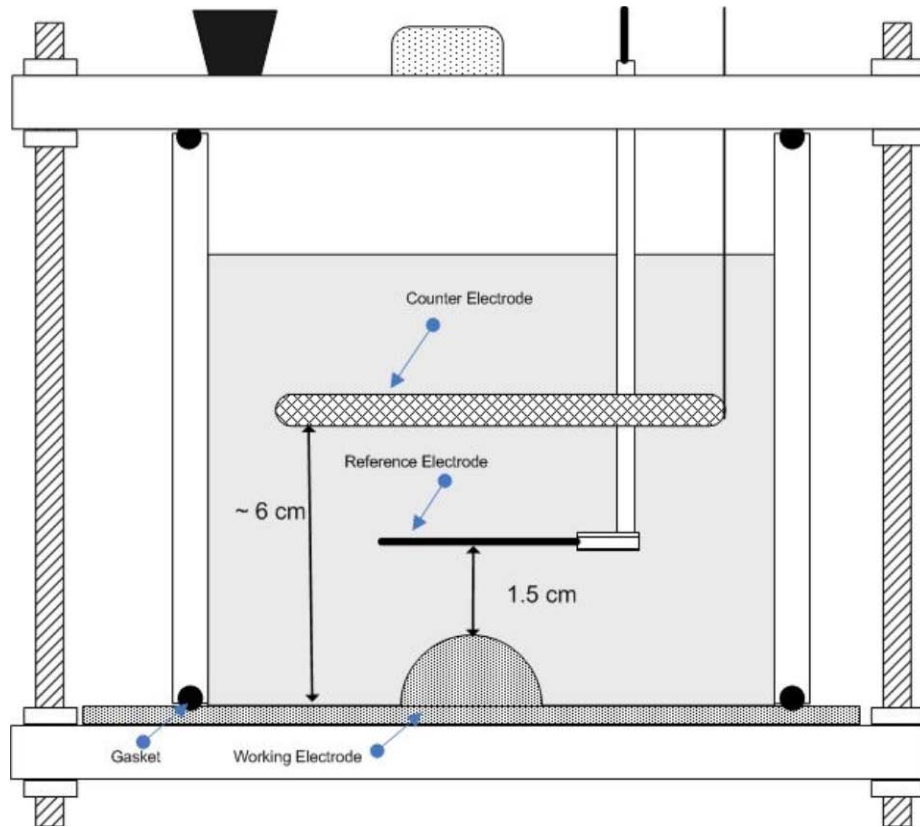


Figure 7-4. Three-electrode cell configuration.

The immersion tests were conducted in duplicate at $22 \pm 2^\circ\text{C}$. Solution pH, conductivity, and open circuit potential (E_{OC}) were monitored periodically. Electrochemical impedance spectroscopy (EIS) measurements were obtained at the E_{OC} with a Gamry™ PCI4-300 potentiostat in the frequency range from 100 kHz to 1 mHz using sinusoidal signals of 10 mV rms amplitude. Results for the ~1,000 hr initial period are presented here.

7.2. 2 Test Solutions, and measurements, second series of experiments

Additional tests were conducted with a solution of greater resistivity more closely approaching those encountered in the field sites addressed in Chapter 5. The methodology and findings for those tests are described in section 7.4, Continuation Studies.

7.3 Results and Discussion, First Series of Experiments

7.3.1 Metallographic analysis

Figure 7-1 (left) shows a metallographic cross section of the as-received (flat) material showing the coating microstructure as described earlier. Figure 7-1 (right) shows the coating condition of a bent sample (radius ~2 mm). The most notable feature is nearly completely brittle fracture of the intermetallic layer, as manifested by its many elongation gaps. The outer coating was much more ductile, with few instances of fracture as that illustrated on the left side of the right figure, apparently originating at one of the larger brittle gaps of the inner layer. The number and severity of fractures in the inner layer increased as the bending stress increased. For completely brittle fracture, the integrated gap length measured on a line parallel to the perimeter, divided by the initial length (that is, that of the remaining visible intermetallic) should equal the total strain at the outer fiber. To test that hypothesis, the strain ϵ_M calculated from measurements of the ratio of inner layer gaps to visible intermetallic length was compared with the strain at the outer fiber expected from the local macroscopic bending radius and the sheet thickness. For a simply bent sheet in which the neutral axis of metal sheet stays constant, the theoretical relationship between the strain of outer fiber and radius of curvature (Dieter, 1986) is given in Equation 7-1, where ϵ_i is the ideal strain, T is the thickness of the sheet (16-gage = 1.52 mm), and R is the outer bending radius.

$$\epsilon_i = \frac{T}{2 \left(R - \frac{T}{2} \right)} \quad (7-1)$$

Figure 7-5 compares the values of ideal outer fiber strain ϵ_i computed per Equation 7-1 from the radius of curvature determined for various specimens from the low magnification micrographs and the sheet thickness, and ϵ_M from the micrographic analysis of the intermetallic layer. Flat samples were assigned a radius > 50 mm in the graph. The results support the hypothesis of nearly completely brittle behavior for the inner intermetallic layer.

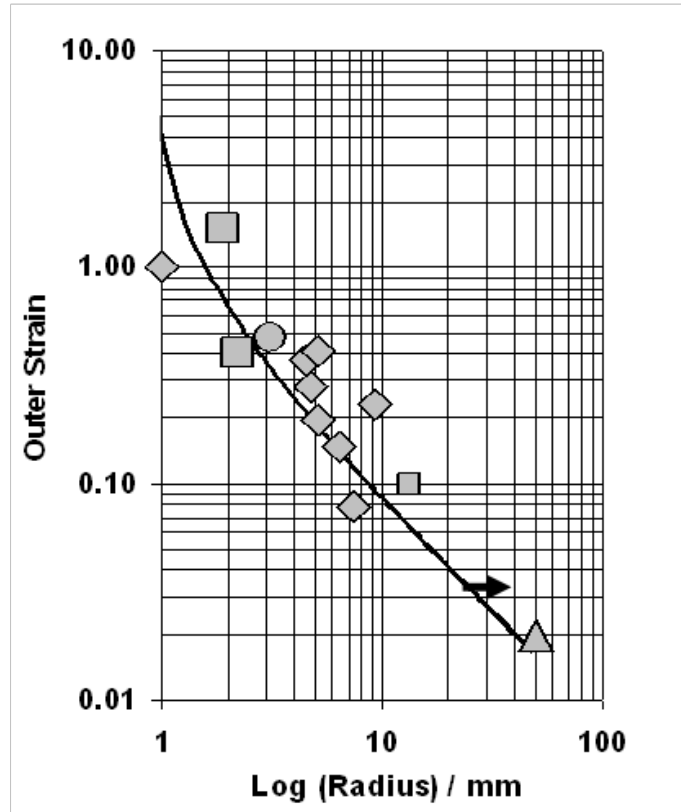


Figure 7-5. Outer strain ϵ_l (per Equation 7-1) (solid line) and ϵ_M per micrographic analysis of intermetallic layer gaps (symbols) as a function of radius of curvature for several samples.

7.3.2 Direct observation of corrosion performance

Visual examination of the specimen surfaces in solution P (high total alkalinity with carbonate precipitation) showed early appearance of light yellowish discoloration uniformly distributed over the convex indentation surface in all dimpled specimens tested, indicative of some corrosion (Figure 7-6, left). Symptoms were more severe in solution C (low alkalinity and no precipitating tendency), where appearance of strong reddish discoloration was first noted early on in the exposure around the convex indentation of all dimpled specimens, and gradually propagating covering the entire indentation surface (Figure 7-6, right). Corrosion appeared to be more intense for the 2.54-cm (1-in) diameter indentation specimens, although it is noted that the affected area was greatest for those even though maximum local strain may have been less severe than for the smaller radius indentation specimens. In both solutions, corrosion of the surrounding aluminized surface was minimal, suggesting little disruption of passive behavior there during the test interval sampled. Correspondingly, no sign of corrosion was observed in any of the flat surface specimens exposed to both solutions, suggesting good corrosion performance to date in those cases. Clearly, for the time being any galvanic protection from the aluminized portion

was insufficient to avoid initiation of active corrosion of the exposed steel especially in the C solution, in agreement with the results reported in Chapter 6 for specimens with machined coating breaks (Cáseres and Sagüés, 2006).



Figure 7-6. Light corrosion on a 2.54-cm (1-in) convex dimple immersed in solution P after 21 days of exposure (left) and severe corrosion on a 2.54-cm (1-in) convex dimple immersed in C solution after 19 days of exposure (right).

7.3.3 EIS measurements

EIS results are exemplified for two typical cases in Figure 7-7. In one set of cases, usually early during the test exposure, the impedance behavior could be accurately fit to that of an analog circuit consisting of a solution resistance in series with a parallel combination of a non-ideal capacitor and a resistor. In the rest of the cases the impedance diagrams showed two time constants and the impedance behavior could be closely approached by incorporating an additional resistor-capacitor parallel combination in series. After subtracting the solution resistance, the value of the resistance of the single resistor or the sum of the two resistors respectively was designated as the apparent polarization resistance R_p of the system and used as an inverse descriptor of the effective corrosion current. Figure 7-8 shows the resulting values of R_p of duplicate specimens in the C and P solutions, at various exposure times and for the various dimple radii used.

The R_p values were typically much greater in the P solution, in agreement with the expected more benign character of that precipitating solution. R_p there tended to increase with time, indicating a maturing of the protective regime. Furthermore, there was little differentiation between the R_p values of the flat and dimpled specimens, indicating that the light corrosion manifested by direct observation had likely been arrested in this medium after some initial active period. These results are consistent with protective regimes reported in Chapter 6 for blemished aluminized steel in the same solution.

The Rp values correspond to more aggressive conditions in the C solution, in agreement with visual observations. There the Rp values were generally much lower than in the P solution and decreased with time indicating increasing corrosion. Moreover, Rp in the dimpled specimens was generally lower than in the flat specimens, indicating an adverse effect of forming. It is noted however that one of the duplicate flat specimens experienced a significant decrease in Rp before 46 days of exposure, which may be indicative of onset of protective corrosion by the aluminized layer (Kimoto, 1999; see also Chapter 6) but also possible development of crevice corrosion artifacts in the cell.

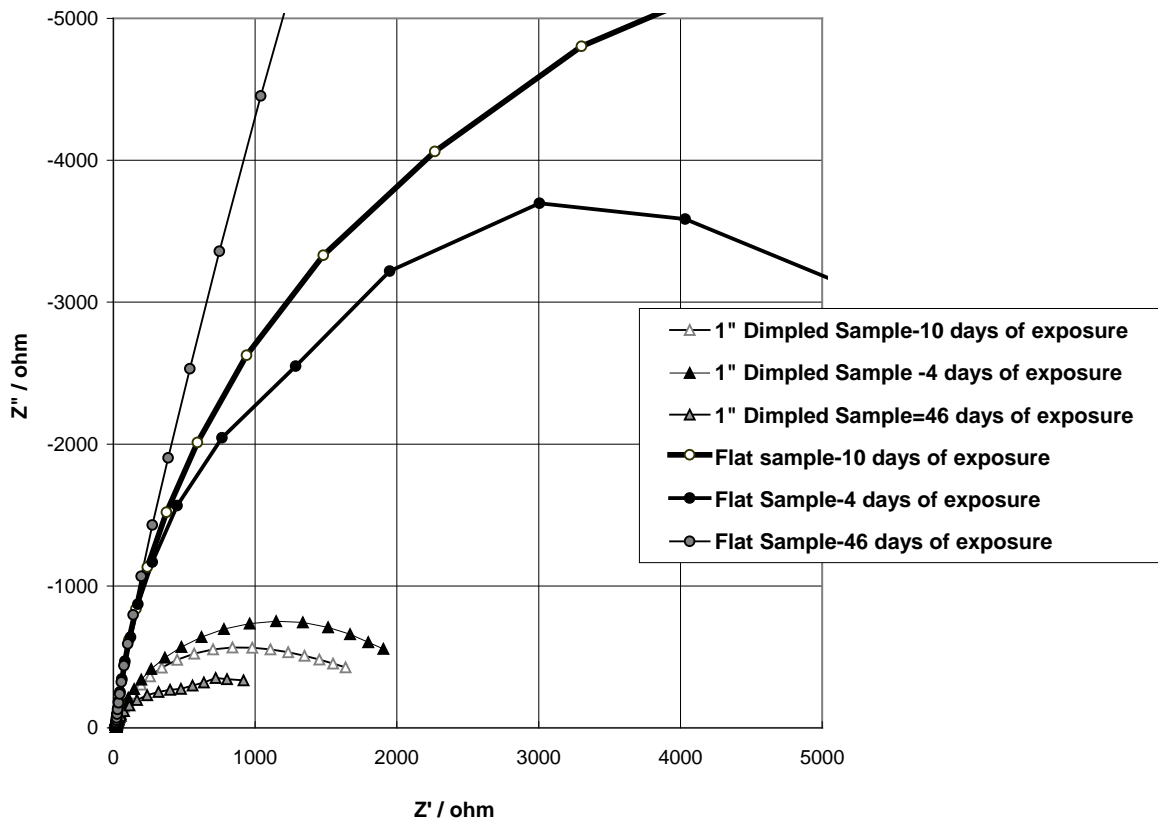


Figure 7-7. EIS results of the flat and 2.54-cm (1-in) indentation specimens exposed to solution C.

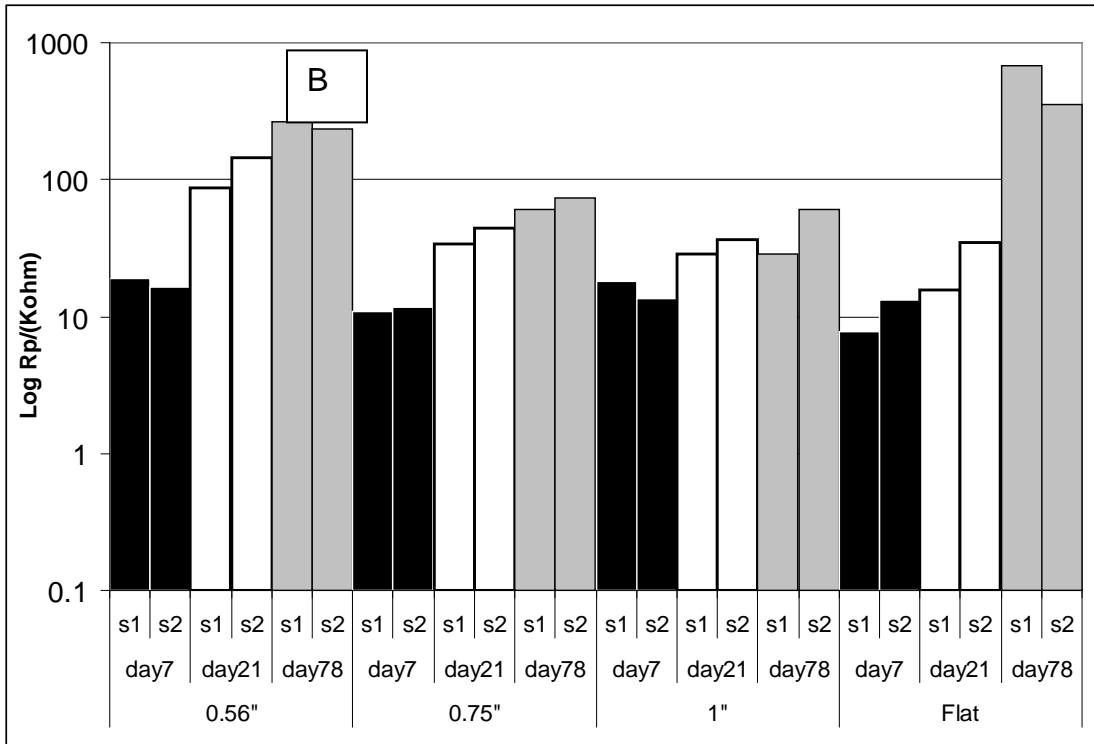
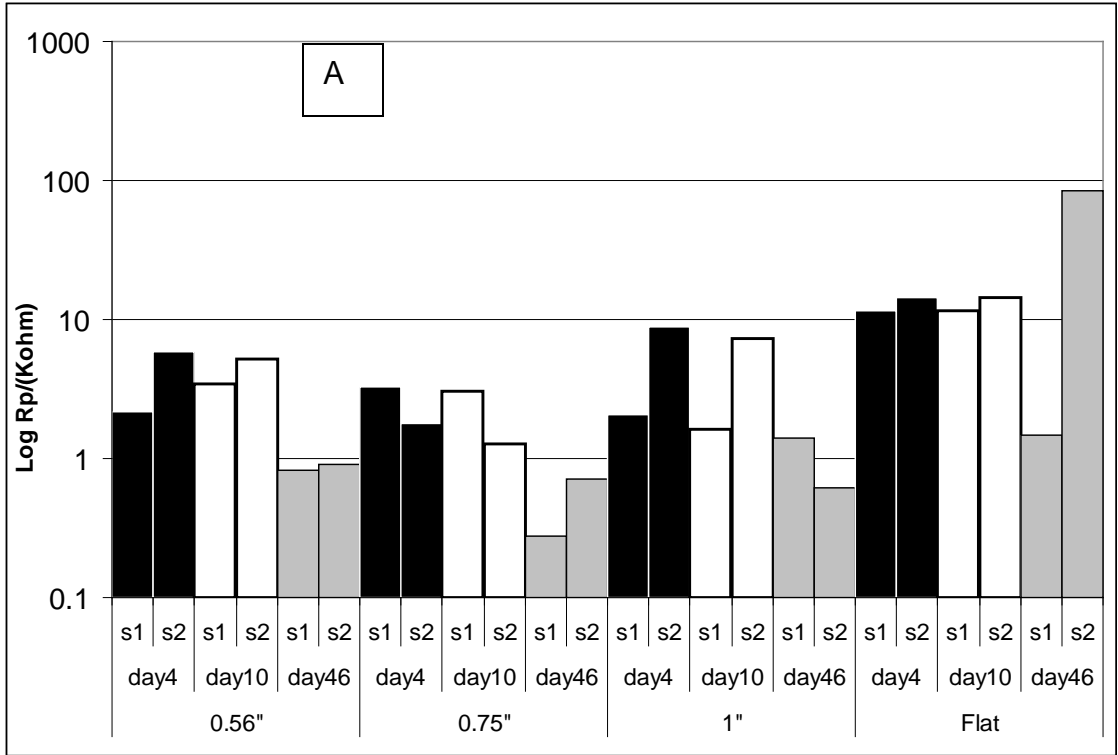


Figure 7-8. Polarization resistance values for different bent categories at three exposure times in C solution (A) and in P solution (B).

7.4 Continuation Studies

7.4.1 Experimental methods

The investigation described in Section 7.3 was essentially repeated using a less aggressive simulated natural water (Solution S) better representative of field conditions. This simulated water had pH ~ 7, conductivity of ~200 $\mu\text{S}/\text{cm}$ and chloride and sulfate concentrations of 34 and 30 ppm, respectively.

Table 7-1
Solution "S" Properties

TA ppm as CaCO_3	TH ppm as CaCO_3	FC ppm as CaCO_3	BI	pH	σ $\mu\text{mho}/\text{cm}$
12.55	65	0.57	76.9	~ 7	~ 200

While not having a high precipitating tendency, this solution is considered as relatively benign due to small content of aggressive ions (chloride and sulfate) and high resistivity ~ 5000 $\Omega\text{-cm}$. Under current FDOT design guidelines for highway drainage culverts, a service life of ~100 years could be expected (Cerlanek and Powers, 1993). According to the alternative service life forecasting method by AK Steel (Bednar, 1998), which incorporates the tendency for water scaling, a service life of ~ 40 years could be expected. Figure 7-9 compares the AK Steel Method service life estimates for various Florida waters including Solution S.

The test cell was redesigned to minimize crevice corrosion formation at the sealing gasket; post test examination confirmed a crevice-free condition in all the cases examined.

7.4.2 Results and discussion

Immediately after exposure, corrosion was observed at high strain areas around the indentations a yellow shade, which agrees with earlier observations (see section 7.3.2). As the time progressed the shade of corrosion product grew wider and became darker and various tuberculation occurred at the formed zones (Figures 7-10 and 7-11). SEM energy dispersive x-ray spectroscopy (EDS) results were consistent with the corrosion product being iron oxide. After the appearance of tuberculation, a very thin layer of white deposit was observed on the surface of aluminum in formed specimens. The layer was later identified by SEM EDS as an aluminum and oxygen rich product. These results suggest that although aluminum was actively corroding to some extent, the galvanic protective effect on the iron was not substantial.

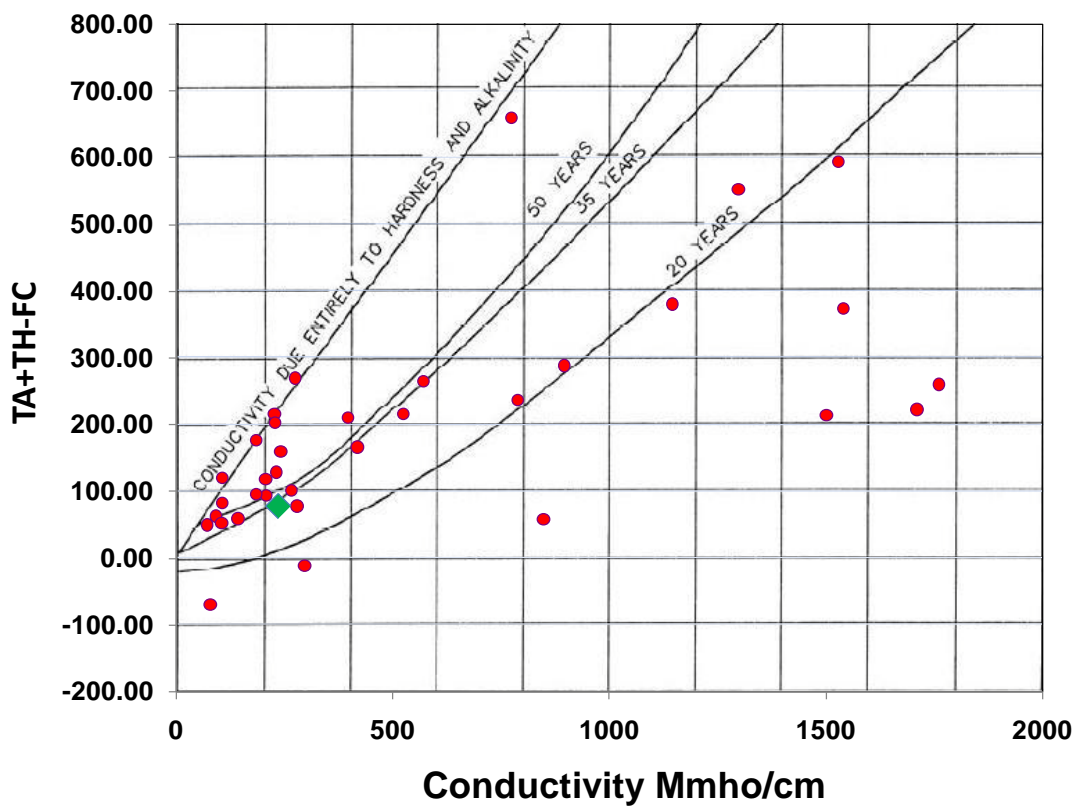


Figure 7-9. Alternative scaling index durability projection (Bednar 1989; Morris 1998) using water data from experimental solution (diamond) and other Florida fresh waters (circles). Diamond: Properties of Solution S.

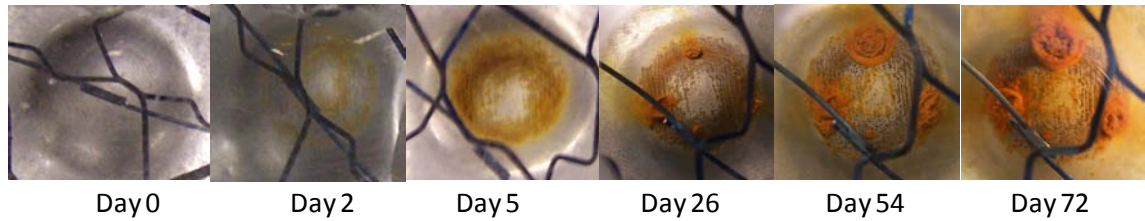


Figure 7-10. Visual observation of corrosion progression with respect to days of exposure to Solution S for a 2.54 (1-in) dimple specimen.

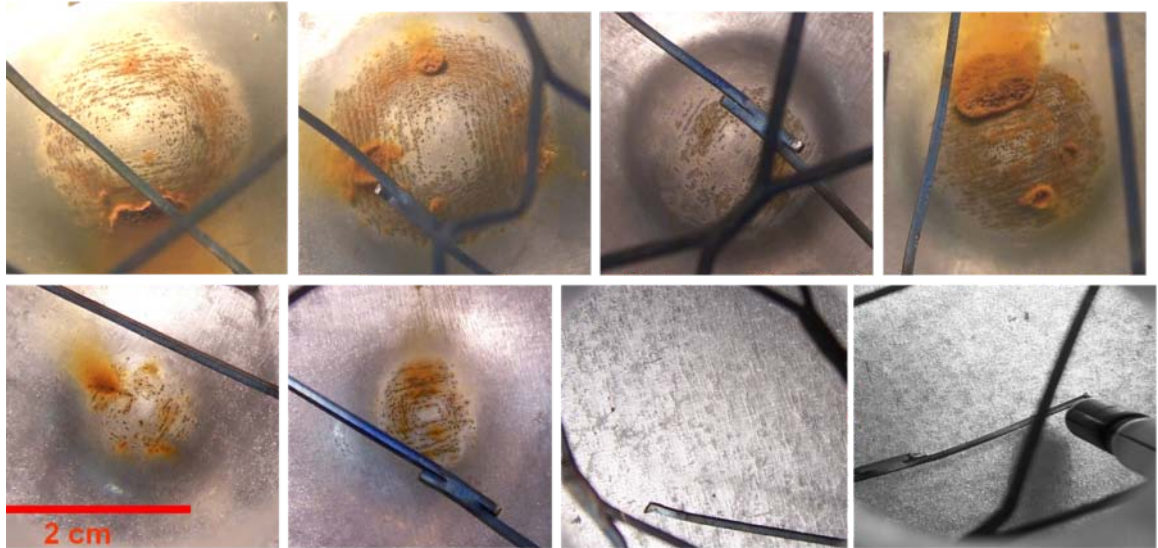


Figure 7-11. Visual comparison of corrosion development in formed and flat specimens immersed in Solution S at 26 days of exposure. Top row: from left to right, duplicate specimens with 2.54 (1-in) and 1.90 cm (3/4 in) dimples respectively. Bottom row: duplicate specimens with 1.43 cm (9/16 in) dimple and flat condition respectively.

Figure 7-12 shows corrosion current (I_{CORR}) for representative specimens calculated from EIS measurements. The results showed sustained corrosion as time progressed, agreeing with visual observations. Mechanically formed specimens tended to have higher corrosion rates compared to flat specimens, in keeping with the other observations.

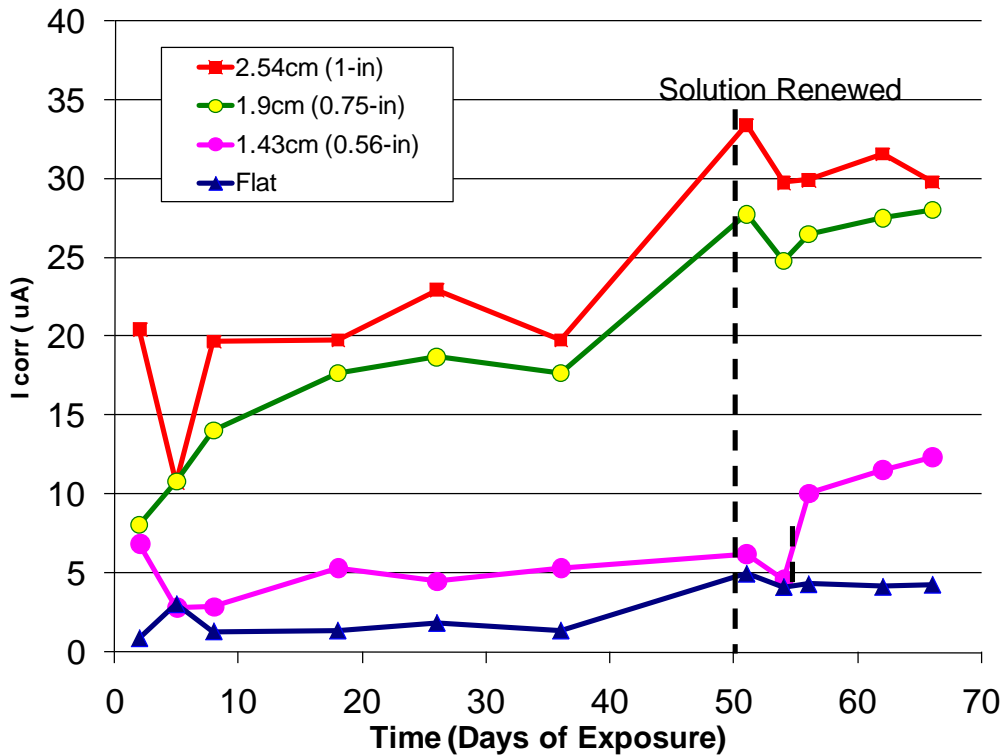


Figure 7-12. Corrosion rates over time for dimpled specimens. Solution S. Average of duplicate specimens.

The open circuit potential measurements (Figure 7-13) indicated that the system's potential was approaching the corrosion potential of freely corroding steel (~ -0.6 V). The results indicated that in this solution the aluminized surface was highly polarizable, indicative of little tendency for passivity breakdown, so that even very small amounts of exposed steel would be likely to result in a mixed potential approaching that of only steel. These results are consistent with the other observations in indicating no strong galvanic protection by aluminum in solution S over the time frame of the tests.

Figures 7-14 and 7-15 are photographs of the cracks (in an unexposed replicate specimen) that developed as a consequence of mechanical forming. The cracks exposed small amounts of base steel to the solution. That exposed steel is likely the cause of the elevation in open circuit potential shown in Figure 7-13. The results suggest that the relatively benign S solution in these experiments provided a condition for the aluminum coating to stay passive during the test interval; therefore, aluminum did not provide galvanic protection of the steel substrate, resulting in early corrosion of exposed steel in the mechanically formed regions.

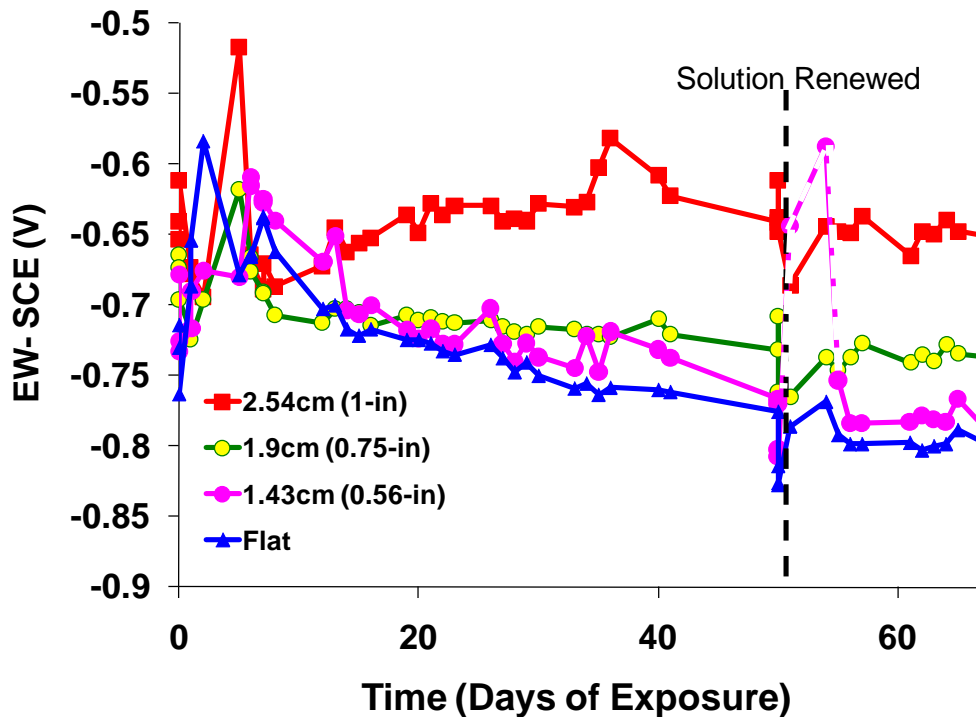


Figure 7-13. Open-circuit potentials of formed specimens over time. Averages of duplicate specimens. Solution S.

Metallographic cross sections near the surface of the 2.54 cm (1-in)-dimpled specimen before and after exposure are shown in Figure 7-16. Corrosion initiated at the steel substrate exposed to the solution underneath the coating crack,; as corrosion progressed, iron corrosion products tended to deposit around the coating break. An SEM view of the crack region for a sharp bend specimen exposed to simulated natural water shows the distribution of aluminum, iron, and oxygen after the onset of corrosion (Figure 7-17).

7.4.3 Planning for longer term exposures and follow up investigation

The findings presented above represent initial results confirming that mechanical distress can induce localized corrosion of aluminized steel and revealing some of the factors that determine the extent of corrosion. Several key issues remain to be resolved. Those include among others more precise determination of the extent and variability of mechanical distress present in as-produced corrugated pipe, the effect of the relative cathodic and anodic areas involved and the extent of coupling between those in actual field situations with various environmental conditions, the extent of self-repairing that may be provided by the accumulation of corrosion products at coating breaks, and the dependence of that effect on the size and number of the breaks. Laboratory

approaches aimed to resolve the issues should include larger samples and examination of other solution compositions representative of Florida natural waters, as well as consideration of the soil pipe interface. The laboratory tests need to be supplemented by a wider field evaluation of corrosion performance of aluminized pipe in Florida to elucidate to what extent the problems observed at the field locations (Chapter 5) represent a broader situation. The field investigations should also provide important information to establish the degree of correlation between corrosion and normal vs. unusual manufacturing mechanical distress of the coating and substrate, and with any local environmental parameters not contemplated by the current FDOT materials selection guidelines.

A follow up investigation to prioritize and execute research to address the above issues is under planning and is anticipated to begin following completion of this project.

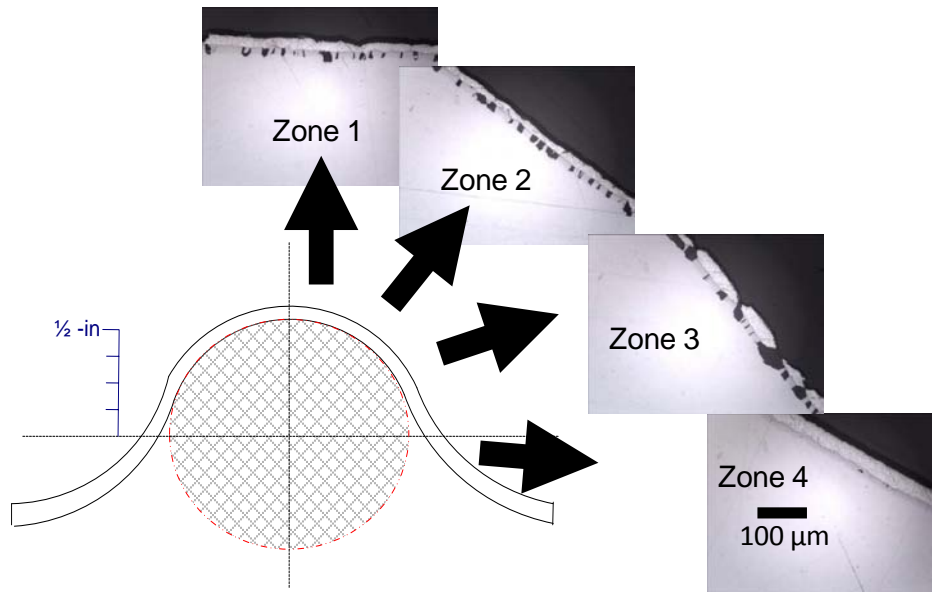


Figure 7-14. Coating damage due to deformation of an aluminized steel type 2 specimen was determined metallographically in the cross-section of a 2.54-cm (1-in) dimple.

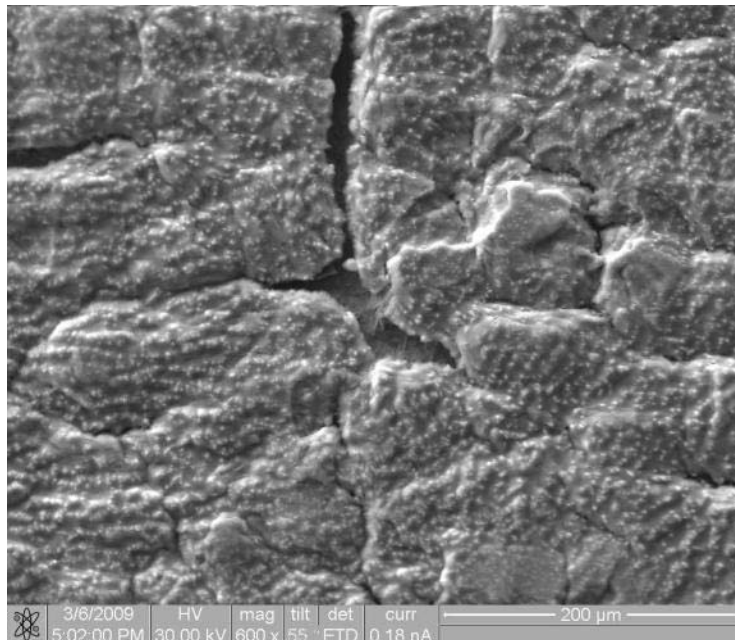


Figure 7-15. SEM view of coating damage (convex region, Zone 3 in Figure 7-14) due to deformation of an aluminized steel type 2 specimen with a 2.54-cm (1-in) dimple.

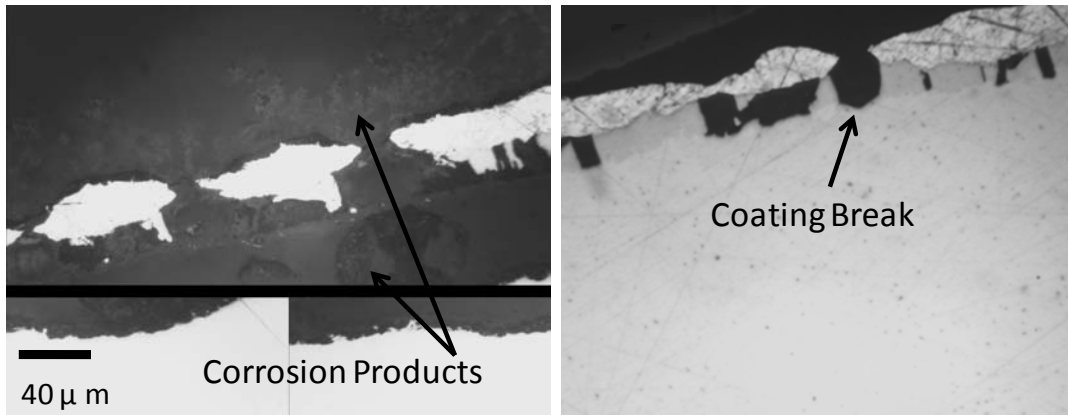


Figure 7-16. Metallography of the cross-section of a 2.54 cm (1-in) dimple specimen exposed to Solution S (left), and a same size dimple unexposed specimen (right).

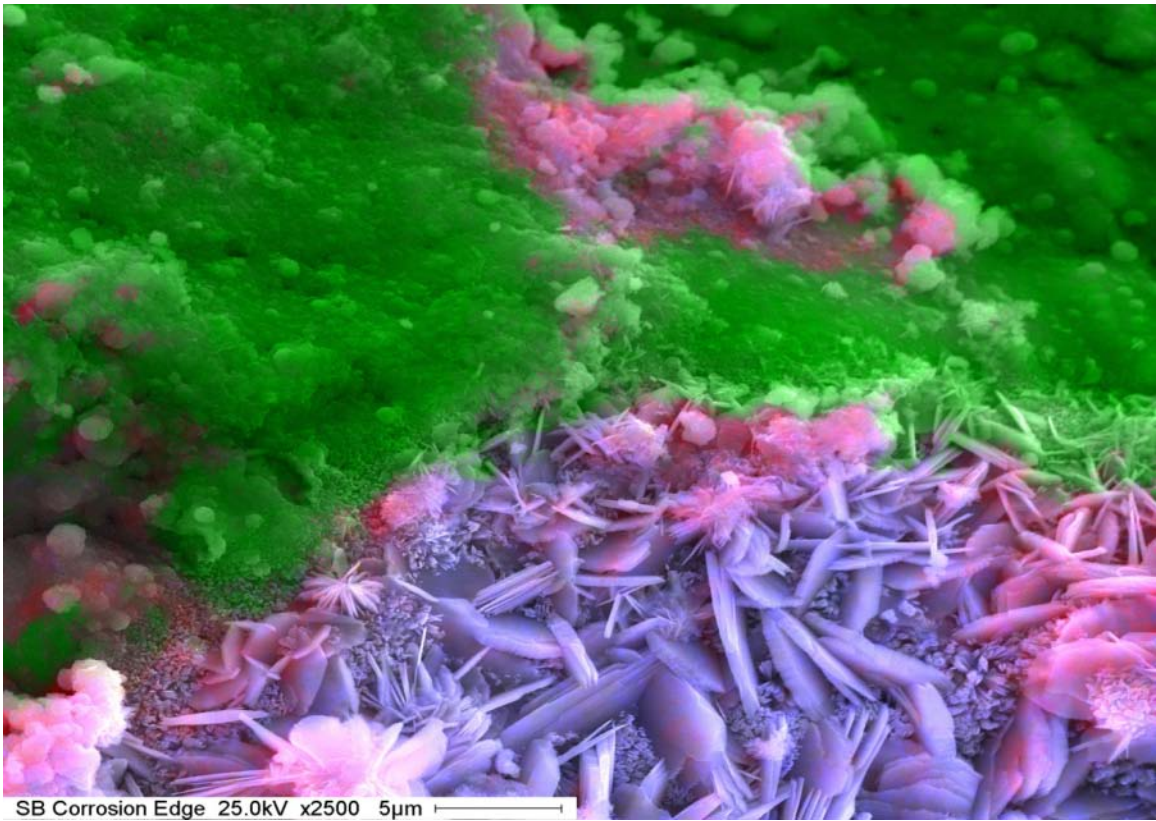


Figure 7-17. SEM photo: Looking at a crack region exposed to the solution, corresponding to a sharp-bend specimen with inner radius of 1.6 mm exposed to Solution S. (Color key: aluminum rich, green; oxygen-rich, pink; iron-rich, purple).

7.5 Summary and Conclusions

- Forming stresses in aluminized steel caused cracks in the inner brittle coating layer, but also at the more ductile outer layer (Al), as evidenced by the metallographic examination and advanced EIS techniques. The cracks expose small amounts of base steel to the water medium, promoting significant increase in half cell potential. That condition was manifested in formed samples.
- Immersion cell experiments demonstrated that, in the absence of a high precipitating tendency, the convex portion of specimens that were strongly formed by spherical indentation was susceptible to early corrosion development. Non-deformed flat aluminized surfaces showed much less deterioration during the test interval.
- The relatively benign S solution was not aggressive enough to induce strong manifestations of localized passivity breakdown or passive film dissolution on the aluminized coating, at least in the short term. Therefore, the aluminized coating did not provide substantial galvanic protection of the steel substrate under those conditions, resulting in early corrosion of exposed steel in formed regions.
- In the tests conducted with the more concentrated C and P solutions, preferential corrosion of the formed steel took place (at least in short duration experiments) in the low scaling tendency C solution, but much less so for the high precipitating tendency P solution.
- The corrosion of the exposed steel was also manifested in decreased polarization resistance and direct observations of rusting in formed specimens.
- EDS analysis of a crack in an exposed specimen also revealed the formation of iron oxide at the crack region with an increasing oxidation state, which agrees with observation of brownish rust around the dimple in high stressed zones.
- This investigation was of exploratory character. Issues needing resolution in a follow up investigation with laboratory and field evaluations were identified.

8 EVALUATION OF ALTERNATIVE SERVICE LIFE ESTIMATION METHODS FOR ALUMINIZED STEEL TYPE 2 CULVERT PIPING

8.1 Estimates of Service Life

The following tentative evaluation of durability projection alternatives considers a total aluminized coating thickness of 45 μm (30 μm outer and 15 μm inner layers) covering uniformly a base steel 1,500 μm thick approximating a gage 16 sheet stock, and focus on the corrosion performance of the aluminized coating layers coated on both sides of the base steel as well as the base steel itself. This evaluation uses the results of tests with model solutions summarized in Chapter 6 . As it was noted there, the composition of those solutions was outside the intended range of application of aluminized steel, to allow differentiation of the effect of environmental variables within practical test durations. Other environmental parameters such as MIC (see Chapter 10) may influence the corrosion performance of the Al/Fe system. Consequently, it is strongly emphasized that these evaluations are intended primarily to compare projection method alternatives, and that any extrapolation to longer service times is only nominal in nature. Continuation work with other solutions (as used in the initial studies documented in Chapter 7) and long term monitoring of actual field installations will be necessary for appropriate validation.

The field sample examinations documented in Chapter 5 showed that the inner aluminized coating layer, of nearly invariant thickness but with several small breaks especially at the rib bends in a spiral rib aluminized steel type 2 culvert component, appears to provide little corrosion protection to the underlying steel. Even in aluminized steel without bends like those used here, breaks not related to corrosion in the inner layer were clearly noted. Based on this observation, no durability credit was assigned to the inner coating layer in these evaluations. Hence, the projected service life SL is defined as the number of years to penetration through the base steel and the outer aluminized layer on both sides of the base steel, considering that penetration occurs from both sides of the metal as it is usually observed in field exposures. For the present calculations, it is also assumed that similar environments exist on each side of a pipe so the corrosion rates at both sides are equal. Thus, the projected SL is for simplicity taken to be equal to the sum of the SL of the outer layer on either pipe side plus the amount of time needed to penetrate half of the thickness of the base steel.

The values of i_{corrAL} as a function of exposure time obtained in the Chapter 6 laboratory experiments with as-received aluminized steel type 2 specimens are summarized in Tables 6-7 through 6-8. Those discrete i_{corrAL} values were used to estimate SL of the outer aluminized layer for as-rolled aluminized steel type 2 in all solutions for the exposure period from $t=0$ to t_f , where t_f is the time for the end of the test and $i_{\text{corrAL}}(t_i)$ is the time dependent corrosion current density obtained from the EIS measurements where $i=1$ to n represents each EIS measurement.

Thus, L for the outer coating layer is computed as shown in Equation 8-1, where A_W is the aluminum atomic weight, $n=3$ for the Al/Al^{3+} reaction, ρ_{AL} is the aluminum density, and the term in brackets corresponds to the aluminum corrosion rate CR_{AL} .

$$SL = 30 \cdot \left[\frac{A_W}{t_f \cdot n \cdot F \cdot \rho_{AL}} \cdot \sum_1^{n-1} i_{corrALi} \cdot (t_{i+1} - t_i) + i_{corrALn} \cdot (t_f - t_n) \right]^{-1} = 30 \cdot CR_{AL}^{-1} \quad (8-1)$$

For blemished aluminized steel type 2, the values of i_{corrAL} and i_{corrFE} , reported in Tables 6-9 through 6-11 were used to compute the SL for the aluminized coating and the base steel using Equation 8-1, replacing accordingly the aluminum parameters with those of the steel. The extent and morphology of coating breaks is assumed to resemble the Chapter 6 conditions examined experimentally. Those would apply for example to a pattern of breaks of small aspect ratio spaced a small fraction of 1 m (a few inches) apart, at the bottom of a shallow pool of stagnant water as it may occur between corrugations in the culvert invert. It is assumed for simplicity that the medium is replenished only infrequently, during episodic flow events. Once the post-potential drop regime is established, corrosion rates are considered to proceed at a space- and time-uniform rate until the outer coating layer is exhausted.

8.2 Results and Discussion

Table 8-1 summarizes the overall SL estimates (SL of the outer layer plus that of the base steel) obtained per the above assumptions and labeled "This investigation". As mentioned in Chapter 4, a variety of predictive methods have been proposed for forecasting the service life of metallic components. Nevertheless, special consideration is given to the most relevant forecasting methods, e.g. the AK Steel, the California, the AISI, and the FDOT methods. The computed SL estimates using those methods are also reported in Table 8-1, determined based on the solution compositions listed in Tables 6-2 and 6-3 for 16-gage aluminized steel type 2. As explained earlier, any minimum resistivity limits for application are ignored. Comparison between the SL projections from the present experiments per Eq. (8-1) and those obtained from the various forecasting methods are presented in the next paragraphs.

8.2.1 Service life estimates for as-rolled aluminized steel type 2

8.2.1.1 Projections from the laboratory tests.

For solution P, which may be taken as representative of media with high carbonate scaling tendency, nearly neutral pH, and moderate chloride content, the extremely small CR_{AL} ($<0.24 \mu\text{m/yr}$) recorded in this investigation if sustained at these levels would indicate a full consumption of the outer layer in >100 yr of service, consistent with the projected SL computed from corrosion rate estimates

of field culvert pipes exposed to tropical environments of composition similar to solution P (Bednar, 1989). Additions of extra CaCO₃ emulating solutions with higher carbonate precipitating tendencies caused a short-term increase to ~1 µm/yr, but even this transient larger rate did not cause visual corrosion damage to the outer aluminized steel.

**Table 8-1
Comparison of Durability Estimates (In Years) Obtained by the Application
of Commonly Used Forecasting Methods and Those Obtained in this
Investigation**

Test solution	AK Steel	California	AISI	FDOT	This investigation		
					A _R =0	A _R ~3 10 ⁻⁴	A _R ~0.3
P	<20	29	57	56	>100 (>100)	>100 (>100)	10 (11,11)
NP	<20	25	50	33	36 (38)	16 (15)	10 (10)
SW	NA	7	15	NA	15 (19)	33 (28)	27 (30)
C	<20	30	62	27	19 (23)	27 (28, 24)	–

Numbers in parenthesis correspond to results from duplicate specimens. Ar indicates the blemished/unblemished zones area ratio; Ar=0 indicates unblemished condition.

Durability projections from the laboratory tests become distinctly more pessimistic for some of the other conditions investigated. For instance, for solution NP, which may be representative of media with high alkalinity but low hardness, high pH, and moderate chloride content, CR_{AL} was modest (~1.04 µm/yr). If this rate is maintained, it would mean a full outer coating loss in ~30 yr of service. The high rate observed for this solution mainly ascribed to the high pH of the solution bulk above the aluminum passivity range is in agreement with the results obtained from field studies conducted on aluminized steel type 2 exposed to environments with solution pH>9 (Pyskadlo and Ewing, 1987). For solution C, which may be taken to be representative of media with both low alkalinity and hardness, high pH, and moderate chloride content, CR_{AL} was ~3.16 µm/yr, which would indicate a full outer coating layer consumption in only ~10 yr, consistent with the strong aluminized surface discoloration observed early on in the exposure.

For solution SW emulating seawater composition, the CR_{AL} was modest (~3.25 µm/yr) indicating a full outer layer consumption in ~9 yr of service. While

subject to considerable uncertainty, the corrosion rate becomes important considering that the corrosion is strongly localized, with consequent risk of aluminized layer penetration early in the life of a component exposed to similar media. This finding is in agreement with the observations reported by Perkins et al. (1982) and Stavros (1984), who asserted that severe pitting corrosion of aluminized steel exposed to very aggressive environments is determinant when forecasting durability in this type of medium.

After full consumption of the outer aluminized layer, corrosion of the base steel starts and is expected to proceed at the rates of $\sim 12 \mu\text{A}/\text{cm}^2$ in SW and $\sim 10 \mu\text{A}/\text{cm}^2$ in the other media as reported in Chapter 6. Those values are in agreement with corrosion rates reported by McCafferty (1974), Oh, et al. (1999), and Sander, et al. (1996). The corresponding projected SL values for the base steel would be ~ 6 yr for SW and ~ 8 yr for the other media.

8.2.1.2 Comparison with various forecasting methods.

For solutions with high scaling tendencies, moderate chloride content, and nearly neutral pH (solution P), the SL estimates computed by the FDOT and AISI forecasting methods were somewhat conservative (and overly conservative in the case of the AK Steel and California methods) compared to the SL projections obtained from the laboratory tests. For the solution with high alkalinity/low hardness, moderate chloride content, and high pH (solution NP), SL estimates obtained from the FDOT method were in good agreement with the results reported in this investigation. On the other hand, the AISI, California, and AK Steel methods yielded either liberal or conservative estimates compared with the present findings. For solutions with moderate chloride content, low both alkalinity and hardness, and high pH (solution C), the laboratory test SL projections were in close agreement with those determined by the AK Steel, California, and FDOT methods, but short compared to durability projections obtained by the AISI method. In extremely aggressive solutions of low resistivity, high chloride content, and nearly neutral pH (solution SW), the AISI method yielded comparable estimates of durability relative to the laboratory projections, whereas the California method projected shorter service lives. In highly aggressive environments, no durability credit is given by the FDOT method and no SL projections are given by the AK Steel method for solutions with scaling indexes beyond ~ 800 ppm.

Based on the above, for unblemished aluminized steel the present findings would support retaining the present FDOT guidelines regardless of scaling tendency for environments approaching the low end of the recommended resistivity range (recall that in the laboratory tests resistivity was near to but below the $1,000 \Omega\text{-cm}$ limit) and neutral to mildly alkaline conditions (e.g. $\sim 7.5 < \text{pH} < \sim 9.0$). The results also suggest that the AISI method would be more adequate for predicting durability in environments with extremely high chloride contents (e.g. resistivity $< 50 \Omega\text{-cm}$) and nearly neutral pH, but those conditions

fall outside the range of specified applications for FDOT purposes. Eventual changes in existing guidelines should consider not only the specific results of this investigation but also the entirety of the performance record of aluminized steel pipe.

It is also noted that the above findings apply to aluminized steel with an initially unblemished metallic coating. As discussed earlier, in actual metal forming and subsequently field application practice, the aluminized steel component (e.g. culvert pipes) is liable to surface distress that may range from minor to severe, exposing a certain amount of base steel. The following section addressed those cases.

8.2.2 Service life estimates for blemished aluminized steel type 2

8.2.2.1 Projections from the laboratory tests.

In solution P which represented conditions of carbonate scale forming solutions, that is high total alkalinity and total hardness, full outer layer consumption would be projected to occur in ~2 yr for $A_R \sim 0.03$ (consistent with moderate aluminized surface discoloration as the main mode of deterioration), but in excess of 100 yr for $A_R \sim 3 \cdot 10^{-4}$. It is also noted that for $A_R = 0$ as in the unblemished aluminized a negligible nominal corrosion rate and bright appearance was noted for solution P, so the outer layer durability projection would also be in excess of 100 yr.

Projections become distinctly more pessimistic for solutions of high alkalinity, negligible carbonate scaling tendency and moderate chloride content (solution NP). Severe corrosion was noted around the exposed steel perimeter for both $A_R \sim 0.03$ and $\sim 3 \cdot 10^{-4}$ with complete consumption of the outer aluminized coating layer after only a few weeks. It is not clear at present if corrosion would tend to progress even further specifically at the aluminized ring around the steel. It can be noted however that since the inner coating layer had remained in place at least for the duration of the experiment, it is suspected that uniform corrosion would take place in this case. If that would be the case, full outer layer consumption would be projected to occur in only ~2 yr for $A_R \sim 0.03$, and after ~7 yr for $A_R \sim 3 \cdot 10^{-4}$, both values in agreement with strong discoloration of the aluminized surface. Longer SL of the outer aluminized layer was obtained for $A_R = 0$ (~30 yr).

In solution SW simulating seawater composition, full outer layer consumption would be projected to occur in ~30 yr of service for both $A_R \sim 3 \cdot 10^{-4}$ and ~0.03, and ~9 yr for $A_R = 0$. However, the strong localized corrosion as opposed to a light uniform corrosion distress was the main form of corrosion in this solution for all A_R . Those values become important considering that the

corrosion is strongly localized, with consequent risk of aluminized layer penetration of a component exposed to similar media.

In solution C which represented solutions with low alkalinity, low carbonate scaling tendency, and moderate chloride content, severe corrosion was noted around the exposed steel (for $A_R \sim 3 \cdot 10^{-4}$) with complete consumption of the outer aluminized coating layer at that spot after a few weeks of exposure. Metallographic evidence permitted to infer, however, that since the inner coating layer had remained in place at least for the duration of the experiment, corrosion would mainly take place uniformly over the entire aluminized surface. If that would be the case, full outer layer consumption would be projected to occur in ~ 20 yr of service for $A_R \sim 3 \cdot 10^{-4}$. For $A_R = 0$, the outer layer would be consumed in ~ 10 yr of service. The shorter durability projections for $A_R = 0$ can be related to a momentary increase in solution pH (>8.8) observed early in the test, not noted for the cases of $A_R \sim 3 \cdot 10^{-4}$.

After consumption of the outer aluminized layer (assuming that the inner coating layer provides little to none corrosion protection to the base steel as described in Chapter 6), corrosion of the base steel starts and is expected to proceed at rates of $\sim 12 \mu\text{A}/\text{cm}^2$ in SW and $\sim 10 \mu\text{A}/\text{cm}^2$ in the other media. Per the assumptions presented in Chapter 6, the projected SL for the base steel would be ~ 6 yr in SW and ~ 8 yr in the other media.

8.2.2.2 Comparison with various forecasting methods.

For the specimens with $A_R \sim 3 \cdot 10^{-4}$ (and for $A_R = 0$ as well) in solution P (high scaling tendency, $\sim 7.5 < \text{pH} < \sim 8.5$ and moderate chloride content), the forecasting methods examined projected shorter durability estimates than those based on the laboratory tests. For $A_R \sim 0.03$, however, the AK Steel method was in close agreement with the laboratory projections whereas the other methods estimated durability by >20 yr above that from the laboratory projections.

For $A_R \sim 3 \cdot 10^{-4}$ and ~ 0.03 in solution NP (high alkalinity, $\sim 7.5 < \text{pH} < \sim 9$, and moderate chloride content), the durability estimates obtained from the AK Steel method were in reasonable agreement with the laboratory projections. In contrast, the other methods overestimated SL by >10 yr compared with the laboratory projections.

In solution SW (extremely aggressive solutions of low resistivity, nearly neutral pH, and high chloride content), the AISI method was in close agreement relative to the laboratory projections for all A_R , whereas the California method projected shorter service lives. In highly aggressive environments, no durability credit is given by the FDOT method and no SL projections are given by the AK Steel method for solutions with scaling indexes beyond ~ 800 ppm.

In solution C (low scaling tendency, nearly neutral pH, and moderate chloride content), the laboratory SL projections were in close agreement with those determined by the AK Steel, California, and FDOT methods, but much smaller than the durability projections by the AISI method. In contrast with the finding for unblemished aluminized steel, the projections from the laboratory tests with blemished material suggest that the AK Steel method may be a more appropriate alternative for environmental conditions approaching the low end of the recommended resistivity range. The results in this section would still support exploring the use of alternative guidelines such as the AISI method for hypothetical seawater service, as it was also the case for unblemished surface conditions.

In closing, it is noted too that the above results indicate that corrosion products from the steel portion may have played a role in creating or accelerating corrosion of the aluminized coating, in part resulting from the limited electrolyte volume involved in the tests. The small electrolyte volume was intended to be representative of worst-case culvert pipe conditions with stagnant water, or of occluded conditions for pore water on the soil side of a pipe. Long term field conditions may be more benign if there is frequent electrolyte renewal. Furthermore, the findings from these laboratory tests (Chapter 6) apply to aluminized steel with a surface condition resembling scratched or otherwise distressed material, with an exposed steel area representing ~3% and 0.03% of the total area. In actual metal forming and subsequently field application practice, the aluminized steel component (e.g. culvert pipe) is liable to surface distress, especially at the sharp bent regions which may expose base steel. The exposed steel area in those cases may be considerably less than 0.03%. Those conditions including the use of a more representative simulated natural water were examined with exploratory tests described in Chapter 7, but continuation experiments are necessary to elucidate the issue. Those examinations as well as additional field assessment will be the subject of follow up FDOT research now being planned.

8.2.3 Status of service life estimation for aluminized steel

The findings described in this chapter plus those stated for mechanically formed aluminized steel in Chapter 7 have revealed key characteristics of the corrosion performance of this material. At the same time, numerous open issues exist as summarized in detail above in Section 8.2.2.2 and earlier in Section 7.4.3. Because of those open issues, it is recommended that the findings documented in this report be viewed as interim determinations. Accordingly, it is proposed that recommendation of specific changes in the method used by FDOT to evaluate service life of aluminized pipe be postponed until a follow up investigation of field performance and concurrent laboratory tests (Section 7.4.3) has developed the necessary information.

8.3 Summary and Conclusions

Tentative durability projections were made for 16-gage aluminized sheet assuming penetration from both sides of the metal and considering consumption of the outer aluminized layer and of the base metal, using the corrosion rates estimated from the tests described in Chapter 6 and focusing on stagnant water conditions. It is emphasized that the projections are nominal in nature considering the short test times and specialized solution compositions used in those experiments. The results obtained in this investigation were used as a first step in proposing refinements of presently used durability guidelines of aluminized steel type 2 culvert pipe based on environmental composition.

- Projections from laboratory tests made for as-received (unblemished) 16-gage aluminized type 2 flat sheet durability were >100 yr for the least aggressive environment (P), and between 15 and 36 yr for the other media based on the assumptions in this investigation.
- For blemished surfaces, the projected service life from laboratory tests was >100 yr for the least aggressive environment (P) with the smallest coating break, whereas for the largest coating break service life was shortened to ~10 yr. For the other media, durability projections were between 16 and 33 yr. These long term extrapolations are nominal values that require confirmation or refinement by means of tests with more realistic simulated natural water solutions and from field evaluations.
- For unblemished aluminized steel the findings would support retaining the present FDOT guidelines for durability forecasting regardless of scaling tendency, at least for environments that approach the low end of the recommended resistivity application range and have neutral to mildly alkaline conditions.
- In contrast, for blemished surface conditions with significant amounts of exposed base steel and for the same environmental conditions as above, the AK Steel method may be a more appropriate alternative.
- The above conclusions are advanced as findings for consideration, but while still retaining the present FDOT approach for determining service life of aluminized steel pipe. Follow up testing in the laboratory and assessment of field performance is needed to establish to which extent the above conclusions should be applied, or how they should be supplemented or updated by considering the effect of other service or manufacturing variables.

9 A SENSITIVE TEST TO ASSESS THE CATHODIC BEHAVIOR OF ALUMINIZED STEEL TYPE 2 IN SCALE-FORMING WATERS

9.1 Introduction

An understanding of mechanistic issues is critical to increase the level of confidence in corrosion rate estimation of aluminized steel. A key mechanistic question is the nature and extent of the cathodic reaction taking place on the micrometer-scale Fe-rich constituent inclusions, e.g. FeAl_3 and Fe_2Al_5 embedded in the solid-solution aluminum matrix (Nisancioglu et al., 1981; Nisancioglu, 1990; Park et al., 1999) as the cathodic reaction will control the overall rate of metal dissolution. Consequently, experiments intended to obtain additional information on the cathodic behavior on aluminized steel in scaling-forming water were performed and are addressed in this chapter.

To isolate the cathodic reaction, experiments were performed by cyclically polarizing to potentials more negative than those encountered under normal E_{oc} conditions (e.g. < -900 mV). The experiments produced some kinetic parameter information useful for calibrating predictive models, but also revealed enhanced cathodic activity at the more negative polarization regimes that merits detailed discussion. The following describes the results and sets the stage for future investigation of the causes of that behavior.

Inclusions act not only as microsites for cathodic reaction but can also promote localized corrosion of aluminum surrounding the inclusions. For instance, Gundersen and Nisancioglu (1990) proposed that aluminum containing ~3% Fe exposed to nearly neutral pH solutions with negligible buffering capacity is preferentially dissolved in the vicinity of the inclusions as a consequence of a local pH increase due to the cathodic reaction occurring at the inclusions. Effectively, this leads to increased exposure of the inclusions at the metal surface, and therefore, an enhancement of the cathodic reaction with consequential further increase in the aluminum dissolution rate. In buffered solutions, however, localized alkalization in the vicinity of the inclusions may be prevented by neutralization of OH^- ions. Thereby preferential aluminum dissolution around inclusions is minimized, as confirmed by Nisancioglu and Holtan (1979) and later by Bjoergum et al. (1995) on AA1100 in buffered neutral pH, NaCl solutions.

At present, there is some controversy in regards to the type of dominant cathodic reaction at the potentials of interest in aluminum containing Fe-rich inclusions. Previous investigations (Seri and Furumata, 2002) conducted to determine the cathodic behavior of commercially pure aluminum exposed to aerated unbuffered 0.05 M NaCl solution at neutral pH identified H_2 evolution under activation control as the main cathodic reaction for potentials ranging from ~ -750 mV to ~ -1400 mV. Seri's results were in agreement with those reported by

Gartland (1987) for aluminum-coated steel exposed to aerated seawater. Rynders et al. (1994) and Park et al. (1999), however, reported O_2 reduction as the dominant cathodic reaction for AA6061 in aerated 0.6 M NaCl solution for up to $\sim -1,000$ mV_{SCE}.

Other types of inclusions, e.g. Cu compounds, have also been reported to act as sites for cathodic reaction sharing possibly similarities to Fe inclusions in the interpretation of the cathodic reaction mechanisms. For example, Vukmirovic et al. (2002) and later Jakab et al. (2005) documented that cathodic polarization of AA2024-T3 containing Cu-rich particles in unbuffered NaCl solution caused detachment of Cu inclusions (by undercutting due to corrosion of the surrounding aluminum) from the aluminum matrix. The mechanically/electrically detached metallic Cu adopted its own corrosion potential leading to formation of Cu^{2+} ions that later re-plated on the metal surface, resulting in an increase in the cathodic reaction rate.

9.2 Experimental Procedure

The aluminized steel type 2 used in this part of the investigation came from the same batch as those described in Chapter 6. Circular unblemished specimens of 95 cm² nominal surface area were cut out from the as-received aluminized steel sheet. The surface had no blemishes detectable by unaided visual inspection. Two specimen surface conditions were tested: as-received (AR) and finely ground (FG). The FG surface, indented to simulate an aged condition after rolling finish may have wasted away and better exposed inclusions, was prepared by hand-rubbing 1 μ m diamond metallographic polishing compound with a soft paper which removed ~ 5 μ m of the outer aluminized layer. Both AR and FG surfaces were ultrasonically cleaned with ethanol and stored in a desiccator before immersion. A 500-mL three-electrode test cell was used exposing horizontally one of the specimen faces (Figure 6-2). All potentials are reported in the SCE scale. For comparison, limited tests were conducted with as-melted bulk alloy specimens (supplied courtesy of Dr. N. Birbilis, Ohio State University) of composition Fe_2Al_5 , similar to that found as intermetallics in aluminized steel, and with commercially pure aluminum (AA1100-H14) sheet stock with nominal Al composition of $\sim 99\%$ and $\sim 1\%$ Fe maximum (supplied by Metal Samples, Inc.). The specimens were mounted in an epoxy resin exposing 1.4 cm² and 4 cm² for the intermetallic and the AA1100 respectively, wet-ground to a 600-grit surface finish, placed in a three electrode configuration corrosion cell (Princeton Applied Research®) with a ~ 0.5 cm Luggin capillary to specimen surface distance. Solution P was used in this part of the investigation with composition and properties the same as that shown in Table 6-2 in Chapter 6. The calculated LSI value was +1.4, a condition that was manifested by the formation of a precipitate of $CaCO_3$ to yield a ~ 0.5 mm thick powdery layer on the specimen surface shortly after exposure.

The immersion tests were conducted in duplicate for nearly 1,700 hr at 22 ± 2 °C. The solution was in contact with laboratory air through a small opening for the first ~410 hr of exposure followed by de-aeration with pure N₂ gas. E_{oc} and solution conductivity were monitored periodically. Also, cathodic cyclic polarization (CYP) tests were conducted sequentially at three different scan rates (1, 0.5, and 0.05 mV/sec) at selected exposure times with potentials shifted first from E_{oc} to ~-1.15 V (forward scan) and then back to E_{oc} (reverse scan). The potentials were corrected afterwards for ohmic drop taking into account the solution resistance R_s determined from the high frequency limit of EIS measurements. Given the buffering capacity of the solution, pH fluctuations at the metal surface were expected to be minimized during cathodic polarization. At the end of the immersion test, all specimens were examined by 40x optical microscopy and with a Scanning Electron Microscope (SEM). The Fe²⁺ concentration of the solution bulk was measured at the end of exposure by atomic absorption spectroscopy.

9.3 Results

Experimental trends exemplified in this Chapter are for single specimens unless otherwise noted. Trends obtained for duplicate specimens were comparable to those shown here. CYP tests of both surface conditions were conducted when the metals were still in passive state. No under-gasket crevice corrosion developed in any of the specimens for which results are reported.

9.3.1 Microstructure analysis

A SEM view of the typical microstructure of the near-surface cross section of the as-received aluminized specimens is shown in Figure 6-1 (Chapter 6). The unexposed surface morphology of the AR and FG conditions is shown in Figure 9-1. Light features are ~1.6 to 3.3 μm Fe-rich inclusions of approximate composition ~85% Al and ~15% Fe. The FG surface appearance was comparable to that of the AR material except that the inclusions covered respectively ~7.6% and ~5.5% of the total specimen surface. The matrix surrounding the inclusions was, as expected, richer in aluminum with average composition of ~98% Al and ~2% Fe. After long term exposure, ~2-10 μm diameter isolated pits were observed in the FG specimens but none in the AR specimens. In addition, light discoloration of the aluminized coating was noted on the FG specimens after ~800 hr of exposure whereas no discoloration was observed for the AR specimens even after ~1,700 hr exposure.

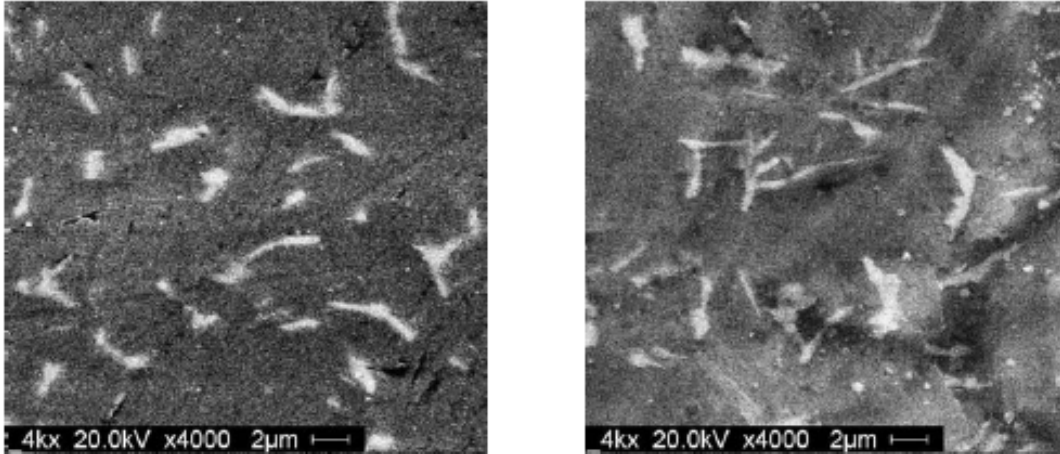


Figure 9-1. SEM images of the unexposed finely ground (FG, left) and as-received (AR, right) surface conditions. Light features correspond to Fe-rich inclusions.

9.3.2 Solution composition

The initial solution pH closely approached the lowest values reported in Table 6-2; increasing to 8.20 after 1,500 hr. Solution resistivity was also constant and close to the value reported in Table 6-2. The Fe^{2+} concentration in solution for both surface conditions at the end of exposure was below the minimum detection level of the instrument (0.01 ppm).

9.3.3 E_{oc} and CYP trends

Figure 9-2 exemplifies the E_{oc} evolution for up to ~1,700 hr for the duplicate specimens. Trends were similar for both FG and AR surface conditions. Shortly after immersion, E_{oc} values were ~-750 mV, and remained nearly constant for 24 hr after which the potential gradually decreased toward a terminal value of ~-900 mV, consistent with the E_{oc} trends obtained in Chapter 6. There unblemished as-received aluminized steel was documented was found to have extremely low nominal corrosion rates and correspondingly clean surface appearance for up to 3,000 hr of exposure in a solution similar to that used in this part of the investigation.

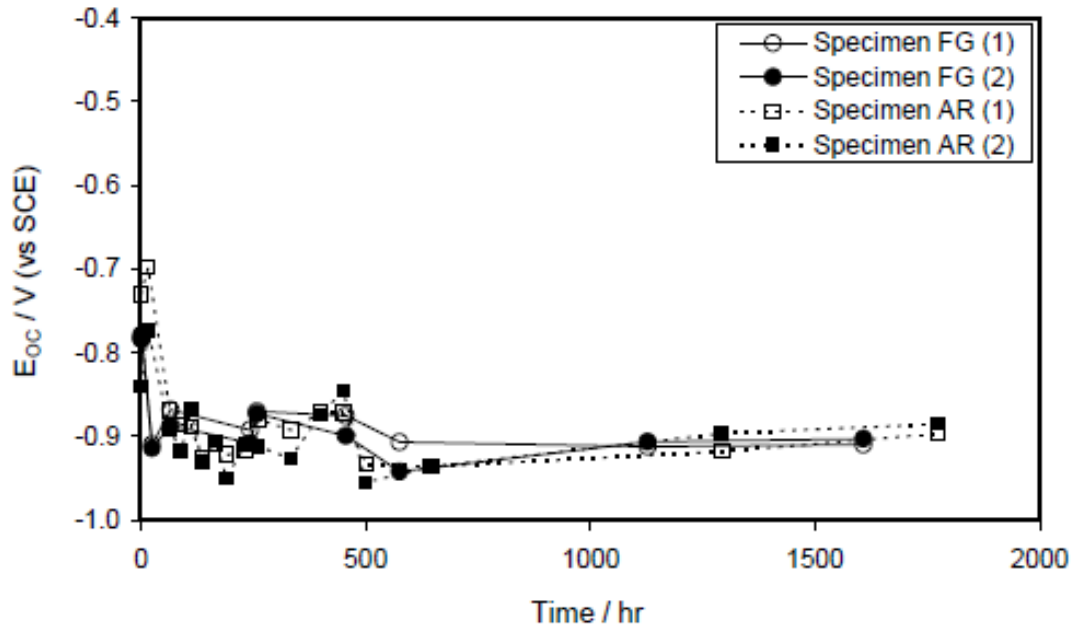


Figure 9-2. Eoc evolution of as-received (AR) and finely ground (FG) surface conditions. Specimen number is denoted in parenthesis.

Typical CYP (E vs. i_c , where i_c is the cathodic current density normalized to total specimen area) behavior of the FG and AR conditions in the naturally aerated solution is exemplified in Figure 9-3. Additional CYP tests conducted at different exposure times and in well-agitated solution showed comparable trends. At the two fastest scan rates both AR and FG conditions had similar CYP trends, with negligible hysteresis at 1 mV/sec and moderate hysteresis at 0.5 mV/sec. The curves for both surface conditions seemingly exhibited a typical activation polarization regime with apparent cathodic Tafel slopes of ~ 170 - 250 mV/dec, comparable to those reported by Armstrong and Braham (1996) for commercially pure aluminum in NaCl solution, and values of i_c at the starting E_{oc} of $\sim 10^{-8}$ – $7 \cdot 10^{-8}$ A/cm². At the apex potential, i_c for the AR condition was $\sim 2 \cdot 10^{-6}$ A/cm² at 1 mV/sec, approximately two times smaller than that for the FG conditions. At the lowest scan rate, 0.05 mV/sec, the polarization curves showed much more pronounced hysteresis and greater current densities at the apex potential for both surface conditions than in the faster tests. In all cases, the i_c values at each potential for the reverse scan was larger than those recorded for the forward scan, suggesting a large signal pseudo-inductive response of the system for negative potential excursions from E_{oc} .

Figure 9-4 shows comparable tests for the FeAl and Al1100 specimens. Those were normally kept polarized at -850 mV (potential representative of the typical E_{oc} of aluminized steel), which was not their natural E_{oc} so the starting point of their CYP curves is not at zero current density but rather at the steady state polarizing current density ($> \sim 0.2$ μ A/cm² for both materials). Additional CYP tests conducted at different exposure times showed comparable trends. For all scan rates, hysteresis was relatively large for FeAl, but not for Al1100.

The curves showed steep cathodic slopes in agreement with the results reported by Seri and Furumata (2002), with i_c values for the reverse scan larger than those for the forward scan. Values of i_c at the apex potential were comparable to those obtained for the FG specimens. Additional experiments conducted on specimens exposed to a well-agitated solution did not cause a significant change in i_c . Figures 9-5 and 9-6 show results of tests as in Figures 9-3 and 9-4, respectively, but conducted while de-aeration had been in progress for at least 72 hr. Additional CYP tests conducted at different exposure times showed comparable trends to those in Figures 9-5 and 9-6. The CYP curves at the faster scan rates for the two surface conditions and the alloys showed comparable trends to those under aeration. At 0.05 mV/sec, however, there was less hysteresis than in the aerated case notably for the AR and FG conditions but also for the alloys. The starting E_{oc} values were in general more negative (~ -40 mV) than for the aerated solution for both AR and FG conditions, although the i_c values at the apex potential were not much changed. After solution re-aeration for >48 hr, the starting E_{oc} and CYP behavior reverted in all cases to that obtained before de-aeration.

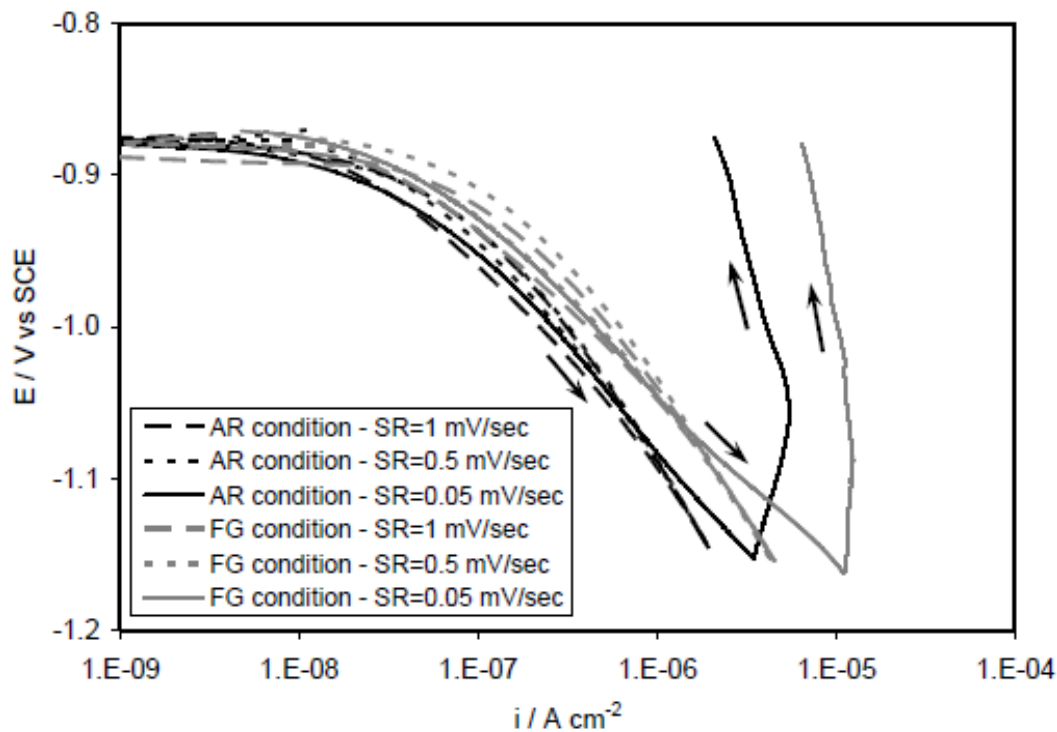


Figure 9-3. Cyclical cathodic polarization of as-received (AR) and finely ground (FG) surface conditions in unstirred naturally aerated solution at 408 hr of exposure. Return scan current was always greater than for the forward scan as exemplified by arrows.

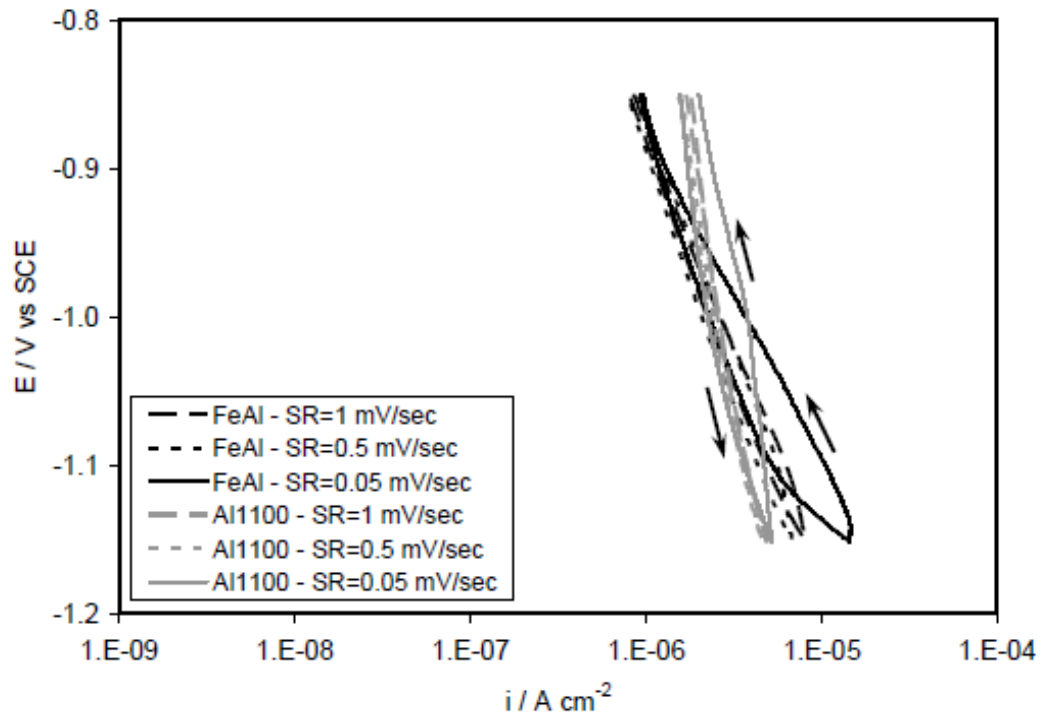


Figure 9-4. Cyclical cathodic polarization of the FeAl and Al1100 alloys in unstirred naturally aerated solution at 408 hr of exposure. Return scan current was always greater than for the forward scan as exemplified by arrows.

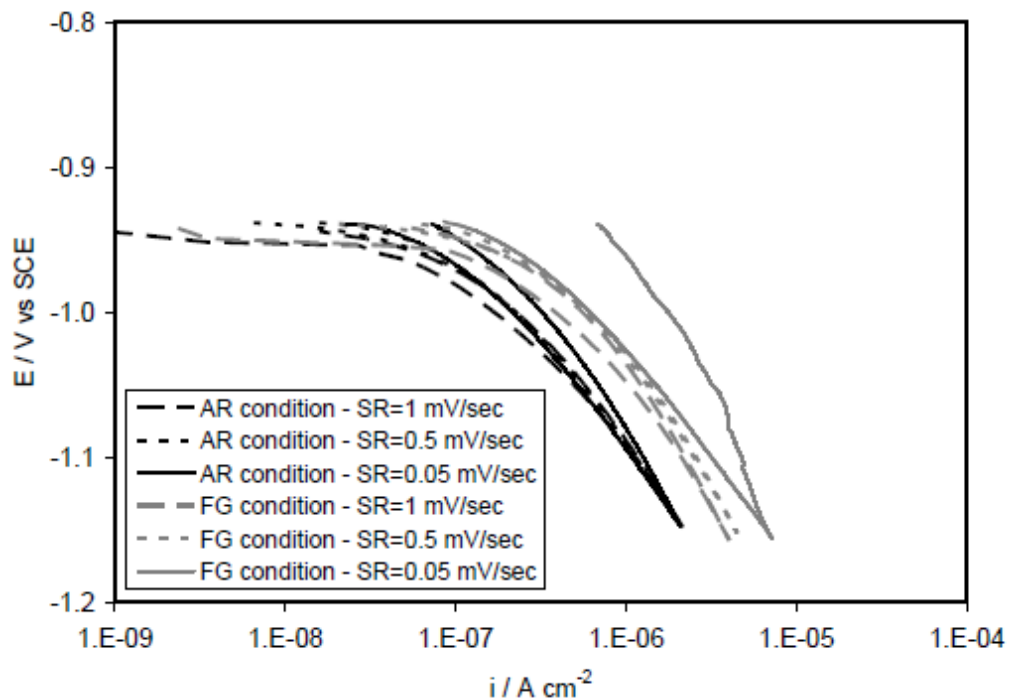


Figure 9-5. Cyclical cathodic polarization of the as-received (AR) and finely (FG) surface conditions in unstirred deaerated solution after 650 hr of exposure.

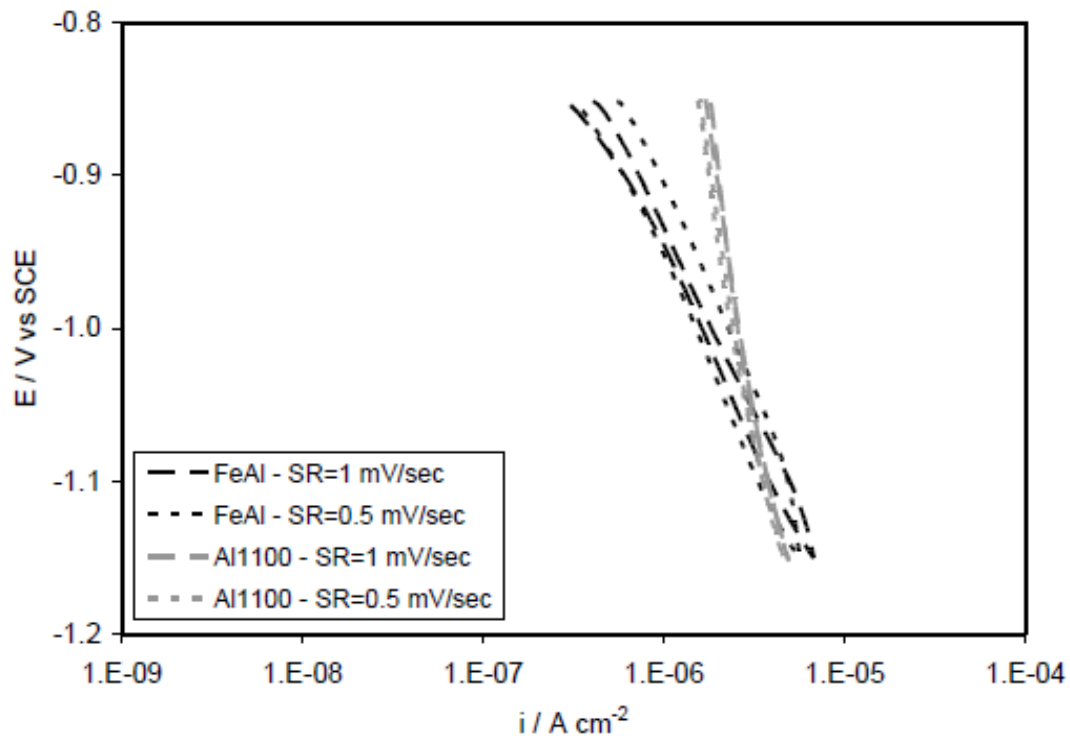


Figure 9-6. Cyclic cathodic polarization of the FeAl and Al1100 alloys in unstirred deaerated solution after 650 hr of exposure.

9.4 Discussion

In both the aerated and deaerated tests the i_c values at a given potential for the AR and FG conditions were in a ratio $\sim 2:1$, respectively, while the SEM examination indicated a ratio of the same order ($\sim 1.4:1$) for the area fraction covered by Fe-rich inclusions. The shape of the polarization curves during the forward scan at the fast scan rates and the lack of sensitivity to solution agitation suggest activation-limited control over much of the test cycle. Those observations are consistent with the Fe-rich inclusions acting as microelectrodes for the cathodic reaction, to an extent that depends strongly on the amount of those inclusions as noted elsewhere (Nisancioglu, 1990) for comparable systems. The nature of the main cathodic reaction(s) active in the potential regime examined is not entirely clear; a situation not uncommon in studying aluminum alloys (Moon and Pyun, 1998). O_2 reduction (OR) can be expected under aeration to be the dominant cathodic reaction at ~ -900 mV E_{oc} . Since that is in the order of the reversible potential for the water/hydrogen system at the near neutral pH of the system, H_2 evolution (HE) may not yet be important. This expectation is supported by the observed decrease in E_{oc} to more negative values upon de-aeration. However, the decrease was modest (~ 40 mV) considering that de-aeration was effectively $\sim 99\%$ based on dissolved oxygen measurements. It is possible then that HE was proceeding at an incipient rate at

the former E_{oc} , and that the 40 mV decrease was enough added over-potential for the rate of HE to be sufficient for establishing a new mixed potential when combined with the anodic reaction.

Another reason to expect HE to be important at the more negative potentials is that the cathodic reaction maintained its activation-limited behavior after de-aeration, at the rates that were comparable to or even higher than before in some cases. The size and typical separation of the inclusions, which is only a few μm (Figure 9-1), is significantly less than the depth δ of the Nernst layer (e.g. several hundred μm (Kaesche, 1985) typically encountered under the nearly stagnant/lightly stirring conditions used. Thus, the diffusion-controlled current density would be given approximately by $i_L = nFC_B D/\delta$ where n , C_B and D are the valence, bulk concentration and diffusivity of the species undergoing reduction. For OR, $n=4$, $D \sim 2 \cdot 10^{-5} \text{ cm}^2/\text{sec}$ and $C_B \sim 3 \cdot 10^{-7} \text{ M}$ under aeration, so for the expected δ values i_L would be $> \sim 10 \mu\text{A}/\text{cm}^2$, which is larger than most of the forward scan i_C values observed. However, under de-aeration i_L for OR would become about two orders of magnitude smaller, with values in the order of 0.1 to $1 \mu\text{A}/\text{cm}^2$, but such limitation was not observed in the cathodic curves under de-aeration even at the low scan rates. Yet, if diffusional transport were not an issue, the sustained high cathodic reaction rates under de-aeration would also be inconsistent with the usual first order kinetics for OR, were i_C is proportional to the concentration of O_2 in the electrolyte. Those discrepancies do not apply to HE, which at the solution pH is most likely to proceed by direct water reduction, which is neither subject to concentration polarization nor greatly dependent on O_2 concentration.

It would appear then that while OR is significant (at least for the forward scans) near the aerated E_{oc} , HE becomes dominant at the more negative potentials perhaps aided by having a smaller Tafel slope than that of OR. It is cautioned that invoking HE does not explain all the polarization effects observed upon de-aeration. For example, upon averaging results of multiple specimens, cathodic currents were somewhat higher after de-aeration. In the context of a simple mixed potential scenario, it would be necessary to propose an increase in the rate of both the anodic and the cathodic reactions, in the appropriate proportions, to explain both a decrease in E_{oc} as well as an increase in the cathodic reaction rates. The present evidence is insufficient to identify if and how an anodic rate increase takes place upon de-aeration and this issue shall remain for later investigation.

Setting aside the issue of the identification of the cathodic reaction, the most striking feature demanding explanation is the strong hysteresis present in the return cathodic curve, notably for the FG condition, as well as the much lesser extent of hysteresis upon de-aeration. Clearly, the extent, direction, and scan rate dependence of the observed hysteresis indicate that the aluminized surface became an increasingly better cathode as the cathodic reactions progressed, but the mechanism for such increase and its dependence on

aeration is not evident. Detailed elucidation of the above issues would require additional experimental evidence such as surface analytical data and controlled transport experiments (e.g. using a rotating disk electrode (Newman, 1966)) that are beyond the scope of the present investigation. Instead, a tentative scenario will be presented below that accounts for the observed behavior in the aerated condition, and for some of the features seen after de-aeration. The scenario may serve as a first step in formulating a future specialized study of the problem. The approach is inspired by well-documented models of cathodic enhancement in aluminum-copper alloys by deposition of copper dissolved in aqueous media (Vukmirovic, 2002).

Analogous to those models, it is speculated that upon cathodic polarization below the starting E_{oc} a species that serves as an efficient host for the operating cathodic reaction (in the following assumed to be only HE for simplicity) deposits somewhere on the aluminized surface. That new surface is in addition to the initially present inclusions, and may have a higher exchange current density for the cathodic reaction than the inclusions. Thus, a small amount of deposition may have a strong effect so that even a small initial concentration of the depositing species in the solution could suffice and even not become exhausted from the solution throughout the entire polarization cycle. The rate of deposition is finite, so consistent with observation the effect would be stronger at the lower scan rates. On first approximation, the cathodic current due to the deposition reaction may be considered to be small compared to that of the main cathodic reaction. Also as an approximation, only a single anodic reaction will be assumed for the cathodic potential regime explored, modeled as potential-independent passive Al dissolution at a constant rate i_{p2} .

The tentatively proposed deposition reaction is Fe reduction ($Fe^{2+} + 2e^- \rightarrow Fe$), where the Fe^{2+} ions are available from prior preferential dissolution of the inclusions. The inclusions may have been in electronic contact with the rest of the metal, or as free particles separated from the matrix due to undercutting cathodic corrosion of the surrounding aluminum (Vukmirovik et al., 2002; Park et al., 1999). Assuming equilibrium with some metallic Fe on the surface at the beginning of the potential scan, the initial Fe^{2+} ion concentration in the pH range of interest is given by $[Fe^{2+}]_i = 10^{(E_{oc} - E_0)/0.03}$, where $E_0 = -681$ mV is the standard Fe^{2+}/Fe redox potential (Bockris and Reddy, 1970). The typical E_{oc} values of -900 mV and -940 mV for the aerated and de-aerated conditions, respectively, correspond then to $[Fe^{2+}]_i$ values of $\sim 3.6 \cdot 10^{-8}$ M to $\sim 3.6 \cdot 10^{-9}$ M (0.002 ppm and 0.0002 ppm), which are consistent with the upper bound concentration observed by atomic absorption spectroscopy. The Fe^{2+} ions present in the solution at the beginning of the polarization cycle increasingly reduce to deposited Fe as cathodic polarization progresses. For simplicity, a high cathodic reaction exchange current density on the newly formed surface will be assumed, so the required amount and rate of deposition is small and $[Fe^{2+}]$ can be treated as being approximately constant over the polarization cycle. Given a slow enough scan rate, the Fe deposition will become significant and the main cathodic

reaction rate will be noticeably greater in the return scan, thus resulting in pseudo-inductive hysteresis as observed experimentally.

The observation of lesser hysteresis for the de-aerated than for the aerated solution in AR and FG surface conditions may be explained by the effect of aeration on the starting E_{OC} (~40 mV higher than in the de-aerated solution). The order-of-magnitude leaner initial Fe^{2+} concentration noted above for the de-aerated solution would result in a correspondingly lower extent of new Fe deposition, and hence, less pronounced hysteresis. At the more negative starting E_{OC} under de-aeration, there would have been some Fe deposition on the surface, which might account for the similar or greater cathodic reaction rates observed after de-aeration compared with before. As indicated above, it would be, however, necessary to invoke a stronger anodic reaction rate upon de-aeration (an increase of i_{P2} in the above simplified assumptions) to explain a more negative E_{OC} in the face of similar or increased cathodic action. That hypothesis and its operating mechanism would necessitate additional experimental evidence for evaluation, so the following will focus on the response observed under aerated conditions.

The predictions of the above scenario for aerated conditions were evaluated by a simplified quantitative model that was formulated by assigning Tafel kinetics to both HE and Fe deposition, with nominal exchange current densities i_{OCi} , equilibrium potentials E_{eqCi} and cathodic Tafel slopes β_{Ci} where the subscript i is replaced by 1 for Fe and by 2 for HE accordingly. HE is assumed to take place at the Fe-rich inclusions initially present, and at the newly deposited metallic Fe surface. The region where Fe deposition takes place is not known, so a cathodic current density for Fe deposition will be nominally assigned to act on the specimen surface not initially occupied by the inclusions or any previously deposited Fe, leaving it up to the choice of i_{OC1} and related parameters to obtain appropriate scaling factors. The aluminum on the rest of the surface is assumed to be experiencing slow passive dissolution at a current density i_{P2} . The solution has high conductivity so the ohmic potential drop is neglected. Per the assumptions above, the time-dependent total cathodic current under activation control comprises that of HE and Fe deposition according to Equation 9-1, where I_{C21} and I_{C2N} are the HE currents on the inclusions and on the newly deposited Fe, respectively, and I_{C1} is the Fe deposition current on the rest of the surface.

$$I_{CT}(t) = I_{C21}(t) + I_{C2N}(t) + I_{C1}(t) = I_{C2}(t) + I_{C1}(t) \quad (9-1)$$

It is also assumed that HE on both inclusions and newly deposited Fe has the same kinetic parameters except for the exchange current density, which is i_{OC1} on the inclusions and greater by a multiplier factor k_2 on the deposited Fe. Thus, $I_{C2}(t)$ can be written as shown in Equation 9-2, where F is the Faraday constant, $E(t)$ is the applied potential, A_{C0} is the initial Fe-rich inclusion area, and

$$\frac{k_1}{2F} \int_0^t I_{C1}(\tau) d\tau \text{ gives the area of the deposited Fe.}$$

$$I_{C2}(t) = i_{0C2} \cdot \left(A_{C0} + \frac{k_1 \cdot k_2}{2F} \int_0^t I_{C1}(\tau) d\tau \right) \cdot 10^{\frac{E_{eqC2} - E(t)}{\beta_{C2}}} \quad (9-2)$$

The parameter $k_1 = A_s N_A$ is the Fe coverage constant in cm^2 per moles of Fe^{2+} , where N_A is Avogadro's number, and A_s represents the area described by a simple cubic structure of Fe atoms with a typical lattice parameter of 0.28 nm (Kepaptsoglou et al., 2007).

Per the assumed locus of Fe deposition $I_{C1}(t)$ is calculated according to Equation 9-3, where A the total specimen area.

$$I_{C1}(t) = i_{0C1} \cdot \left(A - \left(A_{C0} + \frac{k_1 \cdot k_2}{2F} \int_0^t I_{C1}(\tau) d\tau \right) \right) \cdot 10^{\frac{E_{eqC1} - E(t)}{\beta_{C1}}} \quad (9-3)$$

Then, the net cathodic current is given by Equation 9-4.

$$I_{\text{net}}(t) = I_{C2}(t) + I_{C1}(t) - i_{P2} \cdot \left(A - \left(A_{C0} + \frac{k_1}{2F} \int_0^t I_{C1}(\tau) d\tau \right) \right) \quad (9-4)$$

Figure 9-7 shows solutions to Equation 9-4 numerically calculated by finite differences for the aerated condition. Typical values of β_{C1} and i_{0C2} (Kaesche, 1985) were chosen along with values of β_{C2} and i_{P2} numerically calculated from the CYP tests conducted at 1 mV/sec (see Table 9-1). Consistent with specimen dimensions and surface analysis, A was set to 95 cm^2 and A_{C0} to 5 cm^2 (AR condition). A nominal initial Fe^{2+} concentration equal to 0.002 ppm was chosen, calculated as above. Plausible input values of i_{0C1} and k_2 were chosen such that the model calculations simulated a typical CYP trend of the AR condition at 0.05 mV/sec. Those input values were used for the other scan rates as well.

Table 9-1
Parameters Chosen Cyclical Polarization Modeling

β_{C2} mV dec^{-1}	β_{C1} mV dec^{-1}	i_{0C2} A cm^{-2}	i_{0C1} A cm^{-2}	i_{P2} A cm^{-2}	k_2	k_1 $\text{cm}^2 \text{ mol}^{-1}$
200	120	10^{-8}	10^{-10}	$5 \cdot 10^{-8}$	100	$4.7 \cdot 10^8$

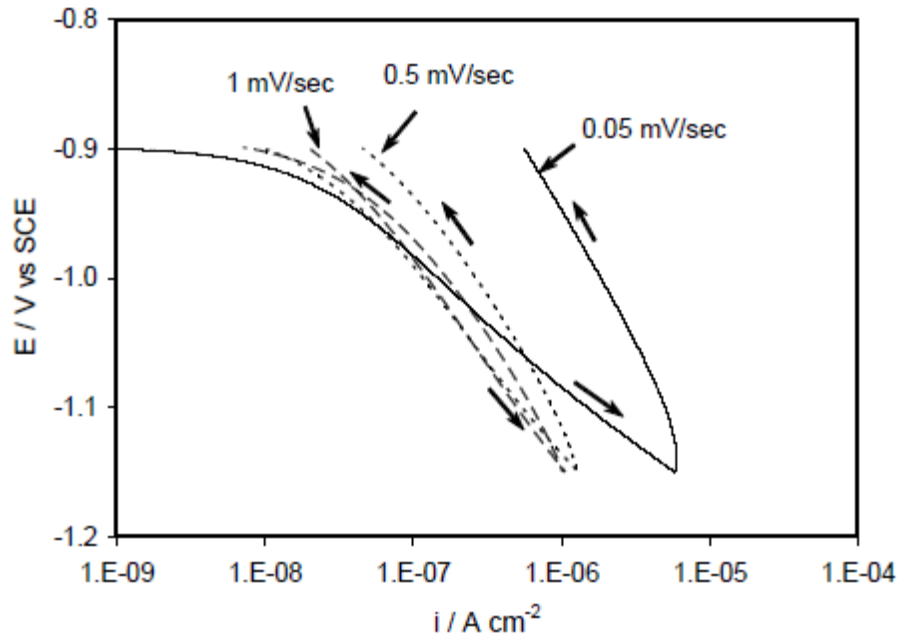


Figure 9-7. Model results for the as-received (AR) surface condition in the aerated solution.

The model results were in reasonable agreement with the experimental trends. However, a slight discrepancy of the model results respect to the experimental data is noted for the return scan at 0.05 mV/sec for the aerated solution. A momentary increase of the experimental cathodic current density followed by a steeper slope was observed for the slowest return scan, not quite well reproduced by the simplified model. This observation is not clear at this moment but it can be speculated that if the Fe deposition mechanism is assumed to be a very slow process compared to the slowest scan rate examined, then its response to the potential change is not instantaneous so that Fe^{2+} ions continue to deposit even during the return scan. The resulting effect yields a pseudo-inductive behavior in accordance with the experimental results.

9.5 Summary and Conclusions

- Cyclic polarization tests conducted on the as received and finely ground surface unblemished aluminized steel type 2 exposed to a solution with high scaling tendency, high alkalinity and moderate chloride content yielded cathodic current densities for the finely ground surface condition that were about twice as much as those recorded for the as-received surface condition, consistent with larger amounts of Fe-rich inclusions noted on the finely ground surface.
- Experimental evidence presented here suggests that there is no clear indication about the type of the cathodic reaction(s) taking place at the Fe-rich inclusions. However, experimental results (e.g. change in E_{oc} due to

solution de-aeration) permitted to speculate that O₂ reduction was the main reaction at potential of ~-900 mV and H₂ evolution reaction took over at more negative potentials.

- Cyclic polarization tests also showed that for the smallest scan rate examined (0.05 mV/sec) a significant hysteresis existed between the cathodic current densities for the forward and reverse scans. The amount of hysteresis decreased for increasing scan rates (0.5 and 1 mV/sec) associated to the amount of Fe²⁺ ions being deposited during polarization. It is proposed that larger hysteresis was observed for the aerated solution compared to the de-aerated solution, especially at the smallest scan rate, because the amount of Fe²⁺ ions is larger in the aerated solution.
- The results obtained from a simplified quantitative model were in reasonable agreement with the experimental results.

10 MICROBIOLOGICALLY-INDUCED CORROSION

10.1 Introduction

Microbiologically influenced corrosion (MIC) assessment is introduced as a possible component of an improved model or method for predicting corrosion rates and/or durability of metallic culverts and related highway components. Determination of factors relevant to MIC is considered as a part of environmental characterization for service life prediction.

Microbiologically influenced corrosion (MIC) has been identified as one of the major causes of corrosion failures of underground metallic structures such as culvert pipes, oil and gas transmission pipes, and storage tanks (Peng and Park, 1994; Lane et al., 2005; Nizhegorodov et al., 2008), a consequence of the ubiquitous presence of microorganisms in soil and water. MIC of mild steel, stainless steel, copper and its alloys, galvanized steel, and aluminum have been reported in literature and themes relevant to corrosion of buried metals used in road construction are summarized in this chapter. Algae, fungi, and bacteria are among the most important microorganisms that contribute to MIC (Lane, 2005).

10.2 Background

10.2.1 Features of MIC

Indirect and direct effects that a biological agent has on the corrosion of metal and metal alloys have been termed microbiologically influenced corrosion (MIC) and biocorrosion, respectively (Lewandowski, 2003), but for this report the term MIC will include both indirect and direct effects. Microorganisms can shift the thermodynamic state or alter the corrosion reaction kinetics at the metal surface to either enhance or inhibit corrosion, and along with their enzymes or metabolic products, distinguish biotic from abiotic corrosion (Duquette and Ricker, 1985; George et al., 2003).

Microorganisms play a main role in the adherence processes leading to biofilm formation. Biofilms, as well as biofouling deposits, modify drastically the characteristics of the metal/solution interface where the corrosion reaction takes place (Videla, 1996). Microorganisms within a biofilm can accelerate and control corrosion reactions by several mechanisms: by establishing concentration cells or differential aeration cells, by production of aggressive metabolites such as acids, sulfide, and phosphine; and through direct metal oxidation and reduction reactions, as examples (Miller and King, 1975; Little and Wagner, 1985; Lewandowski, et al., 1994; Wagner and Ray, 1994). A biofilm can alter the chemistry of a metal's surface, e.g., by lowering the pH, reducing O₂ tension, or catalyzing oxidation/reduction reactions (Miller and King, 1975; Lewandowski, et al., 1994).

Biofilms can inhibit corrosion by acting as a barrier to diffusing gases such as oxygen or hydrogen sulfide, and by harboring bacteria that consume oxygen through respiration, release corrosion inhibiting chemicals, or produce antibiotics (Örnek et al., 2002; Little et al., 2003). Polysaccharides present in biofilms can buffer the pH in regions of active corrosion, and the negative charge on carboxyl ions can repel chloride ions, reducing chloride ion activity at the metal surface (Örnek et al., 2002).

Among the many microorganisms that have been implicated in the corrosion of metals and alloys are iron-oxidizing, sulfur-oxidizing, iron-reducing, sulfate-reducing, acid-producing, methane-producing, and slime-producing bacteria. Enterobacteriaceae (bacteria that inhabit the gut) found on corroding steel piles in a seawater harbor and grown on metal coupons in seawater under laboratory conditions enhanced steel corrosion rates over abiotic conditions (Bermont-Bouis et al., 2007). Sulfate-reducing bacteria (SRB) are commonly found to be responsible for MIC in anaerobic environments (Javaherdashti, 1999).

Most corrosion reactions in MIC are localized in nature. Localized forms of corrosion include pitting, crevice, galvanic, intergranular, dealloying, and under-deposit corrosion and stress-corrosion cracking (George et al., 2003; Lane, 2005; Javaherdashti et al., 2006; Antony, et al., 2008; Nizhegorodov et al., 2008). Microbes may preferentially colonize a metal's surface when the surface has been sensitized by heat treatment e.g., from welds, at grain boundaries, and at cracks or crevices (George et al., 2003). Vanhaeke et al. (1990) demonstrate that bacterial species *Pseudomonas aeruginosa* can attach to the surface of stainless steel in seconds, even to an electropolished surface. Metal alloys such as nickel, chromium, or molybdenum that are present in steel can affect metabolic activity of bacteria present in biofilms (Lopes et al., 2006); likewise, bacterial activity will influence the speciation of metal ions and corrosion products (Clayton et al., 1994; Ilhan-Sungur et al., 2007). SRB can facilitate corrosion of zinc-coated steel, even though zinc is known to be toxic to SRB (Ilhan-Sungur et al., 2007).

Kajiyama et al. (1994) have shown that in a laboratory MIC testing with ductile cast iron, microbiological activities enhanced the rates of corrosion of the ductile cast iron in soils in approximately the following ascending order: sulfate reducing bacteria (SRB), iron oxidizing bacteria (IOB), and iron bacteria (IB) with sulfate oxidizing bacteria (SOB). Kawai et al. (2003) concluded that accelerated corrosion of carbon steel was caused by uneven distribution of dissolved oxygen on carbon steel, resulting from the heterogeneity of bacterial consortia habitat. According to George et al. (2003), stainless steel is especially vulnerable to corrosion in cooling water systems where circulating water is warm, highly oxygenated, and of near neutral pH.

A number of investigators have reported that MIC can result in severe and rapid failure of steels in circumstances where microorganisms are present and aggressive ionic species such as chlorides are present. For example, Beech and Campbell (2008) found that MIC-accelerated corrosion of steel piling at a harbor's low water line increased from an expected rate of 0.05 mm/yr to 0.3 - 1 mm/yr.

Oxygen and organic carbon availability also play important roles in observed corrosion rates. For example, Jack (2001) presented evidence that corrosion rates of steel coupons exposed to SRB-infested wet clay soil had corrosion rates of 0.2 mm/yr (general) and 0.7 mm/yr (pitting), but when air was added the corrosion rates reached 1-5 mm/yr. Marsh et al. (2005) has postulated that accelerated corrosion of steel seen in Duluth-Superior Harbor, Minnesota, is a consequence of an observed increase in dissolved oxygen concentrations (see Section 3.2.3.1).

Many species of MIC-related bacteria consume organic carbon either as a source of electrons to drive reduction-oxidation reactions or for cellular growth, as outlined in Section 10.2.2 (Waksman and Starkey, 1923; Uhlig and Revie, 1985; Magot et al., 1997; Little et al., 1998; Jack, 2001; Lee and Newman, 2003). Westrich and Berner (1984) offer evidence that in marine sediments, bacterial sulfate reduction is carbon-limited. It is recommended that future test site assessments for corrosivity include a standard measure of soil or water organic content (Davies, 1974; ASTM, 2003), as appropriate, to elucidate the relationship between organic content and observed *in-situ* corrosion rates and to determine a criterion for corrosivity.

10.2.2 Characteristics of bacteria that are agents of MIC

10.2.2.1 Sulfate-reducing bacteria

Sulfate-reducing bacteria (SRB) “breathe” sulfate, sulfite, thiosulfate, and/or sulfur instead of oxygen. Oxidized sulfur compounds are reduced to sulfide. SRB “eat” lactate or acetate as a source of electrons, but can also use hydrogen gas as a source of electrons. SRB require other microorganisms to degrade available organic matter into lactate or acetate (Jack, 2001), however, more than 100 different compounds have been identified as carbon or energy sources for SRB (Magot et al., 1997). Bacterial sulfate-reducing reactions are favored for anaerobic conditions where the redox potential is less than -400 mV, pH is greater than 5.5, the free oxygen content is low and sulfate is present (Paul and Clark, 1989) along with organic compounds (Uhlig and Revie, 1985). Czechowski and Rossmore (1980) reported that lactate hydrogenase activity in *Desulfovibrio desulfuricans* was stable between pH 5.8 and 8.4 and had maximal activity at a temperature of ~40 °C. Properties of the bulk water or soil solution may not be predictive of anaerobic conditions, as steep oxygen and nutrient gradients exist within slimes or tubercles (Little and Wagner, 1997). Examples of

sulfate-reducing bacteria include *Desulfovibrio* species *desulfuricans*, *vulgaris*, *salexigens*, and *sapovorans*; *Desulfotomaculum nigrificans*, *orientus*, and *acetoxidans*; *Desulfobulbus propionicus*; *Desulfuromonas acetoxidans*; *Desulfobacter postgatei*; *Desulfosarcina variabilis*; and *Desulfonema magnum* (Miller and King, 1975; Hamilton and Maxwell, 1985). According to Magot et al. (1997), by 1995 some 67 different species of SRB representing 20 genera had been described along with newly found anaerobic thiosulfate-reducing bacteria.

10.2.2.2 Sulfur-oxidizing bacteria

Of the many bacterial species that oxidize reduced sulfide to sulfur, thiosulfate, or sulfate, *Acidithiobacillus* species have been implicated in MIC (Little et al., 2000). *Acidithiobacillus thiooxidans* “breathe” oxygen, live in water and soil environments, and for their sole source of energy “eat” sulfur, sulfide, or thiosulfate, which are oxidized to sulfuric acid or sulfate in the process. Carbon needed for cell growth is supplied as atmospheric carbon dioxide, and neither carbonate nor organic carbon is a substitute. These bacteria thrive in pH 2.0 to 5.5, with optimal growth at pH 3.0-4.0 (Waksman and Starkey, 1923). *Acidithiobacillus ferrooxidans* species produce sulfuric acid from pyrite (FeS_2) (Miller and King, 1975). In contrast, *Acidithiobacillus denitrificans* species oxidize reduced sulfur compounds in either an aerobic or an anaerobic environment, can grow on organic media, and have an optimal growth at near-neutral pH (Waksman and Starkey, 1923). Examples of other species that can oxidize sulfur from either hydrogen sulfide or a sulfide mineral include *Acidithiobacillus albertis*, *neopolitanus*, *tepidarius*, *thermophilica*, *thioparus*, and *versutus*; *Leptospirillum ferrooxidans*, *thermoferrooxidans*; and *Sulfobacillus thermosulfidooxidans* (Little et al., 2000).

Acidithiobacillus species are known to populate the interior crown of sewer piping. Hydrogen sulfide gas escaping from the rotting sewage is converted into sulfuric acid by these bacteria and the sulfuric acid destroys the pipe material (Little et al., 2000). Conceptually, this type of damage can occur in culvert piping if organic-rich sediment accumulates in the invert. As anaerobic conditions develop, microbial consortia within the sediments convert inorganic or organic sulfur to hydrogen sulfide. Possible evidence of this can be seen in Figure 10-2, where a distinct zone of corrosion exists above and parallel to the water/sediment line.

10.2.2.3 Iron-related bacteria

Iron-related bacteria include both iron-oxidizing and iron-reducing bacteria. Iron-oxidizing and iron-reducing bacteria may be “metal-depositing” and “iron-respiring”, respectively, but the latter descriptions are not comprehensive. Iron bacteria are thought to be important in MIC, although their contribution to MIC appears related to their role within a microbial consortium. For example, an iron-reducing bacterium *Shewanella oneidensis* can in the absence of oxygen

“breathe” ferric iron and “eat” organic carbon to supply its needs for growth (Little et al., 1998; Lee and Newman, 2003); abiotic re-oxidation of ferrous to ferric iron keeps the oxygen pressure low. These and similar bacteria can reduce ferric iron whether present as synthetic iron oxides (Little et al., 1998), at the surface of steel (Lee and Newman, 2003; Newman et al., 2006), or embedded in clay minerals (Kostka et al., 2002). The maintenance of a low oxygen pressure (Lee and Newman, 2003) and/or the growth of a protective Fe_xS_y film in the presence of SRB (Lee et al., 2008) may explain observed inhibition of corrosion in laboratory experiments with monocultures and mixed cultures of iron-reducing bacteria, respectively.

Iron-oxidizing bacteria obtain energy for growth from the oxidation of ferrous to ferric iron with oxygen (Starosvetsky et al., 2001) or nitrate (Straub et al., 2001) as electron acceptors. *Sphaerotilus* species need organic carbon for growth, but *Gallienella* species obtain enough energy from iron metabolism to grow on carbon from carbon dioxide (Mulder, 1964). Enzyme-catalyzed oxidation rates are much higher than abiotic rates and copious amounts of rusty slime or distinctive tubercles reveal the deposition of the reaction product ferric hydroxide (Starosvetsky et al., 2001). On corroding steel, pitting is present beneath the tubercles (Starosvetsky et al., 2001; Xu et al., 2008). In laboratory experiments, biotic steel corrosion rates were higher than abiotic rates in monocultures of iron-oxidizing bacteria (Starosvetsky et al., 2001) or mixed cultures of iron-oxidizing bacteria and SRB (Xu et al., 2008).

Under low pH conditions such as is found near acid mine drainage, acidophilic bacteria such as *Acidiphylum organovororum* can reduce ferric to ferrous iron when grown with organic carbon as food, (1) in the presence of or absence of oxygen, and for (2) soluble versus insoluble forms of ferric iron (Johnson and McGinness, 1991). In the presence of oxygen and organic carbon, acidophilic bacteria *Acidithiobacillus ferroxidans* and *Leptospirillum ferroxidans* can oxidize ferrous iron to ferric iron (Johnson and McGinness, 1991).

In a native microbial consortium on corroding steel, both iron-oxidizing and iron-reducing bacteria are likely present together. Bacterial-mediated cycling of iron between ferrous and ferric states has been observed in mixed cultures of iron-oxidizing and iron-reducing bacteria (Johnson and McGinness, 1991).

Growth of iron minerals can occur from the activity of iron-related bacteria: iron that is bound to the bacterial surface serves as a nucleation site for crystal growth, counter ions (calcium, silica, or sulfur, as examples) are contributed by surrounding media or by bacterial excretion, and water conditions—pH and oxygen content, for example—dictate the resulting crystal (Konhauser, 1998). Jeffreys and Melcher (2003) provide photographic evidence for a role of bacteria in iron-sulfur minerals formed on steel corroding in seawater.

10.2.2.4 Other bacteria

Bacteria that are capable of producing acids, methane, slimes, or that can grow in low nutrient environments have also been implicated in MIC. For example, acid-producing bacteria grow in the absence of oxygen and convert organic carbon compounds into organic acids such as lactic acid and acetic acid (*Clostridium acetivum*), which can shift the pH of their immediate environment to several pH units below the bulk pH (Beech and Gaylarde, 1999). These bacteria are likely to be found in a consortium of SRB. *Acidithiobacillus* species can convert reduced sulfur compounds to sulfuric acid (Section 10.2.2.2). Slime from *Pseudomonad* species includes carboxylic acids (White et al., 1986; Beech and Gaylarde, 1999).

Methanogens convert hydrogen gas and carbon dioxide into methane; Boopathy and Daniels (1991) have shown that methanogens can grow on hydrogen produced by the reaction of electrons with protons at the cathode of corroding mild steel. Metal corrosion rates were higher in the presence of methanogens than without, and both methane production and corrosion rates increased at low pH values, e.g, between pH 5.4 to 6.5 (Boopathy and Daniels, 1991).

Slime-forming bacteria, for example, sulfate-reducing *Vibrio* species or *Pseudomonad* species, excrete a polysaccharide that adheres to aluminum, mild steel, and stainless steel surfaces and increases the corrosion current density as an apparent consequence of partial surface coverage (White et al., 1986). Exudates from these bacteria may over time, however, extend to cover the entire metal surface and reduce oxygen, nutrient, and corrosion byproduct transfer rates and thus overall if not localized corrosion rates (Picioreanu and Loosdrecht, 2002). Figure 10-1 is a photograph of a rust-colored deposits—possibly bioslime—discovered in damaged aluminized steel type 2 culvert piping that was installed in Largo, Florida.

Many of the bacteria implicated in MIC are capable of surviving in low nutrient (oligotrophic) environments. Florida's Everglades is an example of an oligotrophic environment penetrated by roads, bridges, and piping. Seawater, freshwater, or soil environments that are characteristically poor in nutrients trigger in bacteria mechanisms for survival (Roszak and Colwell, 1987). Microorganisms adapted for low nutrients conditions may not respond to nutrient-rich culturing techniques. Survival mechanisms in bacteria include formation of spores that are resistant to destructive agents, both chemical and physical; a shift to a smaller size, rounder shape, and more numerous count; or development of abilities to scavenge nutrients including iron at very low concentrations (Roszak and Colwell, 1987).



Figure 10-1. Possible bioslime oozing from damaged seam (left) and on inside wall (right) of in-service aluminized steel type 2 culvert piping.

10.2.3 Mechanisms of MIC

Two general mechanisms have evolved to explain the interaction of microorganisms with a corroding metal surface, as summarized by Hamilton (2003). These models are based on laboratory experiments and failure analysis of corroded metal samples. The first and second of these two models describe the role of sulfate-reducing bacteria (SRB) on the surface of mild steel and manganese-oxidizing bacteria (MOB) on the surface of stainless steel, respectively, in facilitating corrosion.

10.2.3.1 Mechanism for SRB corrosion

The first mechanism for SRB corrosion of iron was proposed by Wolzogen Kühr and Van der Vlugt in 1934 and was called the cathodic depolarization theory (Miller and King, 1975). This mechanism was described in terms of the chemical reactions shown in Table 10-1.

In subsequent years, alternative explanations emerged and were summarized by King and Miller (1971): a role of bacteria in (1) supplying the metal surface with ferrous sulfides, which are efficient sites for the cathodic reaction, and in (2) producing acids such as hydrogen sulfide that may promote passivity breakdown and thus enhance the anodic reaction.

Table10-1
Cathodic depolarization theory

(Kühr and van der Vlugt, 1934, as cited by Miller and King, 1975)

(a) Anodic reaction	$4 \text{ Fe} \rightarrow 4 \text{ Fe}^{2+} + 8 \text{ e}^{-}$
(b) Electrolytic dissociation of water	$8 \text{ H}_2\text{O} \rightarrow 8 \text{ H}^{+} + 8 \text{ OH}^{-}$
(c) Cathodic reaction	$8 \text{ H}^{+} + 8 \text{ e}^{-} \rightarrow 8 \text{ H}$
(d) Cathodic depolarization* by bacteria	$\text{SO}_4^{2-} + 8 \text{ H} \rightarrow \text{S}^{2-} + 4 \text{ H}_2\text{O}$
(e) Corrosion product	$\text{Fe}^{2+} + \text{S}^{2-} \rightarrow \text{FeS}$
(f) Corrosion product	$3 \text{ Fe}^{2+} + 6 \text{ OH}^{-} \rightarrow 3 \text{ Fe(OH)}_2$
(g) Overall reaction	$4 \text{ Fe} + \text{SO}_4^{2-} + 4 \text{ H}_2\text{O} \rightarrow 3 \text{ Fe(OH)}_2 + \text{FeS} + 2 \text{ OH}^{-}$

*The term "cathodic depolarization" is frequently encountered in the MIC literature, with somewhat ambiguous meaning. In this instance the removal of a product of the cathodic reaction would presumably facilitate increase the rate of reaction (c).

According to Hamilton (2003), two key elements of the SRB corrosion mechanism are (1) electrical contact of iron sulfides with the corroding metal surface, and (2) direct involvement of oxygen in the corrosion process. A biofilm coats the surface of metal and in the natural environmental this biofilm contains a consortium of microorganisms that include aerobic and anaerobic bacteria, fungi, and/or algae. An oxygen gradient exists, with no oxygen where the biofilm is in contact with the metal and with oxygen where the biofilm is in contact with the atmosphere or oxygenated water.

In brief, as zero-valence iron (Fe^0) is oxidized at anodic sites (Equation 10-1), hydrogen gas evolved at cathodic sites is consumed by SRB to reduce oxidized sulfur compounds to hydrogen sulfide (H_2S) (10-2), which reacts with ferrous (Fe^{2+}) iron to form ferrous sulfide (FeS) (or more correctly, Fe_xS_y) (10-3). Ferrous sulfide is cathodic to iron and conducts electrons. Ferrous sulfide can form a protective film on the metal surface, but the film is easily ruptured and once ruptured, does not repassivate (Hamilton, 2003). Sulfide and ferrous ions diffusing through the biofilm are oxidized biotically and abiotically by oxygen to elemental sulfur (S^0) and Fe^{3+} oxyhydroxides, respectively. Elemental sulfur if coupled galvanically to iron is reduced to sulfide and thus enhances the cathodic reaction.



Hydrogen gas evolved at the metal surface (e.g., 10⁻²) is a source of electrons for SRB to respire sulfate (SO₄²⁻), sulfite (SO₃⁻), or thiosulfate (S₂O₃²⁻) to S²⁻. Sulfide (S²⁻) reacts with available protons to form sulfide (HS⁻) and hydrogen sulfide (H₂S), a gas with a characteristic rotten egg odor. In some SRB species, simultaneous oxidation of H₂ and reduction of SO₃⁻ can take place on the outside of the cell membrane and are catalyzed by hydrogenase and sulfite reductase enzymes, respectively (Odom and Peck, 1984). Metabolic pathways for SO₄²⁻ reduction occur within the cell (Odom and Peck, 1984). For example, in a biofilm with abundant organic carbon, SRB can “eat” lactate as a source of electrons for intracellular SO₄²⁻ reduction. Hydrogenases within the cell package protons for export as hydrogen gas (H₂); when SO₄²⁻ is present, however, hydrogenases within the membrane recycle H₂ to protons and electrons, releasing protons to the outside of the cell and recycling electrons to the inside of the cell (Odom and Peck, 1984). As H₂ builds up outside of the cell, the SRB’s metabolic pathway can switch from lactate to H₂ oxidation as an electron source. In theory, when SRB are consuming hydrogen via a hydrogenase enzyme pathway, the corrosion rate is proportional to hydrogenase enzyme activity (Bryant et al., 1991; De Silva Muñoz, 2007). In laboratory experiments, the switch by SRB from lactate to H₂ is accompanied by a marked increase in corrosion rate, which occurs as lactate and its daughter product acetate are depleted from solution (Bryant et al., 1991). Elucidation of these metabolic pathways reveals the importance of oxidized sulfur and organic carbon compounds in supporting MIC.

Peng and Park (1994) have reported that in a recent field investigation for Wisconsin DOT nearly half of the corrosion of steel culvert pipes was related to the activities of microorganisms and the effects of sulfate ion concentration and bacteria on corrosion were significant only in fresh water that was under-saturated with calcium carbonate. In subsequent bench-scale experiments with steel coupons immersed in well water, Peng and Park (1994) found that corrosion rates were highest for well water inoculated with a combination of aerobic and sulfate-reducing bacteria, at higher concentrations of sulfate, and when under-saturated with respect to calcium carbonate (negative LSI). Their experiments indicated that natural waters super-saturated with calcium carbonate (positive LSI) may protect steel from corrosion, for example, through pH buffering or because calcium carbonate scale formation.

Other types of bacteria including enterobacteria can also reduce oxidized sulfur to hydrogen sulfide, and different SRB species have alternative metabolic pathways of sulfate reduction (Odom and Peck, 1984).

Another point of view is that the formation of ferrous sulfide corrosion product causes a local decrease in pH (Equation 10-3), which promotes the breakdown of a passive film (Hamilton, 2003). Videla (1985) postulated that biogenic acids first cause the local destruction of a protective iron sulfide film on the metal surface to create an anode, based on the similarity of pitting caused by

inorganic hydrogen sulfide compared with biogenic hydrogen sulfide; and this rupture of the protective layer is only later followed by an increase in the corrosion current density at the cathode. Romero et al. (2005) corroborated a role of hydrogen sulfide and iron-sulfur corrosion products in steel corrosion. The presence of aggressive ions including chloride likely prevents the re-establishment of a passive film (Videla, 1985).

In addition to sulfur compounds, there is evidence that phosphorus compounds may be important in MIC. Experiments with SRB and corroding iron by Iverson (2001) showed the possible production of iron phosphide (Fe_3P), a black precipitate, and phosphine gas (PH_3), which he postulates is released as a consequence of reduction of phytic acid by SRBs. Phytic acid is an organic phosphorus compound that is ubiquitous in plants and can be found in yeast extract typically used in cell culture media. Iverson (2001) speculates that it is the phosphine gas that is responsible for observed metal corrosion. Other researchers have reported deposits of phosphorus adjacent to bacteria in biofilms on corroding metal (Feurgeas et al., 1997; Weimer et al., 1988). Another explanation is that in an environment conducive to SRB activity, corroding steel releases iron phosphide, which is reduced abiotically to phosphine (Roels and Verstraete, 2001). Weimer et al. (1988) reported that in laboratory experiments with mild steel coupons that were immersed in active SRB cultures, corrosion rates increased with (inorganic) phosphate addition. De Silva Muñoz et al. (2007) published experimental evidence that inorganic phosphate at the metal surface increased the cathodic hydrogen evolution reaction, while hydrogen consumption through hydrogenase activity facilitated the cathodic reaction, further increasing the corrosion rate.

10.2.3.2 Mechanism for manganese oxidizing bacteria (MOB) corrosion

For metals such as stainless steel that normally have a tightly adherent passive oxide film, severe localized corrosion can occur when corrosion potential (E_{CORR} , e.g., measured as an open circuit potential), becomes more positive than the pitting potential (E_{pit}). In brackish water or seawater, the presence of chloride ions leads to widespread pitting corrosion, and under these conditions the corrosion rates can be further enhanced by MIC (Antony et al., 2008; Xu et al., 2008), as described for the mechanism of SRB corrosion. In fresh water, however, an increase in corrosion potential beyond the pitting potential can cause pitting in stainless steel even at low chloride concentrations (Hamilton, 2003; Shi et al., 2003).

Corrosion in passive metals appears to be facilitated by manganese- or iron-oxidizing bacteria (MOB, IOB) (Linhardt, 1997; Hamilton, 2003; Shi et al., 2003; Marconnet et al., 2008). In aerated fresh water, as E_{CORR} exceeds ~ 350 mV (standard calomel electrode), MOB present in a biofilm on the surface of stainless steel can oxidize manganese oxyhydroxide (MnOOH) to manganese dioxide (MnO_2). MnO_2 is very insoluble and accumulates on the metal surface.

A cathodic reaction ensues whereby electrons from the stainless steel flow into the MnO_2 and convert Mn(IV) to Mn(II) . This reaction would ennoble the steel toward a pitting condition or enhance corrosion in existing pits. The Mn^{2+} would be subsequently oxidized by oxygen back to MnOOH .

An alternative theory for ennoblement of passive metals and subsequent development of localized corrosion is that extracellular enzymes trapped in the biofilm on the metal surface exert a catalytic effect on oxygen reduction (Scotto and Lai, 1997). Scotto and Lai (1997) showed that for stainless steel immersed in seawater and in a passive state, the open circuit potential was correlated with the carbohydrate and protein content of the biofilm that formed on the metal's surface. Similarly, Marconnet et al. (2008) provided evidence that bacterially-produced hydrogen peroxide trapped in a biofilm could be reduced at a metal's surface.

10.2.4 MIC Monitoring

Direct inspection techniques, growth assays, activity assays, or assays for cellular constituents can confirm the presence of microorganisms in the corrosion environment (Robarge, 1999). MIC is indicated when the direct inspection of corroded surfaces reveals slime (Figure 10-1), black iron sulfide deposits, algal growth, or "swamp gas" odors (Zintel et al., 2001; Blackburn, 2004). A drop of hydrochloric acid on a black sulfide deposit releases hydrogen sulfide and its rotten egg odor (Blackburn, 2004).

In the laboratory, direct inspection techniques include microscopy, for example, with fluorescent dyes to "light up" metabolically active bacteria, or with an electron beam to reveal surface-adhered bacteria. Growth assays of bacteria in selective culture media established the viability of target bacteria present in a sample, and serial dilutions of inoculated culture media allow for an estimate of bacterial number, although this number is normally a small fraction of the natural bacterial population (Robarge, 1999; Zintel et al., 2001). Commercial kits are available for growth assays of bacteria often associated with MIC, and for assays of sulfate reductase and hydrogenase enzymes, which are enzymes commonly found in SRB. Biomolecular assays of cellular constituents permit the identification of bacteria strains from fatty acid profiles or nucleic acid sequencing (Robarge, 1999; Zintel et al., 2001). Cutter and Stroot (2008) demonstrated a novel technique for assessing bacterial growth rates from the ratio of precursor to mature 16S ribosomal ribonucleic acid (rRNA), for example. Comparison of biotic versus abiotic fractionation of stable isotopes, e.g., $^{34}\text{S}/^{32}\text{S}$, is another technique for diagnosing MIC (Little et al., 1994).

Several strategies are possible to guard against the build-up of a corrosion-enhancing biofilm on metal surfaces that are exposed to air, water, soil or sediment (Lane, 2005). First, bulk properties of the environmental media such as temperature, pH, conductivity, total dissolved solids, dissolved ion and gas

concentrations, and bacterial counts or characterization can be routinely monitored to scan for changes indicative of increased bacterial or corrosion activity.

Second, metal coupons placed in areas most susceptible to MIC can be periodically removed and measured for weight loss to establish corrosion rates or to test for presence of a biofilm (Zintel et al., 2001). Biofilms and their chemical and biological constituents can be investigated with scanning electron microscopy and energy dispersive spectrum analysis (SEM-EDS), transmission electron microscopy (TEM), or environmental scanning electron microscopy (ESEM) (Zintel et al., 2001; Xu et al., 2008). Atomic force microscopy revealed a clear pattern of pitting in mild steel that was directly related to colonization of the steel surface by SRB (Xu et al., 2002).

Third, exposed metal surfaces at representative sites can be routinely monitored with resistance probes or electrochemical sensors that respond to changes in corrosion current (Royer and Unz, 2002; Cristiana et al., 2008; Xu et al., 2008). For example, Nielson and Hilbert (1997) found that during ac impedance tests the interfacial capacitance of carbon steel coupons exposed to an SRB-active environment was not only large but was correlated with dissolved HS^- , which in turn was proportional to hydrogenase activity.

Fourth, isotopic enrichment offers a diagnostic test to distinguish biotic from abiotic corrosion. Hutchens et al. (2007) demonstrated that MIC-related corrosion of cast iron enriches heavy isotopes of iron (^{56}Fe and ^{57}Fe) over that of ^{54}Fe , as compared with relative ratios of these stable isotopes in uncorroded metal or metal corroding by abiotic processes.

Detection, measurement and analysis of MIC require techniques that can detect localized forms of corrosion such as pitting. Electrochemical techniques such as electrochemical impedance spectroscopy (EIS), electrochemical noise analysis (ENA) and measurements of pit propagation rates have been evaluated as tools for the study of localized corrosion in MIC (Mansfeld and Xiao, 1994; Zintel et al., 2001; Xu et al., 2008).

10.2.5 Control of MIC

In piping or tanks, MIC control of planktonic (free-swimming) bacteria is often accomplished with a biocide (Lane, 2005). For sessile (attached) bacteria in a biofilm, however, oxidizing and non-oxidizing biocides must be added at much higher doses to be effective, and with or without mechanical removal biofilms and the accompanying microbial consortia can rapidly regrow (Lane, 2005; Little et al., 2007; El-Shamy et al., 2009). In the European power industry, for example, pipes or tanks may be treated with sodium hypochlorite (bleach) to minimize biofouling and if biofouled, cleaned by acid, by drying, or by mechanical

removal techniques include abrading the surface with brushes or rubber balls or high-pressure water (Cristiani and Bianchi, 1997).

For underground structures and piping, providing adequate drainage to prevent stagnant water conditions can mitigate MIC (Lane, 2005). Other pipeline alternatives include emplacement of piping in engineered backfill, cathodic protection of piping, or use of a pipe coating material that is strongly adherent, impermeable to water, and is resistant to microbial attack (Miller and King, 1975).

Novel ways of MIC control such as engineered biofilms, coatings, alloys, or electron acceptors for surfaces that are likely to develop biofilms (Lane, 2005; Little et al., 2007; Nizhegorodov et al., 2008) are more relevant for steel foundations, anchors, and culvert piping. Metal alloys exhibit differential anti-fouling properties. For example, a recent study by Nizhegorodov et al. (2008) demonstrated that stainless steels alloyed with nitrogen were more resistant to microbial adhesion and subsequent MIC than conventional structural steel. They postulated that nitrogen released from corroding steel reacted with hydrogen to form ammonium, which raised the local pH and re-passivated the pit.

10.2.6 Risk factors/risk factor models and mechanistic models for MIC

Progress has been made in modeling MIC with both empirical (risk factor) and mechanistic models, however, of the models presented below, none are recommended as an improvement to current methods in the absence of MIC-related field or laboratory data that corroborates the extension of these models to Florida environments. Melcher's (2003) pseudo-mechanistic model (see Section 10.2.6.2.2) appears to have broad applicability and fit well the data of many test coupon experiments; however, the underlying physical and chemical phenomena are not (yet) sufficiently described to improve over current methods an estimate of service lifetime for buried or immersed metals.

10.2.6.1 Soil

10.2.6.1.1 Risk factors/risk factor models

Wolzogen and van der Vlugt (1934) observed the corrosion of iron in anaerobic wet clay soils. Booth et al. (1967) laid out risk factors for unprotected steel buried in soil that included both biotic and abiotic corrosion damage (Table 10-2).

Christiana et al. (2008) reported that high (40%) soil humidity was important for biofilm growth on stainless steel coupons that formed the cathode of a zinc-steel galvanic couple used as a sensor for monitoring biofilm development on metal surfaces in soil.

Table 10-2
Soil Aggressivity Model
Booth et al. (1967)

Criterion	Aggressive	Non-Aggressive
Resistivity (Ω -cm)	<2,000	>2,000
Redox potential at pH 7 (V, NHE)	<0.400, or <0.430 if clay	>0.400, or >0.430 if clay
Borderline cases to be resolved by water content	>20%	<20%

A power law model was applied to field measurements of soil properties and pit depths in underground steel pipeline to obtain an empirical relationship predictive of observed pitting corrosion (Li et al., 2003). Predictive factors included microbial, chemical, and cathodic protection properties of the soil-pipe system. Properties that explained pitting were sulfate-reducing bacteria population (SRB, cells/g soil); pipe-to-soil potential (P/S, V_{SCE}), chloride concentration (Cl^- , ppm), redox potential (E_h , V_{NHE}), clay content (clay,%), and soil resistivity (ρ , Ω -cm). P_{max} is the predicted maximum pit depth and t is time (Equation 10-4), and P is the pit depth estimated from soil properties (Equation 10-5).

$$P_{max} = 1.573Pt^{0.372} \quad (10-4)$$

$$\begin{aligned} \text{Log}P = & 0.700 + 0.069\text{log}(\text{SRB}) + 0.744(P/S) + 0.203\text{log}(Cl^-) - 0.050(E_h)(Clay) - \\ & 0.014(pH)\text{log}(\rho) \end{aligned} \quad (10-5)$$

10.2.6.1.2 Mechanistic models

Gu et al. (2009) have developed and partly explain in literature a mechanistic model for predicting pit growth in carbon steel in the presence of both planktonic and sessile SRB. This model, based on a “biocatalytic cathode sulfate reduction theory,” includes terms for charge transfer resistance and mass transfer resistance, where charge transfer occurs as protons, organic acids, and sulfate are reduced at the cathode surface. Mass transfer is limited by the flux of these compounds and dissolved iron through the biofilm. Preliminary calibration and simulation of pit growth with this model indicates that charge transfer is important during initial stages of pit growth but as the pit deepens, mass transfer controls the corrosion rate (Gu et al., 2009).

10.2.6.2 Fresh, brackish, and salt water

10.2.6.2.1 Risk factors/risk factor models

Beech and Campbell (2008) identified the below risk factors for MIC corrosion found at the low water level in a southern England harbor, but did not extend the factors in a predictive model:

- Thickness and morphology of corrosion products;
- pH values underneath corrosion products;
- Presence of algae and invertebrates;
- Content of organic carbon, hydrogen, and oxygen in microfouling layers;
- High sulfate oxidizing bacterial counts and presence of SRB;
- Higher mean tidal range; and
- Total organic carbon in seawater.

10.2.6.2.2 Mechanistic models

Picioreanu and Loosdrecht (2002) developed a 3-dimensional numerical model to investigate the potential for an aerobic biofilm to inhibit corrosion. Their model included (1) diffusion and migration, (2) electrochemical reactions at the metal surface, and (3) homogeneous reactions in the liquid volume for 7 species: oxygen, and ions of ferrous iron, ferric iron, hydroxide, hydronium, sodium, and chloride. Simulations including variations in the fractional metal surface area covered by bacterial colonies, and responses to changes in oxygen concentration, pH, and chloride concentration. Simulations showed a reduction in overall corrosion rates with increasing surface coverage by bacteria in response to reduced oxygen availability but at the same time the formation of differential aeration cells because of patchiness in cell coverage. Corrosion rates increased with chloride ion concentrations due to the higher electrolyte conductivity. Anaerobic conditions, sulfate reduction, and formation of iron-sulfide corrosion products were not modeled.

Melchers (2003) presented a novel non-linear pseudomechanistic dynamical model to explain average corrosion loss in low carbon and low alloy steels immersed in marine environments. His model was later extended to fresh and brackish water (Melchers, 2006) and to localized corrosion (Melchers and Jeffrey, 2008). This model assumes that corrosion loss occurs for two distinct and consecutively-occurring and multi-phase regimes: aerobic and anaerobic, with a presumption that biological growth on the corroding metal will sustain terminal anaerobic conditions. The model is specified by a minimum of 6 parameters, which have been obtained by the authors through curve fitting of data from both short-term and long-term field exposures of test coupons at sites around the world.

10.3 Enumeration of MIC-Related Bacteria in Florida Soils

The goal of this research was to enumerate MIC-related bacteria in representative Florida soils at a depth typical for buried metal piping to compare bacterial counts in soil samples taken from in and around corroding metal. Samples of eight different soils (Table 10-3) were collected at selected state parks with written permission from the Florida Park Service. Soil types were chosen in advance to represent a range of Florida soils. Soil samples were collected by hand auger between a depth of 0.9 and 1.2 m and ~ 2 kg of soil were transferred directly from the auger bucket into new plastic Ziploc[®] bags. Plastic bags were sealed and packed in a cooler with ice packs for the trip back to the laboratory. Soil pH was determined on-site by wetting pH paper in a 1 g soil aliquot diluted with 1 mL of deionized (18 M Ω) water. Upon reaching the laboratory, soils were spread onto Teflon[®]-coated trays and allowed to dry for ~3 days, after which they were shaken through a No. 10 sieve and transferred to a 1-l amber glass jar for storage. Stored soils were used to assess proposed improvements to the FDOT method for sulfate determination in soils (Appendix F).

Bacterial counts were made by the most probable number (MPN) method. Each soil was tested for aerobic (AER), anaerobic (ANA), acid-producing (APB), low nutrient bacteria (LNB), iron-related (IRB), and sulfate-reducing (SRB). Each of these six tests was a set of 5 pre-sterilized MPN culture tubes (BTI, Inc.) containing an appropriate culture medium. MPN tubes were inoculated on-site within two hours of sampling. To inoculate the MPN tubes, ~1 g soil was diluted and shaken in a 25-mL vial of pre-sterilized buffer medium and 1 mL per test from this buffer medium began a sequence of five serial dilutions made with a sterilized syringe. Inoculated tubes were returned to laboratory at ambient temperature and incubated in the laboratory in the dark at ~27^o C. Tubes were checked for a positive indication 2, 5, and 15 d after sampling. MPN test results after 5 d of incubation are presented in Table 10-3.

All of the soils tested were positive for aerobic, anaerobic, acid-producing, and low-nutrient bacteria. Well-drained soils Candler and Pomello did not have detectable iron-related and sulfate-reducing bacteria counts for a 5-day incubation period. The results indicate that in every Florida soil tested substantial bacterial populations were present that could lead to the development of MIC.

**Table 10-3
Soils Sampled for MIC**

Series	Date Sampled	Sample Location	Description
Basinger	07/07/2006	Highlands Hammock State Park N 27° 29.123' W 081° 32.762'	Siliceous, hyperthermic Spodic Psammaquents; poorly and very poorly drained; rapid permeability
Candler	06/28/2006	Manatee River State Park N 27° 39.758' W 082° 22.409'	Hyperthermic, uncoated Lamellic Quartzipsamments; excessively drained; rapid permeability
Chobee	06/22/2006	Hillsborough River State Park N 28° 07.965' W 082° 14.397'	Fine-loamy, siliceous, superactive, hyperthermic Typic Argiaquolls; very poorly drained; slow to very slow permeability
Felda	07/07/2006	Highlands Hammock State Park N 27° 29.123' W 081° 32.959'	Loamy, siliceous, superactive, hyperthermic Arenic Endoaqualfs; poorly drained and very poorly drained; moderately rapid to moderate permeability
Myakka	08/25/2006	Koreshan Historic Site N 26° 26.074' W 081° 49.089'	Sandy, siliceous, hyperthermic Aeris Alaquods; poorly to very poorly drained, permeability varies from moderate to rapid (Sample was water-saturated)
Pomello	06/28/2006	Manatee River State Park N 27° 39.906' W 082° 22.170'	Sandy, siliceous, hyperthermic Oxyaquic Alorthods; moderately well and somewhat poorly drained; moderately rapid permeability
St. Augustine	08/25/2006	Lover's Key State Park N 26° 23.534' W 081° 52.549'	Siliceous, hyperthermic Aquic Udipsamments; somewhat poorly drained; moderately rapid or rapid permeability (sea shell fragments)
Winder	06/22/2006	Hillsborough River State Park N 28° 08.592' W 082° 13.806'	Fine-loamy, siliceous, superactive, hyperthermic Typic Glossaqualfs; poorly drained; slow to very slow permeability

**Table 10-4
Enumeration of Bacteria in Selected Florida Soils**

Series	pH	AER	ANA	APB	LNB	IRB	SRB
Basinger	5	4	3	3	5	1	2
Candler	5	3	3	4	3	ND	ND
Chobee	6	4	4	5	5	2	2
Felda	6	4	5	5	5	3	2
Myakka	5	5	5	4	5	1	2
Pomello	4	4	4	2	3	ND	ND
St. Augustine	8	2	5	4	4	1	3
Winder	7	5	4	2	5	1	2
Average	--	4	4	4	4	2	2

(5-d incubation period; ND: not detected; 1: 1-10; 2: 10-100; 3: 100-1,000; 4: 1,000-10,000; 5: >10,000 cells/gram dry weight)

10.4 Enumeration of Bacteria from Culvert Piping Soil, Sediment, Water, and Corrosion Product

Two commercially-available kits were tested for field sampling of SRB bacteria—kits manufactured by BTI Products and by Biosan Laboratories. Both kits come complete and are easy to use. For an SRB test, the BTI Products kit requires serial dilution and mixing of sample through 3 to 5 tubes with a hypodermic needle-type syringe, takes more time, and is more expensive per test than the Biosan Laboratory kit, but concentrations of SRB down to ~10 cells/mL can be detected. Thus, this kit is suitable for a wide range of environmental SRB concentrations. The Biosan markets a quick, easy, and inexpensive SRB test kit; the kit, however, is intended for use in industrial applications at relatively high SRB concentrations and was not sensitive enough to detect SRB concentrations in environmental water or biofilm samples.

10.4.1 Culvert pipe failure in Clearwater, FL

Corrosion on sections of aluminized steel type 2 culvert piping installed along Curlew Road in Clearwater, Florida, was discovered in late 2006. A subsequent investigation and full report was made for FDOT by Concorr Florida, Inc. (CONCORRFlorida, 2007). In tandem with this investigation, samples of corrosion product, bioslime, sediment, and water were collected from the invert of culvert piping on the south side of Curlew Road between S7 and S55 (CONCORRFlorida, 2007). Sampling was done over two days, from 11/30/06 to 12/1/06. Bacterial enumeration was performed as described in section 10.3 with pre-packaged MPN tubes and sampling implements (BTI Products). Results are summarized in Table 10-5.

**Table 10-5
Enumeration of Bacteria in Corrosion Product, Bioslime, Sediment, and Water**

Sample	AER	ANA	APB	LNB	IRB	SRB
Corrosion product (N=3)	5	5	5	5	4	4
Bioslime (N=4)	5	5	3	5	4	5
Sediment (N=1)	4	5	5	5	3	4
Water (N=1)	3	2	2	4	3	4

After 5 days of incubation, these results clearly indicate an active ecosystem of both aerobic and anaerobic (or facultative anaerobic), including sulfate-reducing bacteria in corrosion product, bioslime, sediment, and water found in aluminized steel culvert piping. In comparison with Table 10-4, corrosion product, bioslime, and sediment samples were all enriched in bacteria, including iron-related and sulfate-reducing bacteria, when compared with Florida soils. The water sample had lower aerobic, anaerobic, and acid-producing bacterial counts when compared with Florida soils, but were elevated in iron-related and sulfate-reducing bacterial counts. These results suggest that MIC may have been a factor in the observed culvert pipe corrosion. However, bacterial presence is a necessary but not sufficient condition for MIC (Videla 1997), and other factors could have precluded its appearance. Further investigation of this issue is needed.

Water was present in sections of pipe that were inspected, and a sewer-type odor was detected near S55.

10.4.2 Culvert pipe failure in St. Cloud, FL

City of St. Cloud excavating type II aluminized steel culvert piping after inspection revealed internal and external corrosion of the piping after ~3½ years in service. (Refer to Chapter 5 for in-depth material condition assessment.) To investigate the possibility that metal corrosion was accelerated by MIC, corrosion product was obtained from still in-service culvert piping to identify and quantify MIC-related bacteria.

On 11/2/2005, a sample of corrosion product was collected from the inside top surface of a 72" diameter culvert piping that carried storm water run-off from the streets of St. Cloud to East Lake Tohopekaliga, near the terminus of pipe at the lake. This pipe section was nearly half-full of water at the time of sampling. According to the city engineers, water in the pipe was accumulated rainwater and the pipe was often completely full of water.

On 11/16/2005, soil in contact with the top of a pipe crown on a section of pipe located on Illinois Avenue, between 6th and 7th Streets, was collected for MIC testing. The soil was selected from a region that was nearly black. Bacterial enumeration was performed as described in section 10.3 with pre-packaged MPN tubes and sampling implements (BTI Products). Corrosion product or soil was scraped directly into the pre-sterilized vial containing an appropriate buffer solution and inoculation of the MPN tubes was accomplished within an hour of sampling. The results after 5 days of incubation are presented in Table 10-6.

Table 10-6
Enumeration of Bacteria in Corrosion Product and Adjacent Soil

Sample	AER	ANA	APB	LNB	IRB	SRB
Corrosion product from inside top of culvert pipe	4	4	3	3	ND	5
Soil adjacent to corrosion product on outside top of pipe crown	4	5	4	4	2	2

After 5 days of incubation, these results clearly indicate an active ecosystem of both aerobic and anaerobic (or facultative anaerobic), including sulfate-reducing bacteria. In comparison with Table 10-4, however, only SRB in corrosion product was elevated when compared to SRB counts in Florida soils.

10.4.3 Culvert test pipe exhumation at Nassau Sound, FL

FDOT had a culvert pipe test site located along Route A1A (SR105), 0.8 km north of the new Nassau Sound Bridge and 7.0 km south of Amelia City in Nassau County, Florida. The culvert piping at this site was installed in November 1997, and had a total length of 12 m, but made up of four 3-m sections, each section of a different material. The test pipe sections were 305 g/m² (1 oz/ft²) aluminized steel type 1 (T-1), 305 g/m² (1 oz/ft²) aluminized steel type 2 (T-2), 610 g/m² (2 oz/ft²) galvanized steel (Galv) and 610 g/m² (2 oz/ft²) polymer-coated galvanized steel (Poly), installed in that order. The culvert piping was emplaced along a coastal road, adjacent to the marsh and oriented parallel to the road, partially submerged in the native soil and covered with backfill material. The pipe sections were mechanically coupled but electrically isolated from each other. During installation, electrical connections were made to each pipe section and the free end of the wire was routed to an accessible NEMA-type box enclosure.

This test site was classified as an extremely aggressive environment for corrosion based on FDOT environmental classifications given in Table 2-5. The FDOT Materials Office Corrosion Laboratory provided results of field and laboratory testing of soil and water samples from the site over the 7-year period, which were: pH 6.3 to 7.2; resistivity, 90 to 5,000 Ω -cm; chloride, 100 to 6,000 mg/L; sulfate, 500-1,600 mg/L, and acidity, 20 -60 mg/L. Half-cell potentials measured with a copper/copper sulfate (CSE) reference electrode were reported as given in Table 10-7.

Based on a visual inspection during pipe removal by FDOT, the aluminized steel type 2 pipe was extensively corroded and in several places the walls were perforated. Red corrosion product was visible in the soil along the longitudinal pipe axis at ~mid depth of the pipe (or roughly where the backfill soil met the native soil). It is noted that the plain galvanized pipe had the most negative potentials throughout the test period, indicative of galvanic protection in progress (although less so near the end). The aluminized pipes had significantly less negative potentials suggestive of less galvanic protection and consistent with the greater deterioration observed in at least one of them (T-2).

**Table 10-7
Half-Cell Potentials (V vs SCE) from Middle of Each Culvert Pipe**

Pipe Section	11/12/97	11/16/98	11/03/99	02/26/02	12/06/04
T-1	-0.81	-0.77	-0.69	-0.58	-0.68
T-2	-0.77	-0.79	-0.68	-0.61	-0.67
Galv	-1.17	-1.09	-0.96	-0.79	-0.77
Poly	-1.12	-0.98	-0.79	-0.63	-0.67

On December 7, 2004, engineers and staff with the Florida Department of Transportation met at Nassau Sound to exhume the culvert piping from the test site. Each section was removed separately by backhoe, and loaded onto a waiting truck. The backfill and native soil samples were collected with a stainless steel bulb planter and the invert soil with a stainless steel trowel. The bulb planter and trowel were cleaned with soap and water, and rinsed with a 50:50 (v:v) isopropanol:water mix before and between soil samples. Soil samples were immediately placed into new, Ziploc[®] bags, labeled, sealed, and stored in a cooler with frozen “blue” ice. Within four hours of sampling, the samples were packaged inside the coolers with (replacement) frozen “blue” ice for overnight shipping to BBC Laboratories, Inc., in Tempe, Arizona, for microbial analyses (Appendix B).

In the culvert pipe invert, stagnant water was present in all pipe sections, and accumulated soil was present in all but the galvanized steel section. Samples of the backfill soil and native marsh soil were acquired from the top and beneath the type 2 aluminized steel piping, respectively; along with soil plus water from the invert of the galvanized steel piping, and soil plus corrosion products from the invert of the type 2 aluminized steel piping (T-2). Figure 10-2 shows an interior view from the T-1 end of the pipe.



Figure 10-2. Corrosion is evident in an aluminized steel type 1 culvert pipe after 7 yr of service.

The microbial analyses (Table 10-8; Appendix B) revealed that aerobic (AER) and anaerobic (ANA) bacteria were present at higher concentrations but acid-producing (APB) and low nutrient bacteria (LNB) at lower concentrations than for those Florida soils reported in Table 10-4. Sulfate-reducing bacteria (SRB) were present at detectable levels in the soil found in the aluminized steel piping invert and in the water found in the galvanized steel piping invert. SRB concentrations in soil were comparable with those reported in Table 10-4. The native soil and soil accumulated in the pipes' inverts appeared to be richer in microbes than the backfilled soil based on the laboratory's enumeration techniques, which might be expected if the native soil and pipe inverts were periodically inundated with brackish water rich in inorganic and organic nutrients. Notably, differences between microbial species in the inverts of type 2 aluminized

steel and water from the galvanized steel invert do not directly correlate with the extensive corrosion damage observed in the section of aluminized steel type 2 piping. This further illustrates the earlier observation that bacterial presence is a necessary but not sufficient condition for MIC.

**Table 10-8
Enumeration of Bacteria in Corrosion Product and Adjacent Soil/Water***

Sample	AER	ANA	APB**	LNB	SRB
Backfilled soil	5	4	1	3	2
Native soil	5	5	2	4	2
T-2 invert soil	5	5	3	4	2
Galv invert water	5	5	3	4	4

*Table has been simplified for easy comparison with Table 10-3; refer to Appendix B for the complete microbial analytical results.

**Sulfate-oxidizing bacteria (SOB) were grouped as acid-producing bacteria, but not all SOB are APB and vice versa.

Units are colony forming units (CFU)/gram dry soil or CFU/g of water for soil and water samples, respectively.

10.4.4 Culvert test pipe investigation in Wisconsin

Localized perforation and pitting in culvert pipes of made of aluminized steel and emplaced in a corrosive drainage environment for 25 years were attributed to MIC from SRB (Patenaude, 2003). Sulfide-containing corrosion product accompanied metal loss on both water and soil side in the presence of organic-rich sediment or soils; previously emplaced galvanized steel pipe had failed in a similar manner. Aluminum pipe exposed to similar conditions did not show signs of MIC, but did in some places succumb to corrosion from sodium chloride de-icing salts (Patenaude, 2003).

10.5 Summary and Conclusions

MIC-related corrosion has been observed in laboratory and field experiments with many but certainly not all studies centered around sulfate-reducing bacteria, sulfate-oxidizing bacteria, or iron-related bacteria and their potential influence on both low-strength and high strength steel. Recurring themes in these studies include the (1) acceleration of anaerobic corrosion when the bulk water is aerated, (2) potential for inorganic and organic nutrients—carbon, sulfur, and phosphorus, as examples—to enhance biotic corrosion rates, (3) role of microbial consortia and/or biofilms in dampening or sustaining corrosion, and (4) MIC-assisted development of differential aeration cells that increase localized corrosion rates. High corrosion rates have been seen for the combination of mild steel immersed in natural waters that are both nutrient-rich and well-aerated.

From field observations and laboratory experiments that were accomplished as part of this study or were reported in corrosion literature, conclusions

regarding microbiologically-influenced corrosion (MIC) of metals used in road constructions are as follows:

- Carbon steel, stainless steel, galvanized steel and aluminized steel buried in soil or immersed in natural waters are susceptible to localized corrosion due to MIC;
- Biofilms that develop from microbial activity on metal surfaces in natural waters can promote or inhibit corrosion, however, emplacement of metal structures or components in polluted or stagnant water may thicken biofilms and accelerate corrosion;
- The potential for MIC in metal culvert piping is expected to decrease for conditions where the pipe drains rapidly and is placed above the water table in non-aggressive, fast-draining soils or engineered backfill.
- Concentrations of bacteria implicated in MIC from field samples at investigations sites in Florida revealed a possible but inconclusive role of MIC in the premature failure of aluminized steel culvert piping.
- It is recommended that future test site assessments for corrosivity include a standard measure of soil or water organic content, as appropriate, to elucidate the relationship between organic content and *in-situ* corrosion rates and to determine a corrosivity criterion.

11 PROPOSED MODIFICATIONS FOR METHODS TO DETERMINE DURABILITY FORECASTING INPUT PARAMETERS

Whether testing is done in the field or in the laboratory, a practical approach is to standardize sample collection, transport, preparation and analysis procedures so that results can be confidently used to establish trends in properties over a broad spatial and temporal scale. State and national transportation projects rely on standardized methods to measure water and soil properties for design guidance of roads and bridges (for example, FDOT 2000a, b, c, d). The US Department of Agriculture Natural Resources Conservation Service sponsors a web-based soil survey (WSS, 2009), which can provide preliminary information for planning a soil or groundwater sampling strategy. Soil properties associated with each soil type are included in the web-available database. Properties of interest in predicting corrosion rates and thus durability of metals immersed in water or buried in sediment or soil are pH, resistivity, chloride, and sulfate. In the sections that follow, considerations for sample collection, transport, preparation, and analysis are discussed and rationale presented for the proposed changes.

11.1 Proposed Changes to FDOT Methods for pH, Resistivity, Chloride, and Sulfate Analysis

11.1.1 Sample collection, transport, and storage

It is proposed that FDOT methods for pH, resistivity, chloride, and sulfate (FDOT 2000a, 2000b, 2000c, 2000d) include additional guidelines for sample handling. From the moment a soil or water sample is lifted from its environment, changes in the sample biological, chemical, and physical properties occur. For example, loss of volatile gases such as carbon dioxide and an introduction of oxygen can shift the sample pH (APHA, 1998; Tan, 2005). Microbial and enzymatic activity is modified by exposure to oxygen or swings in temperature, which can cause either an accumulation or a loss of chemical constituents between the time of collection and time of analysis (Asplund et al., 1993; Prietzer, 2001). General approaches to “capture” the *in-situ* properties are (1) make a field measurement without disturbing the soil or water column, (2) minimize the time between sampling and analysis—as an example, use a kit to test a soil property in the field immediately after sampling, or (3) filter (water), add a preservative, or freeze a sample to halt further changes in sample properties. Table 11-1 summarizes the APHA (1998) special sampling and handling requirements for water samples.

**Table 11-1
Special Sampling and Handling Requirements for Water Samples**

Determination	Container	Minimum Sample Size, mL	Preservation	Maximum Storage Recommended
pH	Plastic or glass	50	Analyze immediately	Analyze immediately
Conductivity*		500	Refrigerate	28 d
Chloride		50	None	None given
Sulfate		100	Refrigerate	28 d

*1/Resistivity

Change in pH occurs in water, including soil pore water, during sampling and measurement as trapped carbon dioxide, and other gases are released during sample handling. It is recommended that for both water and soil samples a field measurement of pH in addition to the laboratory measurement be made (Table 11-1). For sample transport from the field to the laboratory, it is recommended that sampling containers be filled to the top with no headspace and sealed to prevent leaks.

At environmental temperatures chemical and biological reaction rates tend to increase with temperature; likewise, gas solubility tends to decrease with temperature (Snoeyink and Jenkins, 1980). No storage temperature is ideal: extreme temperatures—freezing or heating above 100 °C—alter the sample quickly, while ambient temperatures allow the sample to continue to change slowly with time (Tan, 2005). It is recommended that samples be transported sample from the field site to the laboratory at a temperature between freezing and field temperature (4°C and 30°C), with as little delay as possible.

Storage of water and soil samples in the dark limits the opportunity for changes in soil properties due to photolytic reactions. For example, ultraviolet light and visible light acting on light-absorbing organic compounds or semi-conducting metals such as the iron oxide hematite (Fe₂O₃) in water generates hydrogen peroxide (Finlayson-Pitts and Pitts, 1986), which can increase the conversion of chloride to chloromethane or catalyze the reaction of sulfite to sulfate. It is recommended that samples be stored either in opaque containers or in the dark to limit the opportunity for photolytic reactions.

Chloride and sulfate concentrations in a water or soil sample could change over time with storage, especially under conditions that favor continued microbial growth. In the last two decades, researchers have discovered that chloride in soil can be transformed into organic chlorine through abiotic and biotic pathways (Watling and Harper, 1998; Asplund et al., 1993; Keppler et al., 2000; Gribble, 2003; Johansson et al., 2003). Keppler et al. (2000) demonstrated that abiotic oxidation of soil organic matter through the coupled reduction of iron from ferric

iron (Fe^{3+}) to ferrous iron (Fe^{2+}) in the presence of chloride can create chloromethane, chloroethane, chloropropane, and chlorobutane. Chloromethane, which is a gas at room temperature, was formed in the largest proportion relative to the other chloroalkanes. They suggested that a low but measurable alkyl halide production rate in soil samples to which no additional iron was added was explained by presence of mineral ferric iron (Fe^{3+}) in iron oxides and oxyhydroxides.

Chloride in soil can also be transformed through biotic processes to organic chlorine, include simple and more abundant alkyl halides such as chloromethane to more complex molecules that include antibiotics such as vancomycin (Watling and Harper, 1998). Fungi and bacteria present in soil can convert chloride to organic chlorine (Watling and Harper, 1998; Gribble, 2003). Asplund et al. (1993) has identified a chloroperoxidase-like enzyme in soil that in the presence of hydrogen peroxide can catalyze chlorination of soil organic matter. Concentrations of organic chlorine in soils from Swedish forests were proportional to soil organic matter and soil chloride concentrations (Johansson et al. 2003); and Öberg (1998) speculated that over time formation of organic chlorine from chloride is greater than formation of chloride from organic chlorine, or in other words, soil is a sink for chloride and a source of organic chlorine.

Sulfate in the aqueous phase—including soil pore water—inter-converts between oxidized and reduced species. Moving in the direction of reduced to oxidized species; the sulfur cycle includes $\text{S}^{2-} \rightarrow \text{HS}^- \rightarrow \text{H}_2\text{S} \rightarrow \text{S} \rightarrow \text{SO}_2 \rightarrow \text{SO}_3^{2-} \rightarrow \text{SO}_4^{2-}$. Hydrogen sulfide (H_2S) and sulfur dioxide (SO_2) are both gases at room temperature. Under neutral pH and anaerobic conditions, bacteria reduce sulfate (SO_4^{2-}) to sulfide (S^{2-}) and sulfide is likely to react with metal ions, for example, as FeS_2 (refer to Chapter 10 for more detail; Bohn et al., 1985). For pH < 4 and aerobic conditions, bacteria oxidize sulfide (S^{2-}) to sulfur, however, at pH > 4 sulfur is abiotically oxidized to sulfite (SO_3^{2-}) (refer to Chapter 10 for more detail), and in the presence of catalysts such as ferric iron or hydrogen peroxide, to sulfate (SO_4^{2-}) (Seinfeld and Pandis, 1998). Sulfur dioxide (SO_2) gas equilibrates with aqueous-phase sulfite (Seinfeld and Pandis, 1998). Like chloride, sulfur compounds can move between organic and inorganic forms as well. For example, soil bacteria (and fungi) store sulfate as an ester sulfate and control the accumulation of ester sulfate in soil in part by sulfhydrolase enzymes, which break apart the ester to release the sulfate (Prietzer, 2001).

It is recommended that as soon as possible upon return to the laboratory soil samples be air-dried, sieved with a 2-mm sieve, and stored in an air-tight container to avoid contamination by gases, dust, or radioactive particles in laboratory air (Tan, 2005). Air drying at temperatures below 35 °C reduces microbial activity but without significant changes in soil properties caused by elevated temperatures (Tan, 2005). Storage should be in glass jars, plastic containers, or wax-lined boxes in a cool, dry, and well-ventilated atmosphere (Tan, 2005). One advantage of immediately air-drying the entire soil sample is

that the dried sample is available for re-analysis for months, if not years, beyond the sampling date. Soil pH is known to change in stored soil over time, although the reported direction and quantity of the change with time varies with soil properties, method and length of storage (Prodromou and Pavlatou-Ve, 1998; Tan, 2005).

Laboratory chain-of-custody procedures should be followed, including labeling sample containers either on affixed labels or by permanent marker with a sample number, sample type, name of collector, date, and time of collection, place of collection and sample preservative (if any).

11.1.2 Chloride method

The FDOT method of test for free chloride (Cl^-) in soil and water (FM 5-552, Appendix E) is a titrametric method that relies on the quantitative formation of a silver chloride precipitate when the chloride is titrated with silver nitrate under near neutral pH. The titration end point is a color change from yellow to red-tinged yellow as the excess silver reacts with potassium dichromate to form a red silver dichromate precipitate (APHA, 1998).

The advantages of the method are its adaptability to fast and reliable laboratory and field testing of water with reasonable accuracy and precision. The main disadvantage of this method is the potential interference from suspended particles or water-dissolved organic matter that may obscure the end point. A second disadvantage is that silver nitrate and potassium dichromate are toxic substances and must be handled as hazardous materials.

As a summary FM 5-552 (Appendix D), a pre-packaged aliquot of potassium dichromate is added to 100 ml of sample and the sample is titrated with 0.0141 N silver chloride, or 0.141 N silver chloride if chloride concentrations are greater than 500 mg Cl^-/L , to a reddish-yellow end point. For this titrametric method, APHA (1998) reported for a synthetic drinking water sample containing a 241 mg Cl^-/L , the relative standard deviation and relative error were 4.2% and 1.7%, respectively. We found a method detection limit of 2 mg/L.

Error in the determination of chloride concentration can be introduced by:

- Loss or gain of chloride due to sample storage and handling;
- Interference from suspended particles or water-dissolved organic matter in the sample;
- Precipitation of silver with a chemical compound other than chloride;
- Accuracy of the titration buret;

- Cleanliness with respect to chloride of the reagents, distilled water, glassware, filters, and other supplies or equipment used in the analytical procedure.

11.1.2.1 Loss or gain of chloride due to sample storage and handling

Chloride is ubiquitous in water or soils as dissolved salts, as a constituent of organic matter, or in soil minerals. A water or soil sample collected per FM 5-552 will be biologically active, and as such, chloride may interconvert from its reduced and oxidized forms or between organic and inorganic forms, and/or escape through volatilization (as chloromethane, for example) during the collection, transport, and storage of the sample.

FM 5-552 requires that the soil sample be drained of excess water and packaged in a sealed plastic bag with minimal air pockets. This approach reduces the contribution of chloride from evaporating water. Similarly, water samples should fill their containers with no headspace. Keeping the soil or water sample at or below its field temperature would also slow microbial activity and thus changes in chloride concentrations. Once collected, samples should be transported at temperatures within 4-30 °C.

Once the sample reaches the laboratory, the soil sample should be desiccated to constant water content, a step that will slow microbial activity. Air drying versus heating to 110°C is recommended. Water samples should be refrigerated at 4 °C.

Many compounds when exposed to a photon flux or to radicals produced in air or water that is exposed to a photon flux will undergo chemical transformation. Thus, water and soil samples should be stored opaque containers or in the dark.

According to FM 5-552, 100 g of soil is extracted with 300 g of water by mixing the suspension for two 20-second periods an hour apart followed by a 12-hour or longer quiescent period. The quiescent period is intended to settle particles suspended in the water during the mixing phase, however, for a soil containing silt or clay, suspended particles will take days to weeks to settle. The combination of high water content, room temperature and a long quiescent incubation period in a glass flask favors the growth of bacteria, introduction of hydrogen peroxide through photolytic processes, and the possible transformation of chloride to chloromethane and loss of chloromethane through volatilization.

11.1.2.2 Interference from suspended particles or water-dissolved organic matter in the sample

Suspended particles and water-dissolved organic matter that adds color to the water or soil extract sample may mask the titration end point. Centrifugation can improve the separation between water and soil in minutes rather than hours,

and simultaneously reduce the amount of dilution water required. We are recommending that the soil-water extraction be done with a 1:1 soil:water mixture, shaken and allowed to equilibrate, and the water separated from soil by centrifugation for 30 minutes at 4,000 rpm. Following centrifugation, filtration through a coarse filter is still necessary to remove floating debris. If the centrate is still too cloudy or colored to observe the titration end point, micro-filtration of all or part of the soil extract through a 25-mm diameter syringe-tip 0.2 μm pore membrane (Whatman Puradisc) will reduce the background turbidity.

11.1.2.3 Precipitation of silver with a chemical compound other than chloride

Bromide, iodide, cyanide, orthophosphate > 25 mg/L, sulfide, thiosulfate, and sulfite in the sample will quantitate as chloride, i.e., cause a positive bias in the results; however, sulfide, thiosulfate, and sulfite ions can be removed by treatment with hydrogen peroxide (APHA, 1998).

The concentration of silver nitrate titrant can change over time. We recommend that periodically the silver nitrate strength be checked against a standard chloride solution.

11.1.2.4 Accuracy of the titration burette

A 25-mL Class A titration burette can be accurately read to 0.05 mL for a minimum analytical precision of 0.25 mg Cl^-/L .

11.1.2.5 Introduction of a method blank

To assess the introduction of chloride contamination from laboratory reagents, distilled water, glassware, filters, and other supplies or equipment used in the analytical procedure, we recommend preparing a method blank of distilled water, to carry through the entire procedure. The value of chloride determined from this blank is averaged with previous blank values to establish a blank correction for the method. The blank correction is expected to be 0.2-0.3 mL of titrant (1-1.5 mg Cl^-/L) (APHA, 1998).

11.1.3 Sulfate method

The FDOT method of test for free sulfate (SO_4^{2-}) in soil and water (FM 5-553, Appendix F) is a turbidimetric method that relies on light-scattering properties of barium sulfate (BaSO_4) crystals, which are formed when barium chloride (BaCl_2) reacts with sulfate under acidic conditions (APHA, 1998).

The advantages of the method are its adaptability to fast and reliable laboratory and field testing of water with reasonable accuracy and precision. The main disadvantage of this method is the potential interference from suspended particles or water-dissolved organic matter. A second disadvantage is that

barium chloride is a toxic substance and must be handled as a hazardous material.

As a summary FM 5-553 (Appendix F), a pre-packaged aliquot of barium chloride is added to 10 ml of sample, the sample with reagent is initially mixed and then allowed to react for 5-10 minutes without mixing. Light transmittance through the sample is determined with a spectrophotometer within the 5-10 minute reaction window. The sulfate concentration is read from a table of % light transmittance versus concentration. APHA (1998) reported a minimum detection level of 1 mg/L using a 2-cm light path, and for a sample containing a sulfate concentration of 7.45 mg/l, the standard deviation was 0.13 mg/L for a coefficient of variation (CV) of 1.7%. We found a detection limit of 2 mg/L using a 1-cm light path and a CV of 8.9% for a standard solution prepared at a sulfate concentration of 3.0 mg/l.

Figure 11-1 shows a calibration curve for sulfate determination, which is linear if light absorbance (A) rather than light transmittance (T) plotted against sulfate. The relationship between absorbance and transmittance is given by Equation 11-1. Note that for a 1-cm path length this curve is valid down to sulfate concentrations of 2 mg/L. A longer path length would lower the detection limit.

$$A = \log_{10}(1/T) \quad (11-1)$$

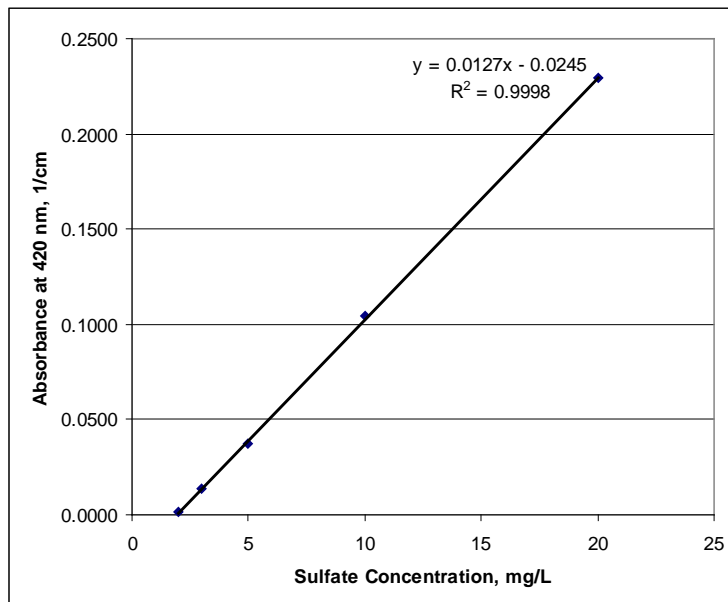


Figure 11-1. Calibration curve for sulfate determination prepared with using a 1-cm path length in a Varian Cary 50 UV/VIS spectrophotometer.

Error in the determination of sulfate concentration can be introduced by:

- Loss or gain of sulfate due to sample storage and handling;
- Interference from suspended particles or water-dissolved organic matter in the sample;
- Coagulation, flocculation, and settling of suspended particles by the addition of barium chloride to the sample;
- Precipitation of barium chloride with a chemical compound other than sulfate;
- Time-dependent barium chloride precipitation;
- Differences in the light spectrum and spectral intensity; between spectrophotometers and between measurements in the same spectrophotometer; and
- Light attenuation by the cuvette placed in the light path.

11.1.3.1 Loss or gain of sulfate due to sample storage and handling

Sulfur is present in water or soils as dissolved salts, as a constituent of organic matter, or in soil minerals. A water or soil sample collected per FM 5-553 will be biologically active, and as such, sulfur may interconvert from its reduced and oxidized forms or between organic and inorganic forms, and/or escape through volatilization (as sulfur dioxide or as hydrogen sulfide) during the collection, transport, and storage of the sample.

FM 5-553 requires that the soil sample be drained of excess water and packaged in a sealed plastic bag with minimal air pockets. This approach reduces the contribution of sulfate from evaporating water and lowers the oxygen pressure within the disturbed soil, and both these measures mitigate potential changes in sulfate concentrations. Similarly, water samples should fill their containers with no headspace. Keeping the soil or water sample at or below its field temperature would also slow microbial activity and thus changes in sulfate concentrations. Once collected, samples should be transported at temperatures within 4-30 °C.

Once the sample reaches the laboratory, FM 5-553 requires that the soil sample be desiccated to constant water content, a step that will slow microbial activity. Air drying versus heating to 110°C is recommended. Water samples should be refrigerated at 4 °C.

Many compounds when exposed to a photon flux or to radicals produced in air or water that is exposed to a photon flux will undergo chemical transformation. Thus, water and soil samples should be stored either in opaque containers or in the dark, or both.

According to FM 5-553, 100 g of soil is extracted with 300 g of water by mixing the suspension for two 20-second periods an hour apart followed by a 12-hour or longer quiescent period. The quiescent period is intended to settle particles suspended in the water during the mixing phase, however, for a soil containing silt or clay, suspended particles will take days to weeks to settle. The combination of high water content, room temperature and a long quiescent incubation period favors the growth of sulfate-reducing bacteria and subsequent transformation of sulfate to hydrogen sulfide and loss of hydrogen sulfide through volatilization.

11.1.3.2 Interference from suspended particles or water-dissolved organic matter in the sample and Coagulation, flocculation, and settling of suspended particles by the addition of barium chloride to the sample

Water or soil extract will contain suspended particles that will absorb or scatter light, which will interfere with the measurement of precipitating barium chloride crystals. FM 5-553 calls for the addition of a few drops of hydrochloric acid (HCl) to the soil extract if the soil extract is cloudy due to the suspension of fine particles. Hydrochloric acid has two effects on these suspended particles: first, the acid digests or dissolves metals and organics, and second, the acid destabilizes suspended particles, which allows them to settle. This is illustrated with light transmittance measurements made on soil extracts before and after the addition of barium chloride reagent (Table 11-2). The higher the light absorbance, the higher is the concentration of suspended particles, which may include barium sulfate if barium chloride has been added.

Absorbance data presented in Table 11-2 revealed some interesting features. Refer to Table 10-2 for a description of each soil. Notice that for Myakka and Candler soil extracts, for example, that the absorbance actually decreases after barium chloride is added. Likely barium chloride, similar to hydrochloric acid, destabilizes suspended particles and allows them to settle faster. The rapid development of a clarified water layer can be seen after addition of barium chloride or hydrochloric acid to cloudy samples. A significant reduction in suspended particle concentrations after hydrochloric acid amendment can be inferred for Myakka, Basinger, Felda soil extracts (Table 11-2).

Table 11-2
Absorbance (1/cm) at 420 nm of Soil Extract Before and After Reaction with Barium Chloride*

Soil Extract	No Reagents	BaCl ₂	HCl + BaCl ₂
Blank	0.0911	0.0925	0.0929
Myakka	0.2864	0.2643	0.1771
Basinger	1.3634	1.7281	0.1299
Chobee	0.1013	0.1025	0.1434
Pomello	0.1188	0.1205	0.1194
Winder	0.2285	0.2343	0.2248
Felda	1.4567	1.9682	0.1208
St. Augustine	0.2159	0.1652	0.2173
Candler	0.2228	0.2099	0.7819

* Soil extracts were allowed to settle for five days.

Centrifugation can improve the separation between water and soil in minutes rather than hours, and simultaneously reduce the amount of dilution water required. We are recommending that the soil-water extraction be done with a 1:1 soil:water mixture, shaken and allowed to equilibrate, and the water separated from soil by centrifugation for 30 minutes at 4,000 rpm. Following centrifugation, filtration through a coarse filter is still necessary to remove floating debris. To clarify the sample before analysis, micro-filtration of the centrate through a 25-mm diameter syringe-tip 0.2 µm pore membrane (Whatman Puradisc) is recommended.

Table 11-3 shows that for the 8 soils tested, absorbance was significantly higher for unfiltered soil extracts. Some reductions in suspended particle concentrations can be seen for unfiltered extracts (no reagents added) that were allowed to settle for 5 days (Table 11-2) instead of 2 days (Table 11-3).

Table 11-3
Absorbance (1/cm) at 420 nm of Soil Extract with and without Filtration through a 0.2-µm Pore Membrane*

Soil Extract	Unfiltered, No Reagents	Unfiltered, BaCl ₂	Filtered, BaCl ₂
Blank	0.0914	0.0925	0.0929
Myakka	0.3145	0.2827	0.1118
Basinger	1.9422	2.2226	0.1008
Chobee	0.4686	0.5784	0.0950
Pomello	0.1494	0.1599	0.1023
Winder	1.6663	0.7370	0.1112
Felda	3.2134	3.3944	0.1069
St. Augustine	0.3275	0.5369	0.1012
Candler	0.3591	0.4089	0.1099

* Soils extracts were settled for 2 days. Note: filtered samples without the BaCl₂ added had the same absorbance as the blank.

Table 11-4 shows the concentrations of sulfate in soil extracts with either hydrochloric acid amendment or micro-filtration employed to remove suspended particles. For soil extracts amended with hydrochloric acid, the barium chloride method yielded sulfate concentrations that were 5 to 10 times higher than for micro-filtered samples.

Table 11-4
Sulfate Concentrations Determined on Unfiltered Soil Extracts Amended with Hydrochloric Acid and on Micro-Filtered Soil Extracts

Soil Extract	SO ₄ ²⁻ Concentration, mg/L	
	Unfiltered, HCl	Filtered
Myakka	22.9 ± 2.8	3.82 ± 0.15
Basinger	17.5 ± 11.7	1.48 ± 0.26
Chobee	13.5 ± 1.4	0.51 ± 0.05
Pomello	10.3 ± 5.3	2.09 ± 0.16
Winder	23.4 ± 13.2	4.16 ± 0.50
Felda	26.7 ± 27.9	3.18 ± 0.38
St. Augustine	24.7 ± 8.7	1.72 ± 0.03
Candler	22.9 ± 2.2	3.55 ± 0.03

11.1.3.3 Time-dependent barium sulfate precipitation

FM 5-553 requires that transmittance measurements be made between 5 and 10 minutes after barium chloride addition to the water or soil extract sample, with the intent to obtain a consistent reading given that particle formation is time-dependent. To characterize this error, a time-dependent absorbance experiment was run with both a 7.5 mg/L SO₄²⁻ standard and a hydrochloric acid-amended extract of Candler soil (Figure 12-2). These results show that the largest changes in absorbance occurred in the first 5 minutes. Between 5 and 10 minutes after the addition of barium chloride, the absorbance changed by 3.8% for the 7.5 mg/L SO₄²⁻ standard and 2.2% for the soil extract.

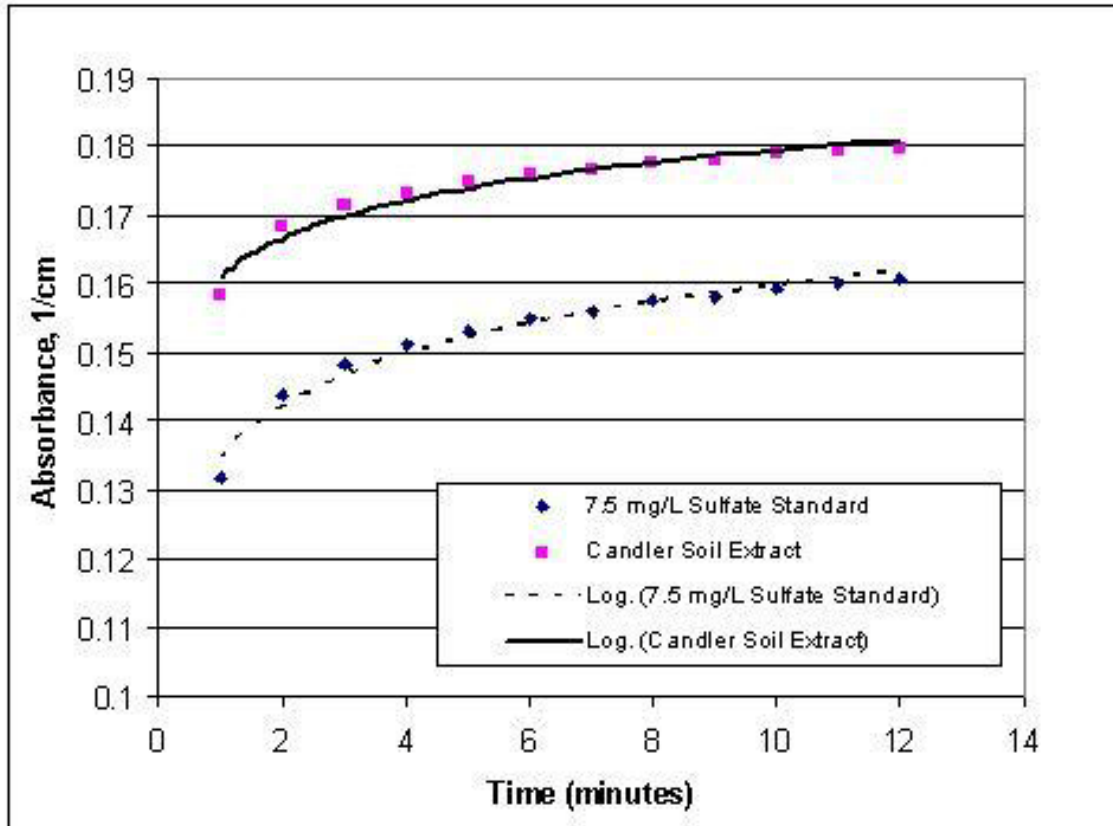


Figure 11-2. Change in sample solution absorbance after the addition of barium chloride.

11.1.3.4 Differences in the light spectrum and spectral intensity; between spectrophotometers and between measurements in the same spectrophotometer and Light attenuation by the cuvette placed in the light path

The Spectronic 20 and similar spectrophotometers use a tungsten lamp, which has a light spectrum from 340 to 950 nm. Near ultraviolet light consists of wavelengths from 200 to 400 nm, visible light consists of wavelengths between 380 and 780 nm, and near infrared light consists of wavelengths from 750 to 1000 nm. Thus, a tungsten lamp generates light that includes not only visible light, but portions of the near ultraviolet and near infrared spectrums.

Within the spectrophotometer, transmitted light intensity can fluctuate with the current through the tungsten filament and with temperature as the filament heats up. Over time the tungsten evaporates from the filament and eventually the light will burn out and need replacement. Between spectrophotometers, differences in the lamp age, the sophistication of the electronic circuitry, cleanliness and alignment of the optics, and extent to which the measurement compartment can be sealed off from stray light will all contribute to the minimum achievable measurement accuracy. Spectronic 20, for example, has an advertised photometric accuracy of 2% of the light transmittance.

FM 5-553 requires transmittance measurements be made at 420 nm. If the spectral bandwidth of the transmitted light is broad enough, a portion of the near ultraviolet spectrum is included in the transmitted light.

Cuvette design, material properties, and cleanliness are essential elements in obtaining an accurate and precise measurement. For measurements made at 420 nm, light transmission will be lower for glass cuvettes than for quartz or polycarbonate cuvettes, as glass cuvettes are not transparent to ultraviolet light. Cuvettes must be handled carefully as smudges, drips, fingerprints, and scratches can scatter or absorb incident light. Further improvements in cuvette design include opaque sides, an arrow marking the side that should face the light source, and a recessed optical face to prevent scratching.

To compensate for the contribution of instrument electronics and optics as well as the optics of the sample cuvette to variations in light transmission through the sample cuvette, FM 5-553 requires that the cuvette containing unreacted water (water with no added barium chloride) be placed in the light path and the % transmittance set equal to 100% prior to a measurement. This method does not include preparation of a calibration curve, an implicit assumption that between measurements and between instruments, the instrument response to increases in suspended barium sulfate particle concentrations is reasonably consistent. In Figure 11-3 is plotted the calibration curve obtained for a Varian Cary and one for a Spectronic 20 spectrophotometer, based on tabulated data in FM 5-553. For the Spectronic 20, the slope changes below 10 mg/L of sulfate, while for the Varian Cary, similar flattening of the slope occurs below 2 mg/L of sulfate. For concentrations of sulfate above 10 mg/L the slopes are different as well: 0.0075 L/mg/cm and 0.0127 L/mg/cm for the Spectronic 20 and Varian Cary, respectively. Table 11-4 summarizes the calculated concentrations for each soil for the two methods. Overall, values determined by calibration curve tended to be lower than those determined by the method and agreement was within a factor of two.

Table 11-4
Summary of Sulfate Concentrations Determined by FM5-553 Spectronic 20
and by Calibration Curve for Varian Cary Spectrophotometers*

Soil	Spectronic 20	Varian Cary	%RE
Basinger	6.11	7.09	-13.8
Candler	16.8	9.35	79.4
Chobee	2.56	6.33	-59.6
Felda	16.2	9.24	75.6
Myakka	17.4	9.50	83.7
Pomello	10.3	7.98	29.4
St. Augustine	8.00	7.49	6.83
Winder	21.2	10.3	106

*Soil extracts were filtered through a 0.2 µm pore size nylon membrane filter prior to analysis by the barium chloride method.

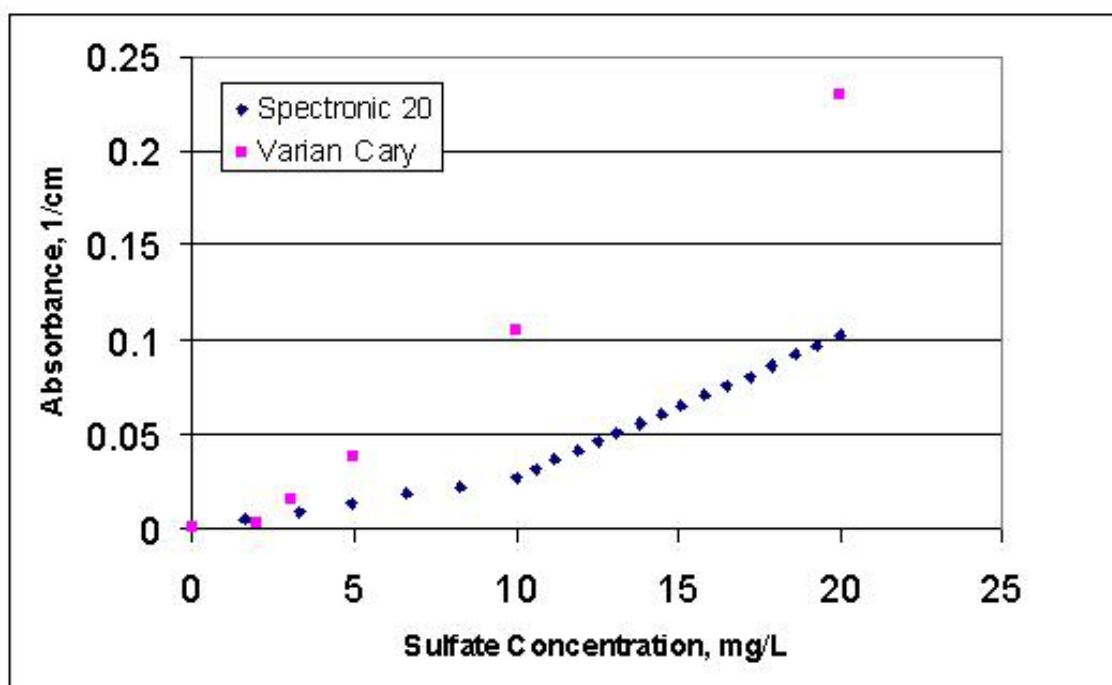


Figure 11-3. Comparison of absorbance versus sulfate concentration for Spectronic 20 and Varian Cary spectrophotometers.

A calibration curve provides the instrument response over the concentration range of interest, and with repeated preparation over time, changes in the slope or intercept of the curve may signal a change in instrument performance or a problem with the calibration standard. The more direct way to detect problems with either the instrument or the standard solutions is to prepare a check standard and test the check standard along with the water or soil extract samples. Ideally the sulfate standard solution used to prepare the check standard should be purchased from a different company than the standard solution used to prepare the calibration curve. The check standard(s) should be

prepared within the range of the calibration curve. Until laboratory data provide the confidence for a lower frequency, run a check standard with every 9 samples, e.g., one-in-ten. The calibration curve is used to calculate the check standard concentration and should agree within $\pm 5\%$ for concentrations between 5 and 100 mg/L, the range over which the slope of absorbance versus concentration is linear. If the check standard fails to agree within $\pm 5\%$, and the problem is not with the method reagents or the check standard, a new calibration curve should be prepared.

11.2 Summary and Conclusions

In summary, several changes are recommended to FDOT methods for pH, resistivity, chloride, and sulfate analysis. Across all methods, the recommended changes are:

- Follow laboratory chain-of-custody and labeling requirements
- Transport in tightly sealed containers in the dark at temperatures between freezing and 30 °C
- Return samples to the lab within 24 hours of sampling if possible;
- Upon return to laboratory, immediately refrigerate water samples at 4° C and air-dry soils at room temperature. Analyze water and soil samples within 28 days.

For individual methods, the recommended changes are:

- Measure pH in the field and report this measurement as field pH.
- For chloride and sulfate analyses, extract soil samples with a 1:1 solution of soil:distilled water, shake samples for 30 minutes, and separate water from soil by centrifugation.
- For chloride and sulfate analyses, measure a standardized solution and method blank, which is carried through the entire procedure, for quality assurance/quality control.
- For sulfate analyses, use a UV/VIS spectrophotometer with UV transparent cuvettes, and quantitative sample concentrations from a calibration curve prepared with dilutions of a standard sulfate solution.
- For sulfate analyses, filter sample extracts through a 0.2 μm nylon membrane filter to remove suspended particles.

12 DURABILITY FORECASTING AND PARAMETER DETERMINATION METHODS. FINDINGS OVERVIEW

12.1 Forecasting methods

This project evaluated FDOT durability forecasting methods for metallic piles and anchors, and for metallic drainage pipes, with a view to assess suitability and recommend changes if needed. The methods are contained in diverse FDOT documents including the SDG and procedures developed by the State Materials Office.

12.1.2 Metallic piles and anchors.

Forecasting methods for these components are contained in the FDOT SDG.

For steel piling, detailed examination of existing alternatives from other agencies and the technical literature revealed no alternative methods to evaluate corrosion related durability that would represent a clear improvement over the present SDG criteria. Caution is advised on the possibility of enhanced corrosion beyond the guideline estimates below the water table and in disturbed soils. Inspection of extracted components is recommended to establish an FDOT-specific performance data base. Recent unexpected severe corrosion incidents in freshwater piling, possibly related to MIC, emphasize the importance of monitoring for corrosion control of these components.

Beyond establishing corrosion protection measures (CPM), durability prediction for anchors in the SDG does not appear to be explicitly addressed for other than wall anchor rods. The CPM follow generally established approaches but no procedure to assess durability of the CPM themselves appears to exist. It is recommended that the issue of CPM durability be considered for possible future development.

12.1.2 Drainage pipes.

Forecasting methods for metallic drainage pipes followed a detailed procedure developed by the State Materials Office.

The procedures for galvanized and clad aluminum pipe are based on nationally established criteria. In the absence of new information to the contrary, no recommendations are made at present for changes. Continuing field performance assessment is recommended.

Until recently, the FDOT method to project durability of aluminized steel type 2 was considered to be similarly adequate. However, newly observed

severe corrosion failure incidents of aluminized pipe took place at much early ages than those predicted by the existing forecasting method. The emphasis of this project shifted to address that issue. Field evidence showed that the corrosion incidents were associated with manufacturing deficiency of the affected pipes. Consequently this investigation examined the factors that determined durability of aluminized steel with mechanical coating distress. It was shown that severe coating distress resulted in enhanced local corrosion, with only modest galvanic protection provided by the coating in the environments for which aluminized pipe is specified. Tests showed that for cases with extensive coating breaks, a precipitation tendency-based method of durability prediction showed promising results. At present the key issue is isolation of the key factors responsible for the accelerated corrosion incidents and continuation research and field assessment is scheduled to follow this investigation.

12.1 Parameter determination methods

This investigation produced improved procedures for the FDOT methods for the determination of pH, resistivity, chloride and sulfate analysis. The procedures include stricter guidelines for sample handling as well as a more reliable instrumentation method for sulfate analysis. Detailed protocols have been provided.

13 REFERENCES

- AASHTO (2007) AASHTO LRFD Bridge Design Specifications, 4th Edition, Customary U. S. Units, American Association of State Highway and Transportation Officials, Washington, D. C., 652 pp.
- Aballe, A., Bethencourt, M., Botana, F. J. (2001), Using EIS to study the electrochemical response of alloy AA5083 in solutions of NaCl, Materials and Corrosion 52, pp. 185-192.
- AISI (1994), T-194, Handbook of Steel Drainage and Highway Construction Products, 5th Edition, American Iron and Steel Institute (AISI), Washington, D. C.
- AISI (1999), Modern Sewer Design, 4th Edition, American Iron and Steel Institute, Washington, D. C., 388 pp.
- AK Steel, Aluminized Steel Type 2 Product Features, (2007)
http://www.aksteel.com/pdf/markets_products/carbon/T2_Data_Bulletin.pdf
- Altech (2007), Final Report Duluth Corrosion Investigation Duluth Harbor, Altech Environmental Services, prepared for U. S. Army Corps of Engineers, DACW35-01-D-0006, Detroit District, MI, 246 pp.
- AMI (2006), DSPA Corrosion Investigation Report, AMI Consulting Engineers, prepared for Minnesota DNR, grant no. 87083, Duluth, MN, 148 pp.
- An, J., Liu, Y. B., Sun, D. R. (2001), Mechanism of bonding of Al–Pb alloy strip and hot dip aluminised steel sheet by hot rolling, Materials Science Technology 17, pp. 451-454.
- Antony, P. J., Raman, R. K. S., Mohanram, R., Kumar, P., Raman, R. (2008), Influence of thermal aging on sulfate-reducing bacteria (SRB)-influenced corrosion behavior of 2205 duplex stainless steel, Corrosion Science 50, pp. 1858-1864.
- APHA (1998), Standard Methods for the Examination of Water and Wastewater, 20th Edition. Clesceri, L., Greenberg, A., Eaton, A., Editors. American Public Health Association, American Water Works Association, and Water Environment Federation, Washington, D. C.
- Armstrong, R.D., Edmondson, K. (1973), Impedance of metals in the passive and transpassive regions, Electrochimica Acta 18, pp. 937-943.
- Armstrong, R.D., Braham, V.J. (1996), The mechanism of aluminum corrosion in alkaline solutions, Corrosion Science 38, pp. 1463-1471.

ASM (1972), Metals Handbook, 8th Edition, Vol. 7, Atlas of Microstructures of Industrial Alloys, Mehl, R., Chairman ASM Handbook Committee, American Society for Metals, Metals Park, OH, 366 pp.

Asplund, G., Christiansen, J. V., Grimvall, A. (1993), A chloroperoxidase-like catalyst in soil: detection and characterization of some properties, Soil Biology and Biochemistry 25, pp. 41-46.

ASTM (2003), D4839-03 Standard Test Method for Organic Carbon in Water by Ultraviolet, Persulfate Oxidation, or Both, and Infrared Detection.

ASTM (2006), G57 - 06 Standard Test Method for Field Measurement of Soil Resistivity Using the Wenner Four-Electrode Method. ASTM International, West Conshohocken, PA. 5 pp.

Augustynski, J., (1978), in: Passivity of Metals, Proceedings of the Fourth International Symposium on Passivity, Frankenthal, R. P., Kruger, J., Editors, The Electrochemical Society, Princeton, NJ, p. 989.

Ault, J. P., Ellor, J. A. (2000), Durability Analysis of Aluminized Type 2 Corrugated Metal Pipe, FHWA-RD-97-140, Federal Highway Administration, Office of Infrastructure Research and Development, McLean, VA, 106 pp.

AWWA (1999), Water Quality and Treatment: A Handbook of Community Water Supplies, 5th Edition, R. Letterman, Editor, American Water Works Association, McGraw-Hill, New York, NY.

AWWA (2005), ANSI/AWWA C105/A21.5-05 American National Standard for Polyethylene Encasement for Ductile-Iron Pipe Systems, 32 pp.

Barchiche, C., Deslouis, C., Festy, D., Gil, O. , Refait, P., Touzain, S., Tribollet, B. (2003), Characterization of calcareous deposits in artificial seawater by impedance techniques - 3-deposit of CaCO₃ in the presence of Mg(II), Electrochimica Acta 48, pp. 1645-1654.

Bard, A. J., Faulkner, L. R. (2000), Electrochemical Methods: Fundamentals and Applications, 2nd Edition, John Wiley & Sons, New York, NY, 856 pp.

Beaton, J. L., Stratfull, R. F. (1962), Field test for estimating the service life of corrugated metal pipe culverts, Highway Research Board Proceedings, Highway Research Board, Washington, D. C., Vol. 41, pp. 255-272.

Beavers, J. A., Durr, C. L. (1998), Corrosion of Steel Piling in Non-Marine Applications, NCHRP Report 408, National Cooperative Highway Research

Program, Transportation Research Board, National Academy Press, Washington, D. C.

Beech, I. B., Campbell, S. A. (2008), Accelerated low water corrosion of carbon steel in the presence of a biofilm harbouring sulphate-reducing and sulphur-oxidising bacteria recovered from a marine sediment, Electrochimica Acta 54, pp. 14-21.

Beech, I. B., Gaylarde, C. C. (1999), Recent advances in the study of Biocorrosion—an overview, Revista de Microbiología 30, 177-190.

Bednar L. (1989), Galvanized steel drainage pipe durability estimation with a Modified California Chart, Transportation Research Record No. 1231, Analysis, Design, and Behavior of Underground Culverts, Washington, D. C., pp. 70-79.

Bednar L. (1989), Durability of plain galvanized steel drainage pipe in South America: criteria for selection, Transportation Research Record No. 1231, Analysis, Design, and Behavior of Underground Culverts, Washington, D. C., pp. 80-87.

Bednar L. (1998), Update of the Status of Field Durability Studies on Aluminized Type 2 Drainage Pipe: Qualifying Durability of Aluminized Type 2 and Clarifying Related Issues, AK Steel research interim document.

Berke, B., Sagüés, A. (2009), Update on Condition of Reinforced Earthwall Straps, Final Report, FDOT Project BD544-32, Florida Department of Transportation, Tallahassee, FL.

Bermont-Bouis, D., Janvier, M., Grimont, P. A. D., Dupont, I., Vallaey, T. (2007) Both sulfate-reducing bacteria and Enterobacteriaceae take part in marine biocorrosion of carbon steel, Journal of Applied Microbiology 102, pp. 161-168.

Berzins, A., Lawson, R. T., Mirans, K. J. (1977), Aluminum corrosion studies. III. Chloride adsorption isotherms on corroding aluminum, Australian Journal of Chemistry 30, pp.1891-1903.

Bessone, J., Mayer, C., Juttner, K., Lorenz, W. J. (1983), AC-impedance measurements on aluminum barrier type oxide films, Electrochimica Acta 28, pp. 171-175.

Bessone, J. B., Salinas, D. R., Mayer, C. E., Ebert, M., Lorenz, W. J. (1992), An EIS study of aluminium barrier-type oxide films formed in different media, Electrochimica Acta 37, pp. 2283-2290.

Bjoergum, A., Sigurdsson, H., Nisancioglu, K. (1995), Corrosion of commercially pure Al 99.5 in chloride solutions containing carbon dioxide, bicarbonate, and copper ions, Corrosion 51, pp. 544-557.

Blackburn, F. E. (2004), Non-bioassy techniques for monitoring MIC, paper no. 04580, Corrosion 2004, NACE International, Houston, TX, 8 pp.

Bockris, J. O'M., Kang, Y. (1997), The protectivity of aluminum and its alloys with transition metals, Journal of Solid State Electrochemistry 1, pp. 17-35.

Bockris, J. O'M., Reddy, A. K. N. (1970), Modern Electrochemistry, in 2 volumes, Plenum Press, New York.

Bohn, H. L., McNeal, B. L., O'Connor, G. A. (1985), Soil Chemistry, 2nd Edition, John Wiley & Sons, New York, NY, 341 pp.

Böhni, H., Uhlig, H. H. (1969), Environmental factors affecting the critical pitting potential of aluminum, Journal of Electrochemical Society 116, pp. 906-910.

Boopathy, R., Daniels, L. (1991), Effect of pH on anaerobic mild steel corrosion by methanogenic bacteria, Applied and Environmental Microbiology Jul., pp. 2104-2108.

Booth, G. H., Cooper, A. W., Tiller, A. K. (1967), Criteria of soil aggressiveness towards buried metals. III. Verification of predicted behavior of selected soils. British Corrosion Journal 2, p. 116.

Bouche, K., Barbier, F., Coulet, A. (1998), Intermetallic compound layer growth between solid iron, Materials Science and Engineering A 249, pp. 167-175.

Bryant, R. D., Jansen, W., Boivin, J., Laishley, E. J., Costerton, J. W. (1991), Effect of hydrogenase and mixed sulfate-reducing bacterial populations on the corrosion of steel. Applied and Environmental Microbiology Oct., pp. 2804-2809.

Burnette (2007) Letter on Behalf of Contech Construction Products to R. Powers, FDOT State Corrosion Technologist.

California Test 643 (1999), Method for Estimating the Service Life of Steel Culverts, State of California, Business, Transportation and Housing Agency, Department of Transportation, Engineering Service Center, Sacramento, CA, 13 pp.

CALTRANS (2003), Corrosion Guidelines Version 1.0, California Department of Transportation, Corrosion Technology Branch, Sacramento, CA, 51 pp. Link: <http://www.dot.ca.gov/hq/esc/ttsb/corrosion/CorrGuidelinesSept03.pdf>.

CALTRANS (2006), Chapter 850 Physical Standards, California Department of Transportation, Highway Design Manual, Sacramento, CA, 42 pp. Link: <http://www.dot.ca.gov/hq/oppd/hdm/pdf/chp0850.pdf>.

CALTRANS (2009) Alternative Pipe Culvert Selection Website, <http://dap1.dot.ca.gov/design/altpipe/>

Camitz, G., Vinka, T. G. (1989), Corrosion of steel and metal-coated steel in Swedish soils—effects of soil parameters, Effects of Soil Characteristics on Corrosion, ASTM STP 1013, Chakar, V. and Palmer, J. D., Editors, American Society for Testing and Materials, Philadelphia, pp. 37-53.

Cáseres, L. (2007), Electrochemical Behavior of Aluminized Steel Type 2 in Scale-Forming Waters, Ph.D. Dissertation, University of South Florida, Department of Civil and Environmental Engineering, 281 pp.

Cáseres, L., Sagüés, A. A. (2005), Corrosion of aluminized steel in scale forming waters, paper no. 05348, 13 pp. Corrosion/2005, NACE International, Houston.

Cáseres, L., Sagüés A. A. (2006), Galvanic behavior of type 2 aluminized steel in simulated natural waters", Corrosion of Infrastructure, The Electrochemical Society, Pennington, NJ, 2007, ECS Transactions Vol. 13, Issue 13, 210th ECS Meeting , Cancun, Mexico, October 29-November 3, 2006, pp. 147-157.

Castro, P., Sagüés, A. A., Moreno, E. I., Maldonado, L., Genesca, J. (1996), Characterization of activated titanium solid reference electrodes for corrosion testing of steel in concrete, Corrosion 52, p. 609-617.

Cerlanek, W.D., Powers, R.G. (1993), Drainage Culvert Service Life Performance and Estimation, State of Florida Department of Transportation Report No. 93-4A.

Chao, C.Y., Lin L.F., MacDonald, D.D. (1981), A point defect model for anodic passive films, Journal of Electrochemical Society 128, pp. 1187-1194.

Chu, D., Savinell, R. (1991), Experimental data on aluminum dissolution in KOH electrolytes, Electrochimica Acta 36, pp. 1631-1638.

Clayton, C. R., Halada, G. P., Kearns, J. R., Gillow, J. B., Francis, A. J. (1994), Spectroscopic study of sulfate reducing bacteria-metal ion interactions related to microbiologically influenced corrosion, Microbiologically Influenced Corrosion Testing, ASTM STP 1232, Kearns, J. R., Little, B. J., Editors, American Society for Testing and Materials, Philadelphia, PA, pp. 141-152.

CONCORRFlorida (2007), Curlew Road Aluminized Steel Type II Pipe Failure Investigation, Prepared for FDOT State Materials Office, Gainesville, Florida.

Cotton, I., Charalambous, C., Aylott, P., Ernst, P. (2005), Stray current control in DC mass transit systems, IEEE Transactions on Vehicular Technologies 54, pp. 722-730.

Creus, J., Mazille, H., Idrissi, H. (2000), Porosity evaluation of protective coatings electrodeposited on steel, Surface and Coatings Technology 130, pp. 224-232.

Cristiani, P., Bianchi, G. (1997), Microbial corrosion prevention in ENEL power plants, Aspects of Microbially Induced Corrosion, European Federation of Corrosion Publications Number 22, papers from EUROCORR '96 and The EFC Working Party on Microbial Corrosion, D. Thierry, Ed., The Institute of Materials, pp. 137-155.

Cristiana, P., Franzetti, A., Bestetti, G. (2008), Monitoring of electro-active biofilm in soil, Electrochimica Acta 54, pp. 41-46.

Cutter, M. R., Stroot, P. G. (2008), Determination of specific growth rate by measurement of specific rate of ribosome synthesis in growing and nongrowing cultures of *Acinetobacter calcoaceticus*, Applied and Environmental Microbiology Feb., pp. 901-903.

Czechowski, M. H., Rossmore, H. W. (1980), Factors affecting *Desulfovibrio desulfuricans* lactate dehydrogenase, Developments in Industrial Microbiology 21, pp. 349-356.

Davies, B. E. (1974), Loss-on-ignition as an estimate of soil organic matter, Soil Science Society of America Journal 38, pp. 150-151.

Davis, J. R. (1999), Corrosion of Aluminum and Aluminum Alloys, ASM International Materials Park, OH. 313 pp.

De Gryse, R., Gomes, W.P., Cardon, F., Vennik, J. (1975), On the interpretation of Mott-Schottky plots determined at semiconductor/electrolyte systems, Journal of Electrochemical Society 122, pp. 711-712.

De Levie, R. (1967), Electrochemical response of porous and rough electrodes, in: Advances in Electrochemistry and Electrochemical Engineering, Delahay, P., Tobias, C. W., Editors, John Wiley & Sons, New York, NY. Pp. 329-397.

De Silva Muñoz, L., Bergel, A., Basséguy, R. (2007) Role of the reversible electrochemical deprotonation of phosphate species in anaerobic biocorrosion of steels, Corrosion Science 49, pp. 3988-4004.

De Wit, J. H. W., Lenderink, H. J. W. (1996), Electrochemical impedance spectroscopy as a tool to obtain mechanistic information on the passive behaviour of aluminum, Electrochimica Acta 41, pp. 1111-1119.

Dieter, G. (1986), Mechanical Metallurgy, 3rd Edition, McGraw-Hill, New York, NY, 800 pp.

Diggle, J. W. (1972), Oxides and Oxide Films, Vol. 1, Marcel Dekker, New York, NY.

Doche, M. L., Rameau, J. J., Durand, R., Novel-Cattin, F. (1999), Electrochemical behaviour of aluminum in concentrated NaOH solutions, Corrosion Science 41, pp. 805-826.

Duquette, D. J., Ricker, R. E. (1985), Electrochemical aspects of microbiologically induced corrosion, Biologically Induced Corrosion, NACE-8, Dexter, S. C., Editor, National Association of Corrosion Engineers, Houston, TX, pp. 121-130.

El-Shamy, A. M., Soror, T. Y., El-Dahan, H. A., Ghazy, E. A., Eweas, A. F. (2009), Microbial corrosion inhibition of mild steel in salty water environment, Materials Chemistry and Physics 114, pp. 156-159.

Emregul, K.C., Abbas Aksut, A. (2000), The behavior of aluminum in alkaline media, Corrosion Science 42, pp. 2051-2067.

Epelboin, I., Keddam, M. (1970), Faradaic impedances: diffusion impedance and reaction impedance, Journal of Electrochemical Society 117, pp. 1052-1056.

Escalante, E. (1989), Concepts of underground corrosion, Effects of Soil Characteristics on Corrosion, ASTM STP 1013, V. Chakar and J. D. Palmer, Editors, American Society for Testing and Materials, Philadelphia, pp. 81-94.

Evans, U. R. (1926), Metal Ind. 29, p. 481.

FDOT (2000) Soils and Foundation Handbook, Florida Department of Transportation, State Materials Office, Gainesville, FL, 163 pp. Link: <http://www.dot.state.fl.us/structures/Manuals/sfh2000.pdf>.

FDOT (2000a) Florida Method of Test for pH of Soil and Water Designation: FM 5-550 Florida Department of Transportation, State Materials Office, Gainesville, FL, 3 pp.

FDOT (2000b) Florida Method of Test for Resistivity of Soil and Water Designation: FM 5-551 Florida Department of Transportation, State Materials Office, Gainesville, FL, 3 pp.

FDOT (2000c) Florida Method of Test for Chloride of Soil and Water Designation: FM 5-552 Florida Department of Transportation, State Materials Office, Gainesville, FL, 3 pp.

FDOT (2000d) Florida Method of Test for Sulfate of Soil and Water Designation: FM 5-553 Florida Department of Transportation, State Materials Office, Gainesville, FL, 5 pp.

FDOT (2007) Standard Specifications for Road and Bridge Construction 2007, State of Florida Department of Transportation, Tallahassee, Florida, 934 pp. Link: <http://www2.dot.state.fl.us/SpecificationsEstimates/Implemented/CurrentBK/Default.aspx>

FDOT (2008), Drainage Handbook: Optional Pipe Materials, Office of Design, Drainage Section, Tallahassee, FL, 40 pp. Link: <http://www.dot.state.fl.us/rddesign/dr/Manualsandhandbooks.shtm>

FDOT (2009a), Drainage Manual, Topic No. 625-040-002-b, State of Florida Department of Transportation, Office of Design, Drainage Section, Tallahassee, FL, 78 pp. Link: <http://www.dot.state.fl.us/rddesign/dr/Manualsandhandbooks.shtm>

FDOT (2009b), Structures Design Guidelines, FDOT Structures Manual, Vol. 1, Structures Design: Florida's Transportation Engineers, 248 pp. Link: <http://www.dot.state.fl.us/structures/manlib.shtm>

Fernandes, J.C.S., Picciochi, R., Da Cunha Belo, M., Moura e Silva, T., Ferreira, M.G.S., Fonseca, I.T.E. (2004), Capacitance and photoelectrochemical studies for the assessment of anodic oxide films on aluminium, Electrochimica Acta 49, pp. 4701-4707.

Feugeas, F., Ehret, G., Cornet, A. (1997), Biofilms analysis of different steels immersed in groundwater, Aspects of Microbially Induced Corrosion, European Federation of Corrosion Publications Number 22, papers from EUROCORR '96 and The EFC Working Party on Microbial Corrosion, D. Thierry, Ed., The Institute of Materials, pp. 77-87.

Finlayson-Pitts, B. J., Pitts, J. M., Jr. (1986), Atmospheric Chemistry: Fundamentals and Experimental Techniques, John Wiley & Sons, New York, NY, 1098 pp.

Foley, R. T. (1986), Localized corrosion of aluminum alloys—a review, Corrosion 42, pp. 277-288.

Frankel, G. S. (1998), Pitting corrosion of metals - a review of the critical factors, Journal of Electrochemical Society 145, pp. 2186-2198.

Furuya, S., Soga, N. (1990), Method for the pitting potential and repassivation potential in crevice corrosion of aluminum alloys, Corrosion 46, pp. 989-993.

Gardiner, C. P., Melchers, R. E. (2002), Corrosion of mild steel in porous media, Corrosion Science 44, pp. 2459-2478.

Gartland, P.O. (1987), Cathodic protection of aluminum-coated steel in sea water, Materials Performance 26, pp. 29-36.

Gerwin, W., Baumhauer, R. (2000), Effect of soil parameters on the corrosion of archaeological metal finds, Geoderma 96, 63-80.

George, R. P., Muraleedharan, P., Sreekumari, K. R., Khatak, H. S. (2003), Influence of surface characteristics and microstructure on adhesion of bacterial cells onto a type 304 stainless steel, Biofouling 19, pp. 1-8.

George, R. P., Marshall, D. Newman, R. C. (2003), Mechanism of a MIC probe, Corrosion Science 45, pp. 1999-2015.

Godard, H. P., Jepson, W. B., Bothwell, M. R., Kane, R. L. (1967), The Corrosion of Light Metals, John Wiley & Sons, New York, NY.

Gribble, G. W. (2003), The diversity of naturally produced organohalogenes, Chemosphere 52, 289-297.

Gu, T., Zhao, K., Nescic, S. (2009), A new mechanistic model for MIC based on a biocatalytic cathodic sulfate reduction theory, paper no. 09390 NACE International Corrosion Conference & Expo, Houston, TX, 12 pp. (See also <http://www.ent.ohiou.edu/~guting/MICORP/> for a copy of the modeling software.)

Gundensen, R., Nisancioglu, K. (1990), Cathodic protection of aluminum in seawater, Corrosion 46, pp. 279-285.

Gupta, S. K., Gupta, B. K. (1979), The critical moisture content in the underground corrosion of mild steel, Corrosion Science 19, pp. 171-178.

Hamilton, W. A., Maxwell, S. (1985), Biological and corrosion activities of sulphate-reducing bacteria within natural biofilms, Biologically Induced Corrosion, NACE-8, Dexter, S. C., Editor, National Association of Corrosion Engineers, Houston, TX, pp. 131-136.

Hamilton, W. A. (2003), Microbially-influenced corrosion as a model system for the study of metal microbe interactions: a unifying electron transfer hypothesis, Biofouling 19, pp. 65-76.

Hannigan, P. J., Goble, G. G., Thendean, G., Likins, G. E., and Rausche, F. (1998), Manual on Design and Construction of Driven Pile Foundations, Workshop Manual--Vol. 1, FHWA-HI-97-013, National Highway Institute, Washington, D. C., 830 pp. Link: http://www.fhwa.dot.gov/engineering/geotech/library_arc.cfm?pub_number=42.

Hicks, R. (2007), Structure of Bacterial Communities Associated with Accelerated Corrosive Loss of Port Transportation Infrastructure, Final Report, Great Lakes Maritime Research Institute, University of Duluth, Duluth, MN, 14 pp.

Hoar, T. P., Mears, D. C., Rothwell, G. P. (1965), The relationships between anodic passivity, brightening and pitting, Corrosion Science 5, pp. 279-289.

Hoch, G. M. (1974), A review of filiform corrosion, Localized Corrosion, R. Staehle, B. Brown, J. Kruger, A. Agrawal, Editors, National Association of Corrosion Engineers, Houston, TX, pp. 134-142.

Hsu, C.H., Mansfeld, F. (2001), Technical note: concerning the conversion of the constant phase element parameter Y_0 into a capacitance, Corrosion 57, pp. 747-748.

Hunter, M. S., Fowle, P. (1956), Natural and thermally formed oxide films on aluminum, Journal of Electrochemical Society 103, pp. 482-485.

Hutchens, E., Williamson, B. J., Anand, M., Ryan, M. P., Herrington, R. J. (2007), Discriminating bacterial electrochemical corrosion using Fe isotopes, Corrosion Science 49, pp. 3759-3674.

Ilhan-Sungur, E., Cansever, N., Cotuk, A. (2007), Microbial corrosion of galvanized steel by a freshwater strain of sulphate reducing bacteria (*Desulfovibrio* sp.), Corrosion Science 49, 1097-1109.

Iverson, W. P. (2001), Research on the mechanisms of anaerobic corrosion. International Biodeterioration & Biodegradation 47, pp. 63-70.

Jack, T. R. (2001), MIC in underground environments: external corrosion in the gas pipeline industry, A Practical Manual on Microbiologically Influenced Corrosion, Vol. 2, Stoecker, J. G., Editor, NACE International, The Corrosion Society, Houston, TX, pp. 6.1-6.12.

Jakab, M.A., Little, D.A., Scully, J.R. (2005), Experimental and modeling studies of the oxygen reduction reaction on AA2024-T3, Journal of Electrochemical Society 152, B311-B320.

Javaherdashti, R. (1999), A review of some characteristics of MIC caused by sulfate-reducing bacteria: past, present, and future, Anti-Corrosion Methods and Materials 46, pp. 173-180.

Javaherdashti, R., Singh Raman, R. K., Panter, C., Pereloma, E. V. (2006), Microbiologically assisted stress corrosion cracking of carbon steel in mixed and pure cultures of sulfate reducing bacteria, International Biodeterioration and Biodegradation 58, 27-35.

Jeffrey, R., Melchers, R. E. (2003), Bacteriological influence in the development of iron sulphide species in marine immersion environments, Corrosion Science 45, pp. 693-714.

Johansson, E., Sandén, P., Öberg, G. (2003), Spatial patterns of organic chlorine and chloride in Swedish forest soil, Chemosphere 52, pp. 391-397.

Johnson, D. B., McGinness, S. (1991), Ferric iron reduction by acidophilic heterotrophic bacteria, Applied and Environmental Microbiology Jan., pp. 207-211.

Johnson, W.K. (1971), Recent developments in pitting corrosion of aluminum, British Corrosion Journal 6, pp. 200-204.

Johansson, T., Nordhag, L. (1984), Corrosion resistance of coatings of aluminum, zinc and their alloys: results of four years' exposure, Interfinish 84, 11th World Congress on Metal Finishing; Jerusalem, Israel, 21-26 October 1984, pp. 412-418.

Jones, D. A. (1996), Principles and Prevention of Corrosion, 2nd Edition, Prentice-Hall, Inc., Upper Saddle River, NJ, 572 pp.

Kaesche, H. (1962), Z. Phys. Chem., Neue Folge 34, pp. 87.

Kaesche H. (1985), Metallic Corrosion: Principles of Physical Chemistry and Current Problems, National Association of Corrosion Engineers, Houston, TX, 492 pp.

Kaesche, H. (1974), Pitting corrosion of aluminum and intergranular corrosion of Al alloys, Localized Corrosion, R. Staehle, B. Brown, J. Kruger, A. Agrawal, Editors, National Association of Corrosion Engineers, Houston, TX, pp. 516-525.

Kajiyama, F., Okamura, K., Koyama, Y., Kasahara, K. (1994), Microbiologically influenced corrosion of ductile iron pipes in soils, in: Microbiologically Influenced Corrosion Testing, STP 1232, Kearns, J. R., Little, B. J., Editors, American Society for Testing and Materials, pp. 266-274.

Kawai, H., Tanji, Y., Miyanaga, K., Hori, K., Unno, H. (2003), Microbiologically influenced corrosion of carbon steel in model soil, paper no. 03558, Proceedings of Corrosion 2003, NACE International, Houston, TX, 16 pp.

Kepaptsoglou, D.M., Svec, P., Janickovic, D., Hristoforou, E. (2007), Evolution of lattice parameter and process rates during nanocrystallization of amorphous Fe–Co–Si–B Alloy, Journal of Alloys and Compounds 434-435, pp. 211-214.

Keppler, F., Eiden, R., Niedan, V., Pracht, J., Schöler, H. F. (2000), Halocarbons produced by natural oxidation processes during degradation of organic matter, Nature 403, pp. 298-301.

Kimoto, H. (1999), Study of galvanic corrosion behavior for aluminized steel in seawater, Corrosion Engineering 48, pp. 432-438.

King, R. A., Miller, J. D. A. (1971), Corrosion by the sulphate-reducing bacteria, Nature 233, pp. 491-492.

Kolics, A., Besing, S., Baradlai, P., Haasch, R., Wieckowski, A. (2001), Interaction of chromate ions with surface intermetallics on aluminum alloy 2024-T3 in NaCl solutions, Journal of Electrochemical Society 148, pp. B251-B259.

Konhauser, K. O. (1998), Diversity of bacterial iron mineralization, Earth-Science Reviews 43, pp. 91-121.

Kostka, J. E., Dalton, D. D., Skelton, H., Dollhopf, S., Stucki, J. W. (2002), Growth of iron(III)-reducing bacteria on clay minerals as the sole electron acceptor and comparison of growth yields on a variety of oxidized iron forms, Applied and Environmental Microbiology Dec., pp. 6256-6262.

Kranc, S. C., Sagues, A. A. (1993), Calculation of extended counter electrode polarization effects on the electrochemical impedance response of steel in concrete, in Electrochemical Impedance: Interpretation and Analysis, ASTM STP 1188, Silverman D. C., Scully, J. R., and Kendig, M. W., Eds., American Society for Testing and Materials, Philadelphia, PA, pp.365-383.

Kranc, S.C., Sagues, A.A. (1993), Polarization current distribution and electrochemical impedance response of reinforced concrete when using guard ring electrodes, Electrochimica Acta 38, pp. 2055-2061.

Lane, R. A. (2005), Under the microscope: understanding, detecting, and preventing microbiologically influenced corrosion, Journal of Failure Analysis and Prevention 5, pp. 10-12, 33-38.

Lasia, A. (1999), Electrochemical impedance spectroscopy and its applications, in: Modern Aspects of Electrochemistry, White, R. E., Conway, B. E., Bockris J. O'M., Editors, Kluwer Academic/Plenum Publishers, New York, NY, Vol. 32, pp. 143-248.

Lazarte, C. A., Elias, V., Espinoza, R. D., Sabatini, P. J. (2003), Geotechnical Engineering Circular No. 7 Soil Nail Walls, FHWA0-IF-03-017, Federal Highway Administration, Office of Technology Application, Office of Engineering/Bridge Division, Washington, D. C., 305 pp.

Lee, A. K., Buehler, M. G., Newman, D. K. (2006), Influence of a dual-species biofilm on the corrosion of mild steel, Corrosion Science 48, pp. 165-178.

Lee, A. K., Newman, D. K. (2003), Microbial iron respiration: impacts on corrosion process, Applied Microbiology and Biotechnology 62, pp. 134-139.

Lee, W., Pyun, S. (1999), Effects of hydroxide ion addition on anodic dissolution of pure aluminum in chloride ion-containing solution, Electrochimica Acta 44, pp. 4041-4049.

Legault, R. A., Pearson, V. P. (1978), Kinetics of the atmospheric corrosion of aluminized steel, Corrosion 34, pp. 344-348.

Lewandowski, Z., Funk, T., Roe, F., Little, B. (1994), Spatial distribution of pH at mild steel surfaces using an iridium oxide microelectrode, Microbiologically Influenced Corrosion Testing, ASTM STP 1232, Kearns, J. R., Little, B. J., Editors, American Society for Testing and Materials, Philadelphia, PA, pp. 61-69.

Li, S., Kim, Y., Kho, Y. (2003), Corrosion behavior of carbon steel influenced by sulfate-reducing bacteria in soil environments, paper no.03549, Proceedings of Corrosion 2003, NACE International, Houston, TX, 20 pp.

Li, S., Kim, Y., Jeon, K., Kho, Y., Kang, T. (2001), Microbiologically influenced corrosion of carbon steel exposed to anaerobic soil, Corrosion 57, pp. 815-828.

Li, W., Liu, S., Huang, Q., Gu, M. (2003), Hot dipped aluminising (HDA) of a low carbon steel wire, Materials Science and Technology 19, pp. 1025-1028.

Linhardt, P. (1997), Corrosion of metals in natural waters influenced by manganese oxidizing microorganisms, Biodegradation 8: 201-210.

Little, B., Lee, J., Ray, R. (2007), A review of 'green' strategies to prevent or mitigate microbiologically influenced corrosion, Biofouling 23, pp. 87-97.

Little, B., J., Ray, R. I., Pope, R. K. (2000), Relationship between corrosion and the biological sulfur cycle: a review, Corrosion 56, pp. 433-443.

Little, B., Wagner, P. (1985), A quantitative investigation of mechanisms for microbial corrosion, Biologically Induced Corrosion, NACE-8, Dexter, S. C., Editor, National Association of Corrosion Engineers, Houston, TX, pp. 209-214.

Little, B., Wagner, P. (1997), Myths related to microbiologically influenced corrosion, Materials Processing 36, 40-44.

Little, B., Wagner, P., Hart, K., Ray, R., Lavoie, D., Neelson, K., Aquilar, C. (1998), The role of biomineralization in microbiologically influenced corrosion, Biodegradation 9, pp. 1-10.

Little, B., Wagner, P., Jones-Meehan, J. (1994), Sulfur isotope fractionation in sulfide corrosion products as an indicator for microbiologically influenced corrosion, Microbiologically Influenced Corrosion Testing, ASTM STP 1232, Kearns, J. R., Little, B. J., Editors, American Society for Testing and Materials, Philadelphia, PA, pp. 180-187.

Little, H. P., Boedecker, K. J., Brawner, J. B. (1977), Performance Evaluation of Corrugated Metal Culverts in Georgia, Southern Corrugated Steel Pipe Association, Washington, D. C., 120 pp.

Lopes, F. A., Morin, P., Olivera, R., Melo, L. F. (2006), Interaction of *Desulfovibrio desulfuricans* biofilms with stainless steel surface and its impact on bacterial metabolism, Journal of Applied Microbiology 101, pp. 1987-1095.

Lorenz, W.J., Mansfeld, F. (1981), Determination of corrosion rates by electrochemical DC and AC methods, Corrosion Science 21, pp. 647-672.

MacDonald, D. D., Real, S., Smedley, S. I., Urquidi-MacDonald, M. (1988), Evaluation of alloy anodes for aluminum-air batteries, Journal of Electrochemical Society 135, pp. 2410-2414.

Magot, M., Tardy-Jacquenod, C., Crolet, J.-L. (1997), An updated portrait of the sulfidogenic bacteria potentially involved in the microbial corrosion of steel, Aspects of Microbially Induced Corrosion, European Federation of Corrosion Publications Number 22, papers from EUROCORR '96 and The EFC Working Party on Microbial Corrosion, D. Thierry, Ed., The Institute of Materials, pp. 3-9.

Mansfeld, F., Lin, S., Kim, S., Shih, H. (1990), Pitting and passivation of Al alloys and Al-based metal matrix composites, Journal of Electrochemical Society 137, pp. 78-82.

Mansfeld, F., Xiao, H. (1994), Electrochemical techniques for the detection of localized corrosion phenomena, in: Microbiologically Influenced Corrosion Testing, STP 1232, Kearns, J. R., Little, B. J., Editors, American Society for Testing and Materials, pp. 42-60.

Mantel, K. E., Hartt, W. H., Chen, T. Y. (1992), Substrate, surface finish, and flow rate influences calcareous deposit structure, Corrosion (Houston) 48, pp. 489-500.

Marconnet, C., Dagbert, C., Roy, M., Féron, D. (2008), Stainless steel ennoblement in freshwater: from exposure tests to mechanisms, Corrosion Science 50, pp. 2342-2352.

Marsh, C. P., Bushman, J., Beitelman, A. D., Buchheit, R. G., Little, B. J. (2005), Freshwater Corrosion in the Duluth—Superior Harbor, Summary of Initial Workshop Findings, 9 September 2004, Final Report, ERDC/CERL SR-05-3, prepared for U. S. Army Corps of Engineers, Washington, D. C., 35 pp. Link: <http://www.seagrant.wisc.edu/CoastalHazards/Portals/5/FreshwaterCorrosionDuluth.pdf>

Martins and Nunes (2006), Reconsidering differential aeration cells, Electrochimica Acta 52, pp. 552-559.

Melchers, R. E. (2003), Modeling of marine immersion corrosion for mild- and low-alloy steels—Part 1: phenomenological model, Corrosion 59, 16 pp.

Melchers, R. E. (2006), Modelling immersion corrosion of structural steels in natural fresh and brackish waters, Corrosion Science 48, pp. 4174-4208.

Melchers, R. E., Jeffrey, R. J. (2008), Probabilistic models for steel corrosion loss and pitting of marine infrastructure, Reliability Engineering and Systems Safety 93, pp. 423-432.

Metwally, I. A., Al-Mandhari, H. M., Gastli, A., Nadir, Z. (2007), Factors affecting cathodic-protection interference, Engineering Analysis with Boundary Elements 31, pp. 485-493.

McCafferty, E. (1995), The electrode kinetics of pit initiation on aluminum, Corrosion Science 37, pp. 481-492.

McCafferty, E. (2003), Sequence of steps in the pitting of aluminum by chloride ions, Corrosion Science 45, pp. 1421-1438.

McCafferty, E. (1974), Electrochemical behavior of iron within crevices in nearly neutral chloride solutions, Journal of Electrochemical Society 121, pp. 1007.

McIntosh, D. H. (1982), Grounding where corrosion protection is required, IEEE Transactions on Industry Applications, 1A-18, pp. 600-607.

Miller, J. D. A., King, R. A. (1975), Biodeterioration of metals, Microbial Aspects of the Deterioration of Materials, Gilbert, R. J., Lovelock, D. W., Editors, Academic Press, London, pp. 83-103.

Moon, S., Pyun, S. (1998), Faradaic reactions and their effects on dissolution of the natural oxide film on pure aluminum during cathodic polarization in aqueous solutions, Corrosion 54, pp. 546-552.

Morley, J., Bruce, D. W. (1983), Survey of Steel Piling Performance in Marine Environments, Commission of the European Communities, Document EUR8492 EN.

Morris, G.E., Bednar L. (1998), Comprehensive Evaluation of Aluminized Steel Type 2 Pipe Field Performance, published by AK Steel Corporation, Middletown, OH.

Morrison, S.R. (1980), Electrochemistry at Semiconductor and Oxidized Metal Electrodes, Plenum Press, New York, NY, 416 pp.

Mulder, E. G. (1964), Iron bacteria, particularly those of the *Sphaerotilus-Leptothrix* group, and industrial problems, Journal of Applied Bacteriology 27, pp. 151-173.

Natishan, P. M., McCafferty, E. (1989), The mechanism of blister formation and rupture in the pitting of ion-implanted aluminum, Journal of Electrochemical Society 136, pp. 53-58.

Newman J. (1966), Resistance for flow of current to a disk, Journal of Electrochemical Society 113, pp. 1235-1241.

Nguyen, T.H., Foley, R.T. (1979), On the mechanism of pitting of aluminum, Journal of Electrochemical Society 126, pp. 1855-1860.

Nielsen, L. V., Hilbert, L. R. (1997), Microbial corrosion of carbon steel by sulfate-reducing bacteria: electrochemical and mechanistic approach, Aspects of Microbially Induced Corrosion, European Federation of Corrosion Publications Number 22, papers from EUROCORR '96 and The EFC Working Party on Microbial Corrosion, D. Thierry, Ed., The Institute of Materials, pp. 11-24.

- Nisancioglu, K., Davanger, K.Y., Strandmyr, O., Holtan, H. (1981), Cathodic behavior of impure aluminum in aqueous media, Journal of Electrochemical Society 128, pp. 1523-1526.
- Nisancioglu K., Holtan H. (1979), Cathodic polarization of commercially pure aluminum, Corrosion Science 19, pp. 537-552.
- Nisancioglu, K., Holtan, H. (1979), Cathodic polarization of aluminum in acetate-buffered chloride media, Electrochimica Acta 24, pp. 1229-1239.
- Nisancioglu, K. (1990), Electrochemical behavior of aluminum-base intermetallics containing iron, Journal of Electrochemical Society 137, pp. 69-77.
- Nizhegorodov, S. Y., Voloskov, S. A., Trusov, V. A., Kaputkina, L. M., Syur, T. A. (2008), Corrosion of steels due to the action of microorganisms, Corrosion 50, pp. 191-195.
- Nord, A. G., Tronner, K., Mattsson, E., Borg, G. Ch., Ullén, I. (2005), Environmental threats to buried archaeological remains, Ambio 34, 256-262.
- NRCS (1999), Soil temperature regimes map, US Department of Agriculture, Natural Resources Conservation Service, Washington, D. C., <http://soils.usda.gov/use/worldsoils/mapindex/str.html>, accessed March 23, 2009.
- Öberg, G. (1998), Chloride and organic chlorine in soil, Acta Hydrochimica et Hydrobiologica 26, pp. 137-144.
- Odom, J. M., Peck, H. D., Jr. (1984), Hydrogenase, electron-transfer proteins, and energy coupling in the sulfate-reducing bacteria *Desulfovibrio*, Annual Reviews in Microbiology 38, pp. 551-592.
- Oh, S.J., Cook, D.C., Townsend, H.E. (1999), Atmospheric corrosion of different steels in marine, rural and industrial Environments, Corrosion Science 41, pp. 1687-1702.
- Oltra, R., Keddari, M. (1988), Application of impedance technique to localized corrosion, Corrosion Science 28, pp. 1-18.
- Örnek, D., Jayaraman, A., Syrett, B. C., Hsu, C.-H., Mansfeld, F. B., Wood, T. K. (2002), Pitting corrosion inhibition of aluminum 2024 by *Bacillus* biofilms secreting polyaspartate or γ -polyglutamate, Applied Microbiology and Biotechnology 58, pp. 651-657.
- Oshe, E. K., Saakiyan, L. S., Efremov, A. P. (2001), Corrosion behavior of aluminum alloys in the presence of hydrogen sulfide, Protection of Metals 37, pp. 572-574.

Palmer, J. D. (1989), Environmental characteristics controlling soil corrosion of ferrous piping, Effects of Soil Characteristics on Corrosion, ASTM STP 1013, V. Chakar and J. D. Palmer, Editors, American Society for Testing and Materials, Philadelphia, pp. 5-17.

Park, J.O., Paik, C.H., Huang, Y.H., Alkire, R.C. (1999), Influence of Fe-rich intermetallic inclusions on pit initiation on aluminum alloys in aerated NaCl, Journal of Electrochemical Society 146, pp. 517-523.

Patenaude, R. (2003), Experimental Culvert Pipe, Sth 80 Juneau and Wood Counties, Wisconsin, Federal Experimental Project # WI 80-02,03,04; Final Report #WI/FEP-09-96, Wisconsin Department of Transportation, Madison, WI, 41 pp.

Paul, E. A., Clark, F. E. (1989), Soil Microbiology and Biochemistry, Academic Press, San Diego, CA, 273 pp.

Peng, C. G., Park J. K. (1994), Principal factors affecting microbiologically influenced corrosion of carbon steel, Corrosion 50, pp. 669-675.

Perkins, J., Cummings, J.R., Graham, K.J. (1982), Morphological studies of occluded cells in the pitting of dilute aluminum alloys in seawater, Journal of Electrochemical Society 129, pp. 137-141.

Pickering, H. W. (2003), Important early developments and current understanding of the IR mechanism of localized corrosion, Journal of Electrochemical Society 150, K1-K13.

Picozzi, O. E., Lamb, S. E., Frank, A. C. (1993) Evaluation of Prediction Methods for Pile Corrosion at the Buffalo Skyway, New York State Department of Transportation, Technical Service Division, Albany, NY, 35 pp.

Piciooreanu, C., van Loosdrecht, M. C. M. (2002), A mathematical model for initiation of microbiologically-influenced corrosion by differential aeration, Journal of the Electrochemical Society 149, pp. B2111-B223.

Porter, F.C., Hadden, S.E. (1953), Corrosion of aluminum alloys in supply waters, Journal of Applied Chemistry 3, pp. 385-409.

Potter, J. C., Lewandowski, L., White, D. W. (1991), Durability of Special Coatings for Corrugated Metal Pipe, FHWA-FLP-91-006, Federal Highway Administration, McLean, VA, 61 pp.

Pourbaix, M. (1974), Atlas of Electrochemical Equilibria in Aqueous Solutions, National Association of Corrosion Engineers, Houston, TX, 644 pp.

Prietzl, J. (2001), Arylsulfatase activities in soils of the Black Forest/Germany—seasonal variation and effect of $(\text{NH}_4)_2\text{SO}_4$ fertilization, Soil Biology & Biochemistry 33, pp. 1317-1328.

Prodromou, K. P., Pavlatou-Ve, A. S. (1998), Changes in soil pH due to the storage of soils, Soil Use and Management 14, pp. 182-183.

Pyskadlo, R., Ewing, J. (1987), Coatings for Corrugated Steel Pipe, Engineering Research and Development Bureau, New York State Department of Transportation, Albany, NY, 34 pp.

Pyun, S.-I., Moon, S.-M., Ahn, S.-H, Kim, S.-S (1999), Effects of Cl^- , NO_3^- and SO_4^{2-} ions on anodic dissolution of pure aluminum in alkaline solution, Corrosion Science 41, pp. 653-667.

Richardson, J. A., Wood, G. C. (1970), A study of the pitting corrosion of Aluminum by scanning electron microscopy, Corrosion Science 10, pp. 313-323.

Robarge, P. R. (1999), Handbook of Corrosion Engineering, McGraw-Hill, New York, NY, 1139 pp.

Roszak, D. B., Colwell, R. R. (1987), Survival strategies of bacteria in the natural environment, Microbiological Reviews Sept., pp. 365-379.

Roels, J., Verstraete, W. (2001), Biological formation of volatile phosphorus compounds, Bioresource Technology 79, pp. 243-250.

Romanoff, M. (1957), Underground Corrosion, National Bureau of Standards Circular 579, U. S. Department of Commerce, U. S. Government Printing Office, Washington, D. C.

Romero, J. M., Velazquez, E., Garcia-Villalobos, J. L., Amaya, M., Le Borgne, S. (2005), Genetic monitoring of bacterial population in a seawater injection system. Identification of biocide resistant bacteria and study of their corrosion effect, paper 05483, NACE Corrosion 2005, NACE International, TX.

Royer, R., Unz, R. (2002), Use of electrical resistance probes for studying microbiologically influenced corrosion, Corrosion 58, pp. 863-870.

Rynders, R., Paik, C., Ke, R., Alkire, R.C. (1994), Use of in situ atomic force microscopy to image corrosion at inclusions, Journal of Electrochemical Society 141, pp. 1439-1445.

Sabatini, P. J., Pass, D. G., Bachus, R. C. (1999), Geotechnical Engineering Circular No. 4, Ground Anchors and Anchored Systems, FHWA-IF-99-015,

Federal Highway Administration, Office of Bridge Technology, Washington, D. C., 281 pp.

Sagüés, A. A. (1989), Corrosion Measurement of Aluminum Alloys and Reinforced Concrete for Determination of Culvert Service Life, Final Report to Florida Department of Transportation, Tallahassee, FL.

Sagüés A.A. (2006), Lectures on Electrochemical Impedance Diagnostic Technique, Department of Civil and Environmental Engineering, University of South Florida.

Sagüés, A. A., Kranc, S. C., Moreno, E. I. (1998), An Improved Method for Polarization Resistance from Small Amplitude Potentiodynamic Scans in Concrete, Corrosion, Vol. 54, p. 20.

Sagüés, A. A., Kranc, S. C., Presuel-Moreno, F., Rey, D., Torres-Acosta, A., Yao, L. (2001), Corrosion Forecasting for 75-year Durability Design of Reinforced Concrete, Report No. BA502, Final Report to Florida Department of Transportation, Tallahassee, FL, 174 pp.

Sagüés, A. A., Pech-Canul, M. A., Al-Mansur, S. (2003), Corrosion macrocell behavior of reinforcing steel in partially submerged concrete column, Corrosion Science, pp. 7-32.

Sagüés, A. A., Scannel, W., Soh, F. W. (1998), Development of a Deterioration Model to Project Future Concrete Reinforcement Corrosion in a Dual Marine Bridge, in: Proceedings International Conference on Corrosion and Rehabilitation of Reinforced Concrete Structures, Orlando, FL, Dec. 7-11, 1998, CD ROM Publication No. FHWA-SA-99-014, Federal Highway Administration.

Sagüés, A. A., Scott, R., Rossi, J., Peña, J., Powers, R. G. (2000), Corrosion of galvanized strips in Florida reinforced earth walls, ASCE's Journal of Materials in Civil Engineering 12, pp. 220-227.

Sander, A., Berghult, B., Elftron Broo, A., Lind Johansson, E., Hedberg, T. (1996), Iron corrosion in drinking water distribution systems—the effect of pH, calcium and hydrogen carbonate, Corrosion Science 38, pp. 443-455.

Sasaki, K., Isaacs, H.S. (2004), Origins of electrochemical noise during pitting corrosion of aluminum, Journal of Electrochemical Society 151, B124-B133.

Sato, N. (1971), A theory for breakdown of anodic oxide films on metals, Electrochimica Acta 16, pp. 1683-1692.

Scannell, W. (2005) Draft Report to FDOT – Phase 1 "Forensic Investigation of Spiral Rib Aluminized Steel Pipe Failures" dated 09/08/05

Scotto, V., Lai, M. E. (1997), Correlation between marine biofilm structure and corrosion behaviour of stainless steels in sea water, Aspects of Microbially Induced Corrosion, European Federation of Corrosion Publications Number 22, papers from EUROCORR '96 and The EFC Working Party on Microbial Corrosion, D. Thierry, Ed., The Institute of Materials, pp. 41-49.

Seinfeld, J. H., Pandis, S. N. (1998), Atmospheric Chemistry and Physics: From Air Pollution to Climate Change, John Wiley & Sons, New York, NY, 1326 pp.

Seri, O., Furumata, K. (2002), Effect of Al-Fe-Si intermetallic compound phases on initiation and propagation of pitting attacks for aluminum 1100, Materials and Corrosion 53, pp. 111-120.

Seri, O., Masuko, N. (1985), Effects of Al-Fe-Si intermetallic compound system on corrosion behaviors of aluminum in NaCl solution, Journal of Japan Institute of Light Metals 35, pp. 98-104.

Serra, E., Glasbrenner, H., Perujo, A. (1998), Hot-dip aluminum deposit as permeation barrier for MANET steel, Fusion Engineering and Design 41, pp. 149-155.

Schwerdtfeger, W. J., Romanoff, M. (1972), NBS Papers on Underground Corrosion of Steel Piling 1962-1971, U. S. Department of Commerce, National Bureau of Standards, Washington, D. C., 63 pp.

Shao, H.B., Wang, J.M., Zhang, Z., Zhang, J.Q., Cao, C.N. (2003), Electrochemical impedance spectroscopy analysis on the electrochemical dissolution of aluminum in an alkaline solution, Journal of Electroanalytical Chemistry 549, pp. 145-150.

Shaw, B. A., Moran, P. J. (1985), Characteristics of the behavior of zinc-aluminum thermal spray coatings, Materials Performance 24, pp. 22-31.

Sherif, E.M., Park, S.-M. (2005), Effects of 1, 5-naphthalenediol on aluminum corrosion as a corrosion inhibitor in 0.50 M NaCl, Journal of Electrochemical Society 152, pp. B205-B211.

Shi, X., Avci, R., Geiser, M., Lewandowski, Z. (2003), Comparative study in chemistry of microbially and electrochemically induced pitting of 316L stainless steel, Corrosion Science 45, pp. 2577-2595.

Snoeyink, V.L., Jenkins, D. (1980), Water Chemistry, John Wiley & Sons Inc., New York, NY, 463 pp.

Starosversky, D., Armon, R., Yahalom, J., Starosversky, J. (2001), Pitting corrosion of carbon steel caused by iron bacteria, International Biodeterioration & Biodegradation 47, pp. 79-87.

Stavros, A.J. (1984), Galvalume corrugated steel pipe: a performance summary, Transportation Research Record N1001, Symposium on Durability of Culverts and Storm Drains, Transportation Research Board, Washington, D. C., p. 69-76.

Stern, M., Geary, A.L. (1957), Electrochemical polarization, I. A theoretical analysis, Journal of Electrochemical Society 104, pp. 56-63.

Straub, K. L., Benz, M., Schink, B. (2001), Iron metabolism in anoxic environments at near neutral pH, FEMS Microbiology Ecology 34, pp. 181-186.

Sullivan, J. P., Dunn, R. G., Barbour, J. C., Wall, F. D., Missert, N., Buchheit, R. G. (2000), Abstract 137, The Electrochemical Society Meeting Abstracts, 2000-1, Ontario, Canada.

Suter, T., Alkire, R.C. (2001), Microelectrochemical studies of pit initiation at single inclusions in Al 2024-T3, Journal of Electrochemical Society 148, pp. B36-B42.

Suzuki I. (1989), Corrosion-Resistant Coatings Technology, Marcel Dekker, New York, NY, 266 pp.

Szklarska-Smialowska, Z. (1999), Pitting corrosion of aluminum, Corrosion Science 41, pp. 1743-1767.

Tan, K. H. (2005), Soil Sampling, Preparation, and Analysis, 2nd Edition, CRC Taylor & Francis, Boca Raton, FL, 623 pp.

Tomlinson, M. J. (1994), Pile Design and Construction Practice, 4th Edition, Taylor & Francis, Inc., London, 411 pp.

Townsend, H. E., Zoccola, J. C. (1979), Atmospheric corrosion resistance of 55% Al-Zn coated sheet steel: 13 year test results, Materials Performance 18, pp. 13-20.

Townsend, H. E., Borzillo, A. R. (1987), Twenty-year atmospheric corrosion tests of hot-dip coated sheet steel, Materials Performance 26, pp. 37-41.

Uhlig, H. H., Revie, R. W. (1985), Corrosion and Corrosion Control: An Introduction to Corrosion Science and Engineering, 3rd Edition, John Wiley & Sons, New York, 441 pp.

Van de Ven, E.P.G.T., Koelmans, H. (1976), The cathodic corrosion of aluminum, Journal of Electrochemical Society 123, pp.143-144.

Vanhaecke, E., Remon, J.-P., Moors, M., Raes, F., de Rudder, D., van Peteghem, A. (1990), Kinetics of *Pseudomonas aeruginosa* adhesion to 304 and 316-L stainless steel: role of cell surface hydrophobicity, Applied and Environmental Microbiology 56, pp. 788-795.

Verhoff, M., Alkire, R.C. (2000), Experimental and modeling studies of single corrosion pits on pure aluminum in pH 11 NaCl solutions II. Pit stability, Journal of Electrochemical Society 147, pp. 1359-1365.

Vermilyea, D. A. (1971), Concerning the critical pitting potential, Journal of Electrochemical Society 118, pp. 529-531.

Videla, H. A. (1985), Corrosion of mild steel induced by sulfate-reducing bacteria—a study of passivity breakdown by biogenic sulfides, Biologically Induced Corrosion, NACE-8, Dexter, S. C., Editor, National Association of Corrosion Engineers, Houston, TX, pp. 162-170.

Videla, H. A. (1996), Manual of Biocorrosion, CRC Lewis Publishers, Boca Raton, FL, 273 pp.

Vijh, A. K. (1973), Pitting potentials of metals, Corrosion Science 13, pp. 805-806.

Vukmirovic, M.B., Dimitrov, N., Sieradzki, K. (2002), Dealloying and corrosion of Al alloy 2024-T3, Journal of Electrochemical Society 149, pp. B428-B439.

Wagner, P. A., Ray, R. I. (1994), Surface analytical techniques for microbiologically influenced corrosion—a review, in: Microbiologically Influenced Corrosion Testing, STP 1232, Kearns, J. R., Little, B. J., Editors, American Society for Testing and Materials, pp.153-169.

Waksman, S. A., Starkey, R. L. (1923), On the growth and respiration of sulfur-oxidizing bacteria, Journal of General Physiology Jan., pp. 285-310.

Wang, J. (1977), Proceedings of Corrosion and Prevention, paper no. 014, Brisbane, Australia.

Wang, H., Sagüés, A. A. (2005), Corrosion of Post-Tensioning Strands, Final Report to Florida Department of Transportation, Report No. BC353-33, 47 pp.

Watling, R., Harper, D. B. (1998), Chloromethane production by wood-rotting fungi and an estimate of the global flux to the atmosphere, Mycological Research 102, pp. 769-787.

Weimer, P., van Kavelaar, M. J., Michel, C. B., Ng, T. K. (1988), Effect of phosphate on the corrosion of carbon steel and on the composition products in two-stage continuous cultures of *Desulfovibrio desulfuricans*, Applied and Environmental Microbiology Feb., pp. 386-396.

Westrich, J. T., Burner, R. A. (1984), The role of sedimentary organic matter in bacterial sulfate reduction: the G model tested, Limnology and Oceanography 29, pp. 236-249.

White, D. C., Nivens, D. E., Nichols, P. D., Mikell, A. T., Jr., Kerger, B. D., Henson, J. M., Geesey, G. G., Clarke, C. K. (1986), Role of aerobic bacteria and their extracellular polymers in the facilitation of corrosion: use of Fourier transforming infrared spectroscopy and "signature" phospholipid fatty analysis, Biologically Induced Corrosion, NACE-8, Dexter, S. C., Editor, National Association of Corrosion Engineers, Houston, TX, pp. 233-243.

Wiersma, B.J., Herbert, K.R. (1991), Observations of the early stages of the pitting corrosion of aluminum, Journal of Electrochemical Society 138, pp. 48-54.

Withiam, J. L., Fishman, K. L., Gaus, M. P. (2002) Recommended Practice for Evaluation of Metal-Tensioned Systems in Geotechnical Applications, NCHRP REPORT 477, National Cooperative Highway Research Program, Transportation Research Board, National Academy Press, Washington, D. C., 142 pp.

Wood, G. C., Richardson, J. A., Abd, M. F., Mapa, L. M., Sutton, W. H. (1978), in: Passivity of Metals, Proceedings of the Fourth International Symposium on Passivity, Frankenthal, R. P., Kruger, J., Editors, The Electrochemical Society, Princeton, NJ, p. 1003.

Wolzogen, Kühr, C. A. H. von, van der Vlugt, L. S. (1934), De grafiteering van gietijzer als electrobiochemisch process in anaerobe gronden, Water, Den Haag, 18, p. 147. Restated in English by Wolzogen, Kühr, C. A. H. von (1961), Unity of anaerobic and aerobic iron corrosion process in the soil, Corrosion 17, p. 293t.

WSS (2009), Web Soil Survey, US Department of Agriculture, National Resources Conservation Service, Link:

<http://websoilsurvey.nrcs.usda.gov/app/HomePage.htm>.

Xanthakos, P. P. (1991), Ground Anchors and Anchored Structures, John Wiley & Sons, New York, NY, 688 pp.

Xu, C., Zhang, Y., Cheng, G., Zhu, W. (2008), Pitting corrosion behavior of 316 stainless steel in the media of sulfate-reducing and iron-oxidizing bacteria, Materials Characterization 59, pp. 245-255.

Xu, L.-C., Chan, K.-Y., Fang, H. H. P. (2002), Application of atomic force microscopy in the study of microbiologically influenced corrosion, Materials Characterization 48, pp. 195-203.

Yu, S.,Y., O'Grady, W. E., Ramaker, D. E., Natishan, P. M. (2000), Investigation of chloride interactions on aluminum with x-ray absorption near edge structure, Journal of Electrochemical Society 147, pp. 2952-2958.

Zintel, T. P., Licina, G. J., Jack, T. R. (2001), Techniques for MIC monitoring, A Practical Manual on Microbiologically Influenced Corrosion, Vol. 2, Stoecker, J. G., Editor, NACE International, The Corrosion Society, Houston, TX, pp. 10.1-10.19.

APPENDIX A SUMMARY OF VISUAL ASSESSMENT AND E_{OC} TRENDS FOR ALUMINIZED STEEL TYPE 2 IN WATERS OF VARYING SCALING TENDENCIES

Test solution	Unblemished ($A_R=0$)		SCB ($A_R \sim 3 \cdot 10^{-4}$)			LCB ($A_R \sim 0.03$)			Macrocell assemblies ($A_R \sim 0.03$)		
	E_{OC} (mV)	Aluminized Surface	E_{OC} (mV)	Steel Surface	Aluminized Surface	E_{OC} (mV)	Steel Surface	Aluminized Surface	E_{OC} (mV)	Steel Surface	Aluminized Surface
P	1: 0-3 hr: ~ -805 2: 0-3 hr: ~ -800 3: 0-5 hr: ~ -800 1: Terminal: ~ -760 2: Terminal: ~ -770 3: Terminal: ~ -800	Bright over the entire exposure time. No visible pits.	1: 0-20 hr: ~ -760 2: 0-20 hr: ~ -760 1: Terminal: ~ -820 2: Terminal: ~ -820	Uniform black/reddish scale from start.	Bright over the entire exposure time. No visible pits.	1: 0-1200 hr: ~ -745 2: 0-1200 hr: ~ -745 3: 0-1500 hr: ~ -740 1: Terminal: ~ -920 2: Terminal: ~ -920 3: Terminal: ~ -905	Uniform black/reddish scale from start. At ~ 450 hr central reddish deposit spot. No preferential corrosion at spot.	Moderate discoloration. Few small isolated pits.	1: 0-1600 hr: ~ -710 2: 0-1700 hr: ~ -740 3: 0-1100 hr: ~ -730 1: Terminal: ~ -885 2: Terminal: ~ -885 3: Terminal: ~ -885	Uniform black/reddish scale from start. At ~ 440 hr, central reddish deposit spot. No preferential corrosion at spot.	Moderate discoloration. Few small isolated pits.
NP	1: 0-5 hr: ~ -650 2: 0-5 hr: ~ -600 1: Terminal: ~ -895 2: Terminal: ~ -930	Moderate discoloration after $\sim 2,250$ hr (1,200 hr). Few small isolated pits.	1: 0-160 hr: ~ -720 2: 0-2 hr: ~ -750 1: Terminal: ~ -900 2: Terminal: ~ -900	Uniform reddish scale from start.	Strong discoloration after $\sim 1,030$ hr (~ 890 hr). ~ 50 μ m outer aluminized coating layer around steel fully lost. Few small isolated pits.	1: 0-1600 hr: ~ -725 2: 0-1200 hr: ~ -725 3: 0-500 hr: ~ -735 1: Terminal: ~ -930 2: Terminal: ~ -725 3: Terminal: ~ -930	Uniform reddish scale from start. At ~ 460 hr central porous reddish deposit spot. Preferential corrosion at spot.	Strong discoloration in #1 and #3 and ~ 70 μ m outer aluminized coating layer around steel fully lost. No discoloration in #2. Few small isolated pits in #1 and #3. No visible pits in #2.	1: 0-800 hr: ~ -710 2: 0-1400 hr: ~ -710 3: 0-850 hr: ~ -710 1: Terminal: ~ -810 2: Terminal: ~ -630 3: Terminal: ~ -925	Uniform reddish scale from start. At ~ 400 hr central porous reddish deposit spot. Preferential corrosion at spot.	Strong discoloration. Few small isolated pits.
C	1: 0-175 hr: ~ -630 2: 0-8 hr: ~ -645 1: Terminal: ~ -840 2: Terminal: ~ -830	Strong discoloration after ~ 310 hr (~ 115 hr). Few isolated pits.	1: 0-1 hr: ~ -615 2: 0-90 hr: ~ -630 3: 0-20 hr: ~ -610 1: Terminal: ~ -695 2: Terminal: ~ -730 3: Terminal: ~ -720	Uniform reddish scale from start in #1. No corrosion scale or discoloration in #2 and #3.	Strong discoloration after ~ 545 hr (~ 648 hr) (~ 624 hr). ~ 50 μ m outer aluminized coating layer around steel fully lost. Few isolated visible pits.	Undergasket corrosion. Data discarded			Undergasket corrosion. Data discarded		
SW	1: 0-3 hr: ~ -780 2: 0-10 hr: ~ -730 1: Terminal: ~ -805 2: Terminal: ~ -835	Light discoloration after ~ 525 hr (~ 585 hr). Few isolated visible pits.	1: 0-1 hr: ~ -750 2: 0-1 hr: ~ -750 1: Terminal: ~ -840 2: Terminal: ~ -850	No corrosion scale or discoloration.	Light discoloration after ~ 275 hr (415 hr). Few isolated visible pits.	1: 0-48 hr: ~ -750 2: 0-30 hr: ~ -750 1: Terminal: ~ -850 2: Terminal: ~ -850	No scale. Very slight discoloration as test progressed.	Light discoloration after ~ 380 hr (~ 360 hr). Few isolated visible pits.	Undergasket corrosion. Data discarded		

A_R = exposed steel/aluminized surface area ratio. Aluminized surface discoloration appeared concurrent with the initiation of E_{OC} drop for the LCB specimens and macrocell assemblies in solutions NP and P, and the SCB specimens in solution C. Initially, the aluminized surface was bright in all specimens. Later on, discoloration, when taking place, was uniformly spread over the entire aluminized surface.

**APPENDIX B RESULTS OF MICROBIAL ANALYSIS FROM SOIL SAMPLES
TAKEN FROM NASSAU SOUND, FLORIDA**

Type of Microbes	Backfill Enumeration CFU/gdw	Backfill SRD ¹	Native Enumeration CFU/gdw	Native SRD	T-2 Invert Enumeration CFU/gdw	T-2 SRD	Galv Invert Enumeration CFU/g	Galv SRD
Heterotrophic Plate Count (Aerobic)	9.7 x 10 ⁶	2.1	1.6 x 10 ⁶	3.2	1.1 x 10 ⁶	3.6	3.0 x 10 ⁶	3.6
Anaerobic Bacteria	4 x 10 ⁴	0.4	3 x 10 ⁵	0.2	4 x 10 ⁵	0.2	1.0 x 10 ⁶	0.3
Yeasts and Molds	7.7 x 10 ⁴	0.6	8.2 x 10 ³	1.5	1 x 10 ³	1.6	2.5 x 10 ³	1.8
Actinomycetes	2.8 x 10 ⁵	0.9	7.3 x 10 ⁴	1.2	2.3 x 10 ⁴	1.4	1.9 x 10 ⁵	1.5
Pseudomonads	3.5 x 10 ⁴	0.9	1.2 x 10 ⁴	3.4	3.1 x 10 ⁴	3.8	4.7 x 10 ⁴	2.6
Nitrogen-Fixing Bacteria	<1 x 10 ³	-0.3	2.0 x 10 ⁴	0.9	8 x 10 ³	1.3	2.2 x 10 ⁴	1.4
Sulfur Oxidizing Bacteria ³	<3		430		930		930	
Sulfate Reducing Bacteria	<1 x 10 ²	-----	<2 x 10 ²	-----	1.4 x 10 ²	-----	1.0 x 10 ⁴	-----
% Moisture (dw)	9.2%	-----	44%	-----	31%	-----	100%	
SRDT ²	-----	4.6	-----	10.4	-----	11.9	-----	11.2

CFU/gdw - Colony Forming Units/gram dry weight sample; CFU/g – Colony Forming Units/gram (applies to aqueous sample). Any analysis result reported as “<” indicates a result below detection limits.

¹ The species richness diversity (SRD) index is derived by weighing the variety of species within a functional group (species richness) from a normalized analysis against the total number of microorganisms associated with that functional group.

² The total species richness diversity index (SRDT) is the sum of the individual SRD's for the six functional groups.

³ Units are most probable number/gram of sample (MPN/g)

APPENDIX C PROPOSED pH METHOD

Florida Method of Test
for
Determining pH of Soil and Water

Designation: FM 5-550

1. SCOPE

This method covers the determination by ion specific electrode of pH for water or soil.

APPARATUS

pH meter and electrode system capable of calibration and having an accuracy of ± 0.1 pH unit.

100 and 250 ml beakers, glass stirring rods, spatula, and paper towels.
Containers for keeping and transporting the sample

REAGENTS

Standard buffered solution for pH 4, 7, and 10. Commercially available solutions are acceptable.

Distilled water

FIELD MEASUREMENT

Immediately after sample collection, use a portable pH meter to measure the pH in a 50-mL water sample or a 25-mL field moist soil sample that is diluted and stirred with 25 mL of distilled water. Follow the manufacturer's instructions for field calibration and measurement. Record this as the sample's field pH.

SAMPLES

Follow laboratory chain-of-custody procedures. Label sample containers either on affixed labels or by permanent marker with a sample number, sample type, name of collector, date and time of collection, place of collection, and sample preservative (if any).

Soil Sampling: Every effort should be made to obtain a soil sample, which is representative of the bulk material. Excessive moisture should be avoided by sampling from an area, which has been allowed to gravity drain for a short time. If the soil sample has excess free moisture, place about 1 kg of the soil on top of

a suitable sieve and cover with plastic. Allow the sample to drain for one hour. This step may be performed in the lab prior to testing. If the soil sample is obtained from a heap, which has been sitting for a long time, take the sample from a depth below the weathered surface where the moisture content appears to have stabilized. Avoid taking the sample from near a weathered soil surface. The soil sample may be taken from underneath standing water, but excess water should not be bagged with the sample. Evaporation will concentrate the ions in solution. A sample volume of 1 to 2 liters (1 to 2 kg) should provide enough samples for all environmental tests.

Transporting Samples: Soil samples should be placed in plastic or plastic-lined bags. The plastic should be squeezed down snugly around the sample and sealed tightly to minimize its contact with the air. Water samples should be collected in clean and leak-proof plastic or glass jars, filled to the top. Keep soil and water samples in the dark and as cool as possible without freezing.

Preparation of Soils: Air dry soil samples as soon as possible after sampling. Spread soil out in a thin layer on wax paper or on plastic trays. Allow soils to air dry at room temperature to a constant weight. Using a rawhide mallet or other suitable device, pulverize the sample as necessary to sieve through an ASTM No. 10 mesh sieve.

Storing Samples: Store air-dried soil samples at room temperature in the dark in air-tight glass or plastic bottles. Store water samples at 4°C in the dark. Analyze samples within 28 days.

PROCEDURE

Calibration of pH Meter: Calibrate the pH meter before each use (refer to manufacturer's instructions). If a series of tests are to be made, recalibrate approximately every 30 minutes. Use a standard buffered solution in the range of the sample to be tested to calibrate, if this is not known, begin with a solution having a pH of 7. The temperature of the solution should not be more than $\pm 10^{\circ}\text{C}$ ($\pm 36^{\circ}\text{F}$) from the temperature of the sample, if it is stabilize the solution to within $\pm 10^{\circ}\text{C}$ ($\pm 36^{\circ}\text{F}$) of the sample. The temperature of the solutions should not, however, be allowed to vary outside the range for which the pH is stable. The manufacturer of the solution will usually provide information of the solution's variation in pH with temperature on the label. In a 100 ml beaker (or other similar size container) pour 25 to 50 ml of the standard solution. This container must be clean. A minimum of two washes with distilled water prior to adding the buffer is recommended. Immerse the electrode in the buffer and adjust the meter to read the known pH. Discard the used buffer. Never put it back in the parent bottle as contamination will take place.

Determining pH of Water: Wash the electrode with distilled water and pat dry with a soft paper. Do not rub the electrode. Immerse the electrode to the depth

recommended by the manufacturer, in the sample to be tested and read the value. If the meter is slow to settle down, gently swirl the sample without removing the electrode for a few seconds then allow the meter to settle and take the reading. Wash the electrode with distilled water between every sample.

Determining pH of Soil: After 5.1 above, wash the electrode with distilled water and pat dry with a soft paper. Do not rub the electrode. Put approximately 100 ml of air-dried, sieved soil sample to be tested in a 250 ml beaker and add a like volume of distilled water. Stir the soil and water mixture thoroughly at 10 minute intervals for a total of 30 minutes. Break up any clumps of soil and do not pass the stirring rod from one sample to another without first cleaning it with distilled water. Continue with Section 5.2.

Sample Integrity: Avoid contamination by cleaning sampling tools after each use and storing samples in clean containers.

Notes:

1. Follow the manufacturer's instructions for maintenance and storage of the pH meter and electrode(s).
2. To avoid transporting laboratory grade equipment to the field it is permissible to use, for field use only, a portable, battery-powered, hand-held pH meter. To be acceptable for this use, the meter must be capable of calibration and must have an advertised accuracy of 0.1 pH unit.
3. Disposable paper or plastic cups may be used in lieu of glass beakers when running the pH test. If this is done never use the cup more than once because absorption will take place in the walls of the container making it impossible to clean.

APPENDIX D PROPOSED RESISTIVITY METHOD

Florida Method of Test for Resistivity of Soil and Water

Designation: FM 5-551

SCOPE

This method covers the determination of resistivity of water or soil using a soil resistance meter and soil box.

APPARATUS

A four terminal, null balancing ohmmeter or multimeter capable of 4-wire resistance measurements from one to one million ohms, with soil box and wire leads.

Spatula, pan for mixing, 100 and 250 ml beakers, squeeze bottle for cleaning and containers for keeping and transporting the sample, distilled water

SAMPLES

Follow laboratory chain-of-custody procedures. Label sample containers either on affixed labels or by permanent marker with a sample number, sample type, name of collector, date and time of collection, place of collection and sample preservative (if any).

Soil Sampling: Every effort should be made to obtain a soil sample, which is representative of the bulk material. Excessive moisture should be avoided by sampling from an area, which has been allowed to gravity drain for a short time. If the soil sample has excess free moisture, place about 1 kg of the soil on top of a suitable sieve and cover with plastic. Allow the sample to drain for one hour. This step may be performed in the lab prior to testing. If the soil sample is obtained from a heap, which has been sitting for a long time, take the sample from a depth below the weathered surface where the moisture content appears to have stabilized. Avoid taking the sample from near a weathered soil surface. The soil sample may be taken from underneath standing water, but excess water should not be bagged with the sample. Evaporation will concentrate the ions in solution. A sample volume of 1 to 2 liters (1 to 2 kg) should provide enough samples for all environmental tests.

Transporting Samples: Soil samples should be placed in plastic or plastic-lined bags. The plastic should be squeezed down snugly around the sample and sealed tightly to minimize its contact with the air. Water samples should be

collected in clean and leak-proof plastic or glass jars, filled to the top. Keep soil and water samples in the dark and as cool as possible without freezing.

Preparation of Soils: Air dry soil samples as soon as possible after sampling. Spread soil out in a thin layer on wax paper or on plastic trays. Allow soils to air dry at room temperature to a constant weight. Using a rawhide mallet or other suitable device, pulverize the sample as necessary to sieve through an ASTM No. 10 mesh sieve.

Storing Samples: Store air-dried soil samples at room temperature in the dark in air-tight glass or plastic bottles. Store water samples at 4°C in the dark. Analyze samples within 28 days.

PROCEDURE

Equipment Set-up: Rinse the soil box with distilled water before starting test. Follow the manufacturer's instructions for hooking up the meter and soil box. A standard soil box will have plates at both ends and a pair of electrode pins spaced out between the plates (Figure 1). The current source from the ohmmeter is connected to the outer plates, and the potential is measured between the pins. Perform a battery check as per manufacturer's instructions before testing if necessary.

Determining Resistivity of Water: Attach wire leads to meter and soil box and fill box with water to be tested, being sure the soil box is level and water is over top of metal plates. If approximate resistivity is not known place the range switch and the dial at the highest position and pull the sensitivity key to the "LOW" position. The meter pointer will move to the right of center indicating too high a setting. While holding the key in the "LOW" position step down through the ranges until the pointer moves to the left of center. Then step back up one range and balance with the dial. For increased sensitivity and a finer balance push the sensitivity key to the "HIGH" position and refine the balance. When balance has been achieved multiply the indicated dial reading by the range switch setting to obtain the resistance in ohms. To get the resistivity apply the multiplying factor, if any, for the box you are using. Most resistance meters come with a soil box calibrated to the meter enabling you to use the direct reading. Wash the soil box with distilled water between each sample. Measurements with an autoranging multimeter capable of 4-wire resistance measurement will of course require less operator interaction.

Determining Resistivity of Soil: Place sample (1000 grams approximately) in a small to medium size pan, round and no more than 12" in diameter allows for better mixing. Mix sample thoroughly, do not add any water at this time. Fill soil box to top taking care to leave no voids and striking excess off top of box. Fill level must be above top of metal plates on ends of box. Obtain resistivity as explained above in Section 4.2. This is the "as is" resistivity, or the resistivity of

the soil in its present condition. Put soil from soil box back in mixing pan, add a small amount of distilled water, 50 or 100 milliliters and mix thoroughly. Fill soil box as before and obtain resistivity. Repeat this process until the resistivity stops dropping or starts to rise again. The result for the test will be the lowest (minimum) resistivity obtained during this process.

Sample Integrity: Wash soil box with distilled water after each sample to avoid contamination between samples. Use clean tools for gathering samples and never transport or store samples in open containers.

Notes:

Follow the manufacturer's instructions for maintenance and storage of the resistance meter and soil box.

The connections of the lead wires must be correct or erroneous readings will result.

Keep all points of connection between lead wires and posts clean and free from corrosion and moisture from the soil or water. A bad connection or broken lead wires will result in the inability to achieve a balance on any range, or an incorrect balance on a number of ranges.

APPENDIX E PROPOSED CHLORIDE METHOD

Florida Method of Test for Chloride in Soil and Water

Designation: FM 5-552

1. SCOPE

This method covers the determination of chloride in water using a silver nitrate buret titration method. Water is tested directly, while soils are tested by first extracting the soluble chloride then testing the solution produced in the extraction. Silver reacts quantitatively with chloride and precipitates as silver chloride. Once the chloride is consumed silver reacts to form a red-colored silver chromate.

2. APPARATUS

Centrifuge

Centrifuge tubes, 50 mL, polyethylene

Buret, Class A, 25 mL, with support stand

Graduated cylinder, 100 mL

Beaker, 250 mL

Erlenmeyer flask, 250 mL

pH paper

Funnel

Filter paper, Whatman No. 4 or equivalent

REAGENTS

Potassium dichromate (supplied as a chloride 2 indicator powder pillow by HACH, catalog number 105766, or equivalent)

Silver nitrate titrant, 0.0141 N or 0.141 N (see Table 1)

Distilled water

Sodium chloride standard solution, 1000 mg Cl⁻ /L

Sulfuric acid, 1 N

Sodium hydroxide, 1 N

SAMPLES

Follow laboratory chain-of-custody procedures. Label sample containers either on affixed labels or by permanent marker with a sample number, sample type, name of collector, date and time of collection, place of collection and sample preservative (if any).

Soil Sampling: Every effort should be made to obtain a soil sample, which is representative of the bulk material. Excessive moisture should be avoided by sampling from an area, which has been allowed to gravity drain for a short time. If the soil sample has excess free moisture, place about 1 kg of the soil on top of a suitable sieve and cover with plastic. Allow the sample to drain for one hour. This step may be performed in the lab prior to testing. If the soil sample is obtained from a heap, which has been sitting for a long time, take the sample from a depth below the weathered surface where the moisture content appears to have stabilized. Avoid taking the sample from near a weathered soil surface. The soil sample may be taken from underneath standing water, but excess water should not be bagged with the sample. Evaporation will concentrate the ions in solution. A sample volume of 1 to 2 liters (1 to 2 kg) should provide enough samples for all environmental tests.

Transporting Samples: Soil samples should be placed in plastic or plastic-lined bags. The plastic should be squeezed down snugly around the sample and sealed tightly to minimize its contact with the air. Water samples should be collected in clean and leak-proof plastic or glass jars, filled to the top. Keep soil and water samples in the dark and as cool as possible without freezing.

Preparation of Soils: Air dry soil samples as soon as possible after sampling. Spread soil out in a thin layer on wax paper or on plastic trays. Allow soils to air dry at room temperature to a constant weight. Using a rawhide mallet or other suitable device, pulverize the sample as necessary to sieve through an ASTM No. 10 mesh sieve.

Storing Samples: Store air-dried soil samples at room temperature in the dark in air-tight glass or plastic bottles. Store water samples at 4°C in the dark. Analyze samples within 28 days.

SAMPLE PREPARATION

Put 100.0 grams of dried soil in a 500 mL Erlenmeyer flask. Add 100.0 mL of de-ionized water, cover, and shake vigorously for 20 seconds. Let stand for 1 hour and repeat agitation. Decant 45 mL into a 50 mL polyethylene centrifuge tube. The approximate yield of clear water per tube is 25 mL. Prepare as many tubes as necessary to obtain the volume required per Table 1. Centrifuge tubes for 40 minutes at 4000 rpm.

For each soil sample, decant the centrate from the centrifuge tubes through Whatman No. 4 filter paper and filter by gravity flow into a clean 250 mL beaker or flask. With pH paper, test the pH of filtrate and adjust to pH 7-9 with 1 N sulfuric acid or 1 N sodium hydroxide. The filtered liquid can now be tested for chloride using the procedure outlined below in section 6.

For each water sample, decant up to 100 mL of sample through Whatman No. 4 filter paper and filter by gravity flow into a clean beaker or flask. With pH paper, test the pH of filtrate and adjust to pH 7-9 with 1 N sulfuric acid or 1 N sodium hydroxide. The filtered liquid can now be tested for chloride using the procedure outlined below in section 6.

If sample water is turbid, put 45 mL of sample water to in a 50 mL polyethylene centrifuge tube. Prepare as many tubes as necessary to obtain the volume required per Table 1. Centrifuge tubes for 40 minutes at 4000 rpm.

Prepare a blank with de-ionized water and carry the blank through every step of the method. This blank will be used to adjust for trace amounts of chloride in the reagent water, bottles, filter paper, tubes, etc.

PROCEDURE

Table 1
Range-Specific Information*

Range (mg/L as Cl ⁻)	Sample volume (mL)	Silver nitrate concentration	Multiplier
0-125	100	0.0141 N	5
100-250	50	0.0141 N	10
200-500	25	0.0141 N	20
500-1,250	100	0.141 N	50
1,000-2,500	50	0.141 N	100
2,500-1,0000	25	0.141 N	200
5,000-25,000	10	0.141 N	500

*If the chloride range is unknown but the soil or water resistivity is known, use a 0.141 N silver nitrate concentration for solutions with resistivity less than 200 Ω -cm.

For a 0.0141 silver nitrate titrant:

Prior to sample analyses, titrate the silver nitrate solution to verify that its concentration has not changed over time. Add 10 mL of the 1,000 mg Cl⁻/L chloride standard solution to a 100 mL volumetric flask then dilute to 100 mL with distilled water and mix thoroughly. This solution has a concentration of 100 mg Cl⁻/L. Add 100 mL of this standard solution to a 250-mL Erlenmeyer flask then add the potassium dichromate reaction indicator and swirl to mix. Record the initial volume of silver nitrate in the buret. Add the silver nitrate by drops to the flask, swirling the flask with each drop, until the color of the sample begins to change from yellow to a reddish-yellow end point. Record the final volume of silver nitrate in the buret. Multiply the difference between the final and initial volumes (in mL) by 5 to obtain the concentration in mg Cl⁻/L. If the result is more than 105 mg Cl⁻/L and the method blank is low (see 6.3), then discard the silver nitrate titrant and replace it with a fresh supply.

For a 0.141 N silver nitrate titrant:

Prior to sample analyses, titrate the silver nitrate solution to verify that its concentration has not changed over time. Add 100 mL of the 1,000 mg Cl⁻/L chloride standard solution to a 250-mL Erlenmeyer flask, then add the potassium dichromate reaction indicator and swirl to mix. Record the initial volume of silver nitrate in the buret. Add the silver nitrate by drops to the flask, swirling the flask with each drop, until the color of the sample begins to change from yellow to a reddish-yellow end point. Record the final volume of silver nitrate in the buret. Multiply the difference between the final and initial volumes (in mL) by 50 to obtain the concentration in mg Cl⁻/L. If the result is more than 1050 mg Cl⁻/L and the method blank is low (see 6.3), then discard the silver nitrate titrant and replace it with a fresh supply.

Determine appropriate sample volume and silver nitrate concentration:

Consult Table 1 to obtain appropriate sample volume and silver nitrate concentration for the expected sample chloride concentration.

Determine chloride blank concentration with a 0.0141 N silver nitrate titrant:

Decant blank into a graduated cylinder to measure a volume of 100 mL. Pour measured volume into a 250 mL Erlenmeyer flask. Add potassium dichromate as a reaction indicator. The sample will turn a bright yellow color. Record the initial volume of 0.0141 N silver nitrate in the buret. Add the silver nitrate by drops to the flask, swirling the flask with each drop, until the color of the sample begins to change from yellow to a reddish-yellow end point. Record the final volume of silver nitrate in the buret. Calculate the difference between the final and initial silver nitrate volumes and record this in mL as the chloride blank. The chloride

blank should be kept as low as possible by minimizing chloride contamination of reagents and glassware. A blank of 0.2 to 0.3 mL is typical.

Determine chloride concentration in soil and water samples:

Decant soil or water filtrate into a graduated cylinder to measure a volume of up to 100 mL per Table 1. Pour measured volume into a 250 mL Erlenmeyer flask. Add potassium dichromate as a reaction indicator. The sample will turn a bright yellow color. Record the initial volume of 0.0141 N silver nitrate in the buret. Add the silver nitrate by drops to the flask, swirling the flask with each drop, until the color of the sample begins to change from yellow to a reddish-yellow end point. Record the final volume of silver nitrate in the buret. Calculate the difference between the final and initial volumes of titrant and subtract from this difference the blank volume. Multiply the net volume of titrant by the appropriate multiplier from Table 1 and record this as the concentration in mg Cl⁻/L.

Notes:

Potassium dichromate and silver nitrate are toxic substances. A material safety data sheet should be included with your reagent kit, if not secure one before attempting to use these chemicals. Store and dispose of potassium dichromate and silver nitrate wastes as hazardous materials.

White paper serves as a suitable background when observing solution colors. Low concentrations of color or suspended particles will not interfere with the titration end point.

The minimum detection level for this method is ~1 mg Cl⁻/L.

This method is adapted from Standard Methods for the Examination of Water and Wastewater, APHA/AWWA/WEF, 4500-Cl⁻ B, Argentometric Method. Refer to this method for details on potential interferences and for laboratory results of relative standard deviation and relative error.

APPENDIX F PROPOSED SULFATE METHOD

Florida Method of Test for Sulfate in Soil and Water

Designation: FM 5-553

SCOPE

This method covers the determination of sulfate in soil and water. Water is tested directly, while soils are tested by first extracting the soluble sulfates then testing the solution produced in the extraction. The water is reacted with barium chloride to precipitate barium sulfate. The amount precipitated is then measured with a spectrophotometer.

APPARATUS

Ultraviolet/visible light (UV/VIS) spectrophotometer

Centrifuge tubes, 50 mL, polyethylene

Beaker, 50 mL

Funnel

Filter paper, Whatman No. 4 or equivalent

Sample vial with cap, 15 mL

Graduated cylinder, 100 mL

Syringe, 10 mL

Syringe-tip filter, 0.2 μm pore size, nylon membrane

UV-transparent cuvette, 1 cm or 2 cm light path

REAGENTS

Barium chloride (BaCl) (supplied as SulfaVer 4 Sulfate Reagent Pillows by HACH, catalog number 21067-69, or equivalent).

Distilled water

Sulfate standard solution: 1,000 mg SO_4^{2-} /L

SAMPLES

Follow laboratory chain-of-custody procedures. Label sample containers either on affixed labels or by permanent marker with a sample number, sample type,

name of collector, date and time of collection, place of collection and sample preservative (if any).

Soil Sampling: Every effort should be made to obtain a soil sample, which is representative of the bulk material. Excessive moisture should be avoided by sampling from an area, which has been allowed to gravity drain for a short time. If the soil sample has excess free moisture, place about 1 kg of the soil on top of a suitable sieve and cover with plastic. Allow the sample to drain for one hour. This step may be performed in the lab prior to testing. If the soil sample is obtained from a heap, which has been sitting for a long time, take the sample from a depth below the weathered surface where the moisture content appears to have stabilized. Avoid taking the sample from near a weathered soil surface. The soil sample may be taken from underneath standing water, but excess water should not be bagged with the sample. Evaporation will concentrate the ions in solution. A sample volume of 1 to 2 liters (1 to 2 kg) should provide enough samples for all environmental tests.

Transporting Samples: Soil samples should be placed in plastic or plastic-lined bags. The plastic should be squeezed down snugly around the sample and sealed tightly to minimize its contact with the air. Water samples should be collected in clean and leak-proof plastic or glass jars, filled to the top. Keep soil and water samples in the dark and as cool as possible without freezing.

Preparation of Soils: Air dry soil samples as soon as possible after sampling. Spread soil out in a thin layer on wax paper or on plastic trays. Allow soils to air dry at room temperature to a constant weight. Using a rawhide mallet or other suitable device, pulverize the sample as necessary to sieve through an ASTM No. 10 mesh sieve.

Storing Samples: Store air-dried soil samples at room temperature in the dark in air-tight glass or plastic bottles. Store water samples at 4°C in the dark. Analyze samples within 28 days.

SAMPLE PREPARATION

Put 100.0 grams of dried soil in a 500 mL Erlenmeyer flask. Add 100.0 mL of de-ionized water, cover, and shake vigorously for 20 seconds. Let stand for 1 hour and repeat agitation. Decant 45 mL into a 50 mL polyethylene centrifuge tube. The approximate yield of clear water per tube is 25 mL. Centrifuge tube for 40 minutes at 4000 rpm.

For each soil sample, decant the centrate from the centrifuge tubes through Whatman No. 4 filter paper and filter by gravity flow into a clean beaker or flask. To remove remaining suspended particles, withdraw 10 mL of filtrate into a syringe, remove any trapped air, and filter through a 0.2- μ m syringe-tip filter into a sample vial. The filtered liquid can now be tested for sulfate using the procedure outlined below in section 6.

For each water sample, decant up to 50 mL of sample through filter paper and filter by gravity flow into a clean beaker or flask. To remove remaining suspended particles, withdraw 10 mL of filtrate into a syringe and filter through a 0.2- μm syringe-tip filter into a sample vial. The filtered liquid can now be tested for chloride using the procedure outlined below in section 6.

If sample water is turbid, put 50 mL of sample water to in a 50-mL polyethylene centrifuge tube. Centrifuge tubes for 30 minutes at 4000 rpm. Decant up to 30 mL of sample through filter paper and filter by gravity flow into a clean beaker or flask.

Prepare a blank with de-ionized water and carry the blank through every step of the method. This blank will be used to adjust for trace amounts of sulfate in the reagent water, bottles, filter paper, tubes, etc.

CALIBRATION CURVE

Prepare an instrument calibration curve for a new instrument, after instrument repair, after lamp replacement, or if the check standard and calibration curve do not agree within $\pm 5\%$.

Spectrophotometer Preparation: Adjust the wavelength control to 420 nm. Perform an instrument and/or lamp warm-up according to the manufacturer's specification if necessary.

Pour 100 ml of a 1,000 mg $\text{SO}_4^{2-}/\text{L}$ sulfate standard solution into a graduated cylinder and allow the solution to reach room temperature. Once the standard solution has reached room temperature, adjust the final volume in the cylinder to 100 mL and transfer the contents of the cylinder to a 1,000-mL volumetric flask. This will result in a 100 mg $\text{SO}_4^{2-}/\text{L}$ sulfate standard. To prepare standards of 0, 20, 40, 60, 80, and 100 mg $\text{SO}_4^{2-}/\text{L}$, transfer 0, 20, 40, 60, 80, and 100 mL into separate 100-ml volumetric flasks and add distilled water to the 100-mL line. If needed, calibration standards can be prepared for a lower range. Refer to Table 1 for guidance on cuvette diameter and dilution factor for a range of sulfate concentrations.

For the 0.0 sulfate concentration: fill a sample vial with 10 mL of a standard solution. Add the contents of one barium chloride pillow to the sample vial and cap the vial. Dissolve the barium chloride crystals by gently inverting the vial a few times. Allow a reaction time of 5 minutes but no more than 10 minutes. Fill a cuvette with the reacted solution and place in the spectrophotometer. Close the sample compartment. Read the absorbance and set to zero.

For each of the remaining sulfate standard solutions: fill a sample vial with 10 mL of a standard solution. Add the contents of one barium chloride pillow to the

sample vial and cap the vial. Dissolve the barium chloride crystals by gently inverting the vial a few times. Allow a reaction time of 5 minutes but no more than 10 minutes. Fill a cuvette with the reacted solution and place in the spectrophotometer. Close the sample compartment. Read and record the absorbance.

Prepare the calibration curve using an electronic spreadsheet such as Microsoft Excel[®]. Plot the sulfate standard concentration on the x-axis and the absorbance on the y-axis. Fit a linear trend model to the data and plot not only the line but the equation for the line. This equation will have the form $y = mx + b$, where m is the slope and b is the intercept of the line.

To calculate the sulfate concentration of the unknown water or soil extract concentration, re-arrange the equation to solve for x : $x = (y-b)/m$.

CHECK STANDARD

Use a check sample between every nine (9) samples, and whenever a new calibration curve is prepared.

Test a check standard solution that is prepared within the range of calibration curve (per 6.3) to assure that the absorbance from the check standard is within 5% of the absorbance predicted by the calibration curve for the check standard concentration. If the agreement is not within 5%, prepare again either the check standard or the calibration curve and re-test.

Fill a sample vial with 10 mL of a standard solution. Add the contents of one barium chloride pillow to the sample vial and cap the vial. Dissolve the barium chloride crystals by gently inverting the vial a few times. Allow a reaction time of 5 minutes but no more than 10 minutes. Fill a cuvette with the reacted solution and place in the spectrophotometer. Close the sample compartment. Read and record the absorbance. Calculate the sulfate concentration (per 6.7).

BLANK

Test the blank that is processed in same way as the samples. Fill a sample vial with 10 mL of the blank solution. Add the contents of one barium chloride pillow to the sample vial and cap the vial. Dissolve the barium chloride crystals by gently inverting the vial a few times. Allow a reaction time of 5 minutes but no more than 10 minutes. Fill a cuvette with the reacted solution and place in the spectrophotometer. Close the sample compartment. Read and record the absorbance. Calculate the sulfate concentration (per 6.7).

PROCEDURE

Table 1
Range-Specific Information*

Range (mg SO ₄ ²⁻ /L)	Pathlength (cm)	Dilution
0-50	2	1
0-100	1	1
100-200	1	2
200-400	1	4
400-1,000	1	10

*If the sulfate range is unknown but the soil or water resistivity is known, use either a factor of 4 or 10 dilutions for solutions with resistivity less than 200 Ω-cm.

Fill a sample vial with 10 mL of the filtered sample solution. Add the contents of one barium chloride pillow to the sample vial and cap the vial. Dissolve the barium chloride crystals by gently inverting the vial a few times. Allow a reaction time of 5 minutes but no more than 10 minutes. Fill a cuvette with the reacted solution and place in the spectrophotometer. Close the sample compartment. Read and record the absorbance.

If the absorbance is outside of the calibration range, dilute the sample and repeat the measurement. Keep track of dilutions and multiply the concentration by the dilution factor to obtain the true sulfate concentration.

Calculate the sulfate concentration (per 6.7). Subtract out the blank concentration. Multiply by the dilution factor.

Notes:

Barium chloride is a toxic substance. A material safety data sheet should be included with your reagent kit, if not secure one before attempting to use this chemical. Store and dispose of barium chloride waste as a hazardous material.

Nylon filters, reagents, and standard solutions have a limited shelf life and are susceptible to contamination during storage and handling.

Note: the minimum detection level for this method is 2 mg SO₄²⁻/L using a 1-cm light path and 1 mg SO₄²⁻/L using a 2-cm light path.

Use a disposable cuvette or between each test wash the cuvette with soap and brush to prevent the build up of precipitate on the cuvette wall.

This method is adapted from Standard Methods for the Examination of Water and Wastewater, APHA/AWWA/WEF, 4500-SO₄²⁻ E, Turbimetric Method. Refer to this method for details on potential interferences and for laboratory results of relative standard deviation and relative error.